Camera-ready copy prepared in Russia by
Alexei Yaremchuk of
Uspekhi Fizicheskikh Nauk

Reviews of Plasma Physics

Edited by B. B. Kadomtsev

Volume 19

CONSULTANTS BUREAU · NEW YORK-LONDON

Camera-ready copy prepared in Russia by
Alexei Yaremchuk of
Uspekhi Fizicheskikh Nauk

Reviews of Plasma Physics

Edited by B. B. Kadomtsev

Volume 19

CONSULTANTS BUREAU · NEW YORK-LONDON

The Library of Congress cataloged the first volume of this title as follows:

Reviews of plasma physics. v. 1–
New York, Consultants Bureau, 1965–
/v. illus. 24 cm.
Translation of Voprosy teorii plazmy.
Editor: v. 1– M. A. Leontovich.

1. Plasma (Ionized gases)—Collected works. I. Leontovich, M. A., ed. II. Consultants Bureau Enterprises, Inc., New York. III. Title: Voprosy teorii plazmy. Eng.

QC718.V63 64-23244

ISBN 0-306-11009-1

10 9 8 7 6 5 4 3 2 1

Printed in the United States of America

CONTENTS

PARAXIAL WKB SOLUTION OF A SCALAR WAVE EQUATION

G. V. Pereverzev

MULTIPLE-MIRROR PLASMA CONFINEMENT

V. V. Mirnov and A. J. Lichtenberg

PLASMA ROTATION IN TOKAMAKS

V. Rozhansky and M. Tendler

PARAXIAL WKB SOLUTION OF A SCALAR WAVE EQUATION

G. V. Pereverzev

Introduction

The ray method or geometric optics is the most powerful and widespread method of solving the wave equation in the short-wavelength limit. It is used in numerous applications of optics, seismology, physics of fluids and solids, quantum mechanics, plasma physics and many other fields [1-3]. The ray method makes use of an asymptotic expansion of the solution sought and reduces the wave equation to an infinite set of coupled equations for successive terms of the expansion. The zero-order term is known as the eikonal approach. It describes the phase behavior in space which represents the most rapid variation of the wave field. It also gives rise to the ray or geometric-optics description in the narrow sense of the latter term. The first-order equation describes the field amplitude evolution along the ray trajectory. This equation has the important corollary that the flux energy is directed along the rays. Only the leading-order equation and this consequence of the first order are mainly used in practice. This reduced approach is usually called the ray-tracing or geometric-optics method. It describes the corpuscular or ray properties of a propagating wave packet.

In many cases of practical interest this method provides almost the only possibility of obtaining a solution. Therefore,

in plasma physics geometric optics is widely used, but, in contrast to conventional optics, it is in most cases far from being really justified and is sometimes clearly irrelevant. For example, as discussed in [4], description of the ballooning instabilities of tokamak plasmas is impossible without modification of the eikonal representation. In many other cases of practical interest, a wave packet is localized in a small enough region and then the wave phenomena which exhibit energy flow transverse to the ray cannot be neglected. Thus in [5] it was shown that diffraction is significant in the lower-hybrid current drive problem. In [6] it was shown that sometimes the ray approximation fails even in the electron cyclotron range of frequencies.

The energy flow transverse to the rays, which has to be included into consideration, appears only on account of the higher-order terms of the asymptotic expansion. However, the higher-order equations of the ray method are very seldom used in practice because of their complexity. The wave properties of the propagating oscillations are usually studied by the quasi-optic approach. This was first introduced as the parabolic-equation technique by Fock and Leontovich [7]. This technique retains the wave description across the ray direction but uses the eikonal approach along with it. Profound developments of the parabolic-equation technique were made by Babič and Buldyrev [8] and Maslov [9]. Some applications of the parabolic equation to plasma physics are described in the review paper [10]. The same physical ideas are used in the concept of the complex eikonal by Choudhary and Felsen [11]. Mathematically, the ray method and the parabolic equation differ in that they use different kinds of asymptotic expansion with respect to the small parameter $\lambda/L \ll 1$, which is the ratio of the characteristic wavelength λ to the characteristic medium inhomogeneity L.

In this paper a method is presented which can be regarded as an application of the parabolic equation to the propagation of narrow wave beams or to eigenfunctions of the "bouncing ball" type [8]. Whereas the ray method uses an asymptotic expansion with respect to integer powers of the small parameter λ/L, in our case half-integer powers of the same parameter are used. Accordingly, the method considered here can also be viewed

as an extension of the WKB technique to the multidimensional case. For the reasons presented below we call this approach the paraxial WKB (pWKB) method. The pWKB method includes conventional ray tracing as a particular case, but it leads to a final set of equations which is different from that of other methods. The approach combines the simplicity of ray tracing with a description of the wave properties, i.e., diffraction and interference. Moreover, in spite of its broader applicability the pWKB method is even more suited to numerical treatment because fewer equations have to be solved in the pWKB method than in the ray-tracing technique.

In Section 1 of this paper the main wave equation to be solved is formulated. The ray-tracing technique and its relation to the pWKB method is briefly discussed. The derivation of the main equations of the pWKB method is described in Section 2. It comprises two successive steps: asymptotic expansion with respect to the small parameter $(\lambda/L)^{1/2} \ll 1$ and then paraxial expansion into Taylor series. The first step gives the trajectory of the center of gravity of a wave packet. This trajectory coincides with the geometric-optics ray and is described by the conventional Hamiltonian set of equations. Another small parameter $\Lambda/L \ll 1$, where Λ is the wave beam width, is used in the subsequent step. As a result, the second-order partial differential wave equation is reduced to a set of first-order ordinary differential equations in terms of the same Hamiltonian function as in the geometric optics. This set of equations is discussed in detail in Section 3. It describes the geometrical frame of the wave packet characterized by such average quantities as the central ray trajectory, the beam width, and the wave front curvature. This frame does not depend upon the amplitude distribution across the beam and is common to a family of wave beams of different transverse structure. The equation for the amplitude is formulated and solved in quadratures in Section 4. It is shown in Section 5 that the pWKB method gives a general solution to the wave equation. Finally, in the Appendices the pWKB technique is described by means of the advanced apparatus of the tensor calculus, which allows a very compact and therefore very transparent representation of the pWKB method.

1. Eikonal approximation of the ray method

1.1. Wave equation and short-wavelength ordering

Let us consider a field of monochromatic waves $e^{-i\omega t}\Phi(\mathbf{r})$ and suppose that the wave amplitude is described by a scalar time-independent wave equation of the form

$$\operatorname{div}(\hat{\varepsilon}\,\nabla\Phi) + \frac{\omega^2}{c^2} N^2(\mathbf{r})\Phi = 0. \tag{1.1}$$

Equation (1.1) represents a rather general form of wave equation and covers a number of cases of practical interest. For instance, if the tensor $\hat{\varepsilon}$ is unitary, then Eq. (1.1) is a Helmholtz equation:

$$\Delta\Phi + \frac{\omega^2}{c^2} N^2(\mathbf{r})\Phi = 0. \tag{1.2}$$

If $N^2(\mathbf{r}) \equiv 0$ and $\varepsilon^\alpha_\beta(\mathbf{r})$ are components of the dielectric tensor $\hat{\varepsilon}$, then Eq. (1.1) describes the electrostatic oscillations of cold plasmas and takes the form

$$\frac{1}{\sqrt{g}} \frac{\partial}{\partial X^\alpha} \sqrt{g} g^{\alpha\gamma} \varepsilon^\beta_\gamma \frac{\partial \Phi}{\partial X^\beta} = 0. \tag{1.3}$$

Here and in what follows we adopt the following summation convention: repeated Greek indices $\alpha, \beta, \gamma, \ldots$ are to be summed from 1 to 3. In addition, $g^{\alpha\beta}$ are the components of the contravariant fundamental tensor $g^{\alpha\beta} = \nabla X^\alpha \cdot \nabla X^\beta$ in the curvilinear coordinate system $\{X^\alpha = X^\alpha(\mathbf{r})\}$, and g is inverse to the determinant of the matrix $g^{\alpha\beta}$, $g = 1/\det|g^{\alpha\beta}|$.

In general, all the coefficients of Eq. (1.1) are space-dependent functions. We seek a solution of Eq. (1.1) taking advantage of the large parameter

$$\kappa = \omega L/c \gg 1, \tag{1.4}$$

where $L = \min\left\{\left|(\nabla \ln|\varepsilon^\beta_\alpha|)\right|^{-1}, \left|(\nabla \ln|N|)\right|^{-1}\right\}$ is the characteristic medium inhomogeneity length. In what follows we mainly use the dimensionless space variables $x^\alpha = X^\alpha/L$.

1.2. Debye asymptotic expansion, eikonal approximation

The conventional technique of solving Eq. (1.1) in the short-wavelength limit $\kappa \gg 1$ is the ray approach based on an expansion of the solution in an asymptotic series with respect to integer powers of κ^{-1} (Debye expansion):

$$\Phi(\mathbf{r}) = \exp\bigl(i\kappa S(\mathbf{r})\bigr) \sum_{n=0}^{\infty} \frac{A_n(\mathbf{r})}{(i\kappa)^n}. \tag{1.5}$$

Substitution of this expansion in the wave equation (1.1) gives to the lowest order the eikonal equation, which determines the eikonal function $S = S(\mathbf{r})$:

$$H \stackrel{\text{def}}{=} \frac{1}{2}\varepsilon^{\alpha\beta} S_\alpha S_\beta - N^2 = 0. \tag{1.6}$$

Here $S_\alpha = \partial S/\partial x^\alpha$ are covariant components of the vector $L\nabla S$, and the tensor

$$\varepsilon^{\alpha\beta} = g^{\alpha\gamma}\varepsilon_\gamma^\beta + g^{\beta\gamma}\varepsilon_\gamma^\alpha \tag{1.7}$$

is real when the tensor ε_β^α is Hermitian (the proof is given in Section 4). The Hamiltonian function $H = H(x^\alpha, S_\alpha)$ as introduced by Eq. (1.6) will play a principal part in our subsequent investigations.

1.3. Ray tracing

The eikonal equation (1.6) is a partial differential equation of the Hamilton–Jacobi type. It may be solved by reduction to the Hamiltonian set of ordinary differential equations

$$\frac{dq^\alpha}{dt} = \frac{\partial H}{\partial S_\alpha}, \tag{1.8}$$

$$\frac{dp_\alpha}{dt} = -\frac{\partial H}{\partial x^\alpha}, \tag{1.9}$$

where the six functions

$$x^\alpha = q^\alpha(t), \quad S_\alpha = p_\alpha(t) \tag{1.10}$$

give the parametric representation of a ray trajectory in 6D phase space. The set of equations (1.8)–(1.9) requires a subsidiary initial condition, which can be given by prescribing the shape of the phase front $S(\mathbf{r}) = \text{const}$. Then the eikonal function S can be determined along all trajectories (1.10) by integration of the equation

$$\frac{dS}{dt} = p_\alpha \frac{dq^\alpha}{dt}. \tag{1.11}$$

The set of equations (1.8), (1.9), (1.11) is widely used in numerous applications. It is known as the eikonal approach or the ray-tracing technique. The next approximation of the ray approach gives the transport equation for the wave amplitude [1]. In accordance with this equation the wave energy propagates strictly along the ray trajectories. No energy flow across rays exists within an accuracy of up to $O(\kappa^{-1})$ of the ray approach. Therefore, such wave phenomena as diffraction and interference are described in the next approximations only. However, higher-order equations of the ray method are practically never used because of their complexity.

It follows from the ray consideration that the Hamiltonian function H determines the ray or corpuscular properties of wave packet propagation. It is far from obvious that the Hamiltonian also affords information about the wave properties of the solution of Eq. (1.1). It will be further shown that, whereas the first derivatives of the Hamiltonian describe propagation of the maximum of the wave packet, the second derivatives describe diffractive broadening of the wave packet. To this end, a new sort of asymptotic expansion differing from Eq. (1.5) is introduced in the next section.

2. Paraxial WKB approach

2.1. Short-wavelength asymptotic expansion

The physical basis of the method discussed here is the concept of taking the functions of the parabolic cylinder as a basis for expanding an approximate solution rather than a Fourier

series with respect to plane waves as in the eikonal approach. It will be seen that, mathematically, this results in an asymptotic expansion with respect to half-integer powers $\kappa^{-n/2}$ of the small parameter κ^{-1}, rather than integer powers κ^{-n} as in the Debye expansion (1.5). The asymptotic expansion considered here is of the same type as in the quasiclassical or WKB approach [12]. Therefore, the method obtained can be regarded as an extension of the WKB method to the multidimensional case. We call it the paraxial WKB (pWKB) method because the essential part of its derivation is based on a paraxial expansion.

A particular solution to the wave equation (1.1) will be sought in the form

$$\Phi_{lm}(\mathbf{r}) = A^{lm}\,\varphi_l(\sqrt{\kappa}u)\,\varphi_m(\sqrt{\kappa}v)\,\exp(i\kappa S), \quad (\text{no sum on } l \text{ and } m), \tag{2.1}$$

where $S = S(\mathbf{r})$, $u = u(\mathbf{r})$, $v = v(\mathbf{r})$, $A^{lm} = A^{lm}(\mathbf{r})$ are unknown functions to be determined. The first three of them are also assumed to be real. $\varphi_l(\xi)$ are the functions of the parabolic cylinder which satisfy the equation

$$\varphi_l''(\xi) + (2l+1)\varphi_l(\xi) - \xi^2\varphi_l(\xi) = 0 \tag{2.2}$$

and can be expressed in terms of the Hermite polynomials $H_l(\xi)$:

$$\varphi_l(\xi) = e^{-\xi^2/2}H_l(\xi)/\sqrt{\pi^{1/2}2^l l!}. \tag{2.3}$$

Substitution from Eq. (2.1) into the wave equation (1.1) results in

$$\begin{aligned}
&-A^{lm}\varphi_l\varphi_m\left[\frac{1}{2}\varepsilon^{\alpha\beta}\left(S_\alpha S_\beta - u^2u_\alpha u_\beta - v^2v_\alpha v_\beta\right) - N^2\right] \\
&+i\kappa^{-1/2}A^{lm}\left(\varphi_l'\varphi_m\varepsilon^{\alpha\beta}S_\alpha u_\beta + \varphi_l\varphi_m'\varepsilon^{\alpha\beta}S_\alpha v_\beta\right) \\
&+i\kappa^{-1}\varphi_l\varphi_m\mathcal{L}[A^{lm}] + \kappa^{-1}A^{lm}\varphi_l'\varphi_m'\varepsilon^{\alpha\beta}u_\alpha v_\beta + O(\kappa^{-3/2}) = 0.
\end{aligned} \tag{2.4}$$

Here

$$\begin{aligned}
\mathcal{L}[A^{lm}] \stackrel{\text{def}}{=} \varepsilon^{\alpha\beta}S_\beta\frac{\partial A^{lm}}{\partial x^\alpha} + \frac{A^{lm}}{\sqrt{g}}\frac{\partial}{\partial x^\alpha}\left(\sqrt{g}g^{\alpha\gamma}\varepsilon_\gamma^\beta S_\beta\right) \\
+iA^{lm}\varepsilon^{\alpha\beta}\left[\left(l+\frac{1}{2}\right)u_\alpha u_\beta + \left(m+\frac{1}{2}\right)v_\alpha v_\beta\right],
\end{aligned} \tag{2.5}$$

and the subscripts α, β denote partial derivatives with respect to the corresponding spatial coordinate, i.e.,

$$S_\alpha = \frac{\partial S}{\partial x^\alpha}, \quad u_\alpha = \frac{\partial u}{\partial x^\alpha}, \quad v_\alpha = \frac{\partial v}{\partial x^\alpha}. \tag{2.6}$$

To satisfy Eq. (2.6), it is not sufficient to annul the coefficients for different powers of κ because the large parameter κ is also included in the argument of the functions φ_l. Therefore, we require

$$\varepsilon^{\alpha\beta}\left(S_\alpha S_\beta - u^2 u_\alpha u_\beta - v^2 v_\alpha v_\beta\right) = 2N^2, \tag{2.7}$$

$$\varepsilon^{\alpha\beta} S_\alpha u_\beta = \varepsilon^{\alpha\beta} S_\alpha v_\beta = \varepsilon^{\alpha\beta} u_\alpha v_\beta = 0, \tag{2.8}$$

$$\mathcal{L}[A^{lm}] = 0. \tag{2.9}$$

The significant feature of the derivation is the assumption that all the functions $S(\mathbf{r})$, $u(\mathbf{r})$, $v(\mathbf{r})$, $A^{lm}(\mathbf{r})$ have the same characteristic size of spatial variation as the medium inhomogeneity length L:

$$\begin{aligned} L &= \min\left(\frac{|\varepsilon^\beta_\alpha|}{|\nabla\varepsilon^\beta_\alpha|}, \frac{|N|}{|\nabla N|}\right) \\ &\approx \min\left(\frac{|A^{lm}|}{|\nabla A^{lm}|}, \frac{|S|}{|\nabla S|}, \frac{|u|}{|\nabla u|}, \frac{|v|}{|\nabla v|}\right). \end{aligned} \tag{2.10}$$

Thus, a faster scale of variation is included in Eq. (2.4) via the functions of the parabolic cylinder φ_l only. It is also seen that in accordance with Eq. (2.2) φ_l'' (and hence φ_l') is of the same order as φ_l. However, $\partial\varphi_l/\partial x^\alpha$ is of order $\kappa^{1/2}\varphi_l$. During the derivation of Eq. (2.4), with allowance for Eq. (2.2), the quantity φ_l'' was split into two terms. With this formal ordering the last term on the left-hand side of Eq. (2.2) is attributed to the leading order in Eq. (2.4), while the second term of Eq. (2.2) appears in the second order of Eq. (2.4). Such a partition seems artificial but is made on strong physical grounds, which will be discussed in Section 4. Here we note only that Eqs. (2.7)–(2.8) do not depend on l and m and determine the Gaussian backbone, which gives the coarse structure of the wave packet, while Eq. (2.9)

describes the amplitude distribution over the beam cross section in more detail.

It is instructive to rewrite this set of equations in terms of the Hamiltonian function H given by Eq. (1.6). To this end, we introduce the notations

$$H_U = u_\alpha \frac{\partial H}{\partial S_\alpha}, \quad H_V = v_\alpha \frac{\partial H}{\partial S_\alpha}, \quad H_{VV} = v_\alpha v_\beta \frac{\partial^2 H}{\partial S_\alpha \partial S_\beta},$$
$$H_{UU} = u_\alpha u_\beta \frac{\partial^2 H}{\partial S_\alpha \partial S_\beta}, \quad H_{UV} = u_\alpha v_\beta \frac{\partial^2 H}{\partial S_\alpha \partial S_\beta}. \tag{2.11}$$

Equations (2.7)–(2.8) now take the form

$$H = \frac{1}{2} u^2 H_{UU} + \frac{1}{2} v^2 H_{VV}, \tag{2.12}$$
$$H_U = H_V = 0, \tag{2.13}$$
$$H_{UV} = 0. \tag{2.14}$$

The system (2.12)–(2.14) constitutes not merely a redesignation of Eqs. (2.7)–(2.8). It is valid for more general Hamiltonians than that given by Eq. (1.6). In particular, a much more complicated case of electromagnetic waves described by a set of Maxwell equations can also be represented in the form (2.12)–(2.14). The treatment presented in what follows makes use only of the general form of Eqs. (2.12)–(2.14) and does not use the specific expression for the Hamiltonian function unless a statement to the contrary is explicitly made.

The system (2.9), (2.12)–(2.14) is a system of five equations in four unknowns $S = S(\mathbf{r})$, $v = v(\mathbf{r})$, $u = u(\mathbf{r})$, and $A^{lm} = A^{lm}(\mathbf{r})$. Nevertheless, the system is consistent and is, moreover, underdetermined; a solution exists and still allows a great deal of arbitrariness. The wave amplitude A^{lm} is included solely in Eq. (2.9). This equation is somewhat different from that describing the transport of the wave amplitude in the ray approach. However, Eq. (2.9) can also be reduced to a linear ordinary differential equation and then solved in a similar way. This will be considered in Section 4.

The set of equations (2.12)–(2.13) is the same as obtained in [11]. An efficient method of solving this set of equations is

described there. In this method the property of Eq. (2.19) is used and the so-called orthogonal trajectories formed by curves $S(\mathbf{r}) = \text{const}$ are found. In what follows, however, we shall use another technique, which is more appropriate to the case under consideration.

2.2. Reference ray

Note that the set of equations (2.12)–(2.14) has the solution

$$x^\alpha = q^\alpha(t), \quad S_\alpha = p_\alpha(t), \quad v(\mathbf{r}) \equiv u(\mathbf{r}) \equiv 0, \tag{2.15}$$

where the functions $q^\alpha(t)$ and $p_\alpha(t)$ are determined by the Hamiltonian set of equations (1.8)–(1.9). On substitution from Eqs. (2.15), Eqs. (2.13)–(2.14) are fulfilled identically and Eq. (2.9) coincides with the amplitude transport equation of the eikonal approach. This means that the eikonal approach is included in the solution (2.1) as a particular case when the initial conditions given on some spatial surface σ are consistent with Eqs. (2.15). In the general case, $u(\mathbf{r}) \not\equiv 0$ and $v(\mathbf{r}) \not\equiv 0$, and Eqs. (2.15) no longer give a solution of system (2.12)–(2.14). However, the first two of Eqs. (2.15) still represent an approximate solution of Eqs. (2.12)–(2.14) in the vicinity of the spatial curve $u(\mathbf{r}) = v(\mathbf{r}) = 0$. It is clear that this curve is a characteristic (ray) of Eq. (1.1). Thus, each ray generates a family of solutions such that $v = u = 0$ on the ray, but $u \neq 0$ and $v \neq 0$ outside this ray. To clarify the difference between such solutions and the eikonal approach, let us consider the behavior of the wave amplitude $|\Phi|$ of Eq. (1.9). To this end, we calculate

$$\begin{aligned} \nabla|\Phi_{lm}| &= \nabla\left[|A^{lm}|\varphi_l(\sqrt{\kappa}u)\varphi_m(\sqrt{\kappa}v)\right] \\ &= \sqrt{\kappa}\,|A^{lm}|\,(\varphi_l'\nabla u + \varphi_m'\nabla v) + o\left(\kappa^{1/2}\right). \end{aligned} \tag{2.16}$$

Equation (2.16) shows that ∇u and ∇v are the directions of the fastest decay of the wave amplitude $|\Phi_{lm}|$. Let us now introduce the quantity

$$V^\alpha = \frac{\partial H}{\partial S_\alpha}. \tag{2.17}$$

Equation (2.17) gives contravariant components of the vector $\mathbf{V}$, which is collinear to a vector of the group velocity. In accordance with Eq. (1.8) $\mathbf{V}$ is tangential to the ray

$$x^\alpha = q^\alpha(t),$$
$$S_\alpha = p_\alpha(t). \tag{2.18}$$

Equation (2.18) coincides in form with Eq. (1.10). However, the difference is that Eq. (1.10) describes a manifold of all geometric-optics rays and Eq. (2.18) gives a single ray which coincides with a skew curve $u(\mathbf{r}) = v(\mathbf{r}) = 0$. Moreover, in contrast to Eq. (2.15), we assume that outside this curve $u(\mathbf{r}) \neq 0$ and $v(\mathbf{r}) \neq 0$. Equation (2.13) can now be written as

$$H_U = \mathbf{V}\nabla u = 0, \quad H_V = \mathbf{V}\nabla v = 0. \tag{2.19}$$

Consequently, both vectors ∇u and ∇v are orthogonal to the vector of the group velocity $\mathbf{V}$. Equation (2.16) shows that Eq. (2.1) describes a wave beam with exponential decay outside the skew curve (2.18). This curve is, therefore, the spatial axis of the wave beam. To be more precise, this curve describes the trajectory of the center of gravity of the wave-packet amplitude [13] and plays a basic part in the following consideration. It is called the *reference ray* and is denoted by $\Re$. By virtue of Eq. (2.16) the wave solution (2.1) is located in the vicinity of the reference ray (2.18). It also follows that the wave energy propagates along this ray and the vector $\mathbf{V}$ retains the same meaning as in the eikonal approach.

2.3. Wave-packet description

Let us introduce the characteristic length of the amplitude decay $\Lambda = \min(|\Phi/\nabla\Phi|)$. It is physically evident that the case $\lambda \approx L$ as well as the case $\lambda \approx \Lambda$ have to be treated numerically when an exact solution cannot be found. Therefore, the inequality $\lambda \ll \Lambda, L$ can be regarded as a natural restriction on any asymptotic approach.

We now discuss the relation between the other two quantities, Λ and L. The ray method is implicitly based on the idea

that the plane wave as an exact solution to the wave equation in a homogeneous medium also remains a reasonable approximation for inhomogeneous media. At first sight, this can indeed be expected to be the case for weakly inhomogeneous media at least. It is in fact never the case, because a plane wave has an infinite localization size $\Lambda = \infty$ which is always more than any finite length of the medium inhomogeneity L. To overcome this contradiction, the amplitude factor (A_n in Eq. (1.5)) is used in the ray method to describe a wave packet of finite size. This allows one to improve the situation, but the ray expansion is still restricted to consideration of nearly plane waves and, consequently, requires that the wave amplitude $A_0(\mathbf{r})$ in Eq. (1.5) vary only slowly in space over a length of order L [1] or, in our notation, $\Lambda \approx L$. In other words, the ray method makes no distinction between characteristic lengths of medium L and wave amplitude Λ variations, viewing both lengths as the same quantity.

As already mentioned in the Introduction, this requirement is rather restrictive. In the solution (2.1) the same restriction as in the eikonal approach is imposed on the function A^{lm} rather than on the wave amplitude. The latter varies, as described, mainly by the exponential factor in the functions of the parabolic cylinder. It is seen from Eq. (2.16) that Λ is intermediate between a medium inhomogeneity length L and wavelength $\lambda = 2\pi c/\omega$ so that $\Lambda \approx \sqrt{L\lambda}$. As known from classical optics, this is just the threshold where diffraction becomes significant and prevents further localization of a wave packet. It follows that the situation $\Lambda \ll \sqrt{L\lambda}$ can hardly be realized because of diffractive broadening. On the other hand, the case $\Lambda \approx L \gg \sqrt{L\lambda}$ is not excluded from Eq. (2.16) and hence from the solution (2.1) because $|\nabla u|$ as well as $|\nabla v|$ can be small and even zero. This means that the pWKB method is valid in the vast majority of practical problems; in particular, the eikonal approach is included in the pWKB solution as a specific case.

We remark in conclusion that in the ray method the effect of diffraction is described with terms of order κ^{-2}, whereas the pWKB method uses terms of order κ^{-1}. It is likely that the latter ordering is inherent to wave phenomena, which results, on

the one hand, in better convergence of asymptotic series and, on the other hand, in a wider applicability of the pWKB technique.

2.4. Paraxial expansion

We now take advantage of the exponential factor present in the functions of the parabolic cylinder (2.3) and hence in all terms of Eq. (2.4). This causes fast decay of a wave amplitude outside $\Re$ and suggests that it is superfluous to know the solution (2.1) in the whole space with equal accuracy. Therefore, we seek an approximate solution of this equation in the vicinity of the reference ray $u(\mathbf{r}) = v(\mathbf{r}) = 0$ in the form of power series involving powers of u and v (paraxial expansion). The estimate

$$\left(\sqrt{u^2+v^2}\right)^l \exp\left(-\frac{\kappa(u^2+v^2)}{2}\right) \le \left(\frac{l}{e\kappa}\right)^{l/2}$$

shows that increasing the powers of u or v by unity is equivalent to transition to the next order in the expansion with respect to $\kappa^{-1/2}$. This means that in the leading order of Eq. (2.4), i.e., in Eq. (2.12), we need to retain terms including $u^0, v^0, u^1, v^1, u^2, v^2$, and uv. The subsequent terms of the paraxial expansion are of order $O(\kappa^{-3/2})$, which is already suppressed in Eq. (2.4). The procedure results in the following equations:

$$H|_{\Re} = 0, \quad D_u H|_{\Re} = D_v H|_{\Re} = 0, \tag{2.20}$$

$$D^2_{uu}H\Big|_{\Re} = H_{UU}\Big|_{\Re}, \quad D^2_{vv}H\Big|_{\Re} = H_{VV}\Big|_{\Re}, \quad D^2_{vu}H\Big|_{\Re} = 0. \tag{2.21}$$

The operators D_u and D_v used above denote partial derivatives with respect to u and v, which are calculated with allowance for both explicit and implicit dependences of $H[u, v, t,\ x^\alpha(u, v, t),\ S_\alpha(u, v, t),\ u_\alpha(u, v, t),\ v_\alpha(u, v, t)]$ and other functions of u, v, and t, respectively. In the next order $O(\kappa^{-1/2})$ equation (2.13) it is necessary to keep terms including u^0, v^0, u^1 and v^1:

$$H_U|_{\Re} = H_V|_{\Re} = 0, \tag{2.22}$$

$$D_u(H_U)|_{\Re} = D_v(H_U)|_{\Re} = D_u(H_V)|_{\Re} = D_v(H_V)|_{\Re} = 0. \tag{2.23}$$

Finally, in the second order of the expansion, $O(\kappa^{-1})$, it is sufficient to retain zero-order terms of the expansion with respect to powers of u and v only:

$$H_{UV}|_{\mathfrak{R}} = 0, \tag{2.24}$$

$$\mathcal{L}[A^{lm}]\Big|_{\mathfrak{R}} = 0. \tag{2.25}$$

In accordance with the procedure discussed, all unknown functions, namely, $S(\mathbf{r})$, $u(\mathbf{r})$, $v(\mathbf{r})$, $A^{lm}(\mathbf{r})$, also have to be expanded in power series, and only a restricted number of terms have to be retained in the expansions. Inspection of Eqs. (2.20)–(2.21) shows that the unknown eikonal $S = S(\mathbf{r})$ has to be determined up to second-order terms of the paraxial expansion, viz.

$$S(\mathbf{r}) = S\Big|_{\mathfrak{R}} + p_\alpha(x^\alpha - q^\alpha) + \frac{1}{2}S_{\alpha\beta}\Big|_{\mathfrak{R}}(x^\alpha - q^\alpha)(x^\beta - q^\beta) + \dots . \tag{2.26}$$

It is understood here that the reference ray $\mathfrak{R}$ is described by Eq. (2.18) and $S_{\alpha\beta}$ is defined as

$$S_{\alpha\beta} = \frac{\partial^2 S}{\partial x^\alpha \partial x^\beta}. \tag{2.27}$$

In practice, however, it is more convenient to use the same expansion for the covariant components of the vector ∇S:

$$S_\alpha(\mathbf{r}) = p_\alpha + S_{\alpha\beta}|_{\mathfrak{R}}(x^\beta - q^\beta) + \dots \tag{2.28}$$

or

$$S_\alpha(\mathbf{r}) = p_\alpha + \frac{\partial S_\alpha}{\partial u}\Big|_{\mathfrak{R}} u + \frac{\partial S_\alpha}{\partial v}\Big|_{\mathfrak{R}} v + \dots . \tag{2.29}$$

The functions u and v are involved in the higher-order equations (2.22)–(2.24), and it is sufficient to retain two terms in the paraxial expansions. However, in view of the vanishing of the functions $u(\mathbf{r})$ and $v(\mathbf{r})$ on $\mathfrak{R}$ only one term remains in the Taylor series

$$\begin{aligned} u(\mathbf{r}) &= u_\alpha\Big|_{\mathfrak{R}}(x^\alpha - q^\alpha) + \dots , \\ v(\mathbf{r}) &= v_\alpha\Big|_{\mathfrak{R}}(x^\alpha - q^\alpha) + \dots , \end{aligned} \tag{2.30}$$

which is equivalent to

$$x^\alpha(u,v,t) = q^\alpha(t) + \left.\frac{\partial x^\alpha}{\partial u}\right|_{\Re} u + \left.\frac{\partial x^\alpha}{\partial v}\right|_{\Re} v + \dots . \tag{2.31}$$

Finally, as can be seen from Eq. (2.25), only the zero-order term has to be retained for the function $A^{lm} = A^{lm}(t)$.

The functions $q^\alpha(t)$ and $p_\alpha(t)$ have already been determined as a solution to the Hamiltonian set of equations (1.8)–(1.9). Similarly, the first term of the expansion (2.26), which determines the eikonal S along $\Re$, is given by Eq. (1.11). The functions $S_{\alpha\beta}$, u_α, v_α, A^{lm} are evaluated on the reference ray solely and they will be viewed further as functions of the only argument t. After these functions are found, they can be substituted into Eqs. (2.26), (2.30) and then into Eq. (2.1), thus solving the problem under consideration. The functions obey the set of ordinary differential equations, which is a corollary to Eqs. (2.20)–(2.25) and will be discussed in the next section.

3. Beam tracing

3.1. Ray coordinates

Let the set of three functions

$$\begin{cases} u = u(\mathbf{r}) \\ v = v(\mathbf{r}) \\ t = t(\mathbf{r}) \end{cases} \tag{3.1}$$

be a new coordinate system in space. In accordance with Kravtsov and Orlov [1] we call the coordinate system (3.1) the ray coordinates. The physical meaning of the ray coordinate system is that within its frame the solution (2.1) represents a straight plane beam of constant width. The generic notations $w^1 = u$, $w^2 = v$, $w^3 = t$ will also be used equivalently to those of Eq. (3.1).

The ray coordinates so far obey the following conditions: (i) the Jacobian of the coordinate transformation $\{x^\alpha\} \to \{u,v,t\}$

does not vanish; (ii) the coordinate line $u(\mathbf{r}) = v(\mathbf{r}) = 0$ coincides with the reference ray $\mathfrak{R}$, which is a solution to the Hamiltonian set of equations (1.8), (1.9). The sense of the first condition is obvious. In view of Eqs. (1.8), (2.17) the second one means that the vector $\mathbf{V}$ of the group velocity tangential to the reference ray is one of the basis vectors of the ray coordinate system. The vectors ∇u and ∇u are reciprocal vectors orthogonal to $\mathbf{V}$. Therefore, Eqs. (2.22) are valid for any choice of $u(\mathbf{r})$ and $v(\mathbf{r})$ satisfying the condition (ii). Equations (2.20) are fulfilled due to Eqs. (1.8)–(1.9). In turn, the fulfillment of Eqs. (2.20), (2.22) means that Eq. (2.4) is satisfied up to first order inclusively with an accuracy of $o(\kappa^{-1/2})$. The remaining second-order equations (2.21), (2.23), (2.24) are discussed in the rest of this section.

3.2. First form of the beam-tracing equations

We now show that the higher-order equations (2.21), (2.23), and (2.24) determine the higher-order terms u_α, v_α, $S_{\alpha\beta}$ in the expansions (2.26), (2.28)–(2.31). First of all, note that Eqs. (2.22) are valid for any t. It follows that $D_t(H_U)|_{\mathfrak{R}} = D_t(H_V)|_{\mathfrak{R}} = 0$. Together with Eqs. (2.23) this means that $D_{x^\alpha}(H_U)|_{\mathfrak{R}} = D_{x^\alpha}(H_V)|_{\mathfrak{R}} = 0$ for any $\alpha = 1, 2, 3$. Calculating these derivatives by means of Eqs. (1.8), (2.11), (2.13), (2.17), we have

$$\begin{aligned} \frac{du_\alpha}{dt} &= -\left(\frac{\partial^2 H}{\partial x^\alpha \partial S_\beta} + \frac{\partial^2 H}{\partial S_\beta \partial S_\gamma} S_{\alpha\gamma}\right) u_\beta, \\ \frac{dv_\alpha}{dt} &= -\left(\frac{\partial^2 H}{\partial x^\alpha \partial S_\beta} + \frac{\partial^2 H}{\partial S_\beta \partial S_\gamma} S_{\alpha\gamma}\right) v_\beta. \end{aligned} \tag{3.2}$$

In accordance with the remark made at the end of the previous section, the full derivatives appear on the left-hand sides of these equations, showing that these quantities are calculated along $\mathfrak{R}$. Moreover, Eqs. (3.2) as well as all the equations in what follows are considered along the reference ray solely, and so the subscript $\mathfrak{R}$ is omitted here and subsequently. Note also that here and throughout the paper the commonly used notations for the derivatives of the Hamiltonian are retained. That is, $\partial H/\partial S_\alpha$

denotes a partial derivative with respect to S_α with x^α fixed, while $\partial H/\partial x^\alpha$ is computed with S_α kept constant. We use the notation $D_{x^\alpha}[H(x^\alpha, S_\beta)]$ for the "full" partial derivative, which is computed with allowance for the dependence $S_\beta(x^\alpha)$ along a ray.

By making use of

$$\begin{aligned} D^2_{x^\alpha x^\beta}(H) &= D_{x^\alpha}\left[\frac{\partial w^\nu}{\partial x^\beta}(D_{w^\nu}H)\right] \\ &= \frac{\partial w^\nu}{\partial x^\beta}D_{x^\alpha}(D_{w^\nu}H) = \frac{\partial w^\mu}{\partial x^\alpha}\frac{\partial w^\nu}{\partial x^\beta}D^2_{w^\mu w^\nu}(H) \end{aligned}$$

and $D_{w^\alpha}H = 0$, $D_t(D_{w^\alpha}H) = 0$, all three equations (2.21) may be replaced with

$$D^2_{x^\alpha x^\beta}H = u_\alpha u_\beta H_{UU} + v_\alpha v_\beta H_{VV},$$

from which, by direct differentiation, we obtain

$$\begin{aligned} &\frac{dS_{\alpha\beta}}{dt} + \frac{\partial^2 H}{\partial x^\alpha \partial x^\beta} + \frac{\partial^2 H}{\partial x^\alpha \partial S_\gamma}S_{\beta\gamma} + \frac{\partial^2 H}{\partial x^\beta \partial S_\gamma}S_{\alpha\gamma} \\ &\quad + \frac{\partial^2 H}{\partial S_\gamma \partial S_\delta}S_{\alpha\gamma}S_{\beta\delta} = u_\alpha u_\beta H_{UU} + v_\alpha v_\beta H_{VV}. \end{aligned} \tag{3.3}$$

The set of ordinary differential equations (3.2), (3.3) for the quantities u_α, v_α, $S_{\alpha\beta}$ can be readily integrated along the reference ray, thus solving the problem of determining the functions $S = S(\mathbf{r})$, $v = v(\mathbf{r})$, $u = u(\mathbf{r})$ within the accuracy required. Initial conditions for the set of equations (3.2), (3.3) are discussed later in this section. In particular, it will be shown that the fulfillment of Eq. (2.24) still unused is ensured by a special choice of initial conditions for u_α and v_α.

Apart from the independent task of solving Eq. (2.25), which is discussed in Section 4, the original problem for wave equation (1.1) is already solved. The procedure of solution is as follows. The set of ordinary differential equations (1.8), (1.9), (3.2), (3.3) is integrated, yielding the functions q^α, S_α, $S_{\alpha\beta}$, u_α, v_α of the single argument t. These functions are substituted in Eqs. (2.26), (2.28), (2.30) and then in Eq. (2.1).

It is worth noting that only the right-hand side of Eq. (3.3) contains terms which are new in comparison with the ray approach. It is clear that these terms are significant in the neighborhood of a point where ∇u and/or ∇v, or u_α and/or v_α, become large. In accordance with Eq. (2.16), this means that the wave amplitude rapidly decreases outside the reference ray. Such a situation occurs, for instance, near caustics or focal points, where diffraction is expected to be significant. Consequently, the two terms on the right-hand side of Eq. (3.3) are responsible for describing the wave properties in our approach. Their smallness may be a quantitative measure of the applicability of the eikonal approach.

Physically, it is clear that the behavior of the wave beam width, or, in other words, the beam convergence or divergence, is coupled with the curvature of the wave front. In agreement with this, the second derivatives $S_{\alpha\beta}$ representing the curvature and the beam width terms appear in the same Eq. (3.3).

3.3. Second form of the beam-tracing equations

A different mode of attacking this problem gives an additional insight into and an alternative representation of the beam-tracing equations. Let us regard the unknown ray coordinates (3.1) in the form $x^\alpha = x^\alpha(u, v, t)$ and use the expansions (2.29), (2.31) instead of (2.28), (2.30). To derive equations for evolution of the quantities $\partial x^\alpha / \partial w^\beta$ along $\Re$, let us use the identities

$$\frac{\partial x^\alpha}{\partial w^\gamma}\frac{\partial w^\gamma}{\partial x^\beta} = \delta^\alpha_\beta. \tag{3.4}$$

On differentiation of Eq. (3.4) with allowance for Eq. (3.2) (for details see Appendix B) we have

$$\begin{aligned}
\frac{d}{dt}\frac{\partial x^\alpha}{\partial u} &= \frac{\partial^2 H}{\partial S_\alpha \partial x^\beta}\frac{\partial x^\beta}{\partial u} + \frac{\partial^2 H}{\partial S_\alpha \partial S_\beta}\frac{\partial S_\beta}{\partial u}, \\
\frac{d}{dt}\frac{\partial x^\alpha}{\partial v} &= \frac{\partial^2 H}{\partial S_\alpha \partial x^\beta}\frac{\partial x^\beta}{\partial v} + \frac{\partial^2 H}{\partial S_\alpha \partial S_\beta}\frac{\partial S_\beta}{\partial v}.
\end{aligned} \tag{3.5}$$

Here we can repeat word for word the comment on Eqs. (3.2) and consider all the terms in Eqs. (3.5) as functions of the single variable t. The counterpart equations for $\partial S_\alpha/\partial w^\beta$ follow directly from Eq. (2.21) and (3.5):

$$\begin{aligned} \frac{d}{dt}\frac{\partial S_\alpha}{\partial u} + \frac{\partial^2 H}{\partial x^\alpha \partial x^\beta}\frac{\partial x^\beta}{\partial u} + \frac{\partial^2 H}{\partial x^\alpha \partial S_\beta}\frac{\partial S_\beta}{\partial u} &= u_\alpha H_{UU}, \\ \frac{d}{dt}\frac{\partial S_\alpha}{\partial v} + \frac{\partial^2 H}{\partial x^\alpha \partial x^\beta}\frac{\partial x^\beta}{\partial v} + \frac{\partial^2 H}{\partial x^\alpha \partial S_\beta}\frac{\partial S_\beta}{\partial v} &= v_\alpha H_{VV}. \end{aligned} \tag{3.6}$$

The set of equations (3.5), (3.6) can be used instead of (3.2), (3.3). In this case, the expansions (2.29), (2.31) have to be used instead of (2.26), (2.28), (2.30). The set of algebraic equations (3.4) may then be used to express the quantities u_α, v_α on the right-hand side of Eqs. (3.6) in terms of $\partial x^\alpha/\partial u$, $\partial x^\alpha/\partial v$, and V^α.

Equations (3.5), (3.6) are linear unless the right-hand-side terms in Eqs. (3.6) responsible for diffraction become significant. Equations (3.5) are nothing but the derivatives of Eq. (1.8) with respect to u and v, and the left-hand sides of Eqs. (3.6) coincide with the results of differentiating Eq. (1.9). The meaning of this coincidence is that, when diffraction is negligible, the beam-tracing equations describe a pencil of ray trajectories adjacent to the reference ray. However, when the ray pencil becomes narrow enough and the transverse energy flow becomes significant, then the right-hand sides of Eqs. (3.3) and (3.6) come into play and the pWKB solution departs from the ray solution.

3.4. Initial conditions for the beam-tracing equations

We still need to prove that Eq. (2.24) is consistent with Eqs. (3.2), (3.3) and (3.5), (3.6). We shall now show that this equation can be viewed as one of the initial conditions for the beam-tracing equations. To this end, we introduce the symmetric matrix

$$B^{\alpha\beta} = \varepsilon^{\alpha\gamma} D_{x^\gamma}\left(\frac{\partial H}{\partial S_\beta}\right) + \varepsilon^{\beta\gamma} D_{x^\gamma}\left(\frac{\partial H}{\partial S_\alpha}\right) - \frac{\partial H}{\partial S_\gamma} D_{x^\gamma}(\varepsilon^{\alpha\beta}), \tag{3.7}$$

where the matrix $\varepsilon^{\alpha\beta}$ is determined by Eq. (1.7) and in general as

$$\varepsilon^{\alpha\beta} = \frac{\partial^2 H}{\partial S_\alpha \partial S_\beta}. \tag{3.8}$$

We also introduce the notations

$$u^\alpha = \varepsilon^{\alpha\beta} u_\beta \quad \text{and} \quad v^\alpha = \varepsilon^{\alpha\beta} v_\beta. \tag{3.9}$$

It is shown in Appendix B that under the additional condition $V^\alpha \varepsilon_{\alpha\beta} V^\beta$ the ray direction V^α coincides with one of the principal directions determined by $B^{\alpha\beta}$. Hence it is always possible to take the vectors u_α and v_α at the initial point of the reference ray $t = 0$ as the two other eigenvectors of the matrix $B^{\alpha\beta}$, i.e.,

$$B^{\alpha\beta} u_\beta \Big|_{t=0} = \lambda_{(u)} u^\alpha \Big|_{t=0}, \quad B^{\alpha\beta} v_\beta \Big|_{t=0} = \lambda_{(v)} v^\alpha \Big|_{t=0}. \tag{3.10}$$

In view of Eqs. (3.9), (3.10) and the symmetry of the matrix $B^{\alpha\beta}$ we have

$$\begin{aligned} \left(\lambda_{(u)} - \lambda_{(v)}\right) u_\alpha \varepsilon^{\alpha\beta} v_\beta \Big|_{t=0} &= \left(\lambda_{(u)} u^\beta v_\beta - \lambda_{(v)} u_\alpha v^\alpha\right)\Big|_{t=0} \\ &= u_\beta v_\alpha \left(B^{\alpha\beta} - B^{\beta\alpha}\right)\Big|_{t=0} = 0. \end{aligned} \tag{3.11}$$

If $\lambda_{(u)} \neq \lambda_{(v)}$, then it follows that $(u_\alpha \varepsilon^{\alpha\beta} v_\beta)\big|_{t=0} = 0$, i.e., Eq. (2.24) is fulfilled at the original point of the ray $\Re$, viz. at $t = 0$. In the case of the multiple eigenvalue $\lambda_{(u)} = \lambda_{(v)}$ it is also possible to choose two different vectors ∇u and ∇v so that Eq. (2.24) is valid at the point $t = 0$. With a straightforward, though somewhat lengthy, calculation (see Appendix B) we arrive at the relation

$$\frac{d}{dt} u_\alpha \varepsilon^{\alpha\beta} v_\beta = -u_\alpha v_\beta B^{\alpha\beta}. \tag{3.12}$$

We can then write

$$\begin{aligned} \left(\frac{d}{dt} u_\alpha \varepsilon^{\alpha\beta} v_\beta\right)\Big|_{t=0} &= \left(-u_\alpha v_\beta B^{\alpha\beta}\right)\Big|_{t=0} \\ &= \left(-\lambda_{(u)} u_\alpha v_\beta \varepsilon^{\alpha\beta}\right)\Big|_{t=0} = 0. \end{aligned} \tag{3.13}$$

One can consecutively show that all the higher-order derivatives $d^n(u_\alpha \varepsilon^{\alpha\beta} v_\beta)/dt^n$ vanish at $t = 0$, which finally proves that with the initial conditions (3.10) Eq. (2.24) is fulfilled identically along $\mathfrak{R}$.

We can now formulate the initial conditions for the set of beam-tracing equations. Initial conditions for the eikonal S and its derivatives S_α, $S_{\alpha\beta}$ are determined if the shape of the phase front is given at the beginning of $\mathfrak{R}$. Like the initial conditions for the quantities $\partial S_\alpha/\partial u = S_{\alpha\beta}\partial x^\beta/\partial u$ and $\partial S_\alpha/\partial v = S_{\alpha\beta}\partial x^\beta/\partial v$, they depend on the choice of u_α and v_α. However, a great deal of uncertainty is still present in the initial conditions for u_α and v_α. The only constraint imposed on these quantities so far is Eq. (3.10), which prescribes the directions of the vectors ∇u and ∇v. The lengths of these vectors are still arbitrary. We shall return to the choice of $|\nabla u|$ and $|\nabla v|$ in Section 5 and show that this freedom can be used to improve the asymptotic convergence to the exact solution.

3.5. Discussion of the beam-tracing equations

The first remark to be made here is that each of the systems (3.2), (3.3) or (3.4)–(3.6), although giving a solution to the problem considered, involves twice as many equations as are really necessary. Actually, with allowance for the symmetry of the second derivative $S_{\alpha\beta}$, Eqs. (3.2), (3.3) give a set of 12 equations. Only half of them are independent. The point is that in accordance with Eq. (2.19) the vectors ∇u and ∇v are normal to the reference ray direction $\mathbf{V}$ at any point of the ray. This, together with Eq. (2.24), imposes three conditions on the components of the vectors ∇u and ∇v. A similar statement is valid for the quantities $S_{\alpha\beta}$. Namely, the three combinations $S_{\alpha\beta}V^\beta = \dot{S}_\alpha$ are already determined by Eq. (1.9), which shows that only three of six equations (3.3) or (3.6) are independent. Therefore, six algebraic conditions (2.8) and $S_{\alpha\beta}V^\beta = \dot{S}_\alpha$ can be used either to check the accuracy of a numerical solution or to reduce the number of differential equations to be solved.

The next remark is that in conventional ray tracing, as also in classical mechanics, the two Hamiltonian equations (1.8)

and (1.9) are fully symmetric. This is not the case in our consideration. To highlight the difference, let us recall the procedure deriving Eqs. (1.8)–(1.9). Equation (1.8) merely introduces a new quantity $\dot{x}^\alpha = V^\alpha = \partial H/\partial S_\alpha$. Then Eq. (1.9) follows from this designation and vanishing of the first spatial derivatives of the Hamiltonian H. In the ray approach, we have $H(x^\alpha, S_\alpha) \equiv 0$ everywhere in space and, therefore, the higher-order spatial derivatives of H vanish and, accordingly, all the equations obtained by differentiation of Eqs. (1.8) and (1.9) are also valid. In the pWKB approach, the Hamiltonian H together with its first derivatives vanishes along $\Re$ only (Eq. (2.20)), while second derivatives do not vanish at all (Eq. (2.21)). In both approaches Eq. (1.8) is viewed as a new designation and has to be fulfilled with all its spatial derivatives. In particular, the sets of equations (3.2) and (3.5) could be formally derived by such differentiation. Vanishing of the first derivatives of H occurs in Eq. (1.9) in the same manner for both approaches. However, higher derivatives of H do not vanish in the pWKB approximation and it can be concluded that the differentiations which could be done on Eq. (1.8) are not allowed for Eq. (1.9), because the derivatives of the two sides of Eq. (1.9) are no longer equal.

As shown in [5], the reference ray describes the trajectory of the center of gravity of the solution (2.1). This trajectory coincides with the geometric-optics trajectory and does not depend on the transverse structure of the solution (2.1). In turn, this structure is described by the functions $u(\mathbf{r})$ and $v(\mathbf{r})$. The larger $|\nabla u|$ and $|\nabla v|$ are the narrower is the wave beam. Therefore, the quantity $(|\nabla u|^2 + |\nabla v|^2)^{-1/2}$ characterizes the width of the wave packet and can be regarded as the second moment of the amplitude distribution across the beam axis. This quantity is determined by the beam-tracing equations and it still describes the gross structure of the solution, i.e., the common backbone for a whole variety of particular solutions of type (2.1) differing in fine structure as described by the different transverse mode numbers l and m. We now proceed to the equation defining this fine structure of the amplitude distribution over the wave packet.

4. Equation for the wave amplitude

4.1. Solving the transport equation

Consider now the transport equation (2.9) describing the amplitude evolution along the reference ray. As follows from the discussion in Section 2.3, all functions included in this equation should be viewed as functions of a single variable t. First of all, we transform the quantities appearing in the second term on the right-hand side of Eq. (2.5):

$$\begin{aligned} g^{\alpha\gamma}\varepsilon_{\gamma}^{\beta} &= \tfrac{1}{2}(g^{\alpha\gamma}\varepsilon_{\gamma}^{\beta} + g^{\beta\gamma}\varepsilon_{\gamma}^{\alpha}) + \tfrac{1}{2}(g^{\alpha\gamma}\varepsilon_{\gamma}^{\beta} - g^{\beta\gamma}\varepsilon_{\gamma}^{\alpha}) \\ &= \tfrac{1}{2}(\varepsilon^{\alpha\beta} + i\tilde{\varepsilon}^{\alpha\beta}). \end{aligned} \tag{4.1}$$

If the dielectric tensor $\varepsilon_{\alpha}^{\beta}$ is Hermitian, then the tensors $\varepsilon^{\alpha\beta}$ and $\tilde{\varepsilon}^{\alpha\beta}$ are real. The statement is obvious for a coordinate system in which $g^{\alpha\beta}$ coincides with the Kronecker symbol. This is the case for a Cartesian coordinate system with one of the axes oriented along the magnetic field. It follows that the tensors $\varepsilon^{\alpha\beta}$ and $\tilde{\varepsilon}^{\alpha\beta}$ are real in any coordinate system.

In view of Eqs. (1.8), (2.5), (2.17), and (4.1), Eq. (2.9) may be written as

$$\begin{aligned} \frac{d\ln(A^{lm})^2}{dt} + \frac{1}{\sqrt{g}}\frac{\partial}{\partial x^{\alpha}}(\sqrt{g}V^{\alpha}) + \frac{iS_{\beta}}{\sqrt{g}}\frac{\partial}{\partial x^{\alpha}}\left(\sqrt{g}\tilde{\varepsilon}^{\alpha\beta}\right) \\ +i(2l+1)H_{UU} + i(2m+1)H_{VV} = 0. \end{aligned} \tag{4.2}$$

The skew-symmetry of the tensor $\tilde{\varepsilon}^{\alpha\beta}$ has been taken into account here. By virtue of the Liouville theorem [1] the second term in Eq. (4.2) can be represented as $d(\ln J)/dt$, where J is the Jacobian of the transformation from the original Cartesian coordinates to the ray coordinates $\{u, v, t\}$:

$$J = \sqrt{g}\frac{D(x^1, x^2, x^3)}{D(u, v, t)}. \tag{4.3}$$

The amplitude A^{lm} can now be obtained by integration along

the reference ray

$$A^{lm}(t) = C^{lm}\sqrt{\frac{J_0}{J(t)}}\exp\Big\{-i\big[\phi_g(t) + (2l+1)\phi_u(t) + (2m+1)\phi_v(t)\big]\Big\}, \tag{4.4}$$

where C^{lm} are arbitrary constants, $J_0 = J|_{t=0}$, and

$$\phi_g = \frac{1}{2}\int_0^t \frac{S_\beta}{\sqrt{g}}\frac{\partial}{\partial x^\alpha}\left(\sqrt{g}\tilde{\varepsilon}^{\alpha\beta}\right)dt,$$
$$\phi_u = \frac{1}{2}\int_0^t H_{UU}dt, \qquad \phi_v = \frac{1}{2}\int_0^t H_{VV}dt. \tag{4.5}$$

The factor $\sqrt{J_0/J(t)}$ appearing in the solution (4.4) is the same as in the ray approach [1]. It describes the changes in the wave amplitude due to ray divergence or convergence. It is worth noting here that the wave energy conservation inside a ray tube which takes place for the ray solution does not hold for the pWKB solution. Indeed, comparing the amplitude A_0 of the geometric-optics solution (1.5) with that of the pWKB solution (2.1), we see that they differ by the additional multiplier $\varphi_l(\sqrt{\kappa}u)\,\varphi_m(\sqrt{\kappa}v)$ describing the wave packet behavior. It is variation of the functions u and v which violates the energy conservation along the ray tube. Physically, this means that the effect of diffraction, which is not included in geometric optics, is manifested as energy flow across the side-wall of the ray tube. It can be shown that in the beam approach the energy conservation law is fulfilled for the wave packet as a whole rather than for separate portions of it, as in geometric optics.

The third term in Eq. (4.2), and correspondingly the first term ϕ_g in the exponent of Eq. (4.4), describes the gyrotropy of the medium. It is also present in the ray approach. The last two terms on the left-hand side of Eq. (4.2) are new in comparison with the ray-tracing description. Similar terms on the right-hand sides of Eqs. (3.3) and (3.6) have already been discussed in the

previous section. However, while the terms in the beam-tracing equations are responsible for the amplitude behavior of the wave beam, the terms in Eq. (4.2) contribute to the phase of the wave. As distinct from the beam-tracing equations, where the terms are real and their magnitude can be compared with other terms in the equations, here the terms are purely imaginary and their significance cannot be estimated on the basis of Eq. (4.2). Thus, we shall resume discussion of them in Section 5.1.

4.2. Accounting for dissipation

So far we have considered a nondissipative medium described by Eq. (1.1), where the tensor $\hat{\varepsilon}$ is Hermitian and the coefficient $N^2(\mathbf{r})$ is real. In this section we waive the restriction. To this end, first we replace N^2 in Eq. (1.1) with $N^2 + i\gamma_N$ and then substitute $N^2 + i\gamma_N$ for N^2 in Eq. (2.4). The absorption is assumed to be relatively small. This assertion will be defined more exactly, but so far we just attribute the term with γ_N to the second order of Eq. (2.4). Then the transport equation (2.9) is replaced with

$$\mathcal{L}[A^{lm}] = -\kappa\gamma_N A^{lm}, \tag{4.6}$$

and consequently its solution takes the form

$$\begin{aligned} A^{lm}(t) = \; & C^{lm}\sqrt{\frac{J_0}{J(t)}}\exp\Big\{-\frac{1}{2}\kappa\int_0^t \gamma_N dt \\ & -i\big[\phi_g(t) + (2l+1)\phi_u(t) + (2m+1)\phi_v(t)\big]\Big\}. \end{aligned} \tag{4.7}$$

In comparison with Eq. (4.4), a new term appears here which describes the exponential amplitude decay along the ray due to power absorption during wave propagation. Applying the condition (2.10) to the quantity A^{lm}, we find

$$\left|\frac{L\nabla A^{lm}}{A^{lm}}\right| \approx \left|\frac{dA^{lm}/dt}{|\mathbf{V}|A^{lm}}\right| \approx \left|\frac{\kappa\gamma_N|L\nabla S|}{V^\alpha S_\alpha}\right| \approx \left|\frac{kL\gamma_N}{N^2}\right| \leq 1, \tag{4.8}$$

where $k = |\kappa \nabla S| = 2\pi/\lambda$ is the wave number. We now conclude that $\gamma_N / N^2 \approx \lambda / L = O(\kappa^{-1})$, thus specifying the claim that the absorption should be small enough and justifying the ordering used in the derivation of Eq. (4.6).

In parallel fashion we can consider the absorption caused by an anti-Hermitian component of the tensor $\hat{\varepsilon}$. Assume that $\hat{\varepsilon} = \hat{\varepsilon}^H + \hat{\varepsilon}^A$ with $\hat{\varepsilon}^H$ being a Hermitian and $\hat{\varepsilon}^A$ an anti-Hermitian tensor. Then the solution of the transport equation will take a form similar to Eq. (4.7), the only difference being that the quantity γ_N in Eqs. (4.6)–(4.8) should be replaced with $\gamma_\varepsilon = i \nabla S \nabla S : \hat{\varepsilon}^A = i S_\alpha S_\beta [g^{\alpha\gamma} (\hat{\varepsilon}^A)^\beta_\gamma + g^{\beta\gamma} (\hat{\varepsilon}^A)^\alpha_\gamma]/2$.

5. Solution of the wave equation

5.1. Partial solution

Making use of Eq. (2.1) and Eq. (4.4), we can now write the particular solution of Eq. (1.1) for the nondissipative case as

$$\Phi_{lm}(\mathbf{r}) = \sqrt{\frac{J_0}{J(t)}} \varphi_l \left(\sqrt{\kappa} u(\mathbf{r})\right) \varphi_m \left(\sqrt{\kappa} v(\mathbf{r})\right) \exp\Big\{ i\kappa S(\mathbf{r}) - i\phi_g(t) - i(2l+1)\phi_u(t) - i(2m+1)\phi_v(t) \Big\}. \tag{5.1}$$

All dependences are shown here explicitly in order to emphasize that, as distinct from the two previous sections, the expression (5.1) should be evaluated for arbitrary values of its arguments rather than on the reference ray only. Thus, Eq. (5.1) represents the wave solution in the whole space. As discussed in Section 3, the unknown functions $u(\mathbf{r})$, $v(\mathbf{r})$, and $S(\mathbf{r})$ contained in Eq. (5.1) are to be found by integration of the set of ordinary differential equations (1.8), (1.9), (1.11) together with either (3.2), (3.3) or (3.5), (3.6) and subsequent use of the expansions (2.26), (2.30) or (2.29), (2.31), respectively. In the second case, Eq. (5.1) together with Eq. (2.31) can be viewed as a parametric representation of the solution. Then u, v, and t have the sense of parameters and the function $S = S(u, v, t)$ is determined by Eq. (2.26). In the latter, the quantities $S_{\alpha\beta}$ are found by solving

the following set of equations:

$$S_{\alpha\beta}\frac{\partial x^\beta}{\partial u} = \frac{\partial S_\alpha}{\partial u}, \quad S_{\alpha\beta}\frac{\partial x^\beta}{\partial v} = \frac{\partial S_\alpha}{\partial v}, \quad S_{\alpha\beta}V^\beta = -\frac{\partial H}{\partial x^\alpha}. \quad (5.2)$$

Inspection of Eq. (5.1) shows that on the reference ray, i.e., at $u = v = 0$, the pWKB solution retains all peculiarities of the geometric-optics solution and, in addition, includes two terms shown in the second line of Eq. (4.4). Therefore, we can conclude that along the ray direction $\mathbf{V}$ the pWKB method keeps all the features of the ray approach but departs from it when the terms ϕ_u or ϕ_v become large enough. The reason for this difference is that, in addition to the ray properties, the pWKB method also incorporates wave properties of the exact solution of Eq. (1.1). These wave properties are most significant across the reference ray $\mathfrak{R}$ direction and mainly affect the field amplitude. However, influence may also be expected on the phase.

Further examination of the phase of the solution (5.1) shows that it is only the first term which contains the large parameter κ. Therefore, the remaining terms might seem insignificant. This, however, is not always correct. Actually, in the significant in practice case of electrostatic plasma oscillations, N^2 in Eq. (1.1) vanishes and as a consequence Eq. (1.11) reads $dS/dt = \varepsilon^{\alpha\beta}S_\alpha S_\beta = 0$. On this zero background any contribution to the phase variation may be significant. Physically, $S|_{\mathfrak{R}} = S(t) = 0$ means that the geometric-optics phase (eikonal) of the electrostatic wave does not vary along a ray. In other words, the direction $\mathbf{V}$ of the group velocity is orthogonal to the direction ∇S of the phase velocity. We now see that this is no longer valid when the higher-order terms of the wave phase are taken into account. It is already seen in the ray approach that the plasma gyrotropy described with ϕ_g can cause phase variation along the ray. The more reliable beam approach shows that the additional terms ϕ_u and ϕ_v appear in the phase. They describe contributions to the wave phase caused by higher transversal harmonics in the wave packet spectrum. As discussed in Section 3.4 and as also follows directly from the uncertainty principle, these terms become especially large for narrow wave

packets or in the vicinity of caustics and focal points, where diffractional phenomena are manifested most distinctly.

5.2. General solution

We can now construct a general solution to the wave equation (1.1):

$$\Phi(\mathbf{r}) = \sqrt{\frac{J_0}{J(t)}} \exp\left\{ i \left[\kappa S(u,v,t) - \phi_g(t) - \phi_u(t) - \phi_v(t) \right] \right\} \times \sum_{l,m} C^{lm} \varphi_l(\sqrt{\kappa} u) \varphi_m(\sqrt{\kappa} v) \times \exp\left\{ -2i \left[l\phi_u(t) + m\phi_v(t) \right] \right\}. \tag{5.3}$$

Indeed, suppose that an arbitrary field distribution $\Phi_0(\mathbf{r})$ is prescribed on some surface σ in space. Without any loss of generality, it can be assumed that this surface is described by the parametric equations $x^\alpha = x^\alpha(u,v,t)|_{t=0}$. It then follows that

$$\Phi_0(\mathbf{r}) = \Phi(\mathbf{r})\Big|_\sigma = e^{i\kappa S_\sigma(u,v)} \sum_{l,m} C^{lm} \varphi_l\left(\sqrt{\kappa} u\right) \varphi_m\left(\sqrt{\kappa} v\right). \tag{5.4}$$

From Eq. (5.4) we immediately find that

$$S_\sigma(u,v) \stackrel{\text{def}}{=} S(u,v,t)\Big|_{t=0} = \frac{1}{\kappa} \mathrm{Arg}\Big[\Phi(\mathbf{r})\Big]\Big|_\sigma, \tag{5.5}$$

and the coefficients of the expansion (2.26) are determined as

$$S\Big|_O = S_\sigma\Big|_O, \qquad p_\alpha\Big|_{t=0} = \left(\frac{\partial S_\sigma}{\partial w^\beta}\frac{\partial w^\beta}{\partial x^\alpha}\right)\Big|_O,$$
$$S_{\alpha\beta}\Big|_{t=0} = \left(\frac{\partial^2 S_\sigma}{\partial w^\nu \partial w^\mu}\frac{\partial w^\nu}{\partial x^\alpha}\frac{\partial w^\mu}{\partial x^\beta} + \frac{\partial S_\sigma}{\partial w^\gamma}\frac{\partial^2 w^\gamma}{\partial x^\alpha \partial x^\beta}\right)\Big|_O. \tag{5.6}$$

Insofar as the functions of the parabolic cylinder form a complete set of basis functions, it is possible to match the amplitude of the

field distribution $|\Phi_0|$ by taking the coefficients C^{lm} according to

$$C^{lm} = \int_{-\infty}^{\infty} \varphi_l(\sqrt{\kappa}u)\, du \int_{-\infty}^{\infty} |\Phi_0(\mathbf{r})|\, \varphi_m(\sqrt{\kappa}v)\, dv. \qquad (5.7)$$

It follows that Eq. (5.3) represents a general solution to the wave equation (1.1) or, more strictly speaking, Eq. (5.3) is an asymptotic approximation to a general solution.

All the quantities on both sides of formulas (5.6) are evaluated at the point $O = \sigma \cap \Re$, which is the initial point of the reference ray $x^\alpha = q^\alpha|_{t=0}$ and the origin of the ray frame of reference $u = v = t = 0$. It is implied in Eqs. (5.6), (5.7) that this point is already chosen. In principle, the position of this point is arbitrary on σ, but the approximation error of the asymptotic solution (5.3) depends on this choice. It is physically evident that the point O should be chosen in the vicinity of the maximum of the field distribution function $\Phi_0(\mathbf{r})$. To express this more accurately, we should state that the point O should coincide with the center of gravity of the field distribution over σ [5].

The directions of the vectors ∇u and ∇v in the point O should be found according to the procedure described in Section 3.4. However, there still remains uncertainty in the choice of the lengths of both vectors, $|\nabla u|$ and $|\nabla v|$. A similar situation exists with the original point O. Namely, the rate of decrease of C^{lm} with growth of the numbers l, m essentially depends upon the choice of $|\nabla u|\Big|_O$ and $|\nabla v|\Big|_O$. For reasons explained below, the numbers l and m have to be small compared with κ, i.e., $l, m \ll \kappa$, which is relevant when the coefficients C^{lm} decrease fast enough. Hence the arbitrariness in the choice of the coordinate system can be used to reduce the number of terms in Eq. (5.3) and thus meet the applicability condition discussed in the next section.

5.3 Applicability of the paraxial WKB approach

We now turn to the applicability conditions for the pWKB approach. As discussed in Section 5.1, the approach retains all

significant features of the geometric optics along the ray direction $\mathbf{V}$ and, in addition, incorporates some wave properties across it. Thus, the usual criteria of validity of the ray solution which are applied to the phase S and to the amplitude A_0 should be fulfilled for the phase S and the amplitude A^{lm} of the pWKB solution, along the reference ray at least. In addition to this, some new restrictions can be expected to be imposed by that part of our derivation which is different from the ray approach. In the first place, there is the second line in Eq. (2.4) and, secondly, the paraxial expansion described in Section 2.4. In the course of deriving Eqs. (2.7)–(2.8) and consequently Eqs. (2.20)–(2.23) it was presumed that the functions φ_l and φ_l' are of the same order. It is certainly true if l is zero or small enough. However, with an increase in l or m the situation changes. Indeed, the recursion formula for the function of the parabolic cylinder $\varphi_l(z)$ is

$$\varphi_l'(z) = \sqrt{2l}\varphi_{l-1} - z\varphi_l(z).$$

It follows that φ_l' is of order $\sqrt{2l}\varphi_l$. We now see that in order to justify the derivation of the beam-tracing equations we have to require satisfaction of the additional inequality

$$l, m \ll \kappa. \tag{5.8}$$

To elucidate the physical meaning of this formal requirement, recall that the quantity l gives the number of zeros of the function of the parabolic cylinder φ_l. So the higher the numbers l and m are, the faster is the transverse (with respect to the direction of the group velocity) field variation. Rewriting Eq. (5.8) as $l, m \ll 2\pi L/\lambda$, we see that this means that the rate of the field variation described by the amplitude of the solution should be much slower than that described by the phase.

A helpful interpretation of the condition (5.8) can be obtained by applying it to a single beam harmonic, Eq. (5.1). Like any wave packet, the beam harmonic has a characteristic carrier wave vector given by $\mathbf{k} = \kappa\nabla S|_{\mathfrak{R}} = \{(\omega/c)p_\alpha(t)\}$. However, its spectrum also contains other Fourier harmonics. Equation (5.8) requires that the width Δ_k of the spectrum be much less than $|\mathbf{k}|$, i.e., $\Delta_k \ll |\mathbf{k}|$. In fact, if this is not fulfilled and $\Delta_k \approx |\mathbf{k}|$,

then long wavelengths $k \approx 0$ are present in the spectrum, thus violating the initial assumption for any asymptotic approach. For this reason, the inequality (5.8) cannot be regarded as imposing an additional restriction. Moreover, inequality (5.8) removes some restrictions rather than imposes new ones. Indeed, we can now abandon the really limiting condition on the amplitude A^{lm} included in Eq. (2.10), namely that on the transversal variation of the amplitude. This now-eliminated condition is certainly in contradiction to many plasma physics applications. For example, launchers used for excitation of Alfvén, ion-cyclotron, and lower-hybrid waves in plasmas are necessarily of a size comparable to the wavelength at the plasma boundary, thus violating the condition (2.10) and restricting the applicability of the ray approach.

5.4. Example of a pWKB solution

In this section we discuss the classic problem of the diffraction at an aperture and compare the exact solution with different short-wavelength asymptotics. Consider a homogeneous medium with a plane wave $\exp(ik_0 z)$ incident upon a plane screen at $z = 0$ with an opening in it. A two-dimensional opening could easily be considered. However, all the wave characteristics of interest to us are seen already in the one-dimensional case, and extension to the two-dimensional case is straightforward. Therefore, we restrict ourselves to the simplest case and assume that the opening is infinitely long in the y direction and the wave field at $z = 0$ is $\Phi_0(x)$. Then the field in the half-space $z > 0$ is described by the problem

$$\begin{cases} \Delta\Phi + \dfrac{\omega^2}{c^2} N^2 \Phi = 0, \\ \Phi(\mathbf{r})\Big|_{z=0} = \Phi_0(x), \end{cases} \tag{5.9}$$

which has an exact solution given by

$$\Phi(\mathbf{r}) = \int \Phi_{0,k}(k_x)\, e^{ik_x x + iz\sqrt{k_0^2 - k_x^2}}\, dk_x, \tag{5.10}$$

where $k_0 = \omega N/c$ and

$$\Phi_{0,k}(k_x) = \frac{1}{2\pi} \int \Phi_0(x)\, e^{-ik_x x} dx. \tag{5.11}$$

We now find two asymptotic solutions to the problem (5.9) in both the ray and beam approaches. It is convenient to set $\kappa = k_0$ and take the Hamiltonian in the form

$$H = \frac{1}{2} S_\alpha S_\alpha - \frac{1}{2} = 0. \tag{5.12}$$

Here and in the rest of this section we lower all indices, making no distinction between co- and contravariant components, and assume that the indices take the values x and z. The ray-tracing set of equations for this particular Hamiltonian is given by

$$\dot{q}_\alpha = S_\alpha, \qquad \dot{S}_\alpha = 0. \tag{5.13}$$

Taking the initial conditions $q_x(0) = q_z(0) = S_x(0) = 0$ and $S_z(0) = 1$, we find from Eq. (5.13) that

$$q_x(t) = S_x(t) = 0, \quad q_z(t) = t, \quad S_z(t) = 1. \tag{5.14}$$

It follows that we can identify the parameter t with the space coordinate z and write the geometric-optics solution in any of the forms

$$\Phi^R(\mathbf{r}) = \Phi_0(x)\, e^{ik_0 z} = \int \Phi_{0,k}(k_x)\, e^{ik_x x + ik_0 z} dk_x. \tag{5.15}$$

We obtain the beam-tracing set of equations, noting first that for the two-dimensional problem under consideration the ray variable v can be omitted. Furthermore, from Eq. (5.12) we have $V_\alpha = \partial H/\partial S_\alpha = S_\alpha$ and, making use of $V_\alpha u_\alpha = S_\alpha u_\alpha = 0$ and Eq. (5.14), conclude that $u_z \equiv 0$. Similarly, $S_{zz} \equiv S_{xz} \equiv S_{zx} \equiv 0$ follows from $dS_\alpha/dt = V_\beta S_{\alpha\beta} = \partial H/\partial x_\alpha = 0$. For non-vanishing components of $S_{\alpha\beta}$ and u_α we have

$$\dot{u}_x = -S_{xx} u_x, \qquad \dot{S}_{xx} + S_{xx}^2 = u_x^4. \tag{5.16}$$

At $z = 0$ we have the plane wave, whence the initial condition for the phase in Eq. (5.16) is $S_{xx}|_{z=0} = 0$. The initial condition

for u_x so far is arbitrary and we take $u_x = (\sqrt{k_0}a)^{-1}$. Such an initial condition is relevant when the x size of the aperture at $z = 0$ is close (but not necessarily equal) to $2a$. The solution to Eq. (5.16) is then

$$S_{xx} = \frac{z}{z^2 + k_0^2 a^4}, \qquad u_x = \frac{\sqrt{k_0}a}{\sqrt{z^2 + k_0^2 a^4}}. \tag{5.17}$$

We can now construct a pWKB solution:

$$\begin{aligned} \Phi^B(\mathbf{r}) = & \frac{\sqrt{k_0}a}{\sqrt[4]{k_0^2 a^4 + z^2}} \exp\left\{ik_0 z + \frac{ik_0 x^2 z}{2\left(k_0^2 a^4 + z^2\right)}\right\} \\ & \times \sum_l C_l \varphi_l\left(\frac{k_0 a x}{\sqrt{k_0^2 a^4 + z^2}}\right) \\ & \times \exp\left\{-i\left(l + \frac{1}{2}\right) \arctan \frac{z}{k_0 a^2}\right\}. \end{aligned} \tag{5.18}$$

The coefficients C_l in Eq. (5.18) are given by

$$C_l = a^{-1} \int_{-\infty}^{\infty} \Phi_0(x) \varphi_l(x/a)\, dx \tag{5.19}$$

so that

$$\Phi_0(x) = \sum_l C_l \varphi_l(x/a). \tag{5.20}$$

To compare the pWKB solution (5.18) with the exact one (5.10), we calculate the Fourier transforms of Eqs. (5.18) and (5.20):

$$\begin{aligned} \Phi_k^B(k_x, z) &= \frac{1}{2\pi} \int e^{-ik_x x} \Phi^B(\mathbf{r})\, dx \\ &= \frac{a}{\sqrt{2\pi}} \exp\left(ik_0 z - i\frac{k_x^2 z}{2k_0}\right) \sum_l (-i)^l C_l \varphi_l(a k_x) \end{aligned} \tag{5.21}$$

and

$$\Phi_{0,k}(k_x) = \frac{a}{\sqrt{2\pi}} \sum_l (-i)^l C_l \varphi_l(a k_x), \tag{5.22}$$

respectively. Combining Eq. (5.21) with Eq. (5.22), we obtain

$$\Phi^B(\mathbf{r}) = \int \Phi_{0,k}(k_x)\, e^{ik_x x + ik_0 z\left(1-\frac{k_x^2}{2k_0^2}\right)} dk_x. \tag{5.23}$$

Let us now compare two approximate solutions (5.15) and (5.23) with the exact one (5.10). As discussed in the previous section, we can expect reasonable agreement only in the case where the spectrum width $|k_x| \leq \Delta_k$ described by the function $\Phi_{0,k}(k_x)$ in Eq. (5.11) is small enough, $\Delta_k/k_0 \ll 1$. Then we can expand the square root in the exponent of Eq. (5.10) with respect to the small parameter $k_x/k_0 \ll 1$ and successively get in the zeroth order of the expansion the ray solution (5.15) and in the first order the pWKB solution (5.23).

This observation shows that the pWKB solution always includes the ray approximation as a particular case but, in fact, describes much more. Thus, it is immediately seen from Eq. (5.18) that two zones along the z axis are physically different. The first one, $z \ll k_0 a^2$, is the near-field or Fresnel diffraction zone and the second region, $z \gg k_0 a^2$, is the far-field or Fraunhofer diffraction zone. Consider first the Fraunhofer diffraction. Equation (5.18) when used with Eq. (5.22) then gives the well-known expression

$$\Phi^B_{\text{far}}(\mathbf{r}) = \sqrt{\frac{2\pi k_0}{z}}\, \Phi_{0,k}\left(\frac{k_0 x}{z}\right) e^{-i\frac{\pi}{4} + ik_0 z\left(1+\frac{x^2}{2z^2}\right)}, \tag{5.24}$$

which describes a spherical wave with its center at $x = z = 0$ and with an angular distribution of the amplitude given by the Fourier transform of the initial condition (5.11).

For the Fresnel diffraction we have

$$\Phi^B_{\text{near}}(\mathbf{r}) = \sum_l C_l \varphi_l(x/a) e^{ik_0 z\left(1+\frac{x^2}{2k_0^2 a^4}\right) - i\left(l+\frac{1}{2}\right)\arctan\frac{z}{k_0 a^2}}. \tag{5.25}$$

It can be shown that the expression describes all features of the near field, including the field behavior near the boundaries of geometrical shadows.

Returning to the subject of the previous section, we notice that for the homogeneous medium under consideration $L = \infty$ and therefore all the applicability requirements are clearly fulfilled. In spite of this, the ray solution (5.15) gives an admissible result for the near zone only. The reason is that the conditions discussed in Section 5.3 and previously in Section 2.1 are only necessary but not sufficient for applicability. Sufficient conditions are formulated in [1] and will not be discussed here.

Probably a somewhat more illuminative description for the limits of the method can be given by formulating a "most sophisticated" problem for which the method still yields an exact solution. Then any further complications of the problem can be considered as something which cannot be described exactly and therefore is a source of discrepancy between the exact and asymptotic solutions. Such a problem for the pWKB method is the quantum-mechanics problem of the multidimensional harmonic oscillator. In other words, it is a time-dependent Schrödinger equation with arbitrary dependence of the external force on time and with a potential given by a second-order multivariable polynomial.

We can conclude that the first source of error is the difference between the wave processes as described by the Schrödinger equation and by the wave equation. Being good for the Schrödinger equation, the pWKB solution, like any WKB solution, considers two waves travelling in opposite directions as fully independent. Therefore, it fails to describe the energy exchange between these two waves. However, the energy transfer is usually exponentially small and can be neglected in most cases. An exception is a neighborhood of turning points, i.e., those points along a ray where $|\mathbf{V}| \to 0$. Another kind of asymptotic expansion has to be used in the vicinity of such points. Note that if only one or two components of $\mathbf{V}$ vanish, the applicability of the pWKB method is not violated.

Another source of error is truncation in the paraxial expansion, where only terms up to the second order with respect to Λ/L are retained. This procedure is exact when the function $N^2(\mathbf{r})$ in Eq. (1.1) is a second-order polynomial but it results in errors if the function is more complicated. The errors are

acceptable when the properties of the medium vary slightly over the region of the wave-packet localization, $\Lambda \ll L$. If $\Lambda \geq L$ but still $\lambda \ll L$, then the appropriate treatment is provided by the ray approach.

6. Conclusions

In conclusion, we outline the main features of the pWKB method presented here. The method differs in two respects from the ray method, which is also often referred to as the WKB method. First, the pWKB method uses Gaussian beams as the basis of the asymptotic expansion rather than plane waves, as the ray approach does. This allows one to describe properly a variety of diffractional phenomena which are not reproduced by the ray method. Second, an additional power series (paraxial) expansion is implemented. It results in a drastic simplification of the final set of equations.

Mathematically, the fundamental difference between the two approaches is that they are based on different asymptotic expansions with respect to the same small parameter $1/\kappa = \lambda/2\pi L \ll 1$. Although the expansions differ as a whole, the zero-order approximations for the two methods coincide, giving the well-known eikonal equation. The next, first-order, approximation of the pWKB method deals with variation of the wave-packet width and wave-front curvature. There is no analogy to this approximation in the ray approach. Nevertheless, the same Hamiltonian function as in the geometric optics is used in this step. The set of equations for the beam width and divergence is formulated in terms of second derivatives of the Hamiltonian. The last-used, second-order, approximation of the pWKB method is somewhat similar to the first-order approximation of the ray approach. It determines the behavior of the field amplitude.

As a consequence of the asymptotic expansion, the order of the differential equation to be solved is reduced by one from the second to the first order. However, the resulting first-order partial differential set of equations is still rather difficult

to solve. An essential further simplification is achieved by subsequent paraxial expansion. This is a power-series expansion with respect to the ratio of the wave-packet width to the medium inhomogeneity length. As a result, the general solution to the wave equation is represented by an analytic formula. Some functions entering this formula have to be found as a solution to a set of first-order ordinary differential equations expressed in terms of the conventional Hamiltonian of the geometric optics. This set of equations has a clear physical meaning. It describes the transformation from the original laboratory coordinate system to the special ray coordinate system. In the ray coordinates the ray trajectory is a straight line, the wave front is a plane, and the wave amplitude does not vary along the ray.

The pWKB method is applicable to a whole variety of problems described by the wave equation. In particular, these include the plasma physics problems of RF heating, current drive, and plasma diagnostics with microwave beams.

Acknowledgments

The author is grateful to M. Brambilla for valuable discussions and for the opportunity to familiarize himself with the manuscript of his new book. The author also wishes to express his appreciation to the Technology Division and the Tokamak Physics Division of the Max-Planck-Institut für Plasmaphysik for help and support received during this work.

Appendices

A. Geometric properties of ray trajectories

A.1. The Fermat principle for Eq. (1.1)

It is well known [12] that an alternative approach to geometric optics is possible on the basis of the Fermat principle. This gives a variational formulation equivalent to the eikonal equation. On the basis of this formalism, some properties of ray trajectories which are used in this report can be derived in the

most general way. For convenient reference, we present here a derivation according to [8]. It is shown that the ray trajectories are geodesics in some Riemannian space. To this end, we start with the first order partial differential eikonal equation

[1.6] $$H(x^\alpha, S_\beta) = H(x^\alpha, \frac{\partial S}{\partial x^\beta}) = 0. \qquad (A.1)$$

Here and below the formula number given in square brackets on the left-hand side refers to the corresponding formula in the main part of the paper. Following Cauchy's method of characteristics, we consider the parametric representation of the coordinates $x^\alpha = x^\alpha(t)$ and wave vector components $S_\alpha = S_\alpha(t)$. Suppose that these six functions are given in 6D phase space $\{x^\alpha, S_\beta\}$ at some 5D hypersurface σ such that $t = t_0$ at σ. The initial values must satisfy the dispersion relation $H|_\sigma = 0$. The requirement

$$\frac{dH}{dt} = \frac{\partial H}{\partial x^\alpha}\dot{x}^\alpha + \frac{\partial H}{\partial S_\alpha}\dot{S}_\alpha = 0 \qquad (A.2)$$

then ensures that the eikonal equation $H \equiv 0$ is fulfilled along any trajectory in the 6D phase space passing through some point of σ. We can require that

[1.8] $$\dot{x}^\alpha = \frac{\partial H}{\partial S_\alpha}; \qquad (A.3)$$

then Eq. (A.2) is clearly valid if

[1.9] $$\dot{S}_\alpha = -\frac{\partial H}{\partial x^\alpha}. \qquad (A.4)$$

The eikonal equation is thus satisfied along any trajectory of the Hamiltonian set of equations (A.3)–(A.4).

Let us now introduce the notations

[2.17] $$V^\alpha \stackrel{\text{def}}{=} \frac{\partial H}{\partial S_\alpha} \qquad (A.5)$$

and

$$F(x^\alpha, V^\beta) \stackrel{\text{def}}{=} S_\gamma V^\gamma - H(x^\alpha, S_\beta). \qquad (A.6)$$

Upon differentiation of Eq. (A.6) with allowance for Eq. (A.3) and the dependences explicitly shown in Eq. (A.6), we

obtain

$$\frac{\partial F}{\partial x^\alpha} = V^\beta \frac{\partial S_\beta}{\partial x^\alpha} - \frac{\partial H}{\partial x^\alpha} - \frac{\partial H}{\partial S_\beta}\frac{\partial S_\beta}{\partial x^\alpha} = -\frac{\partial H}{\partial x^\alpha}, \tag{A.7}$$

$$\frac{\partial F}{\partial V^\alpha} = S_\alpha + V^\beta \frac{\partial S_\beta}{\partial V^\alpha} - \frac{\partial H}{\partial S_\beta}\frac{\partial S_\beta}{\partial V^\alpha} = S_\alpha. \tag{A.8}$$

Equation (A.4) may now be written as

$$\frac{d}{dt}\frac{\partial F}{\partial V^\alpha} - \frac{\partial F}{\partial x^\alpha} = 0. \tag{A.9}$$

These are clearly Euler's equations for the Fermat functional:

$$I = \int F\, dt = \int S_\alpha\, dx^\alpha - H\, dt. \tag{A.10}$$

The general variational problem can now be expressed in the form of the *Principle of Least Action:*

A ray trajectory is an extremal of the action integral

$$\mathcal{A} = \int S_\alpha\, dx^\alpha \tag{A.11}$$

satisfying the subsidiary condition $H = 0$.

The action $\mathcal{A}$ can also be written in any of the following forms:

$$\mathcal{A} = \int S_\alpha \frac{\partial H}{\partial S_\alpha} dt = \int S_\alpha V^\alpha\, dt = \int S_\alpha \frac{dx^\alpha}{dt} dt = \int dS. \tag{A.12}$$

The latter representation results in the *Fermat principle:*

The optical length between two points is minimal along the ray trajectory.

It can be shown, conversely, that the eikonal equation is a corollary to the Fermat principle, thus proving the equivalency of the two approaches. However, this is not done, because no use is made of it here.

A.2. Rays as geodesics in a Riemannian space

Another formulation of the Fermat principle states that a ray trajectory is a geodesic in a (in general, non-Euclidean) space with the arc element dS. We now consider the metric properties of this Riemannian space. Starting at this point, we use a specific expression (1.6) for the Hamiltonian corresponding to the wave equation in the form of Eq. (1.1):

[1.6] $$H = \frac{1}{2}\varepsilon^{\alpha\beta}S_\alpha S_\beta - N^2 = 0. \tag{A.13}$$

First it is assumed that the quantity $N^2(\mathbf{r})$ is not equal to zero in some space region (this is not the case for Eq. (1.3) in the main part of the paper). Then we can pass over to a new Hamiltonian $\mathcal{H}$ by dividing Eq. (A.13) by $2N^2$:

$$\mathcal{H} \stackrel{\text{def}}{=} \frac{H}{2N^2} = \frac{1}{4N^2}\varepsilon^{\alpha\beta}S_\alpha S_\beta - \frac{1}{2} = 0. \tag{A.14}$$

Introducing a new matrix

$$h^{\alpha\beta} = \frac{\varepsilon^{\alpha\beta}}{2N^2} \tag{A.15}$$

and its inverse $h_{\alpha\beta}$ such that $h_{\alpha\gamma}h^{\gamma\beta} = \delta^\beta_\alpha$, we can write

$$S^\alpha \stackrel{\text{def}}{=} \frac{\partial\mathcal{H}}{\partial S_\alpha} = h^{\alpha\beta}S_\beta, \quad S_\alpha = h_{\alpha\beta}S^\beta, \tag{A.16}$$

$$\begin{aligned}\mathcal{H} &= \frac{1}{2}h^{\alpha\beta}S_\alpha S_\beta - \frac{1}{2} \\ &= \frac{1}{2}h_{\alpha\beta}S^\alpha S^\beta - \frac{1}{2} = \frac{1}{2}S_\alpha S^\alpha - \frac{1}{2} = 0.\end{aligned} \tag{A.17}$$

Accordingly, the Lagrangian function $\mathcal{F}$ takes the form

$$\mathcal{F} \stackrel{\text{def}}{=} S_\alpha S^\alpha - \mathcal{H} = \frac{1}{2}h_{\alpha\beta}S^\alpha S^\beta + \frac{1}{2}. \tag{A.18}$$

The significant property of the new Hamiltonian $\mathcal{H}$ is

$$\frac{dS}{dt} = S_\alpha\frac{\partial\mathcal{H}}{\partial S_\alpha} = S_\alpha S^\alpha = h_{\alpha\beta}S^\alpha S^\beta = 1, \tag{A.19}$$

which shows that the parameter of trajectory t coincides with the eikonal function S and that the two vectors of the group velocity $\mathbf{V}$ and phase velocity ∇S coincide, being unity vectors with the contravariant and covariant components $V^\alpha = S^\alpha$ and $V_\alpha = S_\alpha$, respectively.

We now derive an equation for a ray trajectory described by the Hamiltonian set of equations (A.3)–(A.4) with the Hamiltonian $\mathcal{H}$ and show that it is a geodesic in a Riemannian space with the metric $h_{\alpha\beta}$. To this end, we can start with the Fermat principle and consequently with Eq. (A.9) for the Lagrangian (A.18). However, it is more instructive to depart directly from the second of the Hamiltonian equations (A.4). Using also Eqs. (A.16) and (A.17), we have

$$\dot{S}_\alpha + \frac{\partial \mathcal{H}}{\partial x^\alpha} = h_{\alpha\beta}\dot{S}^\beta + S^\beta S^\gamma \frac{\partial h_{\alpha\beta}}{\partial x^\gamma} + \frac{1}{2} h_{\beta\nu} S^\beta h_{\gamma\mu} S^\gamma \frac{\partial h^{\nu\mu}}{\partial x^\alpha} = 0. \tag{A.20}$$

Using the notations below for Christoffel symbols

$$\left\{ \begin{matrix} \alpha \\ \beta\gamma \end{matrix} \right\} = h^{\alpha\delta}[\beta\gamma, \delta] = \frac{1}{2} h^{\alpha\delta} \left(\frac{\partial h_{\delta\beta}}{\partial x^\gamma} + \frac{\partial h_{\delta\gamma}}{\partial x^\beta} - \frac{\partial h_{\gamma\beta}}{\partial x^\delta} \right), \tag{A.21}$$

and by virtue of the obvious relations

$$\begin{aligned} h_{\alpha\gamma} \frac{\partial h^{\gamma\beta}}{\partial x^\nu} &= -h^{\gamma\beta} \frac{\partial h_{\alpha\gamma}}{\partial x^\nu}, \\ \frac{\partial h^{\beta\gamma}}{\partial x^\alpha} &= -h^{\beta\nu} \left\{ \begin{matrix} \gamma \\ \alpha\nu \end{matrix} \right\} - h^{\gamma\nu} \left\{ \begin{matrix} \beta \\ \alpha\nu \end{matrix} \right\}, \end{aligned} \tag{A.22}$$

we can rewrite Eq. (A.20) as

$$h_{\alpha\beta}\dot{S}^\beta + \frac{1}{2} S^\beta S^\gamma \left(\frac{\partial h_{\alpha\beta}}{\partial x^\gamma} + \frac{\partial h_{\alpha\gamma}}{\partial x^\beta} - \frac{\partial h_{\beta\gamma}}{\partial x^\alpha} \right). \tag{A.23}$$

Finally, by multiplying Eq. (A.23) by $h^{\alpha\nu}$ and changing indices we get the desired equation for the ray

$$\dot{S}^\alpha + S^\beta S^\gamma \left\{ \begin{matrix} \alpha \\ \beta\gamma \end{matrix} \right\} = 0, \tag{A.24}$$

which coincides with the equation for a geodesic in a Riemannian space metrized by

$$dS^2 = h_{\alpha\beta}dx^\alpha dx^\beta = h_{\alpha\beta}S^\alpha S^\beta dt^2. \qquad \text{(A.25)}$$

The concept of covariant differentiation [14] of the tensor calculus is now utilized. The covariant derivatives of a vector **B** are determined as

$$B_{\alpha|\beta} \stackrel{\text{def}}{=} \frac{\partial B_\alpha}{\partial x^\beta} - B_\gamma \left\{ \begin{matrix} \gamma \\ \alpha\beta \end{matrix} \right\}, \quad B^\alpha_{|\beta} \stackrel{\text{def}}{=} \frac{\partial B^\alpha}{\partial x^\beta} + B^\gamma \left\{ \begin{matrix} \alpha \\ \beta\gamma \end{matrix} \right\} \qquad \text{(A.26)}$$

for covariant B_α and contravariant B^α components, respectively. Furthermore, the intrinsic (or absolute) derivatives are

$$\frac{\delta B_\alpha}{\delta t} \stackrel{\text{def}}{=} S^\beta B_{\alpha|\beta}, \qquad \frac{\delta B^\alpha}{\delta t} \stackrel{\text{def}}{=} S^\beta B^\alpha_{|\beta}. \qquad \text{(A.27)}$$

Noting that the covariant derivatives of the fundamental tensors vanish (Ricci theorem), we can write the result of differentiation of Eq. (A.16) as

$$S_{\alpha|\beta} = S_{\beta|\alpha} = h_{\alpha\gamma}S^\gamma_{|\beta} \qquad \text{or} \qquad S^\alpha_{|\beta} = h^{\alpha\gamma}S_{\gamma|\beta}. \qquad \text{(A.28)}$$

Equation (A.24) then reads

$$\text{[1.8, 1.9]} \qquad \frac{\delta S^\alpha}{\delta t} = 0 \qquad \text{or} \qquad \frac{\delta S_\alpha}{\delta t} = 0. \qquad \text{(A.29)}$$

These equations show that the vectors of the group and phase velocities **V** and ∇S form parallel vector fields along the ray trajectory.

The condition $N^2 \neq 0$ used above is not necessary. Actually, it was used solely in transition from Eq. (A.13) to Eq. (A.14). The goal of this transformation was to obtain a Hamiltonian which satisfies the condition (A.19). The latter has the geometrical meaning that in the Riemannian space with the metric $h_{\alpha\beta}$ the arc length is described by the eikonal S. Therefore, to represent the ray equation in the form Eq. (A.24), the eikonal

function S must be the parameter of the ray; otherwise the right-hand side of Eq. (A.24) would be nonzero and the ray trajectories would not be geodesics. Consequently, $dt = dS$ and the dots in Eqs. (A.23), (A.24) denote derivatives with respect to S.

Let us assume that in some point of the ray trajectory we have $N^2 = 0$, as with electrostatic waves. Then Eq. (A.19) takes the form $dS/dt = 0$, but all operations performed in Eqs. (A.20)–(A.24) remain valid with one substantial exception. Now we have $S \equiv \text{const}$ along the ray, and it is impossible to use the eikonal S as a parameter of the ray trajectory. Nevertheless, any permitted parameterization of the ray may be chosen and vanishing of the quantity N^2 does not change either the Fermat principle or the conclusion that the ray trajectory is a geodesic in some Riemannian space. The transition to electrostatic oscillations of a cold plasma $H = h_{\alpha\beta}S^\alpha S^\beta = 0$ as a case of practical interest can be done simply by renumbering the ray coordinates [15].

Geometrically, $N^2 = 0$ means that the metric of this Riemannian space is not positive-definite. Actually, in this case $dS/dt = \varepsilon_{\alpha\beta}V^\alpha V^\beta = 0$ and the ray is a null-curve. It is known [16] that if any portion of a geodesic is a null-curve, then the whole geodesic is a null-geodesic. This remark implies that mixed trajectories such that on one part of them $N^2 = 0$ and on another part $N^2 \neq 0$ do not exist or if a ray passes through a point $\mathbf{r}_0$ such that $N^2(\mathbf{r}_0) = 0$, then $N^2 \equiv 0$ in all points of the ray. In other words, if a ray is tangential to the phase front at one point of a trajectory, then the property holds at all points of the trajectory.

B. Tensor form of the beam-tracing equations

The remark made at the end of Appendix A justifies a separate treatment of the two different cases $N^2 = 0$ and $N^2 \neq 0$. For the sake of simplicity it is assumed in this Appendix that the Hamiltonian has the form of Eq. (A.18), i.e., $N^2 \neq 0$. Note, however, that in Section 3 an account of the general case is given without any specification of the value N^2 or even of the form of the Hamiltonian.

B.1. Ray coordinates

Let us consider a single ray as a general member of the variety of rays satisfying Eq. (A.24). In Section 3 this ray was called the reference ray and denoted as $\Re$. Let us also assume that the ray $\Re$ is described by parametric equations $x^\alpha = q^\alpha(t)$ and introduce the ray-related coordinate system $\{u, v, S\}$ such that $u(\mathbf{r}) = v(\mathbf{r}) = 0$ on the ray $\Re$. We also use the notations

[3.1] $$w^1 = u, \qquad w^2 = v, \qquad w^3 = S \tag{B.1}$$

and mark with bars the components of all tensors in the ray coordinate system. It is assumed in what follows that the Latin indices take values 1 and 2 so that w^i can stand for either u or v but not for S. The matrices of the direct and inverse transformations between the coordinate systems $\{x^\alpha\}$ and $\{w^\alpha\}$ are denoted as

$$x^\alpha_\beta = \frac{\partial x^\alpha}{\partial w^\beta}, \qquad w^\alpha_\beta = \frac{\partial w^\alpha}{\partial x^\beta}. \tag{B.2}$$

The components of the fundamental tensors in the ray coordinate system are

$$\bar{h}^{\alpha\beta} = h^{\nu\mu} w^\alpha_\nu w^\beta_\mu, \qquad \bar{h}_{\alpha\beta} = h_{\nu\mu} x^\nu_\alpha x^\mu_\beta. \tag{B.3}$$

The beam-tracing equations now read

[2.20, 2.22, 2.24] $$\begin{aligned} H &= \bar{h}^{33} - 1 = 0, \\ \bar{h}^{13} &= \bar{h}^{23} = \bar{h}^{12} = 0, \end{aligned} \tag{B.4}$$

[2.23] $$D_{w^i}(\bar{h}^{j3}) = 0, \tag{B.5}$$

[2.21] $$D^2_{w^i w^j}(\bar{h}^{33}) = \bar{h}^{ij}. \tag{B.6}$$

The reader is reminded here that in accordance with the sense of Eqs. (2.20)–(2.24) all the quantities in Eqs. (B.4)–(B.6) are evaluated on $\Re$, i.e., for $u = v = 0$. In the rest of this Appendix, if the opposite is not explicitly stated, all terms in all equations are evaluated on the reference ray and the index $\Re$ will be suppressed.

Equations (B.4)–(B.6) represent the metric properties of the considered Riemannian space in the vicinity of the reference ray. However, the tensor $\bar{h}^{\alpha\beta}$ is unknown and the equations cannot serve for determining the ray coordinates. For this purpose the set of equations introduced in the next section has to be used.

B.2. Derivation of the beam-tracing equations

Here we briefly reproduce the derivations of the main part of this paper, taking advantage of the tensor formalism. First of all, we have

$$D_{x^\alpha}[\mathcal{H}_U] = (S^\beta u_\beta)_{|\alpha} = S^\beta u_{\beta|\alpha} + S^\beta_{|\alpha} u_\beta = \frac{\delta u_\alpha}{\delta S} + S^\beta_{|\alpha} u_\beta = 0.$$

Whence, by virtue of $\bar{S}_{3|\alpha} = \bar{S}_{\alpha|3} = \bar{S}^3_{|\alpha} = \bar{S}^\alpha_{|3} = 0$ we get

[3.2]
$$\frac{\delta w^i_\alpha}{\delta S} = -S^\beta_{|\alpha} w^i_\beta = -\bar{S}^i_{|j} w^j_\alpha. \tag{B.7}$$

It is also assumed that here and below only Greek indices are taken into account in the intrinsic derivatives with respect to S, so that in such a differentiation the quantity w^i_α is viewed as a covariant vector and x^α_i as a contravariant vector rather than a mixed tensor of rank 2. To derive an equation for $S_{\alpha\beta}$, we use Eq. (B.6). By virtue of Eqs. (A.20), (A.24), and (A.29) we have

$$\begin{aligned} D_{x^\alpha}[D_{x^\beta}(\mathcal{H})] &= D_{x^\alpha}\left[\frac{\partial \mathcal{H}}{\partial x^\beta} + S^\nu S_{\nu\beta}\right] = D_{x^\alpha}\left[S^\nu S_{\beta|\nu}\right] \\ &= \left(S^\nu S_{\beta|\nu}\right)_{|\alpha} + \left\{ {\nu \atop \alpha\beta} \right\} \frac{\delta S_\nu}{\delta S} \\ &= S^\nu_{|\alpha} S_{\beta|\nu} + S^\nu S_{\beta|\nu|\alpha} \\ &= h^{\nu\mu} S_{\alpha|\mu} S_{\beta|\nu} + S^\nu S_{\beta|\nu|\alpha} \\ &= u_\alpha u_\beta \bar{h}^{11} + v_\alpha v_\beta \bar{h}^{22}. \end{aligned} \tag{B.8}$$

The known formula of the tensor calculus [14] reads

$$S_{\beta|\nu|\alpha} - S_{\beta|\alpha|\nu} = -S^\mu R_{\mu\beta\alpha\nu},$$

where

$$R_{\mu\beta\alpha\nu} = h_{\mu\gamma}R^{\gamma}_{\beta\alpha\nu} = h_{\mu\gamma}\left(\frac{\partial}{\partial x^{\alpha}}\left\{\begin{matrix}\gamma\\ \beta\nu\end{matrix}\right\} - \frac{\partial}{\partial x^{\nu}}\left\{\begin{matrix}\gamma\\ \beta\alpha\end{matrix}\right\} + \left\{\begin{matrix}\lambda\\ \beta\nu\end{matrix}\right\}\left\{\begin{matrix}\gamma\\ \lambda\alpha\end{matrix}\right\} - \left\{\begin{matrix}\lambda\\ \beta\alpha\end{matrix}\right\}\left\{\begin{matrix}\gamma\\ \lambda\nu\end{matrix}\right\}\right)$$

is the covariant Riemann–Christoffel tensor. For the considered problem with the Hamiltonian of the form (A.14) the tensor $R_{\mu\beta\alpha\nu}$ represents the properties of the Riemannian space but does not depend on the specific ray trajectory. We introduce the tensors

$$K_{\alpha\beta} \stackrel{\text{def}}{=} S^{\nu}S^{\mu}R_{\mu\alpha\beta\nu}, \quad K^{\alpha}_{\beta} \stackrel{\text{def}}{=} h^{\alpha\gamma}K_{\beta\gamma} = h^{\alpha\gamma}S^{\nu}S^{\mu}R_{\mu\beta\gamma\nu} \tag{B.9}$$

with properties which follow directly from the general properties of the Riemann–Christoffel tensor:

$$\begin{gathered} K_{\alpha\beta} = K_{\beta\alpha}, \quad \bar{K}_{3\alpha} = \bar{K}_{\alpha 3} = \bar{K}^{\alpha}_{3} = 0, \\ S^{\beta}K_{\alpha\beta} = S^{\beta}K^{\alpha}_{\beta} = S_{\beta}K^{\beta}_{\alpha} = 0. \end{gathered} \tag{B.10}$$

We can now continue the transformations in Eq. (B.8):

$$[3.3]\quad \frac{\delta}{\delta S}S_{\alpha|\beta} + h^{\nu\mu}S_{\alpha|\mu}S_{\beta|\nu} - K_{\beta\alpha} = u_{\alpha}u_{\beta}\bar{h}^{11} + v_{\alpha}v_{\beta}\bar{h}^{22}. \tag{B.11}$$

On differentiation of the obvious relation

$$[3.4]\quad x^{\alpha}_{i}w^{j}_{\alpha} = \delta^{j}_{i} \tag{B.12}$$

we have by virtue of Eq. (B.7)

$$w^{j}_{a}\frac{\delta x^{\alpha}_{i}}{\delta S} + x^{\alpha}_{i}\frac{\delta w^{j}_{\alpha}}{\delta S} = w^{j}_{\alpha}\frac{\delta x^{\alpha}_{i}}{\delta S} - x^{\alpha}_{i}S^{\beta}_{|\alpha}w^{j}_{\beta} = w^{j}_{\alpha}\left(\frac{\delta x^{\alpha}_{i}}{\delta S} - S^{\alpha}_{|\beta}x^{\beta}_{i}\right) = 0.$$

Hence, using again Eq. (B.12), we can write Eq. (3.5) in any of the following forms:

$$[3.5]\quad \frac{\delta x^{\alpha}_{i}}{\delta S} = S^{\alpha}_{|\beta}x^{\beta}_{i} = \bar{S}^{j}_{|i}x^{\alpha}_{j} = \frac{\delta S^{\alpha}}{\delta w^{i}}. \tag{B.13}$$

Equation (B.13), as well as Eq. (B.7), is valid for any i, including $i = 3$, but $x_3^\alpha \equiv S^\alpha$ obeys the more simple equation (A.29) and it makes sense to use Eqs. (B.7), (B.13) for $i = 1, 2$ only. In order to obtain Eq. (3.6), we multiply Eq. (B.11) by x_i^β:

$$\frac{\delta}{\delta S}\left(S_{\alpha|\beta}x_i^\beta\right) - S_{\alpha|\beta}\left(\frac{\delta x_i^\beta}{\delta S} - S^\beta_{|\gamma}x_i^\gamma\right) = x_i^\beta K_{\beta\alpha} + u_\alpha \delta_i^1 \bar{h}^{11} + v_\alpha \delta_i^2 \bar{h}^{22},$$

and by virtue of Eq. (B.13) this yields

[3.6] $$\frac{\delta}{\delta S}\left(S_{\alpha|\beta}x_i^\beta\right) = x_i^\beta K_{\beta\alpha} + u_\alpha \delta_i^1 \bar{h}^{11} + v_\alpha \delta_i^2 \bar{h}^{22}. \qquad \text{(B.14)}$$

B.3. Initial conditions

In line with the derivation made in Section 3.4, we calculate the derivative

$$\begin{aligned}
\frac{d}{dS}\left(w_\alpha^i h^{\alpha\beta} w_\beta^j\right) &= \frac{\delta}{\delta S}\left(w_\alpha^i h^{\alpha\beta} w_\beta^j\right) \\
&= -h^{\alpha\beta} w_\beta^j S^\nu_{|\alpha} w_\nu^i - h^{\alpha\beta} w_\alpha^i S^\nu_{|\beta} w_\nu^j \\
&= -w_\alpha^i w_\beta^j \left(h^{\beta\nu} S^\alpha_{|\nu} + h^{\alpha\nu} S^\beta_{|\nu}\right) \\
&= -w_\alpha^i w_\beta^j \left(h^{\beta\nu} h^{\alpha\mu} S_{\mu|\nu} + h^{\alpha\nu} h^{\beta\mu} S_{\mu|\nu}\right) \\
&= -2w_\alpha^i w_\beta^j h^{\alpha\nu} h^{\beta\mu} S_{\mu|\nu} = -2w_\alpha^i w_\beta^j h^{\alpha\gamma} S^\beta_{|\gamma} \\
&= -2w_\alpha^i w_\beta^j h^{\beta\gamma} S^\alpha_{|\gamma}.
\end{aligned} \qquad \text{(B.15)}$$

The matrix $S^\beta_{|\alpha}$ on the right-hand side of Eq. (B.15) has the eigenvector S_α with zero eigenvalue

$$S^\beta_{|\alpha} S_\beta = 0. \qquad \text{(B.16)}$$

The two other eigenvectors of the matrix $S^\beta_{|\alpha}$ satisfy the equation

[3.11] $$S^\beta_{|\alpha} e_\beta^{(i)} = \lambda_{(i)} e_\alpha^{(i)} \qquad \text{(sum on } \beta \text{ only, } i \text{ fixed).} \qquad \text{(B.17)}$$

With the proper choice of the two different eigenvectors $u_\alpha = e^{(1)}_\alpha$ and $v_\alpha = e^{(2)}_\alpha$, we can always fulfill the orthogonality condition at the initial point $S = 0$:

$$\bar{h}^{12}\Big|_{S=0} = \left(w^1_\alpha h^{\alpha\beta} w^2_\beta\right)\Big|_{S=0} = 0. \tag{B.18}$$

However, we need to prove that $\bar{h}^{12}(S) = 0$ for arbitrary S. To this end, we expand the quantity $\bar{h}^{12}(S)$ in the Taylor series

$$\bar{h}^{12}(S) = \bar{h}^{12}(0) + S\,\frac{d\bar{h}^{12}}{dS}\bigg|_{S=0} + \frac{1}{2}S^2\,\frac{d^2\bar{h}^{12}}{dS^2}\bigg|_{S=0} + \cdots. \tag{B.19}$$

By virtue of Eqs. (B.3), (B.15), and (B.17) we get

[3.13]
$$\frac{d\bar{h}^{12}}{dS}\bigg|_{S=0} = -\left(\lambda_{(1)}\bar{h}^{12}\right)\Big|_{S=0} = 0 \tag{B.20}$$

and see that the second term on the right-hand side of Eq. (B.19) is zero. Repeating the procedure, it is possible to show that all terms on the right-hand side of Eq. (B.19) vanish. This proves that $\bar{h}^{12}(S) \equiv 0$, as required by Eq. (B.4).

B.4. Metric properties of the ray coordinates

We can now state that the fundamental tensor $\bar{h}^{\alpha\beta}$ in the ray coordinates is of diagonal form. It follows that the fundamental tensor $\bar{h}_{\alpha\beta}$ possesses the same property. Similarly to the derivation of Eq. (B.15), we can obtain

$$\frac{d\,\bar{h}_{ij}}{dS} = \frac{d}{dS}\left(h_{\alpha\beta}x^\alpha_i x^\beta_j\right) = 2x^\alpha_i x^\beta_j S_{\alpha|\beta} = 2\bar{S}_{i|j} \tag{B.21}$$

and conclude that the tensor $\bar{S}_{i|j}$ and associated tensor $\bar{S}^i_{|j} = \bar{h}^{ik}\bar{S}_{j|k}$ are also diagonal. In view of Eq. (B.17) the matrix $\bar{S}^\alpha_{|\beta}$ has the form

$$\bar{S}^\alpha_{|\beta} = \begin{pmatrix} \lambda_{(1)} & 0 & 0 \\ 0 & \lambda_{(2)} & 0 \\ 0 & 0 & 0 \end{pmatrix}. \tag{B.22}$$

Substituting Eq. (B.22) into Eq. (B.7) and Eq. (B.13) we obtain

[3.2] $$\frac{\delta w_\alpha^i}{\delta S} = -\lambda_{(i)} w_\alpha^i \qquad \text{(no sum on } i\text{)} \tag{B.23}$$

and

[3.5] $$\frac{\delta x_i^\alpha}{\delta S} = \lambda_{(i)} x_i^\alpha \qquad \text{(no sum on } i\text{)}, \tag{B.24}$$

respectively. Let us assume that in all subsequent formulas no summation is done on Latin indices. In view of Eq. (B.7) and Eq. (B.15) we have

$$\frac{d\,\bar{h}^{ii}}{dS} = -2\lambda_{(i)} \bar{h}^{ii}. \tag{B.25}$$

The equations for the metric coefficients $\bar{h}_{ii}$, which are inverse to $\bar{h}^{ii}$, read

$$\frac{d\,\bar{h}_{ii}}{dS} = 2\lambda_{(i)} \bar{h}_{ii}. \tag{B.26}$$

As follows from Eq. (B.3), the quantities $\bar{h}^{ii}$ give the lengths of the vectors u_α and v_α. Inspection of Eq. (2.1) shows that the characteristic widths $d_{(i)}$ of a wave beam in two orthogonal directions can be introduced as

$$d_{(i)} = \frac{1}{|\nabla w^i|} = \left(\bar{h}^{ii}\right)^{-1/2} = \left(\bar{h}_{ii}\right)^{1/2}. \tag{B.27}$$

These quantities satisfy the equation

$$\frac{d}{dS} d_{(i)} = \lambda_{(i)} d_{(i)}, \tag{B.28}$$

which immediately follows from Eq. (B.25) or Eq. (B.26).

Let us now introduce the unit base vectors of the ray coordinate system

$$\hat{u}_\alpha = d_{(1)} u_\alpha, \qquad \hat{v}_\alpha = d_{(2)} v_\alpha. \tag{B.29}$$

In view of Eqs. (B.7), (B.23), and (B.25) we obtain

$$\frac{\delta\,\hat{u}_\alpha}{\delta S} = \frac{\delta\,\hat{v}_\alpha}{\delta S} = 0. \tag{B.30}$$

In a parallel fashion we introduce the reciprocal vectors

$$\hat{x}_1^\alpha = \frac{x_1^\alpha}{d_{(1)}}, \qquad \hat{x}_2^\alpha = \frac{x_2^\alpha}{d_{(2)}}, \tag{B.31}$$

which obey the set of equations

$$\frac{\delta \hat{x}_1^\alpha}{\delta S} = \frac{\delta \hat{x}_2^\alpha}{\delta S} = 0. \tag{B.32}$$

Equations (B.30) and (B.32) are similar to Eq. (A.29) and mean that each of the vectors $\hat{u}_\alpha$, $\hat{v}_\alpha$, S_α, $\hat{x}_1^\alpha$, $\hat{x}_2^\alpha$, and S^α forms a parallel vector field along $\mathfrak{R}$, so that

$$\hat{w}_\alpha^i h^{\alpha\beta} \hat{w}_\beta^j = \delta^{ij} \qquad \text{and} \qquad \hat{x}_i^\alpha h_{\alpha\beta} \hat{x}_j^\beta = \delta_{ij}. \tag{B.33}$$

It can also be stated that the particular choice of the new coordinate system $\{\hat{u}, \hat{v}, S\}$ results in recovery of the Cartesian metric on the reference ray $\mathfrak{R}$.

Multiplying Eq. (B.14) by x_j^α and making use of Eq. (B.25), we obtain the equation for $\lambda_{(i)} = \bar{S}_{|i}^i$

$$\frac{d\lambda_{(i)}}{dS} + \lambda_{(i)}^2 = \bar{K}_i^i + \left(\bar{h}^{ii}\right)^2. \tag{B.34}$$

The set of beam-tracing equations comprises Eqs. (B.25), (B.31), and (B.34). The four equations Eq. (B.25) and Eq. (B.34) can be also written in the form of two complex equations

$$\frac{d}{dS}\left(\lambda_{(j)} + i\bar{h}^{jj}\right) + \left(\lambda_{(j)} + i\bar{h}^{jj}\right)^2 = \bar{K}_j^j \tag{B.35}$$

or as two second-order equations

$$\frac{d^2}{dS^2} d_{(i)} - \bar{K}_i^i d_{(i)} = \frac{1}{d_{(i)}^3}. \tag{B.36}$$

The quantities $\bar{K}_i^i$ are given by

$$\bar{K}_i^i = S^\nu S^\mu R_{\nu\alpha\beta\mu} \hat{x}_i^\alpha \hat{x}_i^\beta. \tag{B.37}$$

The quantities $S_{\alpha\beta}$ are expressed via the solutions of Eqs. (B.30) and (B.34) as

$$S_{\alpha\beta} = S_{\alpha|\beta} + S_\gamma \left\{ \begin{matrix} \gamma \\ \alpha\beta \end{matrix} \right\}, \quad S_{\alpha|\beta} = \lambda_{(1)} \hat{u}_\alpha \hat{u}_\beta + \lambda_{(2)} \hat{v}_\alpha \hat{v}_\beta. \tag{B.38}$$

REFERENCES

1. Yu. A. Kravtsov and Yu. I. Orlov, *Geometrical Optics of Inhomogeneous Media,* Springer Series on Wave Phenomena, Vol. 6, Springer-Verlag (1990).
2. I. B. Bernstein and L. Friedland, in: *Handbook of Plasma Physics*, M. N. Rosenbluth and R. Z. Sagdeev (eds.), Vol. 1 (1983).
3. M. Brambilla and A. Cardinali, *Plasma Physics,* **24**, 1187 (1982).
4. J. W. Connor, R. J. Hastie, and J. B. Taylor, *Proc. R. Soc. London,* **A.365**, 1 (1979).
5. G. V. Pereverzev, *Nucl. Fusion,* **32**, 1091 (1992).
6. E. Mazzucato, *Phys. Fluids,* **B1**, 1855 (1989).
7. V. A. Fock, *Electromagnetic Diffraction and Propagation Problems,* Pergamon (1965).
8. V. M. Babič and V. S. Buldyrev, *Short-Wavelength Diffraction Theory: Asymptotic Methods,* Springer Series on Wave Phenomena, Vol. 4, Springer-Verlag (1991).
9. V. P. Maslov, *Complex WKB Method in Nonlinear Equations* [in Russian], Nauka (1970).
10. A. G. Litvak, in: *Reviews of Plasma Physics, Vol. 10,* Consultants Bureau (1986), p. 193.
11. S. Choudhary and L. B. Felsen, *Proc. of the IEEE,* **62**, 1530 (1974).
12. L. D. Landau and E. M. Lifshitz, *Quantum Mechanics,* Pergamon Press (1965).
13. G. V. Pereverzev, *JETP Letters,* **44**, 549 (1986).
14. I. S. Sokolnikoff, *Tensor Analysis: Theory and Applications to Geometry and Mechanics of Continua,* John Wiley & Sons (1967).
15. G. V. Pereverzev, *19th EPS Conference on Controlled Fusion and Plasma Physics, Innsbruck, 29 June - 3 July 1992,* Contributed Papers, Vol. 16C, Part II, 1489.
16. D. Lovelock and H. Rund, *Tensors, Differential Forms, and Variational Principles (Pure and Applied Mathematics),* John Wiley & Sons (1975).
17. B. Spain, *Tensor Calculus,* Interscience (1953).

MULTIPLE-MIRROR PLASMA CONFINEMENT

V. V. Mirnov and A. J. Lichtenberg

Introduction

Together with toroidal systems, which now hold a leading position in controlled thermonuclear fusion research, an important place also belongs to open plasma confinement systems. Because of their geometrical simplicity and technological advantages, they are considered to be one of the main alternative concepts for a thermonuclear reactor.

During the last twenty years considerable progress has been made in developing new types of open systems, which possess improved longitudinal confinement in comparison with the "classical" single-cell mirror [1, 2]. The plasma lifetime in a single-cell mirror is roughly equal to the ion–ion collision time, which is marginal for a fusion reactor. Furthermore, if microfluctuations are excited in the plasma, due to the non-Maxwellian velocity distribution, then scattering on these fluctuations can transport velocities into the mirror loss cone, with a corresponding deterioration in the reactor power characteristics. Since the level of fluctuations needed for significant enhancement only exceeds the level of thermal fluctuations by a few times, simple open systems are very sensitive to the presence of high-frequency microinstabilities. Our present understanding is not sufficient to ensure that the known methods of stabilization of these microinstabilities will be effective under thermonuclear reactor parameters. Therefore, one central aspect of open systems is the search for new methods of confinement for which the longitudinal losses are not strongly affected by microinstabilities.

One concept for improving this situation is that of the tandem mirror [3, 4]. In this concept a long central cell has improved ion confinement due to electrostatic forces arising from the higher density of cells. This improves the basic confinement, while at the same time flux from the central cell may inhibit microinstabilities by partially plugging the loss cone. The conditions for inhibiting the instabilities are delicate, and experimental results have not been as favorable as theoretical predictions.

Another solution to this problem is to have an open system whose level exceeds the mean free path of the charged particles. Under this condition the velocity space distribution function is close to an equilibrium Maxwellian, thus eliminating the thermodynamic drive for a wide class of microinstabilities. This makes the physics of plasma confinement simpler and therefore allows more reliable predictions of various confinement systems. However, to have a device of reasonable length, the value of the mean free path must be radically reduced, requiring both low temperature and high density. The practical realization of a device in this temperature and density range also requires a reduction of energy and particle flux to the ends of the machine. One possibility of achieving this reduction consists in corrugating the magnetic field, so that the flux becomes diffusive rather than a free internal flow. Configurations of this type have been called "corrugated open traps" or "multiple mirrors."

A multiple mirror consists of a set of mirrors connected to each other at their ends and having a full length L that exceeds the mean free path λ of the particles. If, at the same time, the corrugation period $l < \lambda$, then a transiting ion will be trapped in one of the mirrors, due to Coulomb collisions, before it leaves the plasma. When, after a few oscillations, it again becomes transiting, the direction of its longitudinal velocity changes with respect to its initial velocity in a random way. The resulting motion of ions is therefore a random walk with characteristic space step λ and time interval λ/ν_{T_i}. As a result, the free inertial plasma flow in a uniform magnetic field turns into slow diffusional expansion along the corrugated magnetic field, which is described by the law

$$z^2 - Dt \sim (\lambda_{T_i})\, t.$$

The effect of the reduction of the plasma expansion rate can be interpreted in another way as the result of the friction of transiting particles colliding with the trapped particles. The latter give their momentum to the magnetic field. One should emphasize that in a straight magnetic field the diffusive process is not possible because the collision of a pair of ions changes their total momentum; in a corrugated field, such scattering results in trapping in mirrors with high probability (i.e., the loss of the total momentum) with a corresponding decrease in the plasma expansion velocity. This effect allows a considerable reduction in the length and energy input in a reactor based on multiple mirror confinement. The multiple-mirror concept has the additional very useful property that if the confinement time (and therefore the reactor Q) falls short of predictions, the desired values can be recovered by making the device a little longer, with τ_{conf} improving proportionally to L^2.

We now give a brief history of the idea of multiple-mirror confinement. The term "corrugated field" has been mentioned in papers on plasma physics for a long time (see, for example, [5]), but these works are not directly related to axial confinement. A mechanism similar to that of multiple-mirror confinement was discussed in [6], which analyzes the slowing down of longitudinal plasma motion inside a dense pinch plasma, by the use of rough walls. The boundary between a plasma and a magnetic field with $\beta = 1$, i.e., no field inside the plasma, was considered, and particle motion in the transverse direction was limited by reflection from the corrugated magnetic surface. Another statement of the problem was considered in [7], where the effect on confinement of a single mirror by adding additional cells was studied. The approach taken in [7] was based on the Monte Carlo calculations of particle behavior in the corrugated field with fixed scattering centers. In connection with this model, we should note that a fixed-scattering-center model can produce diffusion even in a straight magnetic field, so the diffusive character of plasma expansion in a corrugated magnetic field cannot be confirmed using a fixed-center model. As to the results of [7], because the plasma temperature and density were chosen such that $\lambda \gg L$ the wrong conclusion was made that there is a linear dependence

of the lifetime on the number of mirrors. This was pointed out in [8], where the fixed-center model was used in the proper mean free path regime, so that the correct quadratic dependence of the lifetime on the number of mirrors was found. The result was consistent with that obtained in a different problem in which the r.f. induced scattering in small mirror cells was investigated [9]. Although this result was based on the fixed-center model and therefore was not rigorous, it was intuitively clear that trapped particles would behave like fixed scattering; thus, it encouraged the authors to pursue a self-consistent treatment of multiple-mirror confinement [10].

Independently of this work, which was carried out at Berkeley, at approximately the same time a self-consistent analysis of multiple-mirror confinement was performed by a group in Novosibirsk [11] that contained a quantitatively precise description of the effect of corrugation. The diffusion equation for plasma density that was first given in [11] was derived from the full set of kinetic equations based on actual *ii*, *ee*, and *ei* collisions. A detailed presentation of the theory appeared in [12]. The mathematical methods needed for the construction of this theory were partly based on papers published earlier in a study of the electroconductivity of an inhomogeneous plasma [13] and the skin effect in a corrugated magnetic field [14, 15]. However, the study of some aspects of multiple-mirror theory, particularly the construction of macroscopic equations for plasma parameters, requires the creation of new methods.

In summary, the concept of multiple-mirror confinement was independently initiated and developed in Novosibirsk and Berkeley at the beginning of the 1970's. From that time on, it has been extensively studied from both the theoretical and experimental points of view as a new method of longitudinal plasma confinement. The bibliography of multiple-mirror systems now numbers more than 100 papers. Since the basic studies in this field are reasonably complete, it appears to be an appropriate time to present a detailed description of the results. The present review focuses on the results of axial loss theory.

Since the plasma parameters during the expansion along the field vary considerably, the theory should cover this wide

parameter range. In Section 1 the various regimes of reduction of the plasma expansion rate are qualitatively discussed, the velocities of plasma motion are estimated, and the regimes are classified depending on the mean free path, the length of corrugation, and the mirror ratio.

A rigorous theory of longitudinal plasma flow in a corrugated magnetic field is given in Sections 2 and 3. In Section 2 the method of construction of flow equations is described for the case where the particle motion within the length of each mirror can be considered as collisionless (e.g., with small-scale corrugations). Although, in this regime, the flow of plasma does not obey the ordinary two-fluid gas dynamic equations, the smallness of λ compared with the scale of longitudinal inhomogeneity (which can normally be assumed equal to L) is sufficient for the flow of the plasma to be described macroscopically by means of moment equations.

The investigation of the opposite limiting case of collisional cells (the regime of large-scale corrugation) is presented in Section 3. For the case of large-scale corrugations, when the mean free path is small in comparison with the period of the corrugation, the two-fluid gas dynamic equations can be used to describe the motion. Besides the pure gas dynamic case the theory of an "intermediate" regime, which is realized in a magnetic field with narrow collisionless mirrors ("point" mirrors), is discussed as well. Since there are a number of different regimes, it is useful to construct a single approximate equation which covers them. Such an equation proved to be effective, for example, in the analysis of the problem of reducing the length and energy of the reactor due to the insertion of a small amount of heavy impurities with $Z \gg 1$.

In order to be useful as a controlled fusion device, the multiple-mirror confinement scheme must have a reactor embodiment that is feasible, i.e., one that operates with reasonable magnetic field strengths, lengths, and average powers. Although the basic confinement studies at Novosibirsk and Berkeley gave similar results [10, 12], two quite different reactor embodiments were conceived. The Novosibirsk group considered a pulsed reactor concept with dense plasma ($10^{17} - 10^{18}$ cm^{-3}) heated by

means of relativistic electron beams. Since at high density and thermonuclear temperature, megagauss fields are required for magnetic confinement, the alternate radial confinement mechanism of "wall" confinement ($\beta \gg 1$) is considered, for which the magnetic field suppresses only the transverse thermal conductivity, but equilibrium in this direction is provided by the rigid walls. The length is kept short due to the high density ($n \sim 10^{17}$ cm^{-3}), and the average power and wall loading are maintained at a reasonable level by having a low duty cycle. The concept was put forth and developed in a series of papers, which we refer to in Section 4.1.

In contrast, the Berkeley group considered a steady-state reactor with $\beta < 1$. The highest feasible superconducting magnetic fields were used in the central cell to obtain high density ($n \sim 10^{16}$ cm^{-3}), to keep the length short, and to employ a few relatively large mirrors. The average power was high but could be partly controlled with the plasma radius. The concept was set out and further developed in a series of papers referred to in Section 4.3.

Because of the very different reactor concepts, the ancillary physics required to validate the concept also took different paths. For the pulsed concept, the major concerns were the effectiveness of the magnetic insulation and the maintenance of the on-axis mirror ratio, both arising from the high β operation. These concerns were addressed in a series of papers, which we refer to in Section 4.2. For the steady-state concept, the major ancillary concern was MHD stability. Since a multiple-mirror gives, at best, average minimum B, achieving conditions of stability and designing appropriate magnetic field structures, particularly for the large mirror ratios, become quite difficult. Early works considered low β stability, while later works also dealt with ballooning modes. We refer to these studies in Section 4.4.

The early theoretical results of the longitudinal confinement led to parallel experimental efforts in Novosibirsk and Berkeley. These experiments employed alkali plasmas that were easy to produce and could operate in a density–temperature regime in which multiple-mirror confinement could clearly be observed

in small laboratory experiments. MHD stability was insured by line-tying to a cathode at which the plasma was generated. The results of these experiments confirmed the main aspects of multiple-mirror confinement theory, although in a regime very different from the usual fusion experiments.

Following earlier similar results, the experimental work in the Berkeley and Novosibirsk groups diverged, in accordance with the reactor concepts being considered. The Berkeley group was interested in investigating combined confinement and MHD instability in a more realistic, but still scaled, density and temperature regime ($n_e \approx 10^{13}\ \mathrm{cm}^{-3}$, $T_e = T_i \approx 10\ \mathrm{eV}$). Plasma was injected into the center of the device, either from one or both ends, and allowed to decay. Linked quadrupole fields, built according to the results of the low β calculations, were employed. Two devices of length 3 m with 7 cells and, later, 10 m with 10 cells, were employed. The results, particularly in the large machine, were consistent with the multiple-mirror confinement calculations and indicated stability up to $\beta \approx 1$, as predicted. The Novosibirsk group was interested in creating plasmas with $\beta > 1$ on the axis, requiring novel plasma injection and heating schemes. This work has led to the development of a 7-m electron beam plasma interaction experiment with plans to increase the length and multiple mirrors. These experimental investigations are referred to in Section 5, where the results are presented. This is followed by a summary and conclusions.

1. Qualitative consideration of multiple-mirror effects

The main developments of the physics of multiple-mirror confinement were obtained in the process of investigating the possibility of creating a thermonuclear reactor with a dense plasma (dense in the sense that the mean free path λ is small compared with the length L of the system). To estimate what effect the corrugation of the magnetic field can have on such a reactor we first consider the simpler variant of a pulsed reactor without corrugation. Although both pulsed and steady-state variants

can be considered, for simplicity we concentrate our attention on a pulsed system. Following [16], let us take a long solenoid with a straight magnetic field in which a relatively short bunch of hot ($T \approx 10$ keV) dense plasma is prepared at $t = 0$. This bunch then freely expands along a magnetic field for $t > 0$. If the magnetic field suppresses the transverse transport, then the time of energy containment is determined by the time of longitudinal expansion $\tau \cong L/v_{T_i}$, where v_{T_i} is the thermal ion velocity (which holds when there is no contact between the plasma and the ends of the device). During plasma expansion a thermonuclear reaction in a bunch takes place, and this system is effective as a reactor if $n\tau > 10^{14}$ sec-cm^{-3}, where n is the characteristic density. In terms of limitation on the length L, this means that

$$nL > 3 \times 10^{22} \text{ cm}^{-2}. \tag{1.1}$$

This shows that even if the density is very high, $n \approx 10^{17}$ cm^{-3}, the length of reactor, based at free plasma expansion, should be not less than 3000 m. A reactor with these parameters both because of the high plasma pressure and high power needed for heating is not technically feasible. It would become feasible if one succeeded in reducing both the length and the plasma density by about an order of magnitude.

As already mentioned in the introduction, a dramatic improvement in longitudinal confinement can be obtained with a corrugated magnetic field (see Fig. 1.1).

One should point out that in most papers the longitudinal and transverse problems of plasma confinement are considered separately. Under such a separation the statement of the longitudinal problem reduces to specifying the initial density and temperature distributions along a magnetic line, and then it is necessary to describe the space and time plasma parameter evolution during its expansion along the magnetic field. Under this approach the effects concerned with transverse processes that can result in some additional plasma parameter variation are not taken into account. Based on this approach let us consider qualitatively the different regimes of plasma flow in a corrugated magnetic field and estimate the velocity of expansion and con-

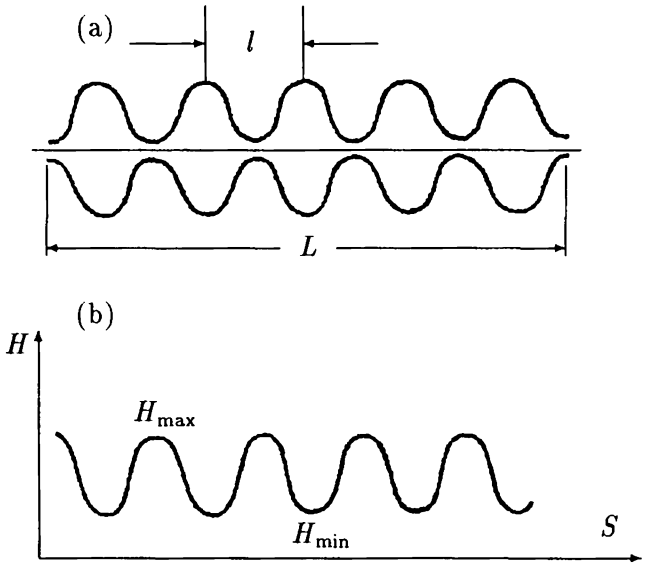

Fig. 1.1. Multiple-mirror magnetic trap: (a) the geometry of the force lines; (b) the strength of the magnetic field on the axis of the system.

finement time as a function of mean free path λ, corrugation period l, and mirror ratio k. To explore the complete parameter range requires investigation of the various limiting cases:

$$\frac{\lambda}{l} \begin{matrix} \gg 1 \\ \ll 1 \end{matrix} \quad , \quad k-1 \begin{matrix} \gg 1 \\ \ll 1 \end{matrix}$$

These four possibilities are not of equal significance, as we shall see below and in the four sections. The intermediate values are approached by extrapolation of the limiting cases. We classify these regimes first by λ/l, designating $\lambda/l \gg 1$ as the regime of "small-scale corrugation" and $\lambda/l \ll 1$ as the regime of "large-scale corrugation." Secondarily we designate $k \gg 1$ as the regime of "strong corrugation" and $k-1 \ll 1$ as the regime of "weak corrugation." In exploring these limiting cases, we shall also find some sub-cases of interest for which explicit calculations can be made. In addition, particularly for the lower-density steady-state concepts, it is desirable to construct cells

with "point" mirrors, i.e., with a mirror scale length $l_m \ll l$, such that it is possible to operate in the regime $l_m \ll \lambda \sim l$, which has improved confinement properties. We also note that because λ varies inversely with n, various regimes of λ/l can exist within a given device.

The axial confinement in the device can be characterized either by the local flow velocity $u(z)$ or by the local diffusion coefficient $D(z)$. The two are related through the flow, such that

$$n(z)\,u(z) = -D(z)\,\frac{dn(z)}{dz}.$$

Sometimes one representation, and sometimes the other, is more convenient for calculating confinement. For the purposes of the qualitative examination in this section, we shall express the local properties in terms of u. Furthermore, since we are only presenting estimates, we shall not consider the z-variation of the quantities. When D is calculated, it can then be converted to u by the simple estimate $u = D/L$. In the following sections, where the local quantities are calculated more precisely, we will also consider the appropriate z-variations.

In the range of mean free path $\lambda \gg l$ it is reasonable to separate particles in each mirror cell into particles trapped between mirrors and transiting ones. Since the trapped particles are able to complete many oscillations from mirror to mirror in the time between two successive collisions, they make only a small contribution to the mass and energy transport, i.e., the plasma flow along the axis is mostly carried by the transiting particles. Consequently, friction occurs between the transiting particles and the trapped particles and the latter transmit the momentum received to the magnetic field. Therefore one can say that the plasma undergoes friction with the magnetic field.

In the case of not-too-large mirror ratio, $k - 1 \sim 1$, the frictional force on a particle can be estimated as

$$F_{\mathrm{fr}} \approx m_i\,\nu_{ii}\,u',$$

where m_i is the mass of an ion, ν_{ii} is the ion–ion collision frequency (in case $k - 1 \sim 1$ this determines the time needed

for transiting particles to scatter through an angle of the order of unity and to become trapped, i.e., lose their momentum), u' is the directed velocity of the transiting particles which at $k-1 \sim 1$ coincides in order of magnitude with the macroscopic velocity of the plasma. Equating $n F_{\mathrm{fr}}$, which is the friction force acting on unit plasma volume, with the plasma pressure gradient $\partial p/\partial z \sim nT/L$, we find the expansion rate

$$u' \sim \nu_{T_i}(\lambda/L) \ll \nu_{T_i}.$$

From this it can be seen that the introduction of even relatively small k $(k-1 \sim 1)$ corrugation causes a marked reduction of u and a corresponding increase in the plasma expansion time compared with the case of a smooth field. In fact, the very character of motion changes: inertial expansion with a velocity $u \sim \nu_{T_i}$ becomes diffusion of the plasma from one magnetic mirror cell to another, and the pressure gradient is counterbalanced by the friction of the plasma with the magnetic field.

A larger mirror ratio further limits the expansion rate by reducing (i) the number of transiting particles and (ii) their effective free path length. The first effect results from the fact that since the trapped particles, the number of which is k times greater than that of the transit ones, on average are not in motion, the mass velocity of the plasma as a whole is smaller than u' by a factor k. The second effect results from the fact that, when $k \gg 1$, for capture in a cell to occur it is sufficient for a transiting particle to be scattered through a small angle $\Delta\theta^2 \sim k^{-1}$. Therefore, the effective mean free path and effective collision frequency, which determine the time of the momentum loss of the transiting particles, become of the order of λ/k and $\nu_{ii}k$, respectively. For this reason "smallness" of a magnetic mirror trap length must be taken to mean

$$l \ll \lambda/k. \tag{1.2}$$

As a result of these two effects the expansion velocity decreases with high mirror ratio by a factor k^2:

$$u \ll \nu_{T_i}(\lambda/k^2 L). \tag{1.3}$$

A reduction of the expansion velocity occurs even with very weak corrugation $k-1 \ll 1$. In this case those particles are trapped for which the pitch-angle θ at the minimal magnetic field is close enough to $\pi/2$:

$$|\theta - \pi/2| \leq (k-1)^{1/2}, \tag{1.4}$$

so the time of transition from trapped particles to transiting ones is of the order of magnitude $(k-1)/\nu_{ii}$. In our classification of different regimes with weak corrugation, the regime of small cell length, when this time exceeds the bounce time of trapped particles in a single-mirror trap $l/\nu_{T_i}(k-1)^{1/2}$, will be called the small-scale corrugation regime. This regime exists when

$$l \ll \lambda(k-1)^{3/2}. \tag{1.5}$$

Here we have taken into account that in a mirror trap with weak corrugation the longitudinal velocity of trapped particles is of the order of $\nu_{T_i}(k-1)^{1/2}$.

The effect of a weak corrugation can be found by introducing the frictional force related to one particle which can be estimated from reasoning quite similar to that described above for the situation with $k \gg 1$. The only difference is that now the characteristic time for the transiting particle to lose its momentum increases correspondingly to the decrease in probability for it to find itself in the narrow interval of pitch angles (1.4). This time increases as $\nu_{ii}^{-1}(k-1)^{-1/2}$. Taking this into account one can easily derive the following expression for F_{fr}:

$$F_{\mathrm{fr}} = -m_i \nu_{ii}(k-1)^{1/2} u.$$

Equating nF_{fr} with the plasma pressure gradient, we estimate the expansion rate as

$$u \sim \nu_{T_i}\lambda/L(k-1)^{1/2} \ll \nu_{T_i}. \tag{1.6}$$

From (1.6) one can see that if both (1.5) and the limitation $\lambda \ll L(k-1)^{1/2}$ are satisfied, then the expansion rate becomes much smaller than the thermal velocity. If the mean free path

becomes smaller than that given by the inequality (1.5), the expansion rate ceases to depend on the collision frequency. In this range of parameters the time of exchange between trapped and transiting particles becomes smaller than the period of trapped particle oscillations. The mechanism of transfer of momentum from plasma to magnetic field is quite analogous the usual collisionless Landau damping. An effect of this kind is also found in the "neoclassical" theory of transport in toroidal devices creating the "plateau" regime [17]. As is known from the solution of the Landau damping problem, the frictional force between particles and wave is proportional to the square of the amplitude of modulation. The condition of the balance of the frictional force and pressure gradient allows one to estimate the expansion velocity as

$$u \sim \nu_{T_i} l/L\,(k-1)^2, \tag{1.7}$$

which shows that in the range $l \ll L(k-1)^2$ the weak corrugation substantially decreases the plasma flow velocity in comparison with the straight magnetic field case.

If one continues to decrease the mean free path, there is a transition to a strongly collisional regime for which the expansion rate can be found from two-fluid gas dynamic equations in which the flow is impeded as a result of the longitudinal ion viscosity. This interval of parameters which corresponds to a very small (in the sense noted above) mean free path will be defined as the regime of large-scale corrugation.

To estimate the plasma expansion rate in this regime let us consider the plasma flow in an individual magnetic mirror cell. The motion of the plasma is due to the pressure difference between the ends of the cell, which is equal in order of magnitude to nTl/L. The work of the pressure force is balanced by viscous dissipation and, with strong enough magnetic field, only the longitudinal viscosity is significant. The energy dissipated per unit time within the trap is

$$\eta_i S \int_0^l \left(\frac{\partial u}{\partial z}\right)^2 dz \sim \eta_i\, S\, u^2\,(k-1)^2/l, \tag{1.8}$$

where η_i is the coefficient of longitudinal ion–ion viscosity [18],

which is given approximately by $\eta_i \sim n_i^m \nu_{T_i} \lambda$, and S is the characteristic transverse plasma cross section. In the estimation of the integral in (1.8) we take into consideration that the variation of u along the length of a single-mirror cell is approximately determined by the variation ΔS of the cross section S: $\Delta u/u \sim \Delta S/S \sim (k-1)$. Comparing (1.8) with the work performed in unit time by the pressure forces, $SunTl/L$, we find the plasma velocity to be

$$u \sim \nu_{T_i} l^2/\lambda L(k-1)^2. \tag{1.9}$$

(Note that some results concerned with this case were published in [17].) Comparing (1.7) and (1.9), one can conclude that the regime of large-scale corrugation is realized if $\lambda \ll l$. Certainly all the results presented above are valid only if $u \ll \nu_{T_i}$; in the opposite case the inertial effects are of major importance. A summary of the different regimes considered above is presented in Fig. 1.2, which qualitatively explores the dependence of the plasma expansion velocity on the factor λ/l for both the cases of weak $k-1 \ll 1$ and moderate $k-1 \sim 1$ values of the mirror ratio.

It shows that under a weak corrugation there is a large range of values of l/λ that corresponds to the "plateau" regime. When the mirror ratio increases this interval gets shorter and if $k-1 \ll 1$ it disappears. The optimal confinement is realized in this situation with $\lambda \sim l$, which separates the cases of small-scale and large-scale corrugations. It should be noted that for $k-1 \sim 1$ the expansion velocity is considerably decreased in comparison with the thermal velocity even if $\lambda < l$ (up to $\lambda \sim l^2/L$).

The classification given above is related to the geometry of a magnetic force line with a single scale, that is, when the areas with weak and strong magnetic field have approximately the same length. A better geometry from a practical point of view has narrow mirrors, i.e., a scale length l_m of the strong magnetic field which is much smaller than l. In the case of a two-scale field geometry there is an intermediate range of mean free paths $l_m \ll \lambda \ll kl$, when the plasma flow inside the individual mirror cells is purely gas dynamical but particles move without collision through the mirrors.

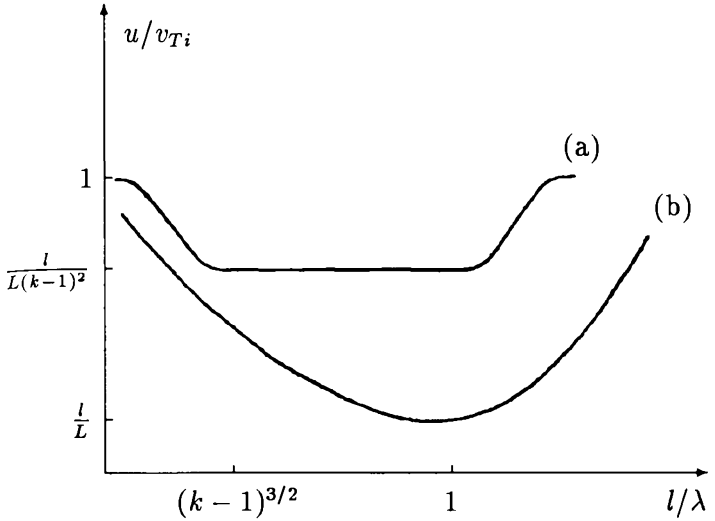

Fig. 1.1. The qualitative dependence of the plasma expansion velocity on the factor l/λ: (a) the case of weak corrugation $k-1 \ll 1$; (b) the case of moderate corrugation $k-1 \sim 1$.

Let us consider an individual mirror cell with $l_m \ll l$. The rate of plasma losses through a mirror throat can be estimated as $n\nu_{T_i}S_{\min}$, where $S_{\min}$ is the plasma cross section in the throat. Dividing the total number of ions in the mirror cell nlS by the loss rate, one obtains an estimate of the particle lifetime in the individual mirror trap as kl/ν_{T_i}. After this time the ion leaves one of the mirror traps in a random direction and becomes trapped in an adjacent cell such that the space step of this random motion is equal to l and the time interval is equal to kl/ν_{T_i}; the diffusion coefficient can then be estimated as $D \sim \nu_{T_i} l/k$. An estimate of the plasma expansion velocity in this "intermediate" regime is then

$$u \sim D/L \sim \nu_{T_i}(l/kL). \tag{1.10}$$

Comparing (1.10) to (1.3), we see that the two expressions are equal for $\lambda/k = l$. This is a considerable reduction of the velocity from the "single-scale" mirror satisfying (1.2). This regime has been called the "ideal" multiple-mirror regime.

Let us now analyze qualitatively the improvement of a pulsed reactor, discussed at the beginning of this section, due to a multiple-mirror geometry. If one takes, for example, the expression (1.3) for the expansion velocity in the case of small-scale corrugation, with plasma lifetime $\tau \sim L/u$, and substitutes it in the Lawson criteria for a temperature of 10 keV, the following limitation for the length of the system is obtained:

$$nL > 2.10^{21}/k \text{ cm}^{-2}. \tag{1.11}$$

Comparing (1.1) with (1.11), we see that with the same densities the corrugation allows a reduction of the length of approximately a factor of $10k$. The finding of such a strong effect warrants a more accurate theory, the development of which will be given in the following sections.

2. Plasma flow in a magnetic field with small-scale corrugation

In the regime of small-scale corrugation, $\lambda \gg l$, the diffusive process is directly related to the scattering of ions in velocity space, which transfers them between trapped and passing distributions. A kinetic description is required to adequately describe this regime. Various approximations have been used to make these kinetic equations tractable; in fact, in the limit of $k \gg 1$, a simple geometric approximation, in which the magnetic field effects depend only on K, gives reasonably accurate values for the local diffusion coefficient [11]. The most systematic kinetic treatment was presented in [13], and extended to weak corrugations in [21]. We follow these presentations here. The derivation of the equations for the averaged plasma parameters is presented in Section 2.1. It is based on the expansion of the kinetic equation solutions in the small parameter λ/L. The mass and energy fluxes are determined from the first order corrections to Maxwellian distributions. They can be calculated analytically in the case of a high mirror ratio in the presence of ii, ee, and ei collisions. The possibility of simplifying the collisional terms results first from the smallness of the number of transiting

particles and second from the narrow interval of pitch-angles occupied by transiting particles in velocity space.

The equations for the first-order corrections, simplified in this way, are solved in Section 2.2 by expansion in another small parameter l/λ with average over a single mirror cell similar to the method suggested by Budker and Belyaev [22]. The solution of these equations allows one to find the mass and energy fluxes and to get a closed system of diffusive equations for macroscopic plasma parameters. The analysis of the properties of this equations is carried out in Section 2.3.

For a weakly modulated magnetic field the regime of small-scale corrugation corresponds to the case (1.5), when the trapped particles' period of oscillation is much longer than the transit time of the untrapped ones. The analysis of this case has similar features to the well-known problem of finite-amplitude Langmuir-wave collision damping [23]. The effect of interaction of the particles with a weakly corrugated magnetic field is given by an expression for the frictional force, which is derived in Section 2.4.

2.1. Derivation of the macroscopic equation

In the limit of small-scale corrugation (1.2) the plasma motion does not obey the two-fluid gas dynamic equations [18]. However, as was shown in [12], the smallness compared with the scale of axial inhomogeneity L is sufficient to enable the flow of the plasma to be described macroscopically by means of moment equations.

We shall regard the magnetic field as large enough to enable us to neglect (i) all transport phenomena perpendicular to the lines of force and (ii) any change in the magnetic field caused by the plasma itself. Given these conditions, the state of the plasma inside an individual field tube is described by the following pair of kinetic equations:

$$\frac{\partial F_a}{\partial t} + \nu \cos\theta \frac{\partial F_a}{\partial s} + \frac{\nu \sin\theta}{2H} \frac{\partial H}{\partial s} \frac{\partial F_a}{\partial \theta}$$

$$\pm \frac{e}{m_a} E_{\parallel} \left(\cos\theta \frac{\partial F_a}{\partial \nu} - \frac{\sin\theta}{\nu} \frac{\partial F_a}{\partial \theta} \right) = \sum_b S\, t_{ab}. \quad (2.1)$$

Here ν is the particle velocity, θ is the angle between the velocity vector and the direction of the magnetic field, s is a coordinate along the line of force, $F_a \equiv F_a(\nu, \theta, s, t)$ is a distribution function (the subscript $a = i, e$ denotes the type of particle), $E_{\parallel}$ is a projection of the electric field onto the line of force, St_ab is the collision operator between species a and b, and the other notation is standard. The plus sign before the last term on the left-hand side of the equation refers to ions and the minus sign to electrons. It is assumed that the corrugation length is large compared with the Larmor electron and ion radii.

The required system of gas dynamic equations is obtained from expression (2.1) by an expansion in the parameter λ/L, where L represents the characteristic scale of inhomogeneity of the plasma. Here we shall regard $E_{\parallel}$ as a first-order quantity with respect to λ/L (since the electric field is created by an electron pressure gradient). In the zero approximation with respect to λ/L (i.e., in a plasma that is uniform along the line of force and has no electric field) Eqs. (2.1) have a steady-state solution in the form of two Maxwellian distributions:

$$F_{Ma} = n_a \left(\frac{m_a}{2\pi T_a} \right)^{3/2} \exp\left(-\frac{m_a \nu^2}{2T_a} \right). \quad (2.2)$$

Contrary to normal two-fluid gas dynamics, the macroscopic velocity is a small quantity [first order with respect to λ/L (see expression (1.3)], which means that the solution of the zero approximation for each type of particle is characterized by only two parameters, n_a and T_a. It should be noted in particular that we consider $T_e \neq T_i$, since the temperature equalization time contains the large parameter m_i/m_e.

If the Maxwellian distribution parameters n_a and T_a vary along the line of force, functions (2.2) cease to be accurate solutions of the kinetic equations. Accurate solutions are then best written in the form

$$F_a = F_{Ma} + f_a, \quad (2.3)$$

where the parameters of the Maxwellian function F_{Ma} are determined from the relations

$$n_a = 2\pi \int_0^\infty \nu^2 d\nu \int_0^\pi \sin\theta\, F_a\, d\theta,$$

$$T_a = \frac{2\pi m_a}{3n_a} \int_0^\infty \nu^4 d\nu \int_0^\pi \pi \sin\theta F_a\, d\theta,$$

and f_a is a small additional term associated with the inhomogeneity and proportional to λ/L. It will be obvious, then, that

$$\int_0^\infty \nu^2\, dv \int_0^\pi \sin\theta f_a d\theta = 0\,, \quad \int_0^\infty \nu^4\, dv \int_0^\pi \sin\theta f_a\, d\theta = 0.$$

For practical applications the most interesting case is that of strong corrugation ($k \gg 1$), and fortunately it is precisely here that we can obtain relatively easily a closed system of gas dynamic equations. Therefore, from now on we shall always consider that $k \gg 1$.

Let us examine a section of the field tube located between two mirrors (Fig. 1.1). Since the plasma parameters vary little over the length of one magnetic mirror trap, the state of the plasma within this section can be adequately described by the mean densities and temperatures over the section:

$$\bar{n}_a = \frac{H_{\max}}{lI} \int_{s_1}^{s_2} \frac{n_a(s)ds}{H(s)}\,, \quad \bar{T} = \frac{H_{\max}}{lI\bar{n}_a} \int_{s_1}^{s_2} \frac{n_a(s)\,T_a(s)ds}{H(s)}, \qquad (2.4)$$

where

$$I = \frac{H_{\max}}{l} \int_{s_1}^{s_2} \frac{ds}{H(s)},$$

and integration with respect to ds is performed from mirror to mirror. Using the kinetic equations (2.1) together with the definitions (2.4) it can easily be shown that

$$\frac{\partial \bar{n}_a}{\partial t} + \frac{q_a(s_2) - q_a(s_1)}{Il} = 0, \qquad (2.5)$$

$$\frac{\partial n_a \bar{T}_a}{\partial t} + \frac{2}{3}\frac{Q_a(s_2) - Q_a(s_1)}{Il} \mp \frac{2eH_{\max}}{3Il}\int_{s_1}^{s_2} \frac{E_{\|}(s) q_a(s) ds}{H(s)} = 0, \quad (2.6)$$

where the quantities

$$q_a = 2\pi \int_0^\infty \nu^3 d\nu \int_0^\pi f_a \sin\theta \cos\theta \, d\theta ,$$

$$Q_a = \pi m_a \int_0^\infty \nu^5 \, d\nu \int_0^\pi f_a \sin\theta \cos\theta d\theta$$

are, respectively, the mass and energy fluxes. In Eq. (2.6) we have omitted terms of two types: (i) terms which describe the temperature exchange between electrons and ions and (ii) terms which appear in the event of directional motion of any of the components and describe the energy dissipation due to mutual friction forces between electrons and ions. We have neglected terms of the second type since they are small when $k \gg 1$. As regards temperature equalization, this can be allowed for directly in the final moment equations.

In view of the small variation of all the plasma parameters along the magnetic mirror trap, it is convenient to introduce the quantities

$$\frac{\partial q_a}{\partial z} = \frac{q_a(s_2) - q_a(s_1)}{l}, \quad \frac{\partial Q_a}{\partial z} = \frac{Q_a(s_2) - Q_a(s_1)}{l} \quad (2.7)$$

with which we can operate formally as with ordinary derivatives. Here, instead of expressions (2.5) and (2.6), we have

$$\frac{\partial \bar{n}_a}{\partial t} + \frac{1}{I}\frac{\partial q_a}{\partial z} = 0, \quad (2.8)$$

$$\frac{\partial \bar{n}_a \bar{T}_a}{\partial t} + \frac{2}{3}\frac{1}{I}\frac{\partial Q_a}{\partial z} \mp \frac{2eH_{\max}}{3Il}\int_{s_1}^{s_2} \frac{E_{\|}(s)\, q_a(s)\, ds}{H(s)} = 0. \quad (2.9)$$

Let us now find the functions f_a. The derivative $\partial F_a/\partial t$ is a quantity of the second order of smallness. Therefore the

equation for determining f_a, obtained by substituting expression (2.3) in (2.1), takes the following form (accurate to terms of the first order):

$$\hat{D} f_a \equiv \nu \cos\theta \frac{\partial f_a}{\partial s} + \frac{\nu \sin\theta}{2H} \frac{\partial H}{\partial s} \frac{\partial f_a}{\partial \theta}$$
$$\equiv \sum_b St'_{ab} - \nu \cos\theta \frac{\partial F_{Ma}}{\partial s} \mp \frac{eE_{\|}}{m_a} \cos\theta \frac{\partial F_{Ma}}{\partial \nu}, \quad (2.10)$$

where St'_{ab} denotes the result of linearization of St_{ab} with respect to f_a.

The variation of f_a over the length of the magnetic mirror trap is a quantity of the second order of smallness, so that the boundary condition for Eq. (2.10) must be written as

$$f_a(s_2) - f_a(s_1) = 0. \quad (2.11)$$

Since $E_{\|}$ is a quantity of the first order of smallness, in the last term on the right-hand side of Eq. (2.10) we can neglect the variation of F_{Ma} over the magnetic mirror trap and put

$$\frac{\partial F_{Ma}}{\partial \nu} = -\frac{m_a \nu}{T_a} \bar{T}_{Ma},$$

where $\bar{T}_{Ma}$ represents a Maxwellian distribution with averaged parameters:

$$\bar{T}_{Ma} = \bar{n}_a \left(\frac{m_a}{2\pi T_a}\right)^{3/2} \exp\left(-\frac{m_a \nu^2}{2T_a}\right).$$

Similarly, it can be assumed that

$$\frac{\partial F_{Ma}}{\partial s} = \left[\frac{1}{\bar{n}_a}\frac{\partial n_a}{\partial s} + \frac{1}{T_a}\frac{\partial T_a}{\partial s}\left(\frac{m_a \nu^2}{2\bar{T}_a} - \frac{3}{2}\right)\right] \bar{F}_{Ma}.$$

As already pointed out, when the condition $l \ll \lambda/k$ applies, mass and energy can be transported only by transit particles. Therefore, to find q_a and Q_a we need to know f_a only in that region of the phase space corresponding to transit particles. Using the small parameter k^{-1}, it is possible to obtain

from expression (2.10) a simplified system of equations for transit particles. The principal simplification is associated with the fact that, when $k \gg 1$, there are few transit particles and the collisions between them can be neglected. Moreover, the collision integrals need retain only those terms in which there are two differentiations with respect to θ (the other terms do not contain the large parameter $\Delta\theta^{-2} \sim k$). As shown in [13, 15], it is then possible to write St'_{ee} and St'_{ii} for the transit particles as follows:

$$St'_{ee} = \frac{\nu\alpha_e(\nu)}{\sin\theta}\frac{\partial}{\partial\theta}\sin\theta\frac{\partial f_e}{\partial\theta},$$
$$St'_{ii} = \left(\frac{m_e}{m_i}\right)^2\frac{\nu\alpha_i(\nu)}{\sin\theta}\frac{\partial}{\partial\theta}\sin\theta\frac{\partial f_i}{\partial\theta},$$

where

$$\alpha_a(\nu) = \frac{4\pi}{\bar{n}}\left[\int_0^{\nu}\left(\nu'^2 - \frac{\nu'^4}{3\nu^2}\right)F_{Ma}(\nu')\,d\nu' + \frac{2}{3}\int_{\nu}^{\infty}\nu\nu' F_{Ma}(\nu')\,d\nu'\right],$$
$$\nu = \frac{2\pi\Lambda e^4\bar{n}}{m_e^2\nu^3}$$

(Λ is the Coulomb logarithm). We have explicitly allowed for quasi-neutrality of the plasma and put $n_e = n_i = \bar{n}$.

The second simplification lies in the fact that for transit ions one can neglect St'_{ie} in comparison with St'_{ii}, since, when there is not too large a difference between T_e and T_i, the transit ions exchange momenta and energy with trapped ions much more effectively than with electrons. The final simplification is that for the purpose of calculating St'_{ei} the ions may be regarded as immobile:

$$St'_{ei} = \frac{\nu}{\sin\theta}\frac{\partial}{\partial\theta}\sin\theta\frac{\partial f_e}{\partial\theta}.$$

Taking all the above into account, one can write the following equations for determining f_e and f_i in the region of transit particles:

$$\hat{D}f_e = \frac{\nu(1+\alpha_e)}{\sin\theta}\frac{\partial}{\partial\theta}\sin\theta\frac{\partial f_e}{\partial\theta} - \nu\cos\theta\bar{F}_{Me}\frac{\partial\phi_e}{\partial s}, \qquad (2.12)$$

$$\hat{D}f_i = \left(\frac{m_e}{m_i}\right)^2 \frac{\nu\alpha_i}{\sin\theta}\frac{\partial}{\partial\theta}\sin\theta\frac{\partial f_i}{\partial\theta} - \nu\cos\theta\bar{F}_{Mi}\frac{\partial\phi_i}{\partial s}, \quad (2.13)$$

$$\phi_a = \frac{n_a}{\bar{n}_a} + \frac{T_a}{\bar{T}_a}\left(\frac{m_a\nu^2}{2\bar{T}_a} - \frac{3}{2}\right) \mp \frac{e}{T_a}\int_{s_1}^{s_2} E_{\|}\, ds.$$

2.2. Calculation of the distribution function correction

First we shall solve Eq. (2.12). To do this, we represent f_e as the sum of the two functions p_e and r_e, respectively even and odd with respect to $\cos\theta$

$$f_e = p_e + r_e,$$
$$p_e = \frac{1}{2}\left[f_e(\theta) + f_e(\pi-\theta)\right], \quad r_e = \frac{1}{2}\left[f_e(\theta) - f_e(\pi-\theta)\right],$$

and proceed from expression (2.12) to the following pair of equations for p_e and r_e:

$$\hat{D}p_e = \frac{\nu(1+\alpha_e)}{\sin\theta}\frac{\partial}{\partial\theta}\sin\theta\frac{\partial r_e}{\partial\theta} - \nu\cos\theta\bar{F}_{Me}\frac{\partial\phi_e}{\partial s}, \quad (2.14)$$

$$\hat{D}r_e = \frac{\nu(1+\alpha_e)}{\sin\theta}\frac{\partial}{\partial\theta}\sin\theta\frac{\partial p_e}{\partial\theta}. \quad (2.15)$$

To find f_e it is sufficient to solve Eqs. (2.14) and (2.15) over the interval $[0, \pi/2]$.

Since the scale of variation of the magnetic field is small compared with the free-path length, it is appropriate in Eqs. (2.14) and (2.15) to introduce the variables $\varepsilon = m_e\nu^2/2$ and $\mu = m_e\nu^2\sin^2\theta/2H$, which are integrals of the motion of charged particles in a magnetic field. The advantage of such a substitution in this kind of problem was pointed out some years ago [22]. Thus, in place of expression (2.14) and (2.15) we obtain

$$\frac{\partial p_e}{\partial s} = \frac{\sqrt{8\,m_e}\nu(1+\alpha_e)}{H}\frac{\partial}{\partial\mu}\left[\mu(\varepsilon-\mu H)^{1/2}\frac{\partial r_e}{\partial\mu}\right] - \bar{F}_{Me}\frac{\partial\phi_e}{\partial s}, \quad (2.16)$$

$$\frac{\partial r_e}{\partial s} = \frac{\sqrt{8\,m_e}\nu(1+\alpha_e)}{H}\frac{\partial}{\partial\mu}\left[\mu(\varepsilon-\mu H)^{1/2}\frac{\partial p_e}{\partial\mu}\right]. \quad (2.17)$$

Equations such as these have been solved in other studies [13, 15, 24] in connection with other problems (calculation of the conductivity of inhomogeneous plasma and plasma in a corrugated magnetic field). The solution is based on the use of the small parameter l/λ. An expansion of the function p_e and r_e in powers of l/λ takes the form

$$p_e = A + B(l/\lambda)^2 + \dots, \quad r_e = \frac{C}{(l/\lambda)} + D(l/\lambda) + \dots .$$

As can be seen from expression (2.17), $\partial r_e/\partial s \sim l/\lambda$. This means that the function r_e may be considered constant over the magnetic mirror trap with a relative accuracy of $\sim (l/\lambda)^2$. Allowing for this, we integrate Eq. (2.16) with respect to ds from mirror to mirror. As a result of this, and taking expression (2.11) into account, we obtain

$$\sqrt{8m_e}\,\nu(1+\alpha_e)\frac{\partial}{\partial\mu}\left\{\mu\left[\int_{s_2}^{s_1}\frac{(\varepsilon-\mu H)^{1/2}\,ds}{H}\right]\frac{\partial r_e}{\partial\mu}\right\} = \bar{F}_{Me}[\phi_e(s_2)-\phi_e(s_1)].$$

The solution of this equation, which is finite when $\mu \to 0$, is elementary:

$$r_e = \frac{\bar{F}_{Me}[\phi(s_2)-\phi(s_1)]}{\sqrt{8m_e}(1+\alpha_e)\nu} \times \int_{\varepsilon/H_{\max}}^{\mu} d\mu' \left[\int_{s_1}^{s_2}\frac{(\varepsilon-\mu' H)^{1/2}\,ds}{H}\right]^{-1} + C(\varepsilon).$$

The function $C(\varepsilon)$ is determined from the condition that r_e should vanish at the transit-trapped particle boundary (i.e., when $\varepsilon = \mu H_{\max}$). This boundary condition is given more formal treatment elsewhere [13, 23]. It can easily be seen that it gives $C(\varepsilon) = 0$.

With a large mirror ratio ($k \gg 1$) the integral with respect to ds in the formula for r_e is expressed in terms of the

quantity I, introduced previously, and is equal to $I\varepsilon^{1/2}l/H_{\max}$. In view of this we can write

$$r_e = \frac{\bar{F}Me[\phi(s_2)-\phi(s_1)]}{\sqrt{8m_e}(1+\alpha_e)\nu\varepsilon^{1/2}Il}(\mu H_{\max}-\varepsilon).$$

Knowing r_e, we can determine the electron mass and energy fluxes after integrating with respect to ε and μ.

The scheme for finding the ion fluxes does not present any new difficulties. The final results of all the calculations can be written in the following form:

$$q_a = -\frac{H}{H_{\max}}\frac{\chi_a I}{\bar{T}_a}\sum_{n=1}^{3}\beta_a^{(n)}\bar{P}_a^{(n)}, \tag{2.18}$$

$$Q_a = -\frac{H}{H_{\max}}\chi_a I\sum_{n=1}^{3}\gamma_a^{(n)}\bar{P}_a^{(n)}, \tag{2.19}$$

where the coefficient χ_a is determined by the formula

$$\chi_a = \frac{\bar{T}_a^{7/2}}{m_a^{1/2}\Lambda e^4 I^2}. \tag{2.20}$$

The remaining symbols in expressions (2.18) and (2.19) are defined in Table 2.1, where e_m and i_m are expressed as integrals:

$$e_m = \frac{1}{\sqrt{2\pi^3}}\int_0^\infty\left[x^2+\frac{xe^{-x^2}}{\sqrt{\pi}}+\frac{1}{\sqrt{\pi}}(2x^2-1)\int_0^x e^{-\xi^2}d\xi\right]^{-1}e^{-x^2}x^m\,dx,$$

$$i_m = \frac{1}{\sqrt{2\pi^4}}\int_0^\infty\left[xe^{-x^2}+(2x^2-1)\int_0^x e^{-\xi^2}d\xi\right]^{-1}e^{-x^2}x^m\,dx.$$

The numerical values of these integrals are given in Table 2.1.

Table 2.1. Integral values.

n	$\beta_e^{(n)}$	$\beta_i^{(n)}$	$\gamma_e^{(n)}$	$\gamma_i^{(n)}$	$\bar{P}_a^{(n)}$
1	$-e_9$	i_9	$-e_{11}$	i_{11}	$\frac{e\bar{E}}{T_a}$
2	e_9	i_9	e_{11}	i_{11}	$\frac{1}{\bar{n}_a}\frac{\partial \bar{n}_a}{\partial z}$
3	$e_{11} - \frac{3}{2}e_9$	$i_{11} - \frac{3}{2}i_9$	$e_{13} - \frac{3}{2}e_{11}$	$i_{13} - \frac{3}{2}i_{11}$	$\frac{1}{\bar{T}_a}\frac{\partial \bar{T}_a}{\partial z}$

$$e_9 = 0.207 \quad e_{11} = 0.81 \quad e_{13} = 4.01$$
$$i_9 = 0.455 \quad i_{11} = 1.74 \quad i_{13} = 8.47$$

The quantities $\bar{E}$, $\partial \bar{n}_a/\partial z$, and $\partial \bar{T}_a/\partial z$ in the last column of the table are defined by analogy with the formulas in expression (2.7):

$$\bar{E} = \frac{1}{l}\int_{s_1}^{s_2} E_{\|}\, ds\,, \qquad \frac{\partial n_a}{\partial z} = \frac{n(s_2) - n(s_1)}{l},$$
$$\frac{\partial T_a}{\partial z} = \frac{T_a(s_2) - T_a(s_1)}{l}.$$

Substituting relations (2.18) and (2.19) in (2.8) and (2.9), we obtain the required system of gas dynamic equations, which may be written as follows:

$$\frac{\partial n_a}{\partial t} = \frac{\partial}{\partial z}\left[\frac{\chi_a}{T_a}\sum_{n=1}^{3}\beta_a^{(n)} P_a^{(n)}\right], \tag{2.21a}$$

$$\frac{\partial n_a T_a}{\partial t} = \frac{2}{3}\frac{\partial}{\partial z}\left[\chi_a \sum_{n=1}^{3}\gamma_a^{(n)} P_a^{(n)}\right] \mp \frac{2}{3}\chi_a P_a^{(1)}\sum_{n=1}^{3}\beta_a^{(n)} P_a^{(n)} \pm n\frac{T_e - T_i}{\tau}, \tag{2.21b}$$

where

$$\tau = \frac{3}{16}\sqrt{\frac{2}{\pi}}\frac{m_i T_e^{3/2}}{\Lambda e^4 m_e^{1/2} n}.$$

The term $n(T_e - T_i)/\tau$ on the right-hand side of Eq. (2.22) describes the heat exchange between electrons and ions. The upper signs in formula (2.22) relate to ions and the lower ones relate to electrons. Here and below we omit the averaging bar above the values E, n_a, T_a, $P_a^{(n)}$.

The characteristics of the corrugated magnetic field are represented in the above system of equations by the integral

$$I = \frac{H_{\max}}{l} \int_{s_1}^{s_2} \frac{ds}{H(s)} \tag{2.22}$$

on which the coefficient χ_a depends [see expression (2.20)]. The effect of the corrugation on mass and energy transfer increases as I. With a fixed mirror ratio the integral I depends only on the magnetic field profile and increases when the length of the mirror l_m decreases in relation to the length of the homogeneous magnetic field region. When $l_m \to 0$ ("point" mirrors) I attains its maximum value, $I = k$. For practical purposes the formula $I = k$ can be used when $l_m \leq l/k$.

2.3. Analysis of the macroscopic equations

We now consider the practical application of the expansion of a plasmoid into a vacuum. Here the quasi-neutrality condition $n_e = n_i = n$ also means that the current in the plasma is zero, i.e., $q_e = q_i$. Determining the electric field from this relation and substituting it in expressions (2.21) and (2.22) we obtain a system of three equations for n, T_e, and T_i:

$$\begin{aligned}
\frac{\partial n}{\partial t} &= \frac{\partial}{\partial z}\left\{\frac{\chi_i}{T_i}\frac{\partial}{\partial z}\left[0.45\left(\frac{T_e}{T_i}+1\right)\frac{\partial \ln n}{\partial z}\right.\right. \\
&\quad \left.\left. +1.10\,\frac{T_e}{T_i}\,\frac{\partial \ln T_e}{\partial z} + 1.06\,\frac{\partial \ln T_i}{\partial z}\right]\right\}, \qquad (2.23) \\
\frac{\partial n T_e}{\partial t} &= \frac{\partial}{\partial z}\left[\chi_e \frac{\partial}{\partial z}(0.55\,\ln T_e)\right] \\
&\quad + \left[\chi_i \frac{\partial}{\partial z}(0.66\,\ln n + 1.62 \ln T_e)\right]
\end{aligned}$$

$$\times \frac{T_e}{T_i}\frac{\partial}{\partial z}\left[0.45\left(\frac{T_e}{T_i}+1\right)\frac{\partial \ln n}{\partial z}\right.$$

$$\left.+1.10\,\frac{T_e}{T_i}\frac{\partial \ln T_e}{\partial z}+1.06\frac{\partial \ln T_i}{\partial z}\right]-n\frac{T_e-T_i}{\tau}, \quad (2.24)$$

$$\frac{\partial n T_i}{\partial t} = \frac{\partial}{\partial z}\left\{\chi_i \frac{\partial}{\partial z}\left[1.16\left(\frac{T_e}{T_i}+1\right)\frac{\partial \ln n}{\partial z}\right.\right.$$

$$\left.\left.+2.82\,\frac{T_e}{T_i}\frac{\partial \ln T_e}{\partial z}+3.91\,\frac{\partial \ln T_i}{\partial z}\right]\right\}$$

$$-\left[\frac{\chi_i T_e}{T_i}\frac{\partial}{\partial z}(0.66\ln n+1.62\ln T_e)\right]$$

$$\times\left[0.45\left(\frac{T_e}{T_i}+1\right)\frac{\partial \ln n}{\partial z}\right.$$

$$\left.+1.10\,\frac{T_e}{T_i}\frac{\partial \ln T_e}{\partial z}+1.06\,\frac{\partial \ln T_i}{\partial z}\right]+\frac{T_e-T_i}{\tau} \quad (2.25)$$

(we have neglected terms of the order of $\sqrt{m_e/m_i}$).

Equations (2.23)–(2.25) conserve the number of particles and their total energy:

$$\int n\,dz = \int n_0\,dz, \quad (2.26)$$

$$\int n(T_e+T_i)\,dz = \int n_0\,(T_{e0}+T_{i0})\,dz \quad (2.27)$$

(n_0, T_{e0}, and T_{i0} denote the initial values of the respective parameters).

It will be seen from expression (2.23) that the characteristic plasmoid expansion time (i.e., the density variation time) is equal in order of magnitude to $t_1 \sim I^2 L^2/\lambda \nu_{Ti}$. The electron temperature equalization time along the plasmoid is much less: $t_2 \sim I^2 L^2/\lambda \nu_{Te} \sim t_1\sqrt{m_e/m_i}$. This means that the electron temperature is uniform along the plasmoid: $\partial T_e/\partial z = 0$. The ion temperature, generally speaking, is not equalized along the plasmoid because ion thermal conductivity is low. But in

the case of practical interest where $L > (\lambda/I)(m_i/m_e)^{1/4}$ the electron–ion energy exchange time is small compared with t_1 and the equality $T_i \simeq T_e = T(\partial T/\partial z = 0)$ is accordingly fulfilled. Hence energy integral (2.27) can be written as

$$T \int n\, dz = \text{const.}$$

But since the number of particles is also conserved [see expression (2.26)], the latter equality means that T is also independent of time.

Thus, the motion of sufficiently long (i.e., $L > (\lambda/I) \times (m_i/m_e)^{1/4}$) plasmoids can be described by the single equation (2.28), which is also considerably simplified in view of the condition $\partial T/\partial z = 0$

$$\frac{\partial n}{\partial t} = \zeta \frac{\partial^2 \ln n}{\partial z^2}, \quad \zeta = \frac{0.91\, T^{5/2}}{m_i^{1/2} I^2 \Lambda e^4}. \tag{2.28}$$

For reference purposes we may show one of the exact solutions of this equation, corresponding to an initial condition of the form

$$n = n_0 \left(1 + \frac{z^2}{d_0^2}\right)^{-1}.$$

For constant ζ this solution is

$$n = \frac{d_0 n_0}{d} \left(1 + \frac{z^2}{d^2}\right)^{-1},$$

where

$$d = d_0 + \frac{2\zeta t}{d_0 n_0}.$$

Let us now consider the results obtained in relation to the problem of thermal insulation of a plasma in a device of finite length. If the plasma is in contact with the ends, its cooling time is $t_2 \sim I^2 L^2/\lambda \nu_{Te}$, where L is the length of the devices. On the other hand, the characteristic expansion time for a plasmoid of length L is $t_1 \sim (m_i/m_e)^{1/2} t_2$. Therefore, it might be thought

that the plasma thermal insulation time could be increased to values of $\sim t_1$ by establishing a plasmoid of length $\sim L/2$ in the center of the device. Then the presence of plasma-free gaps between the ends of the device and the edges of the plasmoid would prevent heat transfer to the ends. In fact, however, immediately after the plasmoid is created its boundary layers, which have a thickness of the order of the effective free-path length (i.e., λ/I), begin to expand freely into the vacuum from both ends of the plasmoid at a rate of $\sim \nu_{Ti}$ and arrive at the ends of the device in the time $\sim L/\nu_{Ti}$. The plasma density between the plasmoid and the ends of the device reaches $n_0(\lambda/I\,L)$ and continues to increase. This means that the effective free-path length in the region between the plasmoid and the ends will not be greater than L, so that heat transfer in this region can be described, at least qualitatively, by the macroscopic equation (2.24). From this equation it will be seen that the plasma thermal conductivity coefficient is independent of the density. However, this means that the plasma cooling time will be of the same order as when the plasma fills the whole space between the mirrors from the very beginning.

The phenomenon just described (which may be termed the "precursor effect") is significant only in conditions where the plasma breaking away from the plasmoid boundaries accumulates between the plasmoid and the ends of the device. If the boundary conditions corresponding to leakage of a plasma into a vacuum are fulfilled at the ends, the confinement time of the hot plasma inside the device will be of the order of t_1. This condition can be provided, for example, by means of regions at the ends of the device which have strongly expanding force lines.

Let us now consider the problem of distortion of the magnetic field by the plasma. This question is of great importance for the pulsed reactor concept since this system, as was mentioned in the introduction, is expected to operate with $\beta \gg 1$. In this "wall" confinement regime the magnetic field suppresses only transverse thermal conductivity but the equilibrium in this direction is provided by the rigid walls.

The distortions of the magnetic field with $\beta \gg 1$ result from both radial and axial plasma flow. The first effect was

studied in a number of papers [25–27]. These papers are mainly devoted to an analysis of the efficiency of thermal conductivity suppression. They are based on the model of an indefinitely long solenoid with a straight magnetic field. Without discussing here the results related to the efficiency of radial thermal isolation, let us consider the main features of the magnetic field evolution. If the conductivity of the wall is high enough, the plasma heating does not lead to a noticeable decrease of the magnetic field in the center of the machine (see, for example, [26]). This result shows that predictions [28] of a complete expulsion of the magnetic field from the central part to a thin layer near the wall are not valid.

A more advanced model of the solenoid, with a corrugated magnetic field but plasma parameters still periodic in the axial direction (without an average pressure gradient), was studied in [29]. It was found that, if the wall is a good conductor and if it has a form close to one of the magnetic surfaces, then magnetic flux conservation prevents noticeable deformation of the magnetic configuration; the mirror ratio increases a little near the axis and is not strongly decreased on the periphery. Note that if the wall is a sufficiently good conductor, a magnetic surface will automatically conform to it. By corrugating the wall it is possible to create practically any magnetic field profile along the axis of the system.

If one uses a well-conducting corrugated wall the longitudinal pressure gradient and plasma axial flow caused by it cannot lead to substantial distortion of the corrugated magnetic surfaces. In fact, the perturbation of the magnetic field results not from the absolute value of pressure but from its axial gradient. Since the pressure difference along one mirror trap is small, $\Delta p \sim pl/L$, the minimum of the magnetic field strength needed for multiple-mirror confinement is determined by the inequality

$$\frac{H^2}{8\pi} \geq \frac{hTl}{L}.$$

One can see that for the case of sufficiently long plasma bunches plasma flow does not result in strong limitation on β ($\beta \leq L/l$). A derivation of this criterion is given in [12].

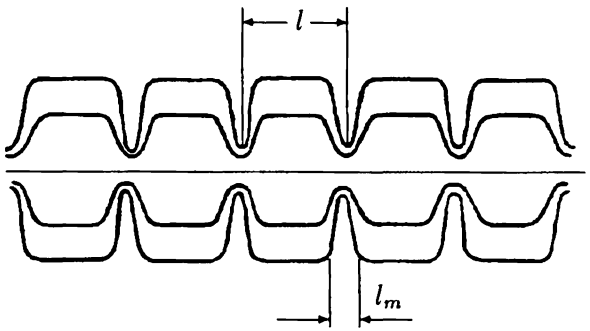

Fig. 2.1. Geometry of the force lines for a magnetic field configuration in which the mirror scale length l_m is much less than the cell length.

Finally, let us consider the case of a strong magnetic field ($\beta \ll 1$). Such a magnetic field allows plasma to be magnetically confined. Then, using the traveling multiple-mirror field (see Fig. 2.1), one can provide a steady-state axial confinement [20]. If $l \ll \lambda/k$, then the steady-state length of the plasma bunch is of the order of

$$L = \lambda \nu_{Ti}/k^2 u_0,$$

where u_0 is the velocity of the field motion. This estimate is valid only if $L \gg \lambda/k$. The same idea was analyzed later in [30].

2.1. Plasma diffusion along a weakly corrugated magnetic field with small-scale corrugation

A qualitative consideration of the plasma flow along a weakly corrugated magnetic field was carried out in Section 1. The flow was classified into three different regimes of plasma motion (see Fig. 1.2). This subsection, based on [21], is devoted to a quantitative description of the small-scale limiting case (1.5), when the trapped particles execute several oscillations from mirror to mirror before they become untrapped.

In both its physical sense and calculation procedure, this regime is quite analogous to the problem of collisional damping of

a finite-amplitude electrostatic Langmuir wave [23]. Because of their similarity we will limit ourselves to only a brief description of the scheme of calculation and will concentrate attention on those features that are inherent in considering the problem for the magnetic field case.

To derive the axial transport equation for the case of a weakly corrugated magnetic field, it is more convenient to use a somewhat different approach than that in Section 2.1. It is based on finding an average, over one mirror cell, of the friction force caused by the interaction between the particles and magnetic field. To calculate this, it is necessary to know the ion distribution function. Under the same assumptions as in Section 2.1, the kinetic equation for the ion component has the form

$$\frac{\partial F_i}{\partial t} + \nu \cos\theta \frac{\partial F_i}{\partial s} + \frac{\nu \sin\theta}{\partial H} \frac{\partial H}{\partial s} \frac{\partial F_i}{\partial \theta} = St_{ii} \,. \tag{2.29}$$

For simplicity we have cancelled the term containing the electric field from the left side of (2.1), which can be taken into account directly in the final equations.

Integrating (2.29) over the velocities with weight $m_i \nu \cos\theta$ and averaging with weight $1/H$ over the single-mirror cell, one gets the expression for the frictional force:

$$F_{\text{fr}} = -\frac{H_{\max}}{I\, l} \int_{s_1}^{s_2} \frac{ds}{H^2} \frac{dH}{ds} \int \frac{m_i \nu^2}{2} \sin\theta \, F_i \, d^3\nu. \tag{2.30}$$

It follows from (2.30) that F_{fr} is governed by that part of the correction f_i to a Maxwellian distribution which is symmetric with respect to $\cos\theta$ and is an odd function of s. This correction f_i is the first term of an expansion of the distribution function F_i in a power of the small parameter $\lambda/(k-1)^{1/2} L \ll 1$ (see (1.6)). It is localized in velocity space on a scale of the order of a few $\Delta\theta$ (1.4) near the value $\theta = \pi/2$. Since this part of the velocity space is very narrow, one can simplify the collision term for f_i using the same arguments as in Section 2.1. After this operation the kinetic equation for f_i takes the form

$$\nu \cos\theta \frac{\partial f}{\partial s} + \frac{\nu \sin\theta}{2H} \frac{\partial H}{\partial s} \frac{\partial f}{\partial \theta} = \frac{\nu_i \alpha_i}{\sin\theta} \frac{\partial}{\partial \theta} \sin\theta \frac{\partial f}{\partial \theta}, \qquad (2.31)$$

where $\nu_i = 2\pi \Lambda e^4 n / m_i^2 \nu^3$ and $\alpha_i(\nu)$ is given in Section 2.1. The term $\partial f_i / \partial t$ is omitted since it is second order with respect to small parameter (1.6), which corresponds to a very slow plasma expansion along a magnetic field.

The factor $\alpha_i(\nu)$ describes the effect of collision between trapped particles and Maxwellian ones. In [23], where the collision damping of a Langmuir wave with a high phase velocity was considered, the relative velocities of these two groups of particles were much greater than the thermal velocities and correspondingly an asymptotic $\alpha_i(\nu) = \text{const}$ was used. In the present context the directional plasma velocity which plays the role of the phase velocity is small compared with the thermal one. For this reason the formal use of the results obtained in [23] for the calculation of the frictional force between the plasma and the magnetic field resulted in a wrong numerical coefficient for F_{fr} in [31].

Equation (2.31) for f_i can be solved by expanding in powers of another small parameter (1.5) in accordance with the scheme described in Section 2.2. Under the integration of the system of equations for r_i and p_i the general boundary condition (2.11) that makes them periodic is used. Two additional boundary conditions in velocity space are applied to find r_i. One of them was already used in Section 2.2 and corresponds to the vanishing of r_i at the transit–trapped particle boundary (i.e., when $\varepsilon = \mu H_{\max}$). Another one provides conversion of F_i into a shifted Maxwell distribution in the region of transiting particles far from the boundary with trapped particles, that is,

$$r_i \to -F_{Mi} \frac{m_i \nu u}{T} \cos\theta$$

when $k - 1 \ll 1 - \mu H_{\max}/\varepsilon \ll 1$. The solution for r_i which satisfies these conditions has the form

$$r_i = \begin{cases} r_0(\varepsilon) \int\limits_{\varepsilon/H_{\max}}^{\mu} \frac{d\mu'}{\mu'} \left[\int\limits_{s_1}^{s_2} (\varepsilon - \mu' H)^{1/2} ds \right]^{-1}, & \mu < \dfrac{\varepsilon}{H_{\max}} \\ 0, & \mu > \dfrac{\varepsilon}{H_{\max}} \end{cases} \tag{2.32}$$

where $r_0(\varepsilon) = -F_{Mi}(\varepsilon)(m_i/2)^{1/2}(\varepsilon l u/T)$. If r_i is known, the even function of $\cos\theta$, p_i can be determined by integrating (2.16) over s:

$$p_i = p_0(\varepsilon) \frac{\partial}{\partial \mu} \left[\int\limits_{s_1}^{s} (\varepsilon - \mu H)^{1/2} ds' \Big/ \int\limits_{s_1}^{s_2} (\varepsilon - \mu H)^{1/2} ds \right], \tag{2.33}$$

where $p_0(\varepsilon) = -2\varepsilon\, u\, l\, \nu_i\, \alpha_i\, m_i\, F_{Mi}/TH$.

In variables ε, μ the expression (2.30) has the form

$$F_{\text{fr}} = -\pi \left(\frac{2}{m}\right)^{3/2} \int\limits_{s_1}^{s_2} \frac{ds}{H} \frac{dH}{ds} \int\limits_{0}^{\infty} d\varepsilon \int\limits_{0}^{\varepsilon/H} \frac{\mu d\mu\, p_i}{(\varepsilon - \mu H)^{1/2}}. \tag{2.34}$$

In calculating F_{fr} we should break up the integral over μ into three parts: over the phase space corresponding to trapped particles, untrapped particles, and the narrow transition layer which arises near the boundary $\mu = \varepsilon/H_{\max}$ because of Coulomb collisions. Since the collisions result in diffusion of the particles in velocity space, the width $\delta\mu$ of this layer can be easily estimated as follows:

$$\varepsilon \delta\mu H_{\max}/\varepsilon \simeq l/\lambda\,(k-1)^{1/2}.$$

In this layer the solutions given above are not valid. In calculating the fluxes q_a and Q_a in Section 2.2 it was of no importance, since the contributions to the corresponding integrals from the transition layer were small in comparison with the contribution from the transiting particles. In calculating (2.34) the situation changes and contributions from the transiting particles and from the layer are quite comparable while the contribution from trapped particles is negligibly small.

Although the function p_i is unknown in the transition layer the contribution from it in (2.34) can be calculated by the standard method of integrating the exact equation (2.16) across the layer. Since the layer is narrow, the coefficients in (2.34) can be considered as constants over the integration. So finally the integral through the transition layer is expressed by the derivative $\partial r_i/\partial\mu$ outside of the layer where it is described by expression (2.32). This operation allows the contribution of the transition layer to be taken into account in an explicit form.

In the final expression for $F_{\rm fr}$ the integral of $\alpha_i(\varepsilon)$ over ε is calculated analytically. The integration over the variables μ and s leads to integrals that can be found for a specific dependence $H(s)$. As an example we adopt a field with a sinusoidal profile

$$H(s) = H_{\min} + (H_{\max} - H_{\min}) \sin^2 \frac{\pi s}{l}; \tag{2.35}$$

then the integral becomes an elliptic integral of the second kind, the numerical value of which gives

$$F_{\rm fr} = -1.82 \frac{h_2 m_i^{1/2} \Lambda e^4}{T_i^{3/2}} u(k-1)^{1/2}. \tag{2.36}$$

A somewhat more detailed description of this calculation can be found in [32].

Using (2.36), one can derive axial transport equations in a weakly corrugated magnetic field. To illustrate this approach we use the diffusive plasma equation for the case where $T_e = T_i = T$ and $\partial T/\partial z = 0$. The velocity of plasma expansion is determined by the balance of the forces acting on an ion component.

$$enE_{\|} - \frac{\partial p_i}{\partial z} + F_{\rm fr} = 0. \tag{2.37}$$

Since the frictional force for the electron component is negligibly small, the electric field can be written as follows: $enE_{\|} = -\partial p_e/\partial z$. Finding the expansion velocity from (2.37) and substituting it in the equation of mass conservation, one obtains the diffusive equation for the plasma density:

$$\frac{\partial n}{\partial t} = \frac{\partial}{\partial z} D \frac{\partial n}{\partial z}, \quad l(k-1)^{-3/2} \ll \lambda \ll L(k-1)^{1/2}, \tag{2.38}$$

where

$$D = 1.1 \frac{T^{5/2}}{n} m_i^{1/2} \Lambda e^4 (k-1)^{1/2} .$$

The inequalities in (2.38) provide the conditions for small-scale corrugation and the smallness of the expansion velocity $u \sim D/L$ in comparison with the ion thermal velocity.

3. Plasma dynamics with large-scale corrugation

As already defined in Section 1, the large-scale corrugation regime corresponds to a regime where the mean free path is sufficiently small in comparison with the characteristic space scale of the magnetic field so that the plasma obeys the ordinary two-fluid gas dynamic equations. The method of reduction of these equations in an application to the case of slow plasma expansion developed in [12] is described in Section 3.1. Note that a few years after [12] the derivation of the same equations was independently carried out in [33, 34]. While the results in [33] did not coincide exactly with those in [12], in the subsequent paper [34], equations were obtained which were identical with the results of [12].

A maximum efficiency of multiple-mirror confinement and a saving of the energy consumption required to maintain the magnetic field is achieved in multiple-mirror fields with "point" mirrors, whose length l_m is much less than the corrugation period l. In this two-scale field there is an intermediate range of (1.10) which is between the cases of small-scale and large-scale corrugation. The plasma confinement theory developed in [35] for this interval of parameters is described in Section 3.2. Approximately at the same time, independently from [35], some results concerned with this case were published in [22]. In contrast to [35], the effects of ambipolar potential and temperature gradients were not taken into account so that the results of [22], related to this regime, were more qualitative. The ambipolar effects were taken into consideration by the authors later in [36]. Both in [22] and in [36] the results were extended to the important regime of $\lambda \sim l$, a regime not treated in [35].

In accordance with the classification of Section 1, in the case of a weakly modulated magnetic field there is also an intermediate regime ("plateau" regime) which is between the cases of small-scale and large-scale corrugation. In Section 3.3 the derivation of the frictional force based on [21] is described. The theoretical results are extended to parameters which were realized in some multiple-mirror experiments [37].

The idea of increasing the Coulomb collision frequency by means of inserting in the plasma a small amount of heavy impurities with $z \gg 1$ was suggested long ago (see, for example, [38]). The possibility of improving the efficiency of multiple-mirror confinement was pointed out in [39] and was studied in detail in [40–42]. As developed in these papers, the quantitative theoretical description of the impurity dynamics in a multiple-mirror magnetic field is discussed in Section 3.4.

3.1. The description of plasma motion with two-fluid gas dynamic equations

When $\lambda \ll l \ll L$, plasma behavior can be described from the outset with double-fluid gas-dynamic equations. To obtain the equations describing slow ($u \ll \nu_{Ti}$) expansion of the plasma, we use the same method as in Section 2; first, by studying plasma flow inside an individual magnetic mirror cell we find the mass and energy fluxes and then, substituting these in conservation laws of the type (2.8) and (2.9), we obtain a closed system of equations for slow processes.

For solving the first part of the problem the motion inside each cell can be regarded as steady-state, because all the parameters of the problem vary with a characteristic time L/u, which is much greater than the time l/u determining the passage of the plasma through the trap. A further simplification is associated with the fact that over the length of one trap there is little variation in any of the plasma parameters: $\Delta n = n(s_2) - n(s_1) \ll n$, $\Delta T_a = T_a(s_2) - T_a(s_1) \ll T_a$, and so on. Thus only first-order terms with respect to Δn and ΔT_a need to be retained in the gas dynamic equations.

Since our main practical interest here is expansion of the plasma into the void, we shall consider the macroscopic electron and ion velocities to be equal from the very outset: $u_e = u_i = u$.

We shall project a system of double-fluid gas dynamic equations onto the line of force. As a result, taking the above points into consideration, we find that

$$-n\frac{\partial T_a}{\partial s} - T_a\frac{\partial n}{\partial s} \mp R \pm enE_{\|} + \frac{4\eta_a}{3}\frac{H^{3/2}}{\tilde{n}}\frac{\partial}{\partial s}H^{-2}\frac{\partial}{\partial s}(qH^{1/2}) = 0, \tag{3.1}$$

$$\frac{\partial}{\partial s}\frac{q}{H} = 0, \tag{3.2}$$

$$\frac{\partial}{\partial s}\frac{Q_a}{H} = 0, \tag{3.3}$$

where $q = nu$ is the mass flux, $Q_a = -\kappa_a(\partial T_a/\partial s) + (5/2)qT_a$ is the energy flux, $R = -0.71n(\partial T_e/\partial s)$ is the thermal force, and η_a and κ_a are the longitudinal viscosity and thermal conductivity determined by the relations [2][1]

$$\eta_i = 0.404\frac{m_i^{1/2}T_i^{5/2}}{\Lambda e^4}, \qquad \kappa_i = 4.04\frac{\eta_i}{m_i},$$

$$\eta_e = 0.215\frac{m_e^{1/2}T_e^{5/2}}{\Lambda e^4}, \qquad \kappa_e = 4.33\frac{\eta_e}{m_e}.$$

The upper sign in Eq. (3.1) relates to ions and the lower one to electrons.

It should be noted that when $l > \lambda(L/\lambda)^{1/3}$ the equation for ion movement must include an inertial term, $m_i nu\partial u/\partial s$. However, this term does not affect the expressions for q and Q_a given below.

The quantities q and Q_a can be found from the given values of ΔT_a and Δn using Eqs. (3.1)–(3.3):

$$q = \frac{-H}{I_1 H_m a x}\frac{l^2 n\frac{\partial}{\partial z}n(T_e + T_i)}{\eta_i}, \tag{3.4}$$

[1] To avoid misunderstanding, we should point out that our notation differs slightly from that used by Braginski [18].

$$Q_a = \frac{5}{2} q T_a - \frac{H}{I_2 H_{\max}} \kappa_a \frac{\partial T}{\partial z}. \tag{3.5}$$

Here

$$I_1 = \frac{3l}{H_{\max}} \int_{s_1}^{s_2} \frac{ds}{H} \left(\frac{\partial H}{\partial s} \right)^2, \quad I_2 = \frac{1}{l H_{\max}} \int_{s_1}^{s_2} H ds.$$

The derivatives $\partial/\partial z$ in expressions (3.4) and (3.5) are introduced as in expression (8). The averaging bars above n and T_a are omitted.

In deriving relations (3.4) and (3.5) we neglected the electron viscosity (since it is much smaller than the ion viscosity) and, in addition, excluded the electric field with the aid of the equation for electron movement:

$$enE_{\parallel} - R = -n \frac{\partial T_e}{\partial s} - T_e \frac{\partial n}{\partial s}. \tag{3.6}$$

The law of conservation of matter in gas dynamics coincides precisely with expression (2.8). Substituting in that equation the expression obtained above for q, we find the equation for n:

$$\frac{\partial n}{\partial t} = \frac{l^2}{I I_1} \frac{\partial}{\partial z} \frac{n}{\eta_i} \frac{\partial}{\partial z} [n(T_e + T_i)]. \tag{3.7}$$

The gas dynamic energy conservation law is written as follows [18]:

$$\frac{\partial n T_a}{\partial t} + \frac{2}{3I} \frac{\partial Q_a}{\partial z} \mp \frac{2 H_{\max}^2}{3lI} \int_{s_1}^{s^2} \frac{\left(eE_{\parallel} - \frac{R}{n} \right) q(s) ds}{H(s)} = 0. \tag{3.8}$$

Substituting relations (3.5) and (3.6), we find the equations for T_e and T_i:

$$\frac{\partial n T_a}{\partial t} = \frac{2}{3I} \frac{\partial}{\partial z} \left[\frac{\kappa_a}{I_2} \frac{\partial T_a}{\partial z} + \frac{5}{2} \frac{l^2 n T_a}{I_1 \eta_i} \frac{\partial}{\partial z} n(T_e + T_i) \right] \pm \frac{2l^2}{3 I I_1 \eta_i} \left[\frac{\partial}{\partial z} n(T_e + T_i) \right] \left(\frac{\partial}{\partial z} n T_e \right) \pm n \frac{T_e - T_i}{\tau}. \tag{3.9}$$

To illustrate the results obtained, let us consider the motion of a plasmoid when $\lambda > l(I_2/I_1)^{1/2}(m_e/m_i)^{1/4}$ and $L > l(II_1)^{-1/2}(m_i/m_e)^{1/4}$. The first of these conditions indicates that the electron thermal conductivity provides uniform T_e along the plasmoid, and the second indicates that heat exchange between electrons and ions maintains $T_i = T_e = T$. Considerations similar to those in Section 2 show that T is then independent not only of the coordinates but also of time. The system of gas-dynamic equations then resolves into a single equation for the density

$$\frac{\partial n}{\partial t} = \xi \frac{\partial}{\partial z} n \frac{\partial n}{\partial z}, \qquad \xi = \frac{2Tl^2}{\eta_i II_1}. \tag{3.10}$$

With the initial condition

$$n|_{=0} \begin{cases} n_0\left(1 - \dfrac{z^2}{d_0^2}\right), & |z| < d_0 \\ 0, & |z| > d_0 \end{cases}$$

this equation has the solution

$$n = \begin{cases} \dfrac{n_0 d_0}{d}\left(1 - \dfrac{z^2}{d_0^2}\right), & |z| < d \\ 0, & |z| > d \end{cases}$$

where

$$d = (6d_0 n_0 \xi t)^{1/3}.$$

The effect of the magnetic field profile on the plasma expansion rate is represented in Eq. (3.10) by the product II_1. Whenever the function $H(s)$ takes the form shown in Fig. 3.1, II_1 is equal to

$$\frac{6l}{l_m}(k-1)\ln k\left[1 + 2\frac{l_m}{l}\left(\frac{\ln k}{k-1} - 1\right)\right].$$

If $k \gg 1$ and $l_m \ll l$, then $II_1 \simeq 6(l/l_m)k \ln k$. The plasma expansion rate is then of the order of $\nu_{Ti} l l_m/(\lambda L k \ln k)$.

The validity condition for the gas dynamic approximation $\lambda(\partial \ln u/\partial s) \ll 1$ in the case of the magnetic field shown in

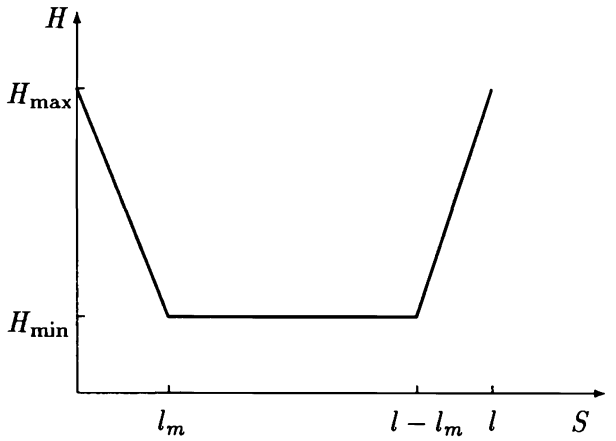

Fig. 3.1. An approximate form for the magnetic field strength, which is useful for calculations.

Fig. 3.1 may be written in the form $\lambda \ll l_m$. Thus, between the zones of validity of the results in Section 2 ($l < \lambda/k$) and the results in this section ($l > l_m > \lambda$) there is a region $l_m < \lambda < kl$ where none of these results is valid. The reason is that when $l_m < \lambda < kl$ the effective free-path length is large compared with the size of the mirror but small compared with the length of the whole of the cell. Thus, a kinetic approach is called for in the mirror region, and double-fluid gas dynamics in the rest of the cell. Based on the results of [35], we now describe this intermediate parameter range.

3.1. The intermediate regime in a multiple-mirror field with "point" mirrors

Since in the range of mean free paths $l_m \ll \lambda$ the dynamics of the plasma expansion should not depend on the size and shape of the mirror, we will solve the problem in the null approximation with respect to the parameter l/λ, assuming that $l_m = 0$ and the field in the space between mirrors is uniform (the square magnetic well approximation). Such a magnetic field profile is shown in Fig. 3.2.

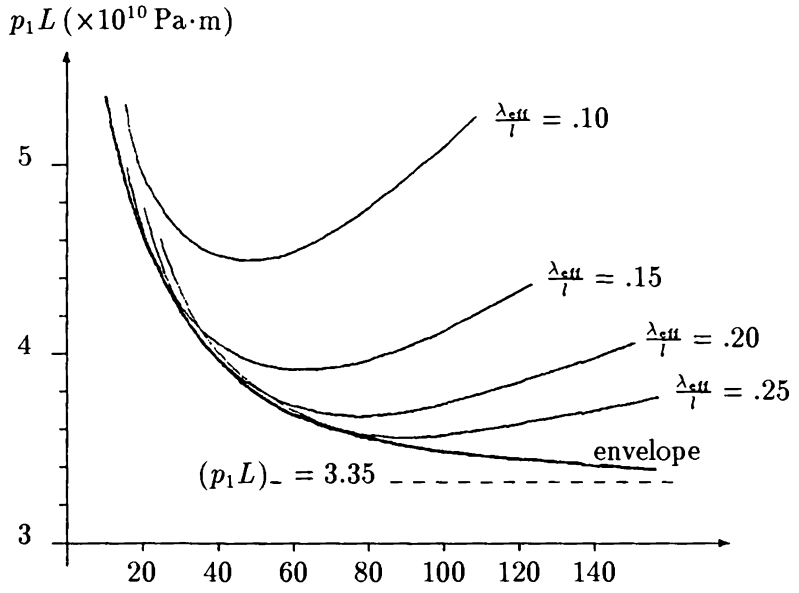

Fig. 3.2. Optimum $p_1 L$ versus the number of cells $2N + 1$ for different values of λ_{eff}/l for $k_1 = 3.36$ and $Q = 2$.

The procedure for the derivation of the gas dynamic equations describing the dispersion along a field tube of a plasmoid with a characteristic longitudinal scale L is analogous to the system of calculations used in Section 2.1. First one must solve the steady-state problem and relate the fluxes of matter q_a and energy Q_a of the two plasma components with the drops in concentrations Δn_a and temperatures ΔT_a and the potential $\Delta\phi$ between the centers of two adjacent mirror cells. At this stage of the calculation one must assume that the differences Δn_a, ΔT_a, and $\Delta\phi$ are given and do not depend on time.

For determinacy we introduce the coordinates along the field tube in such a way that a mirror separating two mirror cells is located at the point $s = 0$. Then

$$\Delta n_a = n_a(l/2) - n_a(-l/2),$$

$$\begin{aligned} \Delta T_a &= T_a(l/2) - T_a(-l/2), \\ \Delta\phi &= \phi(l/2) - \phi(-l/2). \end{aligned} \tag{3.11}$$

We assume that the plasma bunch is sufficiently extended and occupies a large number of mirror machines ($N \approx L/l \gg 1$). In this case the values of n_a, T_a, and ϕ vary only slightly on the scale of a single mirror cell ($\Delta n_a \ll n_a$, $\Delta T_a \ll T_a$). The nature of their variation is different in different sections of a field tube; within the mirror cell where the flow has a collisional nature the parameters n_a, T_a, and ϕ vary smoothly in accordance with the equations of two-fluid hydrodynamics. In the region of a mirror the hydrodynamic approximation breaks down. Here the plasma parameters can undergo sharp jumps whose spatial scale is on the order of the size of the mirror. Therefore, in a solution of the problem in zero order with respect to l_m/λ one must take into account the fact that the boundary values of n_a, T_a, and ϕ may not coincide to the left and to the right of the mirror.

We can determine the jumps in these values upon the transition through a mirror by the equalities

$$\begin{aligned} \delta n_a &= n_a(+0) - n_a(-0), \\ \delta T_a &= T_a(+0) - T_a(-0), \\ \delta\phi &= \phi(+0) - \phi(-0). \end{aligned} \tag{3.12}$$

For further calculations we will use the assumption that the mirror ratio is large ($k \gg 1$). This assumption allows us to find in explicit form the connection between the fluxes of matter and energy, and the values (3.12). Let us examine the flow of any component of the plasma through a mirror. If the mirror ratio were equal to infinity, then the exchange of particles between mirror cells would be absent and a Maxwellian velocity distribution with parameters corresponding to the given mirror cell would be established within each of them. With a finite mirror ratio the Maxwellian distribution near a mirror is disturbed by the flux of particles from the next mirror cell which has different values of the parameters (concentration, temperature, and potential). The disturbance in the distribution function is proportional to the difference in the values of the parameters and

also, since the mirror ratio is large, to the smallness of the number of particles, $\sim n/k$, penetrating from mirror cell to mirror cell

$$F(\nu) - F_M(\nu) = f(\nu) \sim \frac{1}{k}\frac{\Delta n}{n}.$$

In the calculation of the fluxes of matter and energy the contribution to the integral from the function $F(\nu)$ gives a narrow region of phase space $\nu_\perp^2/\nu^2 = \sin^2\theta \leq 1/k$. Keeping this in mind, one can verify that the allowance for a disturbance $f(\nu)$ would lead to the appearance of terms containing the small value k^{-1} in the equations for the fluxes. Therefore, the fluxes of matter and energy can be calculated with an accuracy of the terms of order k^{-1} by assuming that the distribution functions near a mirror are Maxwellian. The results of these calculations performed in a linear approximation with respect to δn_a, δT_a, and $\delta\phi$ have the form

$$\begin{aligned} q_a &= -\frac{n_a}{k}\left(\frac{T_a}{2\pi m_a}\right)^{1/2}\left(\frac{\delta n_a}{n_a} + \frac{1}{2}\frac{\delta T_a}{T_a} \pm \frac{e\delta\phi}{T_a}\right), \\ Q_a &= -\frac{n_a T_a}{k}\left(\frac{T_a}{2\pi m_a}\right)^{1/2}\left(2\frac{\delta n_a}{n_a} + 3\frac{\delta T_a}{T_a} \pm 2\frac{e\delta\phi}{T_a}\right). \end{aligned} \tag{3.13}$$

In the mode where the plasma bunch expands freely the condition of quasineutrality is expressed by the equality $q_e = q_1 \cong q$, which allows one to eliminate from (3.13) the jump in potential at a mirror. Equations (5) take the form

$$\begin{aligned} q &= -\frac{1}{k(2\pi m_i T_i)^{1/2}}\left[(T_e + T_i)\delta n + \frac{n}{2}(\delta T_e + \delta T_i)\right], \\ Q_c &= -\frac{n}{k}\left(\frac{2T_e}{\pi m_e}\right)^{1/2}\delta T_e, \\ Q_i &= -\frac{1}{k}\left(\frac{T_i}{2\pi m_i}\right)^{1/2}\left[2(T_e + T_i)\delta n + 3n\delta T_i + n\delta T_e\right]. \end{aligned} \tag{3.14}$$

Terms containing the small value m_e/m_i are omitted in Eqs. (3.14).

Now we can find the connections between the jumps at a mirror, which figure in (3.14), and the assigned drops in the

parameters (3.11) between adjacent mirror machines. The transition from free flow at the mirrors to hydrodynamic flow in the central section of a mirror cell takes place near a mirror at distances on the order of the effective mean free path. We can take the effective mean free path as the distance $\lambda_{\text{eff}} \approx \lambda/k$ in which a flying particle is scattered through an angle $\Delta^2 \approx k^{-1}$ and enters the region of phase space occupied by trapped particles. If $\lambda_{\text{eff}} \ll l$, then the equations of two-fluid hydrodynamics can be used everywhere within the mirror cells to describe the plasma flow [18].

We can join the steady-state solutions for the regions of Knudsen and hydrodynamic flows by using the fact that the fluxes of matter and energy are constant along a field tube with good accuracy. The variations in these values along the length of a mirror cell are quantities of the second order of smallness with respect to the parameter l/L, whereas the fluxes are values of the first order of smallness. By equating the hydrodynamic equations for the fluxes of matter and energy with the values of (3.14), we obtain equations describing the temperature distributions in the hydrodynamic region:

$$-\chi_a \frac{\partial T_a}{\partial s} + \frac{5}{2} q T_a = Q_a. \tag{3.15}$$

The thermal-conductivity coefficients are given by the equations

$$\chi_i = 1.63 \frac{T_i^{5/2}}{\Lambda e^4 m_i^{1/2}}, \quad \chi_e = 0.93 \frac{T_e^{5/2}}{\Lambda e^4 m_e^{1/2}}.$$

These equations must be supplemented by the condition of the steady-state flow. Neglecting viscosity, this comes down to the requirement of constancy of the total pressure along a field tube:

$$\frac{\partial}{\partial s} n(T_e + T_i) = 0. \tag{3.16}$$

We integrate Eqs. (3.15) and (3.16) with respect to s between the centers of the mirror machines (from the point $s = -l/2$ to $s = l/2$), excluding a region of width δ ($\lambda_{\text{eff}} \ll$

$\delta \ll l$) on both sides of the mirror where the hydrodynamic approximation breaks down. As a result we obtain

$$\begin{aligned} \frac{x_a}{l}\left[\Delta T_a - T_a(\delta) + T_a(-\delta)\right] &= Q_a - \frac{5}{2} q T_a, \\ n(\Delta T_e + \Delta T_i) + (T_e + T_i)\Delta n &= (T_e + T_i)\left[n(\delta) - n(-\delta)\right] \\ &+ n\left[T_e(\delta) - T_e(-\delta)\right] + n\left[T_i(\delta) - T_i(-\delta)\right]. \end{aligned} \tag{3.17}$$

Since $\delta \ll l$, the differences $T_a(\delta) - T_a(-\delta)$ and $n(\delta) - n(-\delta)$ are equal to the jumps (3.12) in concentration and temperature at the mirror with the accuracy of terms of order δ/l. With allowance for this we can rewrite (3.17) in the form

$$\begin{aligned} \frac{x_a}{l}\left(\Delta T_a - \delta T_a\right) &= Q_a - \frac{5}{2} q T_a, \\ T_a \Delta n + n \Delta T_a &= n\left(\delta T_e + \delta T_i\right) + \left(T_e + T_i\right)\delta n. \end{aligned} \tag{3.18}$$

Together with Eqs. (3.14), Eq. (3.18) forms an algebraic system of equations relating the jumps δn and δT_a with the total drops Δn and ΔT_a.

The solutions of this system, which are, in general, cumbersome, are considerably simplified if the dimensionsless parameter $\lambda k/l$, which figures in (3.18), is small or large compared with unity. For example, in the case where $\lambda k/l \gg 1$ the solutions have the form

$$\delta n = \Delta n, \quad \delta T_a = \Delta T_a. \tag{3.19}$$

In this case the entire drop in density and temperatures occurs in the region of the mirror. In the opposite limiting case of $\lambda k/l \ll 1$ the changes in n and T_a are distributed more uniformly along the mirror cell, while the jumps at the mirror are

$$\begin{aligned} \delta n &= \frac{7}{9}\left(\Delta n + n\frac{\Delta T_e + \Delta T_i}{T_e + T_i}\right), \\ \delta T_e &= \frac{k x_e}{n l}\left(\frac{\pi m_e}{2 T_e}\right)^{1/2} \Delta T_e, \\ \delta T_i &= \frac{2}{9}\left[\frac{\Delta n}{n}(T_e + T_i) + \Delta T_i + \Delta T_e\right]. \end{aligned} \tag{3.20}$$

By substituting Eqs. (3.19) or (3.20) into Eqs. (3.14) we arrive at the desired expressions for the fluxes of matter and energy for the assigned drops Δn and ΔT_a between the centers of the mirror cells:

$$\lambda k/l \ll 1, \tag{3.21a}$$

$$q = -\frac{8}{9k}(2\pi m_i T_i)^{-1/2}[(T_e + T_i)\Delta n + n(\Delta T_e + \Delta T_i)],$$

$$Q_e = -x_e \frac{\Delta T_e}{l},$$

$$Q_i = -\frac{20}{9k}\left(\frac{T_i}{2\pi m_i}\right)^{1/2}[(T_e + T_i)\Delta n + n(\Delta T_e + \Delta T_i)]$$

or

$$\lambda k/l \gg 1, \tag{3.21b}$$

$$q = -\frac{(2\pi m_i T_i)^{-1/2}}{k}\left[(T_e + T_i)\Delta n + \frac{1}{2}(\Delta T_e + \Delta T_i)\right],$$

$$Q_e = -\left(\frac{2T_e}{\pi m_e}\right)^{1/2}\frac{n}{k}\Delta T_e,$$

$$Q_i = -\frac{1}{k}\left(\frac{T_i}{2\pi m_i}\right)^{1/2}[(T_e + T_i)\Delta n + 3\Delta T_i + \Delta T_e].$$

The further procedure for the derivation of the equations describing the time and space distribution of the plasma parameters is analogous to that described in Section 2.1. We will confine ourselves to the consideration of one particular case, which is of practical interest, of the evolution of rather long plasmoids with $L \gg l(m_i/m_e)^{1/4}$, when the temperatures of the electrons and ions are able to become equal to each other and are equalized along the magnetic field in the time of expansion:

$$T_e = T_i = T, \quad \frac{\partial T}{\partial s} = 0. \tag{3.22}$$

Under these conditions the dynamics of the plasma is described by a single equation for the concentration. Substituting q from

(3.21) into (2.8) and keeping (3.22) in mind, we obtain the equation for n:

$$\frac{\partial n}{\partial t} = D\frac{\partial^2 n}{\partial z^2}, \tag{3.23}$$

$$D = \begin{cases} D_1 = \dfrac{8l}{9k}\left(\dfrac{2T}{\pi m_i}\right)^{1/2}, & l_m \ll \lambda \ll l/k \\ D_2 = \dfrac{l}{k}\left(\dfrac{2T}{\pi m_i}\right)^{1/2}, & l/k \ll \lambda \ll lk\,. \end{cases}$$

The equation formulated describes the process of diffusional expansion of the plasma along the magnetic field. The inequalities pertaining to the coefficient of diffusion are obtained through a combination of conditions (1.10) and the inequalities $\lambda k/l \ll 1$ and $\lambda k/l \gg 1$ which were used in solving the system of equations (3.18).

By using Eq. (3.23) one can estimate the velocity of expansion u and the time of longitudinal confinement $\tau \approx L/u$ of the plasma by the corrugated field in the range of mean free paths (1.10):

$$u \sim \nu_{Ti}\frac{l}{Lk}, \quad \tau \sim \frac{L}{\nu_{Ti}}\frac{lK}{l},$$

which coincides with the estimate (1.11) obtained by another method in Section 1.

At the limits of their applicability with respect to the mean free path (1.10), the equations obtained coincide with the corresponding equations derived in Section 2.3 and Section 3.1 with the accuracy of the numerical coefficient. The results presented are intermediate between the purely kinetic and hydrodynamic modes analyzed above, and along with these results they give a complete picture of the dynamics of plasma flow in a strongly corrugated ($k \gg l$) magnetic field.

3.3. The "plateau" regime of plasma motion in a weakly corrugated magnetic field

As was already discussed in Section 1, among the various regimes of plasma motion in a weakly corrugated magnetic field

there is one of intermediate type, which corresponds to the transition between the limiting cases of small-scale and large-scale corrugation studied in Section 2.4 and Section 3.1. It is realized under the condition in which the transition time of trapped particles into untrapped ones is smaller than the bounce time of the trapped particles (see (1.5)), while at the same time $\lambda \gg l$. In the opposite case, with $\lambda \ll l$, the flow becomes purely hydrodynamical and is described by the equations obtained in Section 3.1.

With fast exchange between trapped and transiting particles in a phase space, the distribution is close to a Maxwellian one. The mechanism of transfer of momentum from the plasma to the magnetic field is quite analogous to the usual Landau damping. An effect of this kind is well known in the "neoclassical" theory of transport phenomena in toroidal devices [17], which makes the use of the term "plateau" reasonable for this regime. It is convenient to consider it quantitatively by means of the same approach used in Section 2.4, finding an average over one mirror cell of the friction force between the plasma and a magnetic field. Based on [21], we present details of the calculation.

The frictional force (2.30) is determined by the correction to the Maxwellian distribution which can be found in a linear approximation with respect to a field modulation from the collisionless version of the kinetic equation (2.29). Integrating this equation over the trajectories of unperturbed motion $s = s_0 + \nu \cos\theta t$, we find

$$f_i = -F_{Mi} \frac{m_i u \nu}{T} \frac{\sin^2\theta}{\cos\theta} \frac{H(s) - H(s - \nu t \cos\theta)}{H(s - \nu t \cos\theta)}, \qquad (3.24)$$

where it is taken into account that the unperturbed distribution function is a "shifted" Maxwellian one.

Substituting (3.24) into (2.30) and integrating over θ in the limit $t \to \infty$ (such that the main contribution in integral (2.30) results from the values of θ close to $\pi/2$ and, correspond-

ingly, $\sin\theta = 1$) we get the expression for frictional force:

$$F_{\rm fr} = -\frac{2nu\,(T_i m_i)^{1/2}}{\pi H^2 l}\int_0^l ds\,\frac{dH}{ds}\int_{-\infty}^{+\infty}\frac{H(s)-H(s-s')}{s'}ds'. \quad (3.25)$$

Making use of the periodic structure of the magnetic field, the integration over an infinitive interval can be substituted by a sum. This sum is calculated in an explicit form, which is convenient for finding the values of $F_{\rm fr}$ under the various magnetic field profiles:

$$F_{\rm fr} = -\frac{(2\pi T_i m_i)^{1/2} nu}{H^2 l^2}\int_0^l \frac{dH}{ds}\,ds \times \int_0^l [H(s)-H(s-s')]\cot\frac{\pi s'}{l}\,ds'. \quad (3.26)$$

The velocity of the slow plasma expansion can be found from the balance of forces which is quite similar to that used in Section 2.4. Under the conditions $T_e = T_i = T$, $\partial T/\partial z = 0$ all information about the plasma evolution is given by the diffusive equation for the plasma density

$$\frac{\partial n}{\partial t} = \frac{\partial}{\partial z}D\frac{\partial n}{\partial z}, \quad D = \left(\frac{2}{\pi}\right)^{3/2}\frac{T^{1/2}l}{m_i^{1/2}(k-1)^2}, \quad (3.27)$$

$$l \ll \lambda \ll l(k-1)^{-3/2} \ll L(k-1)^{1/2}.$$

The numerical coefficient in the expression for D corresponds to a sinusoidal profile (2.35). The set of inequalities provides the condition for the plateau regime and the smallness of the expansion velocity in comparison with the ion thermal velocity.

One of the possible applications of this theory was developed in [37] to explain the data obtained in Novosibirsk experiments with an alkali plasma. The experiments were carried out in a multiple-mirror field with 11 mirror cells under two values of mirror ratios: $k = 1.83$ (moderate corrugation) and $k = 1.15$ (weak corrugation). The results for $k = 1.83$ will be discussed

later in Section 5. Here it is reasonable to concentrate on the results related to the case of a weakly modulated magnetic field.

In these experiments the density drop Δn in a steady-state alkali plasma flow was measured while it passed through 11 mirror cells. The values of the density and of the temperature were such that the regime of plasma flow was within the scope of the plateau regime. The last inequality in (3.27), $l/L \ll (K-1)^2$, was not satisfied, so the frictional force was comparatively small and could not produce a large decrease of the flow velocity in comparison with thermal velocity; correspondingly, $\Delta n/n \ll 1$. Since the plasma velocity was high ($u \simeq \nu_{Ti}$), the factor $\exp(-m_i u^2/2T_i)$ was added in (3.26) to take this into account.

For comparison of the experimental result with the theory the two-fluid gas dynamic equations with frictional force (3.26) was analyzed:

$$m_i n u \frac{\partial u}{\partial z} = -\frac{\partial}{\partial z}(p_e + p_i) + F_{\text{fr}},$$

$$nu = \text{const}, \quad enE = -\frac{\partial p_e}{\partial z}.$$

Because of the high electron thermal conductivity, the flow of electrons in all of the regimes is isothermal, while the ion component has a very low thermal conductivity. Under these conditions, the work performed by the electric field on the ion motion can be given by

$$\frac{\partial}{\partial z}\left(\frac{m_i u^2}{2} + \frac{5}{2}T_i\right) = eE. \tag{3.28}$$

Combining expressions (3.27), (3.28) one gets the equation for the plasma density:

$$\frac{\partial n}{\partial z}\left[T_i + \frac{3}{5}\left(T_e - m_i u^2\right)\right] = F_{\text{fr}}.$$

Taking the frictional force as a perturbation one finds the density drop

$$\frac{\Delta n}{n} = 11\frac{(T_i m_i)^{1/2}\, u(k-1)^2}{T_i + \frac{5}{3}(Te - m_i u^2)} \exp\left(-m_i u^2/2T_i\right). \tag{3.29}$$

The numerical coefficient corresponds to the field profile (2.35).

The value of (3.29) depends on a number of parameters which can vary over wide ranges. Taking into account the possible variations of the values of T_i, T_e, and u, one can estimate Δn with expression (3.29) as $\Delta n/n \simeq 0.3 - 0.5$, in good agreement with the experimental data.

3.4. The effect of heavy impurities on plasma multiple-mirror confinement

The results presented above and in Section 2 cover practically all of the possible cases for hydrogen plasma flow in multiple-mirror fields. New possible conditions of plasma flow appear if a small amount of heavy impurities is added to the device. Inserting the impurities with $z \gg 1$ allows, as will be shown below, considerable improvement in the multiple-mirror reactor characteristics.

At a temperature $T = 10$ keV the fusion power output in a pure DT-plasma is known to be approximately 30 times greater than the bremsstrahlung losses. By inserting the impurities with a charge $Z \gg 1$ the bremsstrahlung losses rise by a factor of $n_Z Z^2/n_H$, where n_Z and n_H are, respectively, the densities of impurities and of hydrogen isotopes (the density of impurities is assumed to satisfy the condition $n_Z Z \lesssim n_H$, under which the electrons have mainly a "hydrogen" origin). Therefore the ultimate permissible density of impurities is determined by the condition

$$n_Z Z^2/n_H \lesssim 30. \tag{3.30}$$

On the other hand, at densities $n_Z Z^2/n_H \gtrsim 1$ the impurities can considerably increase the scattering frequency of hydrogen ions. It was suggested in [38] to use this circumstance to decrease the absorption length of CO_2-laser radiation in a plasma (the absorption length is inversely proportional to the scattering frequency of electrons on ions). It is evident that by inserting impurities one can reduce the absorption length by an order of magnitude without violation of the condition (3.30).

It is obvious that, in the same way, one can appreciably reduce the length of a multiple-mirror trap [39, 40]. Indeed, if $n_Z Z^2/n_H \gtrsim 1$, the hydrogen-ion scattering path decreases by a factor of $n_Z Z^2/n_H$ in comparison to the case of a pure hydrogen plasma. The scattering path reduction results in a slowing down of the plasma diffusion along the multiple-mirror magnetic field. This allows a reduction in the installation length needed to provide the given confinement time.

In the case $n_Z Z^2/n_H \gtrsim 1$, the hydrogen ions' mean-free path λ_{HH} with respect to collisions among themselves is connected to their mean-free path λ_{HZ} with respect to collisions with impurities and with the impurity mean-free path λ_{ZZ} by the following relationships: $\lambda_{ZZ} \sim \lambda_{HZ}/Z^2 \sim \lambda_{HH} n_H/n_Z Z^4$. For the quantitative illustration of the impurity effect on the expansion velocity, the case will be examined where the spacing l between two mirrors is smaller than the minimum scattering length, λ_{ZZ}. All species of particles are therefore in the small-scale corrugation regime. The longitudinal diffusion coefficients of the various components according to (2.28) can be estimated by the following relations:

$$D_e \sim \nu_{Te}\lambda_{HZ}/k^2, \quad D_H \sim \nu_{TH}\lambda_{HZ}/k^2, \qquad D_Z \sim \nu_{TZ}\lambda_{ZZ}/k^2 \tag{3.31}$$

(the mirror ratio k is taken to be large, $k \gg 1$, and the width of the mirrors is assumed to be smaller than the distance l between them). Here, in the order of magnitude estimates, we neglect the difference between deuterium and tritium masses.

The estimates (3.31) show that the electron diffusion is fast compared to the other particles. However, in the case where the plasma expands into a vacuum the electrons move together with the light ions due to the effect of a polarization electric field. As to the heavy ions, they can be regarded as immovable (due to their very small diffusion coefficient) within the scale of the light component expansion time.

Based on the estimates (3.31), let us compare, numerically, the case of confinement of a pure DT-plasma with that of

a plasma with a small heavy ion admixture. For the parameters $T \sim 10$ keV, $n \sim 3 \times 10^{17}$ cm^{-3}, and mirror ratio $k = 3$, the length L of the multiple mirror device, with pure plasma confinement, to obtain the Lawson time, $t_L \sim 3 \times 10^{-4}$ sec, is of the order of 30 m. If 10% of impurities with $Z = 10$ are inserted, the length of the machine can be reduced to 10 m (to obtain this, one should note that for a given confinement time, the installation length is proportional to the square root of the diffusion coefficient). However, in this case the mean-free path λ_{ZZ} equals 0.6 cm, so it is rather hard to satisfy the condition $l < \lambda_{ZZ}$ with a reasonable installation diameter. Therefore we shall analyze the case in which $\lambda_{ZZ} \ll l \ll \lambda_{HZ}$.

Over this range of parameters the impurity flow is purely hydrodynamic ($\lambda_{ZZ} \ll l$), while the light ion motion corresponds to the regime of a small-scale corrugation. The expansion velocity of a heavy component is defined by the balance of two forces: the accelerating force, which is due to the polarization electric field, and the friction force against the magnetic field, which is connected with the longitudinal ion viscosity: $\eta_{HZ} u_Z / l^2 \sim eZn_Z E$ (this estimate holds for not-too-large mirror ratios, $k - 1 \sim 1$). Hence, taking into account that $\eta_{HZ} \sim \lambda_{ZZ} \nu_{TZ} Z M_Z n_Z$ and $E \sim T/eL$, one gets $u_Z \sim \nu_{TH} \sqrt{Z} l^2 / \lambda_{ZZ} L$. Comparing this with (3.31), we find the condition $l < Z^{3/4} \lambda_{ZZ}$ for the heavy component expansion to be slower than the light one. For the numerical example considered above, this inequality gives $l \lesssim 5$ cm; this estimate is quite acceptable if the installation radius is smaller than 2–3 cm.

Since in the case of $l < Z^{3/4} \lambda_{ZZ}$, the heavy ions can be considered as immovable within the scale of a light component expansion time, the exact equations describing a light component flow can be obtained in a way analogous to that used in Sections 2.1–2.3. Thereby it is quite sufficient to take into account only the collisions of electrons and light ions with heavy ions (Lorentz plasma model). As was shown in Section 2.3, the temperatures of all species can be considered to be equal ($T_e = T_H = T_Z = T$) and constant ($\partial T / \partial x = 0$) along the plasma column, which holds in many cases of practical inter-

est. Under these assumptions the equations for deuterium and tritium densities have the form

$$\frac{\partial n_{D,T}}{\partial T} = \frac{3T^{5/2}}{\sqrt{2\pi^3} m_{D,T}^{1/2} \Lambda e^4 Z^2 K^2} \frac{\partial}{\partial x} \left\{ \frac{1}{n_Z (n_D + n_T)} \times \left[(2n_{D,T} + n_{T,D}) \frac{\partial n_{D,T}}{\partial x} + n_{D,T} \frac{\partial n_{D,T}}{\partial x} \right] \right\},$$

where Λ is the Coulomb logarithm and $n_Z \cong n_Z(x)$ is the initial distribution of impurities (the polarization electric field is excluded by means of a quasineutrality condition). These equations allow one to predict the time-space evolution of a DT-plasma with heavy impurities in a multiple-mirror magnetic field. The practical use of these equations for impurity parameter optimization has several difficulties since the conditions of their applications can be easily violated under the parameter variation. To derive equations which have no such disadvantages another approach was further developed. It is based on the less accurate but more convenient force balance equations for each group of particles (deuterium and tritium ions were considered as one group with $m_i = 2.5 m_H$). A brief description of this equation was published in [41], and a detailed one with an analysis of the results of optimization was given in [42]. Since this theory was mostly developed in an application to the problem of optimization of the reactor parameters, we will discuss it in the next section, which is devoted to the consideration of different reactor aspects.

4. Multiple-mirror reactor concepts

The general theoretical treatment can be used to quantitatively optimize the different types of multiple-mirror fusion reactors. With this objective we will present a brief review of these studies. Two main types of multiple-mirror reactor were studied: a pulsed reactor with dense plasma, first described in [43], heated by relativistic electron beams and confined in the radial direction by a magnetically insulated rigid wall (so-called

"wall" confinement), and a steady-state reactor with magnetic confinement, first described in [27]. The procedure of optimization of axial confinement for the pure DT pulsed reactor is described in Section 4.1. In the same section, the results of a quantitative analysis of the effect of heavy impurities is presented. The physics of the radial nonmagnetic confinement and the complete concept of the pulsed multiple-mirror reactor with $\beta \gg 1$ are discussed in Section 4.2. Section 4.3 is devoted to a review of the optimization of the steady-state multiple mirror reactor confinement. The stability, radial confinement, and complete concept are considered in Section 4.4.

4.1. Optimization of the axial confinement of a pulsed reactor

Comparing (1.1) with (1.11), one can see that the corrugation of the magnetic field allows an improvement of pulsed reactor characteristics by approximately a factor of $10k$. We now consider what a more accurate analysis, based on the equations presented in Section 3.3, gives. The case of pure DT plasma was treated in [44]. The statement of the problem was very close to that described at the beginning of Section 1. At $t = 0$ the initial space density distribution, initial temperature T_0, which was assumed to be constant along z, and the energy W_0 per unit of transverse plasma cross section were fixed. A numerical integration of Eq. (2.28) for $t > 0$ determined the time evolution of the space density distribution while the time evolution of the temperature was found by including the plasma cooling due to the bremsstrahlung radiation, the end losses, and the α particle heating. With this data the fusion energy output per unit of plasma cross section was calculated during the plasma expansion along the multiple-mirror field. Dividing this value by W_0 one finds the reactor Q.

One feature of the small-scale corrugation regime (2.28) is that the peak value of the initial density distribution n_0 and the length of the installation L do not come into the expression for Q separately, but in the combination $n_0 L$. This product can be expressed in terms of T_0 and W_0, so the value of Q can be

Table 4.1. Pulsed multiple-mirror reactor axial confinement including α-particle heating ($k = 2$).

	$Q = 0.4$ $W_0 =$ 2.5MJ/cm^2	$Q = 1$ $W_0 =$ $5\ \text{MJ/cm}^2$	$Q = 4$ $W_0 =$ 10MJ/cm^2
$n = 8\times10^{16}\ \text{cm}^{-3}$ $p_0 = 1000$ bar	170 m	340 m	700 m
$n = 2\times10^{17}\ \text{cm}^{-3}$ $p_0 = 3000$ bar	60 m	120 m	230 m

analyzed as a function of only these two parameters. The study of the dependence $Q(T_0)$ with a given value of W_0 showed that a maximum value of this function is achieved with $T_0 = 4-5$ keV, which is, therefore, the optimal range of values from the point of view of the axial confinement.

The energy supply W_0 required for the achievement of moderate values of Q ($Q \simeq 1$) to some extent exceeds the value obtained from estimate (1.11). This difference arises because plasma cooling is faster than particle loss from the system. It results from the higher energy losses through the electron channel (if one assumes that each electron takes out energy of the order of $5T_e - 6T_e$). The possibility of reducing the requirements of the reactor parameters by allowing the mirror ratio k to increase toward the ends of the system was analyzed in [44]. This allows a reduction of the value of W_0 by approximately 1.5.

Finding the optimal values of T_0 and W_0 for each value of Q, one can calculate the values of n_0L. It is obvious that by means of choosing higher values of density the length of the system can, in principle, be made shorter. The main limitation on n_0 in [44] is concerned with the limitation on the pressure which the containing walls can support. To illustrate the results of an optimization we show the dependence of the length of the reactor for the achievement of given values of Q under the different values of n_0 and, correspondingly, the pressure p_0.

The possibility of further improvement of the reactor characteristics by inserting a small amount of heavy impurities into the plasmoid was studied in [41, 42]. Before describing an accurate optimization theory we will estimate the value of the expected effect. Let us define W_Z as the energy input needed for the reactor with impurities and W as the energy without impurities, which produce the same values of Q. We introduce then the energy lifetime

$$\frac{1}{\tau} = \frac{1}{\tau_{||}} + \frac{1}{\tau_r},$$

where $\tau_{||}$ is the time of the axial confinement; $\tau_r \sim W_Z/P_r(1+\mu)$ is the time of bremsstrahlung losses, where the factor $\mu = n_Z Z^2/n$ takes into account the presence of the impurities. Taking into consideration that the fusion power $P_f \simeq n^2 L f(T) \simeq 30 P_r$ and $W \simeq nTL$, we find

$$\frac{1}{Q} = \frac{W_Z}{P}\left(\frac{1}{\tau_{||}} + \frac{1}{\tau_r}\right) \simeq \frac{1}{W_Z^2 F(T)(1+\mu)} + \frac{1+\mu}{30},$$

where the function $F(T) \sim f(T)/T^{1/2}$ should be optimized with respect to temperature. Noting further that if $\mu = 0$ we have

$$\frac{1}{Q} = \frac{1}{W^2 F(T)} + \frac{1}{30},$$

we can substitute $F(T)$ by W^2. If we neglect the difference between optimal temperatures for the plasma with and without impurities (the numerical factor 30 changes a little with the temperature), then the relation W_Z/W can be written as follows:

$$\frac{1}{Q} = \frac{W^2}{W_Z^2(1+\mu)}\left(\frac{1}{Q} - \frac{1}{30}\right) + \frac{1+\mu}{30}.$$

Maximizing W_Z/W, the maximum improvement from impurities is achieved for $1+\mu = 15/Q$ and it equals

$$\frac{W_Z}{W} = \sqrt{Q/7.5}.$$

If we consider another statement of the problem and calculate the increase in Q that can be obtained when W is fixed, the result is the same,

$$Q_Z/Q \simeq \sqrt{7.5/Q}.$$

This consideration shows the main characteristic features of the effect of the impurities, which plays a small role for values of $Q \geq 5$. On the other hand, for increasing values of Q, the α-particle heating becomes more and more important in the energy balance. The estimate obtained shows that for $Q \simeq 2-3$, the impurities allow a reduction of W by about a factor of 2. Larger effects can be achieved by means of an inhomogeneous initial impurity density distribution, with impurities mostly located within the maximum of the plasma density gradient.

The search for an optimal form of the impurity density distribution and the value of the temperature and the other plasma parameters was carried out by means of a numerical solution of the equations which describe the self-consistent motion of the plasma and heavy impurities. The problem was analyzed in the same way as described above for pure DT plasma. Given, at $t = 0$, the initial plasma and impurity density distributions, find the slow (in comparison with thermal velocity) diffusive flow of each of the components, the pressure gradient, the electric field, the joint frictional forces, and the friction of the magnetic field. The macroscopic equations for the velocities u_H, u_Z of the components, which follow from the balance of these forces, have the form

$$-n_H u_H m_H v_{TH}\left(\frac{\alpha}{\lambda_{HZ}}+\frac{\beta}{\lambda_{HH}}\right) - \gamma\frac{n_H M_H v_T H}{\lambda_{HZ}}(u_H-u_Z)+en_HE-\frac{\partial p_H}{\partial Z}=0,$$

$$-\gamma\frac{n_H m_H v_{TH}}{\lambda_{HZ}}(u_Z-u_H)-\frac{n_Z u_Z m_Z v_{TH}}{l} + \frac{1}{(l/\lambda_{ZZ}+\lambda_{ZZ}/l)}+eZn_ZE-\frac{\partial p_Z}{\partial Z}=0.$$

Here p_H and p_Z are, respectively, the pressure of the plasma and of the impurities. The factors α, β, γ, δ, η are the numerical

coefficients whose values depend on the geometry of the magnetic field and, correspondingly, are functions of the mirror ratio.

The calculations using this equation showed that the optimal values of Z are in the range $Z \leq 10$. For small Q and optimal parameters the value of Q_Z increases $3-4$ times in comparison with the case of a pure hydrogen plasma. Correspondingly the energy decreases by the same factor if Q is fixed. A comparison of the cases of homogeneous and inhomogeneous initial impurity density distributions shows that by the appropriate choice of the profile the effect of impurities can be increased by approximately 2 times. Similar effects were found for steady-state reactors [45] and will be discussed briefly in Section 4.3.

In considering the thermonuclear aspects of multiple-mirror axial confinement, one should keep in mind that only the ions with $\lambda/k \ll L$ are effectively confined in these systems. We assume that this condition is fulfilled for most of the particles, but this can prove to be violated for high-energy ions with $\lambda(\varepsilon)/k \geq L$. Since it is the high-energy particle that gives the main contribution to DT fusion power output, it is essential to clarify how large is the difference between the actual distribution function and the Maxwellian one at high energies. This problem was resolved in [46]. This difference was shown to be insignificant at large mirror ratios ($k \geq 3$), but at small k it is possible to have some decrease of the neutron yield. In the same paper it was found that the addition of some impurities does not lead to a noticeable variation of the Maxwellian distribution provided $n_Z Z^2/n < (Lk/\lambda)^{1/2}$. At high concentrations of impurities there is a substantial deviation of the distribution function from a Maxwellian distribution.

4.2. The complete pulsed reactor concept

The procedure of axial confinement optimization described above allows us to minimize the value of the initial energy input per unit of plasma cross section. The full amount of energy that is needed for the achievement of the given value of Q is determined by the transverse size of the system. The axial optimization of a pulsed reactor shows that for reduction of the length

of the reactor to 100 m it is necessary to use the plasma with high density $n \geq 3 \times 10^{17} \mathrm{cm}^{-3}$. At a temperature $T_0 = 5\,\mathrm{keV}$ magnetic containment requires the use of magnetic fields in the megagauss range, which is not practical. For this reason, for a pulsed multiple-mirror reactor, "wall" confinement is employed. The magnetic field is then required only to reduce the transverse heat conduction, and radial equilibrium is provided by the rigid walls. Besides the obvious features, concerned with the contact between plasma and wall, substantial differences appear in the plasma behavior as a whole. The most important of these are convective plasma and magnetic field motions which are practically absent in plasma with $\beta < 1$, but become dominant in the case $\beta \gg 1$.

A number of papers have been devoted to the theoretical study of these questions. In most of them a pure transverse problem is analyzed, in which the magnetic field and plasma parameters are considered to change only along the radius and to be homogeneous along the z-axis which coincides with the direction of the magnetic field. Since the plasma is considered to be heated by means of a relativistic electron beam (REB), the problem of initial conditions was studied which corresponds to the radial cold plasma density distribution which is homogeneous in the direction of the magnetic field. The heating pulse and the plasma cooling processes are described with one-fluid MHD equations. The analysis of the cooling rate allows one to find the scaling of the transverse confinement time $\tau_\perp(R)$; then the optimal value of the plasma radius can be found from the condition $\tau_\perp(R) = \tau_\parallel(L)$.

The analytical study of the plasma cooling process is very complicated because of the strongly inhomogeneous profiles $n(r)$, $T(r)$, $H(r)$ which are created due to the passage of an REB through the plasma bunch. The first numerical calculations [25] showed that the plasma cooling rate is approximately 10 times faster than follows from the simple estimate

$$\tau_\chi = R^2/\chi_\perp, \tag{4.1}$$

where $\chi_\perp$ is the coefficient of thermal conductivity.

There is now a clear understanding of the physical mechanisms which are responsible for the resulting thermal conductivity becoming much greater than the classical value (4.1) (see the review [27]). The main feature of nonmagnetic confinement is that the plasma pressure remains almost uniform in the radial direction during cooling: $nT = \text{const}$. Hence, the temperature drop near the wall causes a corresponding rise in the density which is provided by plasma convective flow from the center to the wall. Although the velocity of this plasma radial expansion is much slower than the thermal velocity, it can (as shown in [27]) be considerably higher than $\chi_\perp/R$, the velocity of the propagation of the cooling wave. Thus the convective plasma flow results in a cooling time for the plasma which is much shorter than the estimate of (4.1). In the case, for example, of nonconducting walls, the cooling time can reach the value of the Bohm time, despite the classical values of the transport coefficients.

These results are mostly related to the case of the uniform initial density distribution of the cold plasma. Numerical calculations [26, 41] showed that by means of the choice of a nonuniform initial density distribution the confinement time can be increased by an order of magnitude as compared to the uniform case. If, for example, the plasma occupies the central part of a tube before the beam is switched on it expands during heating and compresses the magnetic field in the gap until its pressure becomes locally equal to the plasma pressure. As a result the hot plasma is isolated from the walls by the magnetic field. Since the diffusion of a magnetic field is $(m_i/m_e)^{1/2}$ times slower than the temperature conductivity the cooling time increases. The efficiency of this method is limited by the finite time of the magnetic field diffusion into the chamber walls. This effect decreases the improvement of a nonuniform initial distribution with values of $\beta \simeq 100$ and it makes moderate values of $\beta \simeq 5 - 10$ more optimal. The final result of the computer study of the problem can be approximated by means of the expression for the transverse confinement time $\tau_\perp = 7.2 \times 10^{-2} \tau_\chi/\beta^{1/2}$ [41], where τ_χ is given by (4.1). From this calculation, achievement of $Q = 1$ with $H = 100$ kG required a plasma radius not less than $4-5$ cm.

The effect of microinstabilities on the confinement time can be estimated, as usual, by introducing the Bohm thermal conductivity $\chi_{\perp B} = (1/16)(cT/eH)$. It is interesting to note that, in contrast to the case of the classical transport coefficient, with Bohm scaling the rough estimate and the exact numerical calculations of the transport equations give approximately the same result. This is caused by the difference in the temperature dependences of the Bohm and the classical coefficients.

The radiative effects during the cooling of high-β plasma were examined in number of papers (see the review [27]). We will not discuss them here since, in the parameter range close to the optimal reactor ones, they play no role. The additional impurity flux caused by contact between the plasma and the metallic walls can lead, in principle, to a large increase in the radiative losses. Consideration of the problem showed that the diffusion of heavy impurities into a dense plasma is substantially suppressed due to the convective plasma flux and the ion thermal force [47].

Apart from the microinstabilities that might result in an increase in the radial transport, flute-type MHD perturbations can be very dangerous for axisymmetric multiple-mirror systems. They certainly would appear in the case of the magnetically confined plasma ($\beta < 1$) because of the considerable pressure drop along the radius. However, this instability is absent in the case where the plasma pressure is constant in the transverse direction (pure wall confinement). In a real situation of finite β there is an intermediate case; plasma pressure varies along the radius, but its variation does not exceed p/β. The study of the MHD stability of a $\beta > 1$ multiple-mirror system carried out in [48] showed that variation of p along the radius equals, in order of magnitude, just the value p/β. This means that the question of stability of the system depends on what concrete profile $p(r)$ is realized. Stable profiles of $p(r)$ certainly exist, and one of them seems to be established automatically.

The effects of ion–ion viscosity have substantial influence on the dynamics of the flute instability in corrugated magnetic fields with $\beta \gg 1$. They result in a reduction of the growth rate by a factor of $\beta^{1/2}$ [48]. If the inequality $\beta > N^2/\Lambda$ is satisfied, it was found that the time for the development of

the instability becomes greater than the axial confinement time. These arguments show that in wall-confined systems the flute instability is not as dangerous as in traditional systems with $\beta < 1$.

In summarizing the optimization of the axial and radial confinement, we will describe the parameters of a multiple-mirror pulsed reactor with $Q = 1$ [49]. The full length of the reactor is equal to 60 m, radius of the chamber is 4 cm, magnetic field strength is 75 kG, and the mirror ratio equals 2. The maximum plasma density is 6×10^{17} cm^{-3}, temperature is 5 keV, and the total energy is 120 MJ. The suggested method for plasma heating is by means of an REB with the use of a "two-stage" scheme. The main feature of this scheme is that the central part of the reactor is occupied by a smaller density plasma $n \simeq 10^{15}$ cm^{-3}, where the beam effectively transfers its energy by a collective interaction. This energy is rapidly transported by the electron heat conductivity to the adjacent areas with the high-density plasma which makes the main contribution to the fusion power output. For the parameters given above the heavy impurity improvement has been taken into account.

The operation of the reactor as a practical energy source requires another optimization, which includes economic variables, which have not been considered above. A reactor has to operate with higher values of Q and there are more rigid restrictions on the maximum pressure and density of the plasma. These requirements result in a substantial increase in both the reactor size and its total energy. For example, including the reduction of the maximum plasma pressure below 500 atmospheres leads to a reactor length of $L = 1000$ m.

4.3. Optimization of the axial confinement of a steady-state reactor

The steady-state concept for a multiple-mirror reactor (MMR) has basic advantages over the pulsed concept, which is shared by all reactor configurations. It also differs from the pulsed concept in a number of important respects that can be either advantageous or disadvantageous. Because the average

power must be held to reasonable levels, the density is much lower in a steady-state reactor than in a pulsed reactor. This requires longer confinement times to achieve a given reactor Q, requiring more attention to optimization of the magnetic field configuration in order to keep the reactor of reasonable length. The lower density opens the possibility of full magnetic confinement, with $\beta < 1$, which is reasonably well understood. However, since the axisymmetric field is not MHD stable, quadrupole fields are required to obtain stability, which can introduce new problems, both of a fundamental and a practical nature. In this subsection we consider the results of the reactor studies considering only axial confinement issues. In the following subsection the MHD stability and radial transport issues will be considered.

As we have seen, when $l_m \ll \lambda \ll kl$, there is a minimum local diffusion rate given by

$$D_{\min} = \frac{9}{9k} \left[\frac{2T}{\pi m_i}\right]^{1/2} .$$

The steady-state operation of a multiple-mirror reactor was studied [39] using a local diffusion coefficient slightly differing from this value [11]. The reactor model consists of a solenoid with multiple-mirrors added to both ends. The central-solenoid length was assumed to be half of the device length and the multiple-mirror cells were assumed to have equal cell lengths. Assuming an upper limit of 20 T for the superconducting solenoid coils, peak mirror fields of 30 T, and reasonable values of conversion efficiency from plasma loss energy and thermal neutron energy to electricity, then for $P_{\text{net}} = P_{\text{recirculating}}$ ($Q \equiv P_{\text{fusion}}/P_{\text{recirculating}} \approx 2$) the reactor parameters were found to be $L = 400$ m, $T = 4.5$ keV, and the central-cell density, $n_1 = 8 \times 10^{22}$ m^{-3} for $\beta = 0.8$. The system had 20 cells, each 5 m long, at each end. They also found that the break-even reactor, $P_{\text{net}} = 0$ ($Q \approx 1$) is 140 m long, and the ignited reactor, $P_{\text{recirculating}} = 0$, is 1100 m long. Since the density decreases toward the end of the machine and $\lambda \sim T^2/n$, the assumption of constant cell length leads to a device which does not operate in the ideal multiple-mirror regime near the ends, resulting in larger axial loss. Thus, the reactor

length found in [39] is somewhat shorter than it would be if the axial loss were accurately computed.

Realizing this problem, a device with variable cell lengths was considered [45]. The cell lengths increase toward the end of the device to keep the plasma in the ideal multiple-mirror regime throughout the machine. In addition, it was assumed that the recirculating power is provided by means of fast-neutral D-beam injectors. The fusion reactions between the fast beam particles and the background plasma increase the total fusion power over the studies of Logan et al., resulting in a shorter reactor. Both studies also assumed that the only loss processes are bremsstrahlung and axial loss; the entire alpha particle power is deposited in the plasma, and $T_e = T_i = T$. The second study did not include a long central solenoid, but rather a central cell which operates in the same mean-free-path regime as the other cells, which results in a reactor length about 13% longer than a reactor with optimum central-cell length.

Another mode of operation was also studied, called the wetwood-burner mode (pure-T background plasma) with depressed ion temperature [51]. In the wetwood-burner mode, the fusion power is produced by reactions between plasma T and beam D ions. In this case, Q increases with T_e and is almost independent of T_i because the background ion temperature is low compared to the beam energy, $E_b (T_i \ll E_b)$. Since the axial power loss scales as $T_i^{7/2}$, depression of the ion temperature results in a shorter MMR for a given Q. By adjusting the reactor parameters so that most of the beam and alpha particle power is deposited in the electrons, one can make the ion temperature lower than the electron temperature. It was found that the depression of the ion temperature can be achieved by using high-energy neutral-beam injectors ($E_b \sim 170$ keV) in MMRs with only a few (5 to 15) cells to make $\tau_{\text{mm}} \cong \tau_{\text{eq}}$ (τ_{eq} is the electron–ion equilibration time). For a central-cell field of 9.3 T and a peak mirror field of 16 T, the reactor parameters were found to be $T_e = 5.6$ keV, $T_i = 3.1$ keV, $E_b = 170$ keV, $n_1 = 5.8 \times 10^{21}$ m^{-3}, and $L = 230$ m for $\beta = 0.8$. The resulting value of $Q \approx 1.1$ was probably too low to be viable, even considering a blanket multiplication by approximately 1.5.

These studies [39, 45, 51] ignored the pressure of the alpha particles and assumed that the entire alpha particle power is deposited in the plasma. However, the alpha particles which are born in the loss cone carry almost all their energy out of the system. Furthermore, some of the confined alpha particles scatter into the loss cone while they are slowing down. Therefore, only about 80% of the alpha particle power (for $R \sim 3$ and $T_e \sim 5$ keV) will be deposited in the plasma, which results in a longer MMR.

Based on the reactor studies [45, 51], a cost analysis study of an MMR has also been performed [52]. Minimization of the unit direct capital cost ($/kW($e$) output) was chosen as the optimization goal. The economic trade-offs among reactor length, magnetic field strength, mirror ratio, recirculating power fraction (or Q), wall loading, and other related parameters were studied. It was found that the reactor cost versus Q shows a broad minimum in the range $Q \approx 5$ to 20; an MMR operating in the wetwood-burner mode, even though short, was not found to be economical, although optimistic unit costs were assigned to the recirculating power systems. The study also showed that, because of the $B^2L = \text{const}$ scaling of the MMR, the economics of the system favors high magnetic fields. In addition, the optimum mirror ratio and number of cells (and, therefore, the reactor cost) were found to be sensitive to the Joule losses in the mirror-quadrupole assemblies needed for average-minimum-B stabilization. The effects of the wall loading on reactor cost were also studied. Because of the high power density in an MMR, the first wall is located far from the plasma and the first-wall radius is basically determined by the desired wall loading. The study indicated that the optimum wall loading (minimum direct plus indirect cost of replacing the blanket) is about 1 to 2 MW m^{-2}.

The most complete steady-state reactor model took these various effects into account, and, although not explicitly considering cost optimization, used the results of that study to consider high central cell magnetic fields, and a relatively small total number of mirror cells [53]. Because of the small number of cells and the not-too-large value of k in the central cells, a local diffusion model underestimates the density. A cell-by-cell analysis,

which we have already described in Section 3.2, can be used to obtain more accurate results. This was done using a somewhat different, but mainly equivalent, theoretical treatment [36].

The basic assumptions for a steady-state MMR which consists of a central solenoid with length l_{c1} and multiple mirrors at both ends are as follows. The background plasma (the warm component) consists of deuterium ions with density $f_D n_i$ and tritium ions with density $(1 - f_D)n_i$, where f_D is the fraction of the D ion density in the total background ion density. The recirculating power P_b is supplied by means of fast-neutral D-beam injectors. The beam particles, slowing down in the plasma, form a hot component with density n_h and deposit part of their energy in the plasma (with $a_{eh}P_b$ going to electrons and $a_{ih}P_b$ going to ions). The remaining beam power $a_{sh}P_b$ is lost because of the scattering of the beam particles into the loss cone. Fusion power is produced by reactions between hot D and warm T ions (P_{fh}) and warm D and T ions (P_{fw}). For other means of heating (e.g., ICRH), one can set $n_h = P_{fh} = 0$. Alpha particles, produced by fusion reactions, deposit some fraction of their power P_α into the plasma (with $a_{e\alpha}P_\alpha$ going to electrons and $a_{i\alpha}P_\alpha$ going to ions). The remaining power, carried by either the particles which are born in the loss cone or those that scatter into the loss cone, is lost ($a_{s\alpha}P_\alpha$). Particle loss and bremsstrahlung are the only loss processes; synchrotron radiation (unimportant in these low-T, high-n devices), radial diffusion, and axial heat flow are ignored. Radial loss can be important in high-Q MMR and will probably determine the highest β at which a reactor can operate [54]. A comparison of the radial confinement time with the axial confinement time is given in the next subsection. As in the pulsed reactor the elimination of axial heat flow to the end walls requires insulating sheaths in an expanding plasma at the device ends, and the electron and ion temperatures are assumed to be constant throughout the device.

Using these assumptions, either in a diffusion model or a cell-by-cell matching model for the axial loss, an equation connecting all of the reactor parameters can be found in the form

$$p_1 L = f\,(Q, k_1, l_{c1}/L, \lambda_{\text{eff}}/l, 2N+1, T)\,,$$

where p_1 is the central cell pressure, k_1 is the mirror ratio of the central cell including pressure effects, l_{c1} is the length of the central cell, $2N+1$ is the total number of cells, and T is the temperature, assumed to be constant and equal for ions and electrons. The quantity $\lambda_{\text{eff}}/l \approx \lambda/kl$ is the ratio of trapping mean free path to cell length, which it is necessary to take into account because the operation is in the transition region $\lambda_{\text{eff}}/l \sim 1$, where the formulas for large-scale corrugation must be corrected. The results of an approximate correction given in [11] are used for the calculation. The magnitudes of the mirror field and β are taken to be constant in all cells, so that the mirror ratio k increases as the density decreases, and is therefore a variable in the optimization process. The optimization procedure is to minimize f to obtain a minimum of $p_1 L$ for a given Q, with k_1 taken as fixed. A simple optimization of T, as a function of $2N+1$, is then performed, with λ_{eff}/l a parameter. The results of this study for a given Q are shown in Fig. 3.2. We see that good results are obtained with λ_{eff}/l in the range 0.2–0.25. As expected, the operation improves with increasing number of cells [the envelope of the λ_{eff}/l_c curves, with a reasonable operating condition with 20 cells on each end $(2N+1=41)$], which was then held fixed for a study of other Q values. The economic optimum might well occur with fewer cells, e.g., ten cells on either end, with a 10% longer length. The complete set of reactor parameters for a range of Q-values is shown in Table 4.2.

The results of this study included some conservative features that overestimated the energy flux and therefore predicted a larger $p_1 L$ than was actually required. A recent unpublished work [55] indicates that a considerable reduction in both the length and the magnetic field may be possible.

4.4. Steady-state multiple-mirror reactor

In common with tokamaks and tandem mirrors, multiple-mirrors are at best ave-min-B devices. A magnetic configuration consisting of magnetic mirrors and linked quadrupole fields produces an ave-min-B well in a region near the axis [56]. As an example, choosing $l_m/l_c = 0.1$, and assuming a realizable form

Table 4.2. Parameters of a 41-cell MMR with $k_1 = 3.36$ and $\lambda_{\text{eff}}/l_c = 0.2$ $(\lambda/l_c = 1.4)$.

Q	1	5	Ignition
T (keV)	4.6	6.0	7.4
l_{c1}/L	0.46	0.50	0.53
$p_1 L$ ($\times 10^{10}$ Pa · m)	2.5	6.3	12.5
$B_1^2 L$ ($\times 10^5$ T^2 · m)[a]	0.8	2.0	3.9
L (m)[b]	312	773	1534
n_1 ($\times 10^{22}$ m^{-3})[b]	5.5	4.2	3.4

[a] $\beta = 0.8$ $(R_v = 1.75)$.
[b] $\beta = 0.8$ $(R_v = 1.75)$ and $B_1 = 16$ T.

for the quadrupole field, the last stable radius at the midplane, r_w, is found to have a broad maximum if $r_w/R \approx 15\%$, where R is the mirror coil radius. These values are consistent with the typical parameters of a steady-state reactor calculation for which $r_w = 3$ cm, $R \approx 50$ cm, and $l_c \approx 5$ m. One limitation of min-ave-B stabilization is the onset of localized (ballooning) modes with finite β. Calculations indicate that substantial β's are possible in realistic reactor configurations [57, 58].

The fan-shaped flux surfaces that are created by min-ave-B coils have certain undesirable features. The enhanced radial diffusion can also add to the overall losses [59]. The asymmetry breaks the p_θ invariant that would otherwise prevent radial diffusion arising from nonadiabaticity. In addition, the quadrupoles increase the Joule heating in nonsuperconducting coils by about a factor of five and increase the complexity of coil design and construction [52].

The theoretical studies of the ave-min-B low β magnetic field structures explored the relationship between the well radius and flux surface ellipticities for various ratios l_m/l and mirror ratios. An idealized coil configuration was considered, consisting of local mirrors and two sets of quadrupole bars, one carrying weak currents extending the full cell length l (the "weak quadrupoles") and quadrupole bars with strong currents extend-

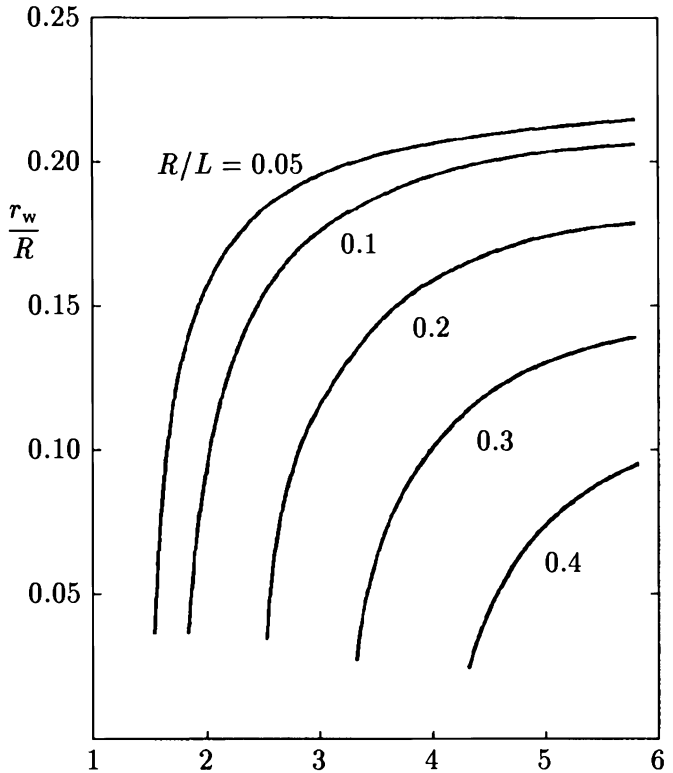

Fig. 4.1. Optimized well radius normalized to mirror radius versus mirror ratio.

ing over the mirror scale length, with a mirror radius R (the "strong quadrupoles"). The well radius was optimized with respect to weak and strong quadrupole currents and strong quadrupole length. The results of the optimization are summarized in Figs. 4.1–4.2.

In Fig. 4.1 the well radius at the center of the cell r_w is given, and in Fig. 4.2 the corresponding well radius in the mirror throat $r_{\min}$ is shown. Fortuitously, both large mirror ratios and small values of R/L, which are required for efficient longitudinal confinement, are more effective in producing large midplane wells. On the other hand, large mirror ratios also lead

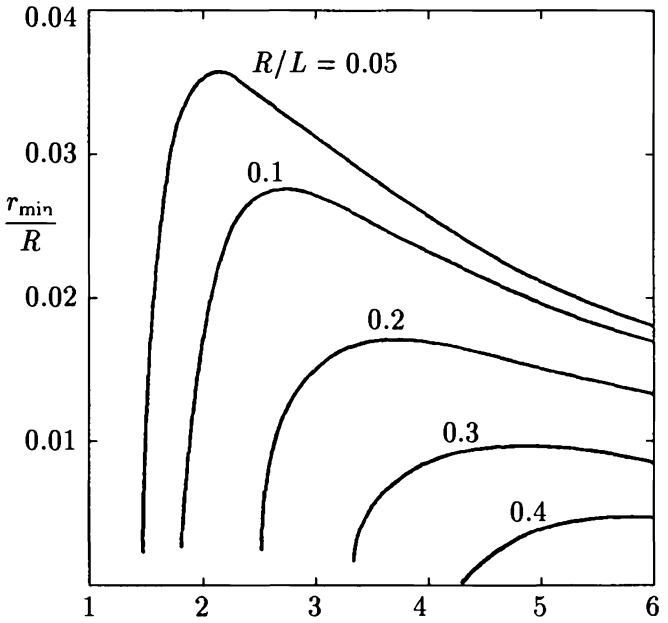

Fig. 4.2. The minimum well dimension in the mirror throat.

to large ellipticities, such that $r_{\min}/R$ decreases as the mirror ratio increases, leading to enhanced radial loss.

Although ave-min-B fields are subject to ballooning modes, which can limit the β of tandem mirrors, multiple-mirrors do not appear to have such a limitation. The reason for this is that the unfavorable curvature is concentrated in a small region near the mirror throat, with a short connection length to the favorable curvature regions that extend over most of the cell. An approximate stability criterion can be written [57]:

$$\beta_c \leq 8\pi^2 \gamma r_p R_c / l_m^2 ,$$

where γ is the ratio of average good curvature to the maximum destabilizing curvature R_c, r_p is the plasma radius, and l_m is the connection length. With the scaling for the multiple-mirror, $\gamma \sim 0.1 l_m / l_c$ and $R_c \sim l_c l_m / r_p$, the critical beta is predicted to be $\beta_c \leq 8$. These calculations were performed for practical

geometries used in experiments, indicating stability at all $\beta \leq 1$ [57]. This work was extended to a general study of resistive ballooning which was more relevant to the experimental studies. The results were similar, except that resistive effects allow residual slow-growing modes [58]. The resistive effects become unimportant under reactor conditions. The experimental results and comparison with the theory are given in Section 5.

Particularly for devices with β near unity, the radial diffusion time can become comparable to the axial diffusion time. In this case a more complete theory, including both radial and axial diffusion, is required. We have already given a simple estimate of the combined effect, for pulsed systems, in Section 4.2. For steady-state systems, in which the plasma is far from any radial wall, the actual process of combined radial and axial loss is that the central density diffuses radially toward the plasma edge, where the density is lower. At the lower density the axial diffusion is enhanced, so that all flux is eventually lost axially.

An analytic investigation of this combined phenomenon was made, showing that with proper definitions the overall confinement time could still be cast in the form

$$\frac{1}{\tau} = \frac{1}{\tau_z} + \frac{1}{\tau_r},$$

as used in Section 4.2 [54]. The theory shows that as $\beta \to 1$, the radial profiles are essentially flat with sharp gradients near the plasma edge. The results of the theory can be characterized in terms of a single parameter $\alpha \sim (\tau_z/\tau_r)^{1/2}$, and show that one can trust, quantitatively, a heuristic evaluation of the axial and radial loss using an effective mirror ratio $\bar{k}$ and an average magnetic field $\bar{B}$ given, even for values of β close to unity, by

$$\bar{k} = k_v \left(\frac{1 - \beta/k_v^2}{1 - \beta} \right)^{1/2}$$

and

$$\bar{B} = B_v (1 - \beta)^{1/2},$$

where k_v and B_v are the vacuum values of k and B, respectively. Radial losses are unimportant (e.g., less than 10% de-

crease in confinement time) for $\alpha \lesssim 0.5$. It was shown qualitatively that some improvement in overall confinement can be made by increasing the β of a system beyond the $\beta = 0.8$ value usually used. However, for the usual parameters of steady-state reactors, radial losses play a substantial role and cannot be neglected. Such designs should be optimized with the inclusion of the effect of radial losses.

5. Experimental evidence of the multiple-mirror confinement

Since the mean free path of the charged particles in plasma scales as $\lambda \propto T^2/n$, the predictions of the multiple-mirror theory can be easily checked in a laboratory by using a wide range of temperatures and densities which correspond to the range of parameters for which $\lambda \sim l$. The steady-state alkali plasma, obtained in Q-machines, is a very convenient medium for carrying out such experiments. Shortly after the first suggestions on multiple-mirror confinement were published, these experiments were performed in Novosibirsk and Berkeley.

The first Berkeley installation had a length of about 150 cm; the diameter was 6 cm, the number of mirror cells N could be varied from 1 to 5, and the mirror ratio could be varied from 1 to 4. The main part of the experiments was carried out with $N = 5$, $k = 3.7$, and the mirror cell length $l = 28$ cm. The plasma, created by the ionizer near one end of the device, was absorbed, after passing through the corrugated field, by a collector placed at the other end of the system. The length of the plasma column could be varied by moving the collector in the axial direction. The number of cells in the system could be changed either by moving the collector or by switching coils on or off. The plasma density was determined by Langmuir probes which measured the density distribution in the axial and radial directions.

The first results of the Berkeley experiments were published in [60] practically at the same time as [61] appeared, giving results of experiments carried out at Novosibirsk. More

detailed results of the Berkeley experiments were given later in [27]. The experiments were performed over a wide range of densities 10^{-9} cm$^{-3} \leq n \leq 10^{11}$ cm, which made it possible to observe the behavior from the free Knudsen plasma flow at small densities to strongly collisional MHD flow at high values of density. The results of the measurements of the effective plasma confinement time confirmed the theoretical predictions of the quadratic dependence on the number of cells and demonstrated, as well, the theoretical prediction of the dependence on the average mirror ratio. In the first Berkeley experiments a comparatively small number of cells was used and there was no reliable information about radial losses. In addition, the ion temperature, which is needed for the mean free path determination, was estimated from known alkali plasma properties. Despite these limitations, the results of the measurements of the effective plasma confinement time confirmed the theoretical predictions of the quadratic dependence on the number of cells and demonstrated, as well, the theoretical prediction of the dependence on the average mirror ratio.

An example of the experimental results is given in Fig. 5.1, which shows the probe current ($\propto$ density) in the first cell next to the source as a function of the collector position in the (a) low-, (b) intermediate-, and (c) high-density regimes. For the intermediate-density case, the density at the source is seen to increase in a stepwise fashion as the collector passes each mirror throat, adding another cell to the system. (The first density jump corresponding to the collector passing the second mirror is a result of partial loss of velocity space due to ion trapping when the first cell is created, and is not a multiple-mirror effect.) The increases in the measured first-cell density are smaller with the collector moving into cells 4 and 5, due to increasing radial loss. However, this can be taken into account in the measurement of the longitudinal confinement time by using the flux to the collector in the calculation. When this was done, the $\tau_{mm} \propto N^2$ scaling was obtained over the cells in the intermediate-density case. The low-density ($\lambda \sim L$) case and the high-density ($\lambda \ll L$) case are characteristic of Knudsen flow and collisional MHD flow, respectively. These regimes were confirmed by measurements with sliding axial probes.

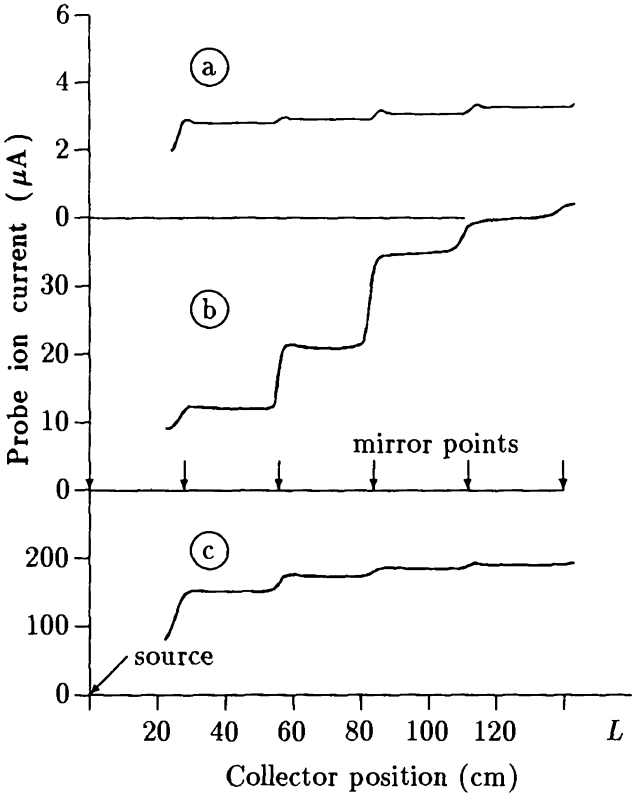

Fig. 5.1. Langmuir probe ion saturation current (proportional to n) in the first cell as a function of the collector position in (a) low-density, (b) intermediate-density, and (c) high-density regimes, for a 5-cell multiple-mirror device.

The Novosibirsk installation had a length of 240 cm and consisted of 14 mirror cells with mirror ratio $K = 1.83$. The range of densities corresponded to the condition $\lambda \geq l$, which allowed both the free Knudsen flow regime and the small-scale corrugation regime to be studied. Sometimes the boundary of the large-scale regime (hydrodynamical regime) was reached. The experiments were carried out in both the steady-state regime [62], and the impulse regime [63], where the plasma behavior was

analyzed after a rapid switching off of the flow from the ionizer. The method of performing and analyzing the experiment allowed a comparison of theory with experiment without exact knowledge of the ion temperature.

We now discuss the results of the Novosibirsk experiments in greater detail. If everywhere in the device $\lambda > l$, then Eq. (2.28) predicts the stationary density profile to be exponential:

$$n(z) = n_L \exp\left(\frac{L-z}{\lambda_L}\right), \tag{5.1}$$

where z is the distance from the ionizer, L is the coordinate of the last probe which was located in the cell with number $N = 11$, n_L and λ_L are the plasma density and the ion mean free path (the exact definition of λ_L follows from (2.28)) at the exit of the system $z = L$. It follows from (5.1) that for $\lambda_L \ll L$ the plasma density near the ionizer is much greater than the density n_L. This theoretical variation was checked experimentally.

The results of the measurements of the plasma density distributions confirmed the exponential dependence of $n(z)$. Calculating the slope of the linear function $\ln\left(n(z)/n_L\right)$, the value of λ_L was found for a given experiment. In this way λ_L is calculated without using the ion temperature. This λ_L was then checked for self-consistency with the assumption leading to (5.1). With this treatment of the measurements for each experiment, the dependence $n(0)/n_L = f(L/\lambda_L)$ was then found from the results of a number of experiments. The value of λ_L and the corresponding n_L was varied from one experiment to another by changing the plasma flux at the ionizer.

The results of measurements are illustrated in Fig. 5.2. As one can see, over a reasonably wide range of parameters there is good agreement between theory and experiment. The transition to the high-density regime ($\lambda_L \ll l$) proved to be difficult to reach because of the appearance of plasma losses. Some deviation from the exponential dependence that occurred at a small λ_L seemed to be concerned with the beginning of the large-scale corrugation regime. If this happens, then the small-scale approximation is violated first within some area near the

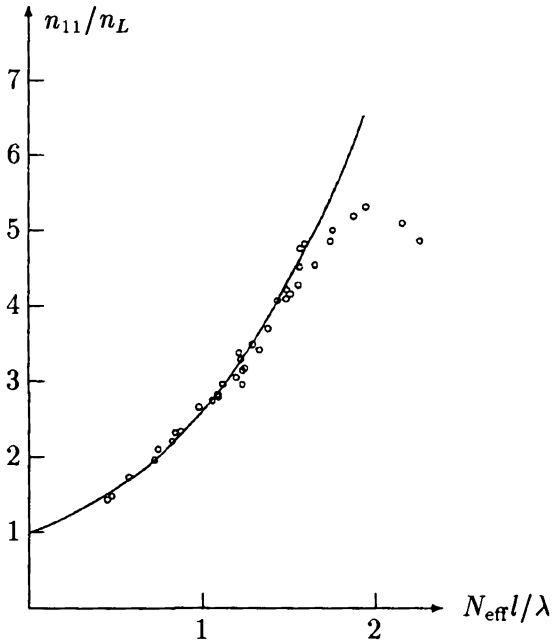

Fig. 5.2. Comparison of theory and experiment for $n(0)/n_L$ as a function of L/λ_L.

ionizer, where the approximation of large-scale corrugation starts to apply. One theory, developed for this situation and based on the matching of the solution of Eqs. (2.28) and (3.23) across the boundary $\lambda \simeq l$, predicts the existence of the maximum for the function $f(L/\lambda_L)$ at $\lambda_L \sim Nl$. The maximum value of this function is estimated as $N/(2\ln N)^{1/2}$, which gives $(n(0)/n_L)_{\max} \simeq 5$ at $N = 11$, in reasonable agreement with the results presented by Fig. 4.1–4.2. In summarizing the experiments with an alkali plasma, one should conclude that they not only qualitatively but also quantitatively confirmed the validity of the multiple-mirror confinement theory.

After a few years, the Berkeley multiple-mirror alkali device was modified for experiments with hydrogen plasma. A θ-pinch was used as a plasma source which allowed a density within the range $n \simeq 10^{13} - 10^{14}$ at a temperature $T = 10$ eV

to be obtained. The geometrical characteristics of the device and a number of cells in it were practically the same as in the experiments with alkali plasma. The magnetic field configuration was reconstructed into a set of nonaxisymmetric mirror cells with an average min-B. This was done for stabilization of the MHD flute perturbation, which was absent in alkali plasma because of the contact with the ionizer. The main purposes of this set of experiments [64] was an analysis of the MHD stability and the measurements of the radial and axial plasma losses. A quantitative comparison of the axial loss with the theoretical prediction was difficult because of the small number of the mirror cells and the small length of each of them.

This difficulty was decreased in a larger installation which had a full length $L = 10$ m, $N = 9$, $l = 75$ cm [65]. The magnetic system provided the nonaxisymmetric magnetic field with a small width of the mirrors $l_m = 10$ cm, which made it possible to realize all of the plasma confinement regimes, including the "ideal" one (Section 3.2). The plasma sources consisted of a θ-pinch and a plasma gun providing initial density values up to $n \simeq 10^{15}$ cm^{-3} at a temperature $T \simeq 3-8$ eV. The probe measurements, which were made simultaneously in many cells, allowed the time and the spatial plasma bunch evolution to be measured during its expansion along a field line. Since the density decreased with time, the various regimes of the plasma motion could be observed from the large scale to the small scale. A comparison of the numerical calculations using (2.28) and (3.23) with the experimental dependences $n(z,t)$ showed that they are in good quantitative agreement [66]. This conclusion relates to the moderate density range $n \lesssim 10^{13}$ cm^{-3}. At high densities $n \simeq 10^{14}-10^{15}$ cm^{-3}, where plasma flow was purely hydrodynamic, a comparison of axial confinement theory and experiment could not be done because the plasma was dominated by radial losses.

A series of experiments on multiple-mirror confinement was also carried out at Nagoya University [67–69]. Using a small installation with $L = 1$ m, $N = 10$, $l = 10$ cm, the researchers at Nagoya University could observe at $n = 10^{14}$ cm^{-3} and $T \simeq 10$ eV the regime of large-scale corrugation ($\lambda < l$).

The experimental results summarized above generally confirm the theory in practically all of the regimes of multiple-mirror confinement. These conclusions hold both for experiments with alkali plasma and for experiments with hydrogen plasma.

The experiments in which the plasma was not stabilized by line-tying were also useful in checking the predictions of MHD stability. A set of quadrupole coils of the type investigated theoretically [56] was installed in the first Berkeley experiment. Because of design constraints of the existing magnets it was not possible to obtain complete stabilization with the added quadrupoles. The resulting confinement system was tested both using the alkali plasma that was disconnected from the ionizing source and with a hydrogen plasma created by a θ-pinch source. For both types of plasmas a flute instability was clearly seen when the quadrupole coils were not activated. The flutes were not totally stabilized, as expected, when the quadrupole coils were activated, but the reduction in growth rate predicted by the theory was observed [70].

MHD stability studies were also undertaken in the Berkeley 10-m device. The coil design for this system included fully stabilizing weak and strong quadrupoles such that an ave-min-B magnetic field was achieved over a range of mirror ratios. The experiments indicated that stable plasmas could be achieved up to the highest β's obtained by the counterstreaming θ-pinch and the Marshall gun hydrogen sources ($\beta > 25\%$) [57]. Other ave-min-B magnetic field configurations, with longer connection lengths, were also tested, and were found to become unstable at lower values of β, as predicted theoretically [57, 58]. The conclusion of these studies was that ave-min-B coil structures could be designed to stabilize magnetically confined plasmas up to $\beta \sim 1$.

6. Summary and discussion

A theory of plasma diffusion through a corrugated magnetic field (multiple mirrors) has been developed that is applicable to the complete range of ratio of mean free path to cell length, and of mirror ratios. Estimates of the local flow rate, and there-

Table 6.1. Summary table of local diffusion coefficients D.

$$\left(u = -D\frac{1}{n}\frac{dn}{dz}\right), \quad \tau_{mm} \approx L^2/D$$

	$\lambda \gg lk$		$\lambda \ll l_m, l$
$k \gg 1$	$0.9\nu_{Ti}\lambda/k^2$		$\frac{5}{6}\nu_{Ti}\frac{ll_m}{\lambda k \ln k}$
	$\lambda \gg \frac{l}{k(k-1)^{3/2}}$	$l \ll \lambda \ll \frac{l}{(k-1)^{3/2}}$	$\lambda \ll l$
$k-1 \ll 1$ sinusoidal mirrors	$1.1\nu_{Ti}\frac{\lambda}{(k-1)^{1/2}}$	$\left(\frac{2}{\pi}\right)^{3/2}\frac{\nu_{Ti}l}{(k-1)^2}$	$\frac{3.3}{\pi^2}\frac{\nu_{Ti}l^2}{\lambda(k-1)^2}$
		$l_m \ll \lambda \ll lk$ (point mirrors)	
		$l/k \ll \lambda \ll lk$	$\lambda \ll l/k$
$k \ll 1$		$\sqrt{\frac{2}{\pi}}\frac{l}{k}\nu_{Ti}$	$\frac{8}{9}\sqrt{\frac{2}{\pi}}\frac{l}{k}\nu_{Ti}$

$$\nu_{Ti} \equiv \sqrt{T/m_i}, \quad \lambda \equiv T^2/\left(e^4\Lambda n\right), \quad l_m \approx (1/B)\, dB/dz$$

fore the local diffusion, are given in Section 1. These regimes naturally divide, for study, into the long mean free path regime ("small-scale corrugation") with $\lambda/l \gg 1$, and the short mean free path regime ("large-scale corrugation") with $\lambda/l \ll l$, and are treated rigorously in Sections 2 and 3 respectively. Analytic results can be obtained for the cases in which $k \gg 1$ (strong corrugation) and $k \ll 1$ (weak corrugation). The results are summarized in Table 6.1.

A case of considerable importance for the application of plasma confinement in multiple mirrors to fusion reactors occurs

if the scale length of the individual mirrors l_m is much less than the length of an individual mirror cell l. In this case the inequality $l_m \ll \lambda \ll l$ can be satisfied, such that the individual cells are collisional but the mirror regions are collisionless. The resulting confinement properties are very favorable for reactor design, particularly for the steady-state concept, which has been called the "ideal" multiple-mirror regime. The analysis of this case is presented in Section 3.3. The flow velocity found there is approximately

$$u \approx \frac{l/k}{L} v_{Ti},$$

which, for $l/k \ll L$, is a dramatic improvement over the free flow. The results for this case are also given in Table 6.1.

Detailed studies of axial confinement in both pulsed and steady-state reactors have been made, using the results presented in Sections 2 and 3, or similar results obtained from alternate calculations. The basic procedure is to find a feasible configuration and then to optimize the variable parameters to obtain a device with minimum length at a given value of Q. The pulsed concept uses very high densities ($\beta \gg 1$) in which the magnetic field, in addition to supplying the magnetic mirrors, also thermally insulates the plasma from the wall, which contains the plasma pressure. The procedure for calculating the axial confinement is outlined in Section 4.1, and the results of the optimizations are given in Table 4.1. The steady-state concept relies on magnetic confinement with the wall far from the plasma. The plasma density is limited by the necessity of balancing the plasma pressure with the magnetic pressure. The calculation procedure is outlined in Section 4.3, and the optimized parameters are given in Table 4.2.

Each of the main reactor concepts have some special features that must be considered separately. Since the pulsed reactor operates with $\beta \gg 1$ on the axis, the questions of plasma displacement of the magnetic field and of radial heat conduction to the wall become critical. Both of these questions have been considered in detail, and the results appear to be favorable for reactor operation. An important advantage of the pulsed concept is that the wall provides stability against MHD modes in

an axisymmetric magnetic field. This stabilization is sensitive to the overall configuration, and therefore has been carefully analyzed. These analyses are discussed and results given in Section 4.2. A main consideration in a magnetically confined steady-state reactor is MHD stability. Stabilization requires the use of linked quadrupoles which give distorted magnetic surfaces and a limited range of stabilization. In addition, the resulting field is only ave-min-B and therefore may be subject to ballooning modes for $\beta \simeq 1$. Calculations indicate that the well radius is sufficiently large for reactor operation. Because of the short connection length between good and bad curvature regions, ballooning modes are found to be stable up to $\beta \lesssim 1$. Finally, radial diffusion, which is enhanced because of the fanned magnetic field, is found to be acceptable at a reactor design value of $\beta = 0.8$. The results are summarized in Section 4.4.

The basic confinement theory has been checked experimentally in most of the confinement regimes discussed. Because $\lambda \propto T^2/n$ it is quite easy to scale the mean free path to laboratory plasmas that operate over the range of values of λ/l. This was initially done in steady-state alkali plasmas with simple mirrors, in which the plasma was stabilized by line-tying to the ionizing source, giving reasonable agreement between theory and experimental results, over the complete range $1 \ll \lambda/l \ll 1$, with mirrors that had a single scale length. Later, the important regime $l_m < \lambda < l$ was investigated with a 10-m device in which $l_m \ll l$, giving good agreement with theory. In this device a pulsed hydrogen source was used to create the plasma, which therefore had to be stabilized with quadrupoles. The stabilization was achieved in agreement with the theoretical predictions of ave-min-B stability. The plasma was also stabilized up to the highest β obtainable in the device ($\beta \sim 0.25$) in agreement with the predictions of ballooning theory. These results are discussed and summarized in Section 5.

The results given in Tables 4.1 and 4.2 for the parameters of pulsed and steady-state reactors are feasible and competitive with the Tokamak concept. Nevertheless, there are various features that are not desirable. Consequently many suggestions have been made to improve the reactor operation or to oth-

erwise modify the less desirable aspects of the reactors. Although optimization procedures were employed for minimizing the reactor length, certain parameters were held fixed, without optimization. For example, β was considered fixed at the value $\beta = 0.8$ for the steady-state reactor calculation. If we assume classical losses between unlike charged particles only, then the confinement time scaling with β for axial loss τ_z and radial loss τ_r is as follows: $\tau_z \propto (1-\beta)^{-1}$ and $\tau_r \propto 1-\beta$. Approximating the total confinement time as $1/\tau \approx 1/\tau_z + 1/\tau_r$, then τ is maximized for $\tau_r = \tau_z$. We can therefore vary β to achieve this condition. For an axisymmetric device this optimization has been performed [54], indicating that some improved confinement could be achieved particularly for the wetwood-burner concept.

More radical methods of achieving improved performance have also been proposed. One method mentioned briefly at the end of Section 2.3 involved the creation of traveling-wave mirrors [20]. It was shown that mirrors traveling at the expansion speed of the plasmoid could essentially stop the expansion. A steady-state version of this idea was also examined [30] under different assumptions, and it was found that large improvements in confinement could be achieved. An important limitation on this type of confinement, which was not discussed by either of the above authors, is plasma heating. The time-varying mirror fields magnetically pump the plasma, which, together with collisions, leads to irreversible energy transfer [71].

A simplified analysis of the containment time $\tau_t w$ with traveling-wave multiple-mirrors gives [71]

$$\tau_{tw} = \frac{1}{\nu_0}\left[\frac{p}{v_0}\left(e^{\frac{v_0}{D}\frac{L}{2}} - 1\right) - \frac{L}{2}\right], \tag{6.1}$$

where v_0 is the mirror velocity and D (assumed to be independent of n) is the diffusion coefficient in the absence of v_0. For v_0 significantly greater than $v_L = 2D/L$, the flow velocity in the absence of moving mirrors, the exponential term dominates the behavior, giving

$$\tau_{tw}/\tau_{mm} \approx (v_L/v_0)^2 \exp(\nu_0/\nu_L) \gg 1. \tag{6.2}$$

To obtain the heating we use the magnetic pumping equations [72] giving

$$\tau_h \approx \frac{1}{2\pi^2(R-1)^2}\left(\frac{l_c}{\nu_0 \tau_{ii}}\right)^2 \tau_{ii}. \tag{6.3}$$

We use the restriction that $\tau_h \leq \tau_{tw}/8$ to prevent overheating and find that the improvement in confinement is limited to about $\tau_{tw}/\tau_{mm} \approx 3$. This improvement, although not dramatic, is still interesting, and merits a more exact calculation.

The traveling mirror concept is a specific example of the general concept of producing asymmetric scattering. If the random walk distance that an ion moves could be made asymmetrical such that it moves further toward the center of the device than toward the ends, a large improvement in confinement could theoretically be obtained. The scaling for an orbiting asymmetry was examined for the special case of a large central cell, with the end cells used for confinement only, to obtain the ratio of the confinement to the center cell confinement [73]

$$\tau_{\text{eff}}/\tau_0 = [1 + (1-p_0)N^*], \tag{6.4}$$

where $N^* = (k_1^N - 1)(k_1 + k_2 - 1)(k_1 - 1)$, $k_1 = f_c/f_e$, $k_2 = 1 - f_c/f_e$, where f_c and f_e are the probabilities of escape toward the center and end, and p_0 the probability of a particle being untrapped in the center cell. For k_1 large, N^*, and therefore τ_{eff}/τ_0, are very large. The authors did not clearly demonstrate that such an asymmetry could be produced, but they reasoned physically that one nonadiabatic and one adiabatic mirror should produce an asymmetry. Although the asymmetry achieved in this manner is likely to be small, it can still have a significant effect on confinement. For example, a 10% asymmetry with 10 mirror cells will give a $\tau_{\text{eff}}/\tau_0 \approx 2$. Clearly, more detailed calculations of the amount of asymmetry that can be achieved in this manner should be undertaken.

Another interesting possibility is collision-independent scattering. We have seen that the power loss for collisional scattering has the temperature proportionality $P_l \propto T^{7/2}$. For collision-independent scattering, if we assume that the random

walk distance l_z is independent of n and T, then the multiple-mirror confinement time has proportionality $\tau_{mm} \approx L^2/v_T l_z \propto T^{-1/2}$ and power loss $P_l \propto nT^{3/2}l_z$. An optimum temperature of $T_{\text{opt}} \approx 15$ keV was found [74]. The more favorable temperature allows significant reduction in density and therefore in B. If l_z can be made significantly smaller than that for the comparable collisional reactor, further improvements are possible.

One method of achieving collision-independent scattering is to have sharp gradients in the d.c. magnetic field. These are further enhanced by high β. However, the nonadiabaticity is strongly energy dependent, only scattering the higher energy particles. Although some improvement can be achieved in this manner, dramatic improvement requires nonadiabaticity of the lower energy particles also. A method of obtaining nonadiabatic scattering that is particularly suitable to lower energy particles is by cyclotron resonance heating (CRH). If we assume that the fields can penetrate into the plasma at the ion cyclotron resonance, which appears to be possible, then the collision-independent scattering process works as follows: Rapid stochastic heating is obtained up to a stochastic energy W_s. Beyond this energy, slower heating takes place up to a barrier energy $W_b = 5W_s$, with the steady-state energy distribution function having a maximum around W_s. Individual particles rapidly diffuse both up and down in their perpendicular velocity, thereby scattering in and out of the loss cone, thus giving a short effective random walk distance for energies below W_B. However, on a collisional time scale the plasma is heated beyond W_B, which can lead to overheating. An analysis of a reactor employing this mechanism indicated only modest improvements in confinement time of about a factor of 2 [75].

In conclusion, multiple-mirror devices hold considerable promise for confining fusion plasmas. They have the specific advantages of simplicity and ease in extending the confinement time by increasing the device length. The fundamental confinement theory has been worked out in detail. Using the results of the confinement calculations, both pulsed and steady-state reactor concepts have been developed and appear to be feasible.

REFERENCES

1. G. I. Budker, *Plasma Physics and the Problem of Controlled Thermonuclear Reactions,* Vol. 3, Pergamon Press, New York (1959), pp. 1–33.
2. R. F. Post, *Proc. of Second U.N. Int. Conf. on Peaceful Uses of Atomic Energy,* Vol. 32, Geneva (1958), p. 245.
3. G. I. Dimov, V. V. Zakaidakov, and M. E. Kishinevski, *Fiz. Plazmy,* **2**, 597 (1976).
4. T. K. Fowler and B. G. Logan, *Comments on Plasma Physics and Controlled Fusion,* **2**, 167 (1977).
5. B. B. Kadomtsev, "Magnetic traps with a 'corrugated' field," *Plasma Physics and the Problem of Controlled Thermonuclear Reactions,* Vol. 3, Pergamon Press, New York (1959), pp. 340–355.
6. J. L. Tuck, "Monte Carlo and computer plasma simulation studies of the inhibition of end loss from a θ-pinch by non-adiabatic 'rough' magnetic walls," Rep. CN-24/K-5 on 3rd Int. Conf. on Plasma Physics and Controlled Thermonuclear Fusion, Vol. 2, Novosibirsk (1968), pp. 595–605.
7. R. F. Post, "Confinement of charged particles by multiple-mirror systems," *Phys. Rev. Lett.,* **18**, 232–236 (1967).
8. B. G. Logan, A. J. Lichtenberg, and M. A. Lieberman, "Multiple-mirror confinement for fusion reactors," *Bull. Amer. Phys. Soc.,* **15**, 1432 (1970).
9. B. G. Logan, A. J. Lichtenberg, and M. A. Lieberman, "Multiple-mirror confinement in plasmas," *Phys. Rev. Lett.,* **28**, 144–147 (1972).
10. A. Makhijani, B. G. Logan, A. J. Lichtenberg, and M. A. Lieberman, "Plasma confinement in multiple-mirror systems. I: Theory," *Phys. Fluids,* **17**, 1291–1301 (1974).
11. G. I. Budcer, V. V. Mirnov, and D. D. Ryutov, "The influence of magnetic field corrugation on the expansion and cooling of a dense plasma," *JETP Lett.,* **14**, 320–324 (1971).
12. V. V. Mirnov and D. D. Ryutov, "Gas-dynamic description of a plasma in a corrugated magnetic field," *Nucl. Fusion,* **12**, 627 (1972).

13. B. N. Briezman, V. V. Mirnov, and D. D. Ryutov, "Ohmic resistance of an inhomogeneous plasma," *Sov. Phys. JETP,* **12**, No. 5, 948 (1970).

14. V. V. Mirnov, "Electroconductivity and the skin-effect in a corrugated magnetic field," *Collection of abstracts of the Int. Conf. on Closed Systems Plasma Confinement* [in Russian], Dubna (1969), p. 53.

15. V. V. Mirnov, "Skin effect in a corrugated magnetic field," *Nucl. Fusion*, **11**, 221–230 (1971).

16. G. I. Budker, E. P. Kruglyakov, V. V. Mirnov, and D. D. Ryutov, "On the possibility of a thermonuclear reactor with a dense plasma contained by a corrugated magnetic field," in: *Proc. of USA–USSR Seminar on System Analysis and Thermonuclear Power Station Construction* [in Russian], Energetics and Transport, Leningrad (1974); *Izv. Akad. Nauk SSSR,* **6**, 35–40 (1975).

17. A. A. Galeev and R. Z. Sagdeev, "Transport phenomena in a collisionless plasma in a toroidal magnetic system," *Sov. Phys. JETP,* **26**, No. 1, 233 (1968).

18. S. I. Braginski, "Transport processes in a plasma," in: *Reviews of Plasma Physics,* Vol. 1, Consultants Bureau, New York (1965), pp. 205–311.

19. J. M. Dawson, A. Hertzberg, R. E. Kidder, G. G. Vlasses, H. G. Ahlstrom, and L. G. Steinhauer, "Long-wavelength, high-powered lasers for controlled thermonuclear fusion," Report CN-28/D-13 on *4th Intern. Conf. on Plasma Physics and Controlled Thermonuclear Fusion,* Vol. 1, Madison (1971), pp. 673–687.

20. G. I. Budker, V. V. Mirnov, and D. D. Ryutov, "Gas-dynamics of a dense plasma in a corrugated magnetic field," *Proc. of the Int. Conf. on Plasma Theory* [in Russian], Kiev (1972), pp. 145–151.

21. V. V. Mirnov and D. D. Ryutov, "Expansion of a plasma along a weakly corrugated magnetic field," *Proc. 5th Europ. Conf. on Plasma Physics and Controlled Thermonuclear Fusion,* Vol. 1, Grenoble (1972), p. 100.

22. G. I. Budker and S. T. Belyaev, "Boltzmann's equation for an electron gas in which collisions are infrequent," *Plasma Physics and the Problem of Controlled Thermonuclear Reactions,* Vol. 2, Pergamon Press, New York (1959), pp. 431–457.

23. V. E. Zakharov and V. I. Karpman, "On the nonlinear theory of the damping of plasma waves," *Sov. Phys. JETP,* **16**, No. 2, 351 (1963).

24. F. L. Hilton and C. Oberman, "Electrical conductivity of a plasma in a spatially inhomogeneous magnetic field," *Nucl. Fusion,* **9**, No. 4, 319–327 (1969).

25. G. E. Vekstein, D. D. Ryutov, M. D. Spektor, and P. Z. Cheboteev, "Nonmagnetic containment of a dense plasma," *J. Appl. Mech. Tech. Phys.,* **15**, No. 6, 731–739 (1974).

26. G. E. Vekstein, V. V. Mirnov, D. D. Ryutov, and P. Z. Cheboteev, "Theory and calculations of non-magnetic dense plasma confinement," *Proc. of the 6th Int. Conf. on Plasma Physics and Controlled Thermonuclear Fusion,* Munich (1976); *IAEA,* CN-351E-21, Vol. 3, Vienna (1977), pp. 535–545.

27. G. E. Vekstein, "Magnetothermal processes in a dense plasma," in: *Reviews of Plasma Physics,* Vol. 15, Consultants Bureau, New York (1990), pp. 1–57.

28. C. E. Seyler, W. Grossman, and L. C. Steinhauer, "End stopping by the reversed magnetic multiple-mirror concept," *Comments Plasma Phys. Conf. Fus.,* **4**, 21 (1978).

29. S. L. Musher and M. D. Spector, "Transverse confinement of a high pressure plasma in a corrugated magnetic field," *Nucl. Fusion,* **20**, No. 2, 149–157 (1980).

30. S. Aihara, "Travelling wave multiple-mirror field for confinement of high temperature plasmas," Research Report IPPJ-234, Institute of Plasma Physics, Nagoya University (1975).

31. A. A. Galeev and R. Z. Sagdeev, "Nonlinear plasma theory," in: *Reviews of Plasma Physics,* Vol. 7, Consultants Bureau, New York (1979), p. 88.

32. D. A. Shapiro, "Equations of motion of a plasma in a slightly bumpy magnetic field," *Sov. J. Plasma Phys.,* **3**, No. 3, 545–550 (1977).

33. R. V. Bravenec, A. J. Lichtenberg, M. A. Lieberman, and H. L. Berk, "Viscous plasma flow in a multiple-mirror configuration," *Phys. Fluids,* **24**, 1320–1325 (1981).

34. R. V. Bravenec, H. L. Berk, and J. H. Hammer, "An alternative derivation of the parallel ion viscosity," *Phys. Fluids,* **25**, 608–609 (1982).

35. Yu. V. Vasiljev, and V. V. Mirnov, "Gas-dynamics of a plasma in multiple-mirror magnetic trap with 'point mirrors'," *J. Appl. Mech. Tech. Phys.*, No. 6, 14–19 (1974).

36. F. Najmabadi, A. J. Lichtenberg, and M. A. Lieberman, "Effect of ambipolar potential on multiple-mirror confinement," *Phys. Fluids,* **26**, No. 4, 1018–1027 (1983).

37. G. I. Budker, V. V. Danilov, V. A. Kornilov, E. P. Kruglyakov, V. N. Lukyanov, V. V. Mirnov, and D. D. Ryutov, "Confinement in a multiple-mirror magnetic field," Report CN-33/H8-3 on *5th Intern. Conf. on Plasma Physics and Controlled Thermonuclear Fusion,* Vol. 2, Tokyo (1974), pp. 763–776.

38. J. M. Dawson, R. E. Kidder, and A. Hertzberg, *Preprint MATT-782,* Plasma Physics Lab., Princeton University (1971).

39. B. G. Logan, I. G. Brown, A. G. Lichtenberg, and M. A. Lieberman, "Plasma confinement in multiple-mirror magnetic systems. II: Experiment and reactor calculations," *Phys. Fluids,* **17**, 1302–1313 (1974).

40. V. V. Mirnov and D. D. Ryutov, "The effect of heavy impurities on plasma motion in a multiple-mirror magnetic field," *Proc. 7th Europ. Conf. on Plasma Physics and Controlled Thermonuclear Fusion,* Lausanne (1975), p. 143.

41. P.Z. Chebotaev, B. Z. Knyazev, V. V. Mirnov, and G. E. Vekstein, "Plasma confinement optimization in a multiple-mirror magnetic trap," *Proc. of the X Europ. Conf. on Controlled Fusion and Plasma Physics,* Vol. 1, C-6, Moscow (1981).

42. B. A. Knyazev, V. V. Mirnov, and P. Z. Chebotaev, "The improvement of longitudinal plasma confinement in multiple-mirror trap," Preprint INP Novosibirsk No. 81-100; *Voprosy Atomnoi Nauki i Tekhniki. Termoyadernij Sintez,* **3**, No. 13, 12–17 (1983).

43. G. I. Budker, "Thermonuclear fusion in installations with a dense plasma," *Proc. 6th Europ. Conf. on Plasma Physics and Controlled Thermonuclear Fusion,* Vol. 2, Moscow (1973), pp. 146–158.

44. B. A. Knyazev and P. Z. Chebotaev, "Pulsed multi-mirror fusion reactor: longitudinal confinement," *Nucl. Fusion,* **24**, No. 5, 555–563 (1984).

45. S. T. Yang and M. A. Lieberman, "Power balance and impurities in two-component, multi-mirror reactors," *Nucl. Fusion,* **17**, 697–712 (1977).

46. Yu. V. Vasiljev and D. D. Ryutov, "High-energy part of the ion distribution function in a multiple-mirror magnetic trap," *J. Appl. Mech. Tech. Phys.*, **18**, 295–299 (1077).

47. G. E. Vekstein, D. D. Ryutov, and R. Z. Chebotaev, "Diffusion of heavy impurities in a dense, wall-confined plasma," *Fiz. Plazmy*, **1**, No. 3, 220–222 (1975).

48. M. D. Spector, "Hydrodynamic stability of dense plasma in a corrugated magnetic field," *J. Appl. Mech. Tech. Phys.*, **16**, No. 1, 22–30 (1975).

49. D. D. Ryutov, "The study of open-ended fusion systems at the Novosibirsk Institute of Nuclear Physics," *Voprosy Atomnoi Nauki i Tekhniki. Termoyadernij Sintez,* No. 1–2 (1978), pp. 96–112.

50. M. V. Krivosheev, A. V. Komin, C. N. Krilov, E. V. Seko, B. A. Knyazev, and D. D. Ryutov, "Parameter studies of the power installation based on a multi-mirror trap," *Voprosy Atomnoi Nauki i Tekhniki. Termoyadernij Sintez,* No. 2 (10) (1982), pp. 2–16.

51. S. T. Yang and M. A. Lieberman, "Two-component, multiple-mirror reactor with depressed ion temperature," *Nucl. Fusion,* **18**, 965–969 (1978).

52. F. Najmabadi, A. J. Lichtenberg, and M. A. Lieberman, in: *Engineering Problems of Fusion Research,* Proc. 8th Symp. IEEE, Vol. 2, San Francisco, California, November (1979), p. 632.

53. F. Najmabadi, A. J. Lichtenberg, and M. A. Lieberman, "Parameter optimization of multiple-mirror reactors," *Nucl. Fusion,* **23**, No. 5, 609–637 (1983).

54. M. Tuszevski and M. A. Lieberman, "Radial losses in high-β multiple-mirror plasmas," *Phys. Fluids,* **24**, No. 2, 320–327 (1981).

55. E. S. Zawaideh, "Generalized fusion equations for parallel transport in collisional to weakly collisional plasmas," Ph.D. Thesis, University of California, Los Angeles (1985).

56. J. C. Riordan, A. J. Lichtenberg, and M. A. Lieberman, "Minimum-average-B wells in linked magnetic mirror fields," *Nucl. Fusion,* **19**, 21–31 (1979).

57. H. D. Price, M. P. Benjamin, B. K. Kang, A. J. Lichtenberg, and M. A. Lieberman, "Study of high beta ballooning modes," *Phys. Fluids,* **28**, No. 1, 392–408 (1985).

58. B. K. Kang, A. J. Lichtenberg, and W. M. Nevis, "Resistive effects on rigid mode ballooning instability," *Phys. Fluids,* **30**, 1415–1429 (1987).

59. M. Tuszewski and A. J. Lichtenberg, "Two-dimensional boundary-value problem for ion-ion diffusion," *Phys. Fluids,* **20**, 1263–1274 (1977).

60. B. G. Logan, I. G. Brown, A. J. Lichtenberg, and M. A. Lieberman, "Experimental evidence of multiple-mirror plasma confinement," *Phys. Rev. Lett.,* **29**, 1435 (1972).

61. G. I. Budker, V. V. Danilov, E. P. Kruglyakov, D. D. Ryutov, and E. V. Shun'ko, "Experiment on alkali plasma confinement in a corrugated magnetic field," *JETP Lett.,* **17**, 117–120 (1973).

62. G. I. Budker, V. V. Danilov, E. P. Kruglyakov, D. D. Ryutov, and E. V. Shun'ko, "Experiments on plasma confinement in a magnetic multi-mirror trap," *Sov. Phys. JETP,* **38**, No. 2, 276–282 (1974).

63. V. V. Danilov and E.D. Kruglyakov, "Plasma dynamics in a multi-mirror magnetic system," *Sov. Phys. JETP,* **41**, No. 6, 1055–1058 (1975).

64. M. Tuszewski, A. J. Lichtenberg, and S. Eylon, "Transient confinement of a high density plasma in a multiple-mirror magnetic field configuration," *Nucl. Fusion,* **17**, No. 5, 893–902 (1977).

65. M. Tuszewski, D. Price, and M. A. Lieberman, "MHD-stabilization of finite β multiple-mirror plasma," *Nucl. Fusion,* **19**, No. 9, 1244–1247 (1979).

66. H. D. Price, A. J. Lichtenberg, M. A. Lieberman, and M. Tuszewski, "Radial and axial losses in a multiple-mirror experiment," *Nucl. Fusion,* **23**, No. 8, 1031–1052 (1983).

67. M. Inutake, A. Komori, R. Hatakeyama, and N. Sato, "Stability of high density plasma in a multiple-mirror," *9th Europ. Conf. on Contr. Fusion and Plasma Physics,* Oxford (1979), p. 51.

68. M. Inutake, A. Komori, R. Hatakeyama, and N. Sato, "High density plasma confinement in a multiple-mirror," *Phys. Lett.*, **78A**, No. 2, 143–144 (1980).

69. M. Inutake, R. Hatakeyama, and N. Sato, "Low-frequency plasma instability in a multiple-mirror configuration," *Proc. of Int. Symposium on Physics and Open-Ended Fusion Systems,* Tsukuba, Japan (1980), p. 313; *J. Phys. Soc. Jpn.*, **48**, No. 2, 707–708 (1980).

70. J. C. Riordan, M. Tuszevski, and A. J. Lichtenberg, "Stabilization of interchange modes in multiple-mirror confined plasmas," *Plasma Phys.*, **20**, 139–155 (1978).

71. A. J. Lichtenberg, "New ideas in multiple-mirror confinement," *Proc. Int. Symp. on Physics of Open-Ended Systems,* Tsukuba, Japan (1980), p. 321.

72. J. M. Dawson and M. F. Uman, *Nucl. Fusion,* **5**, 242 (1965).

73. R. F. Post and X. Z. Li, "Particle confinement in asymmetric cell multiple-mirror systems," *Nucl. Fusion,* **21**, 135 (1981).

74. A. J. Lichtenberg and M. A. Lieberman, "Multiple-mirror confinement with collision independent scattering," *Nucl. Fusion,* **16**, 532 (1976).

75. K. J. Donninger, M. A. Lieberman, and A. J. Lichtenberg, "A theoretical study of ICRF effects on multiple-mirror confinement," *Nucl. Fusion,* **25**, 3–20 (1985).

PLASMA ROTATION IN TOKAMAKS

V. Rozhansky and M. Tendler

Introduction

From early studies on the neoclassical transport theory in a tokamak [1], it is well known that a tokamak plasma rotates both in the poloidal and toroidal directions. The neoclassical theory predicts a poloidal rotation velocity of order $\sim cT/eBr$ and a toroidal velocity within the upper limit $\sim cT/eB_pr$ (where B_p is the poloidal magnetic field) for discharges with ohmic heating and balanced neutral beam injection. The resulting poloidal and toroidal rotation velocities are of order 105–106 and 106–107 cm/s, respectively. Notwithstanding these large values, rotation in a tokamak is determined by rather subtle physical effects such as viscosity and inertia. Therefore, quantitative assessment of the rotation in a tokamak is a complicated problem. The issue has been addressed by a number of authors within the framework of neoclassical theory [2–4]. Experimental measurements performed on many tokamaks have shown that there is incomplete agreement between experimental results and theoretical predictions on rotation. This is borne out by measurements of the toroidal rotation velocity and the electric field. In fact, neoclassical theory predicts that the effect of the perpendicular viscosity results in large values of toroidal rotation up to $\sim cT/(eB_pr)$. Furthermore, the electric field vanishes in the collisional regime. However, these large values of toroidal rotation are not observed experimentally and the radial electric field turns

out to be of the order $T/(er)$ provided there is no unbalanced neutral beam injection [5–7]. Generally it is asserted that transport parallel to the magnetic field is in good agreement with neoclassical theory. By contrast, cross-field transport of energy, momentum, and particles in the thermal plasma are grossly anomalous. Therefore, it is plausible that the disagreement stems from an anomaly of the momentum transport perpendicular to a magnetic field. The contradiction between theoretical predictions and reality is also encountered in experiments on relaxation of toroidal momentum after switching off an unbalanced neutral beam in the toroidal direction [7–9]. However, some results of neoclassical theory are confirmed. For example, the electric field does not differ too much from neoclassical theory, provided there is no fast toroidal rotation. This is also true both for measured values and for the direction of the resulting poloidal rotation. Recently, it has been shown that the majority of results based on the neoclassical theory [10, 11] on rotation remain valid, provided the real transport driven by a turbulence is taken into account [12–14]. The bulk of the results were derived from the main balances of density and momentum and therefore are justified. The fundamental approach, based on momentum balance [10, 11], appears to yield useful values. Furthermore, the extension of this approach by incorporating anomalous terms driven by turbulence allows us to obtain velocities of rotation from the components of tensors for viscosity and inertia and thereby to employ the solutions of the drift kinetic equation for regimes with varying collisionality [12–14]. An analysis carried out along these lines has demonstrated the existence of bifurcated solutions yielding both steep and gradual profiles of the poloidal rotation in the vicinity of the separatrix. Steep profiles emerge at the plasma edge for the H-mode of confinement. These profiles are considered to improve confinement [15–18]. Indeed, steep profiles of the poloidal rotation velocity may provide for the suppression of a turbulence level and thereby reduce transport coefficients at the edge [19]. In general, there is renewed interest in nonlinear phenomena caused by plasma rotation. Some of these nonlinear effects, for example, the enhancement of radial transport due to the resonant interaction of poloidal rotation with a natural drift

wave [20], the existence of different poloidal rotation equilibria for a given density and temperature profile [21], the emergence of shocks on a magnetic surface [22], the redistribution of plasmas due to centrifugal force owing to fast toroidal rotation [23–26], and modifications of the neoclassical transport due to a fast poloidal rotation [27, 28], have been considered before. Focusing on the separatrix, new effects influencing rotation were pointed out, i.e., collisions with neutrals [29] and ion orbit losses occurring on the separatrix [30–37]. In order to explain the large rotation velocities in the vicinity of the separatrix, in particular in the H-mode, the effect of ion losses from orbits crossing a separatrix has been invoked in [32, 33]. In these models, the algebraic bifurcation for values of poloidal rotation within a very narrow location has been derived from the nonlinear dependence of neoclassical parallel viscosity on the velocity of poloidal rotation. However, in spite of the merits of this idea, an attempt was made to compute the fluid parameters at the separatrix in these studies, whereas only the kinetic approach is truly warranted. In an important study in [38], the kinetic approach was employed for the same region in the banana regime neglecting anomalous transport. This work yielded only qualitative results for the value of the electric field at the separatrix. This value is also affected by the complicated flow pattern occurring in the scrape-off (SOL) plasmas outside the separatrix. The important issue of the electric field at the separatrix has been addressed by numerical methods for the banana regime in [39]. It was shown that the radial and poloidal electric fields emerge for a given density profile. Moreover, steeper density profiles imply stronger negative radial electric fields, and vice versa. At the edge below the separatrix, where gradients may become steep and the anomaly of the transport is particularly pronounced, terms stemming from these effects have their main bearing on the momentum balance and result in steep profiles of the poloidal rotation velocity and the subsequent L–H transitions. An idea related to the one described in [12–14], but accounting for the poloidal inhomogeneity of anomalous transport coefficients, has been put forward in [40, 41]. The issue of the poloidal rotation caused by anisotropy of the background turbulence has been

addressed in [42]. In [43, 44], the generation of rotation by the peeling of the convective cells is discussed. The latter considerations are restricted to the two-dimensional models, thereby making it inapplicable to a tokamak in which the impact of toroidicity is crucial. In summary, the point of view advocated in the present review is as follows. Since anomalous transport is of fundamental importance at the plasma edge in a tokamak, terms of momentum balance originating from turbulence cause steep profiles of poloidal rotation and their impact results in the L–H transition, thereby accounting for the universality of the phenomenon. It should be mentioned that there is a different school of thought based on the heat-transport equation advocated in [46]. In general, it is important to keep in mind that, if the issue is addressed from the strictly neoclassical point of view, a steep temperature profile results in increased poloidal rotation. Therefore, it is difficult to discriminate between the various models suggested to explain the natural L–H transition because the governing parameters of each of the theories, such as the diamagnetic drift velocity and/or the poloidal sound speed ΘC_S, turn out to be quantitatively almost the same near the separatrix during the H-mode. The complexity of the issue is further aggravated by the difficult diagnostics for measurements of poloidal rotation employing impurity lines. These measurements have yielded data different from poloidal rotation for the main ions due to diamagnetic terms [47]. Yet, it would appear that the crucial test in validating different models for L–H transitions is through experiments using a biased electrode [48–51]. These experiments allow an electric field to be excited at the plasma edge in a tokamak in a controlled manner and thereby to vary the poloidal rotation. This enables more information to be obtained by introducing a new variable (i.e., the current, which is zero otherwise due to ambipolarity) and thereby to increase the dimensionality of the parameter space for this problem. This approach has demonstrated substantial radial current densities, which are presumed to be exactly zero within the framework of standard neoclassics [52]. In contrast to the neoclassical approach, the theory described in detail below yields a perpendicular conductivity and a maximum attainable current that agree

well with experimental measurements [53, 14]. Fast toroidal and poloidal rotations affect significantly the redistribution and flows of impurities within a magnetic surface and thereby affect their transport. Different aspects of these issues were addressed in [23], [47], and [54–57]. In conclusion, the effects resulting from poloidal and toroidal rotations are considered in the review presented here. The emphasis is on the underlying physics, and calculations of solutions of the kinetic equation are mainly restricted to the simplest cases. Since the underlying physics is the same for all toroidally symmetrical geometries, we adopt, for simplicity, a model in which the magnetic flux surfaces are concentric circular and the inverse aspect ratio ϵ is small. The focus is on the plateau regime, which has its bearing on the plasma edge for most if not all modern tokamaks. Other regimes are addressed when nontrivial effects result from them. Last, but not least, the issues of the poloidal and toroidal rotation within the SOL differ from the corresponding issues on closed field lines. However, the role of the inertia and viscosity for both regions is emphasized in these concepts. Thus, issues stemming from convective flows within the SOL are also addressed along these lines. The focus remains on both the natural electric field and the radial electric field caused by biasing.

1. Momentum balance

1.1. Plasma flows within a magnetic surface. The interrelation between the poloidal and the toroidal rotations

For the purpose of macroscopic analysis the fundamental system of moment equations reads

$$\frac{\partial n}{\partial t} + \nabla \cdot (n\mathbf{u}_i) = I, \tag{1.1}$$

$$\frac{\partial n}{\partial t} + \nabla \cdot (n\mathbf{u}_e) = I, \tag{1.2}$$

$$nm_i \frac{d\mathbf{u}_i}{dt} = ne\mathbf{E} + \frac{ne}{c}(\mathbf{u}_i \times \mathbf{B}) - \nabla \cdot \overleftrightarrow{\pi}_i - \nabla p_i + \mathbf{F}_i - \mathbf{R}, \tag{1.3}$$

$$0 = -neE - \frac{ne}{c}(\mathbf{u}_e \times \mathbf{B}) - \nabla\cdot\overleftrightarrow{\pi} - \nabla p_e + \mathbf{F}_e + \mathbf{R}, \tag{1.4}$$

where n is the density, $u_{i,e}$ is the fluid velocity of ions and electrons, $\nabla\cdot\overleftrightarrow{\pi}_i$ is the ion viscosity (small electron viscosity and inertia are ignored), $p_{e,i}$ are partial pressures for electrons and ions, $\mathbf{R}$ is the friction force, $d/dt = \partial/\partial t + (\mathbf{u}_i \cdot \nabla)$, and $\mathbf{F}_{e,i}$ is the external force acting on electrons and ions (for example, due to unbalanced beam injection). The viscous term is considered to originate from both the neoclassical viscous stress tensor and the shear anomalous viscosity caused by the dependence of the parallel flow on the minor radius coordinate. Since the underlying physics is the same for all toroidally symmetrical geometries, we adopt, for simplicity, a model in which the magnetic flux surfaces are concentric circular flux surfaces and the inverse aspect ratio is small. Standard coordinates are used with polar coordinates r and θ centered on the toroidal magnetic axis, while ϕ measures angular distance along the axis. The magnetic field is taken to be

$$\mathbf{B} = B_0 \frac{\mathbf{e}_\phi + \mathbf{e}_\theta}{1 + \varepsilon\cos\theta}, \qquad \varepsilon = \frac{r}{R}. \tag{1.5}$$

Here, $\varepsilon = r/R$ is the inverse aspect ratio and $\Theta = B_\theta/B_\phi$ is the ratio of the poloidal to the toroidal field. The coordinate system is shown in Fig. 1.1.

Some of the results below will be presented in Appendix 1 for magnetic surfaces with an arbitrary shape. The curvature element has the form $dl^2 = dr^2 + r^2 d\theta^2 + R_0^2(1 + \varepsilon\cos\theta)^2 d\phi^2$. Therefore, the components of the metric tensor are

$$g_{11} = 1, \qquad g_{22} = r^2, \qquad g_{33} = R_0^2(1 + \varepsilon\cos\theta)^2, \tag{1.6}$$

where 1, 2, and 3 correspond to r, θ, ϕ and $R_0 = R(\theta = \pi/2)$. The average value of any function f over a flux surface is defined as follows:

$$\langle f \rangle = \frac{1}{2\pi}\int (1 + \varepsilon\cos\theta) f\, d\theta. \tag{1.7}$$

The density and the potential are sought in the form

$$\begin{aligned} n(r,\theta) &= n_0(r) + n_1(r,\theta) + \ldots, \\ \varphi(r,\theta) &= \varphi_0(r) + \varphi_1(r,\theta) + \ldots, \end{aligned}$$

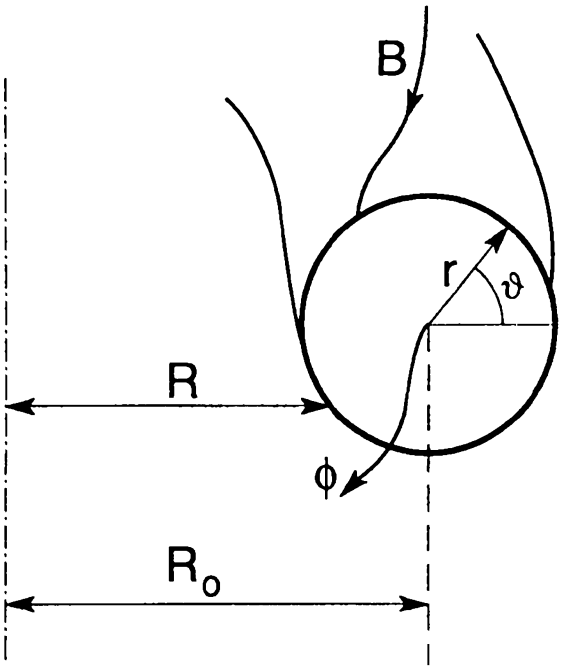

Fig. 1.1. The coordinate system.

where ordering with ε and

$$\rho_{ci}/(\mathcal{Q}L) \ll 1 \tag{1.8}$$

is employed. Equation (1.8) yields the ratio of the poloidal Larmor radius to the radial scale length of the density or the temperature profiles. The toroidal component of Eq. (1.4) governs the radial velocity of the electron transport

$$\langle nu_r \rangle = \langle cR/(eB_\theta) \rangle. \tag{1.9}$$

It is well known that the friction force caused by collisions results in a negligibly small radial particle loss within the framework of standard neoclassics. Therefore, anomalous transport can be conceived macroscopically to result from an anomalously large

friction force due to a strong level of turbulence. In the present study it is assumed that u_r is poloidally homogeneous. Here, the radial velocity $u_r = u_r^{(A)}$ in terms of the anomalous transport,

$$u_r^{(A)} = -\frac{D\,dn}{n\,dr} + V(r) \tag{1.10}$$

(where D and $V(r)$ are the anomalous diffusion coefficient and pinch velocity), is included. Note that Eq. (1.10) must be incorporated into Eqs. (1.1)–(1.4) both for ions and electrons, since $u_{ir}^{(A)} = u_{er}^{(A)}$ [109] includes a convective derivative in the operator d/dt. Taking the radial component of Eq. (1.3) and neglecting the radial inertia and viscosity, one obtains

$$en\,E_r - \frac{dp_i}{dr} - \frac{en}{c}\left(u_{i\theta}\,B_\phi - u_{i\phi}\,B_\theta\right) = 0. \tag{1.11}$$

To the highest order in ε, Eq. (1.11) yields the relation between the flux-surface average poloidal and toroidal rotation velocities

$$V_\theta = V_0 + u_{pi} + \Theta\bar{u}_\phi, \tag{1.12}$$

where $V_0 = -cE_r/B$ is the $\mathbf{E} \times \mathbf{B}$ rotation velocity, $u_{pi} = (c/eBn_i)dp_i/dr$ is the diamagnetic drift of ions, and $\bar{u}_\phi$ and V_θ are the toroidal and poloidal rotation velocities averaged over the flux surface times B_0/B_ϕ, defined as

$$\bar{u}_\phi = \langle (B_0/B_\phi)\,u_{i\phi}\rangle, \tag{1.13}$$

$$V_\theta = \langle (B_0/B_\phi)\,u_{i\theta}\rangle. \tag{1.14}$$

Equation (1.12) shows that the poloidal rotation velocity is a function of $(V_0 + \Theta\bar{u}_\phi)$. The result stems from the following arguments. Changing the frame of reference from the laboratory to one rotating along the major radius and employing $\bar{u}_\phi \ll C_S$, where $C_S = \sqrt{2T_i/m_i}$, thereby neglecting the centrifugal force, one obtains for the electric field

$$E'(r) = E_0(r) + \frac{\bar{u}_\phi}{c\,B_\theta}.$$

Therefore, the velocity of the poloidal rotation in this frame of reference yields $V_0' = -cE'/B_0 = V_0 + \bar{u}_\phi$, which together with the diamagnetic drift for ions determines the poloidal rotation (1.12). Equations (1.3) and (1.4) yield poloidal and radial components to the first order in ε as

$$u_{jr} = -\frac{c\partial\varphi_1}{Br\partial\theta} - \frac{c}{e_j n B}\left[\frac{\partial p_{1j}}{r\partial\theta} - \left(\nabla\cdot\overleftrightarrow{\pi}\right)\theta - nm_i\frac{d\mathbf{u}_{i\theta}}{dt}\right] + u_r^{(A)},$$

$$u_{j\theta} = V_0 + \Theta u_{j\phi} + \frac{c}{e_j n B}\frac{dp_j}{dr}. \tag{1.15}$$

Assuming that $nu_r(A)$ determines the evolution of the average density, one obtains

$$\frac{\partial n}{\partial t} + \nabla_r\cdot\left(nu_r^{(A)}\right) = I.$$

Hence,

$$\nabla\cdot\left[n\left(\mathbf{u}_j - u_r^{(A)}\mathbf{e}_r\right)\right] = 0. \tag{1.16}$$

Accounting for axisymmetry, Eq. (1.16) yields

$$\frac{1}{r(1+\varepsilon\cos\theta)}\left\{\frac{\partial}{\partial r}\left[r(1+\varepsilon\cos\theta)(u_{jr} - u_r^{(A)})\right] + \frac{\partial}{\partial\theta}\left[(1+\varepsilon\cos\theta)u_{jq}\right]\right\} = 0. \tag{1.17}$$

Substituting Eq. (1.15) into Eq. (1.17) and neglecting terms of order higher than ε^2, one obtains

$$-\frac{c}{B_0}\frac{dn_0}{dr}\left(\frac{\partial\varphi_1}{r\partial\theta} - \frac{m_j}{e}\frac{du_{j\theta}}{dt}\right) + V_0\frac{\partial n_1}{r\partial\theta} + \frac{n_0\Theta}{r}\frac{\partial u_{j\phi}}{\partial\theta} + \frac{n_0\Theta u_{j\phi}}{r}\frac{\partial(1+\varepsilon\cos\theta)}{\partial\theta} + (V_0 + u_{pj})\frac{n_0}{r}\frac{\partial[1+\varepsilon\cos\theta]^2}{\partial\theta} = 0. \tag{1.18}$$

Here, $n_0 = \langle n\rangle$ is the average density over the flux surface. It is well known that divergences of the diamagnetic and the electric

drifts cancel in a homogeneous magnetic field. Thus, the corresponding terms vanish from Eq. (1.18). The plasma density and the potential are often assumed to be functions of magnetic flux surfaces. Indeed, perturbations n_1 and φ_1 contribute slightly to the particle balance equation (1.18). The constraint on the validity of this assumption is

$$|V_0| \ll \Theta C_S, \qquad C_S = \sqrt{2T_i/m_i}. \tag{1.19}$$

The values n_1/n_0 and $e\varphi_1/T_e$ are computed for the plateau regime in the next section. These are

$$\frac{e\varphi_1}{T_e} = \frac{n_1}{n_0} \sim \frac{\varepsilon\rho_{ci}}{\Theta L}. \tag{1.20}$$

Note that in the banana and Pfirsch–Schlüter regime perturbations are even smaller than in Eq. (1.20). However, perturbations attain large values of order ε, provided the plasma is rotating rapidly either toroidally or poloidally. Hence, perturbations $e\varphi_1/T_e$ and n_1/n_0 contribute significantly to Eq. (1.18). In contrast, when Eq. (1.19) is fulfilled, the first and second terms in (1.18) may be neglected. Moreover, the inertia and the viscosity may be neglected as well. Integrating Eq. (1.18) and employing these assumptions, one obtains

$$u_{j\phi} = \bar{u}_\phi(1 - \varepsilon\cos\theta) - \frac{2\varepsilon}{\Theta}(V_0 + u_{pj})\cos\theta. \tag{1.21}$$

Note that the poloidally dependent second term in Eq. (1.21) attains large values of order $V_\theta(\varepsilon/\Theta)$ even when toroidal rotation averaged over the flux surface is absent. This flow, which is often called the "Pfirsch–Schlüter current," stems from the varying poloidal rotation within a flux surface due to inhomogeneity of the magnetic field and provides for the divergence-free constraint on the flow pattern. The pattern is shown in Fig. 1.2 for the negative electric field directed inwards and $|V_0| > |u_{pi}|$.

Equation (1.21) yields the well-known expression for the Pfirsch–Schlüter current [1]

$$j_\phi = en(u_{i\phi} - u_{e\phi}) = -\frac{2qc}{B_0}\frac{dp}{dr}\cos\theta,$$

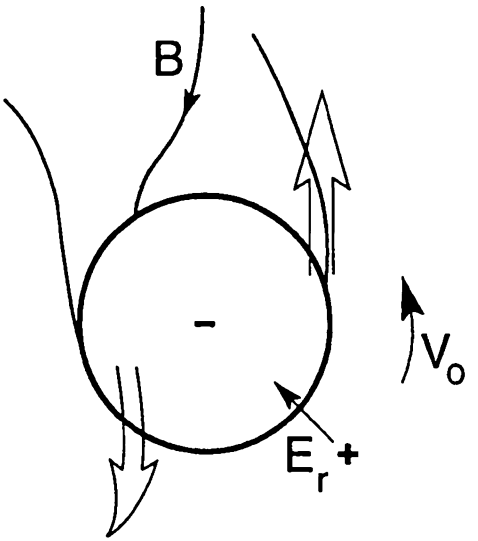

Fig. 1.2. Schematic view of the Pfirsch–Schlüter fluxes for ions $E_r < 0$ and $|u_{pi}| < |V_0| < \Theta C_S$.

where $q = \varepsilon/\Theta$ is the safety factor and $p = p_e + p_i$ is the total pressure. Here and subsequently a value of u_ϕ with accuracy to order ε^2 will be required. However, there is no need to solve Eq. (1.18) to the order of ε^2. It is sufficient to add terms of the order ε^2 to Eq. (1.21) to provide for the validity of Eq. (1.13) to the order ε^2. Hence, for ions

$$u_{i\phi} = \bar{u}_\phi(1 - \varepsilon\cos\theta) - 2qV_\theta\cos\theta + 2\varepsilon qV_\theta - 1.5\bar{u}_\phi\varepsilon^2. \quad (1.22)$$

Terms proportional to $\varepsilon^2\cos 2\theta$ and $\varepsilon^2\sin 2\theta$ are ignored because they cancel upon averaging. In conclusion, the important second term in Eqs. (1.21)–(1.22) stems from the plasma rotation in the inhomogeneous magnetic field. The field is weaker at the outer half and therefore the velocity $(V_0 + u_{pi})$ is faster. This results in a parallel flow from the outer to the inner half where the velocity is of the order of the toroidal rotation.

1.2. Flux surface average momentum balance

We start from the momentum balance equation for plasma

$$nm_i\frac{d\mathbf{u}_i}{dt} = \frac{1}{c}(\mathbf{j}\times\mathbf{B}) - \nabla\cdot\overleftrightarrow{\pi}_i - \nabla(p_e + p_i) + \mathbf{F}. \tag{1.23}$$

Assuming for the moment that $\mathbf{F} = 0$, taking the scalar product of Eq. (1.23) with the magnetic field $\mathbf{B}$ and performing the averaging over magnetic flux surfaces, we obtain the parallel component of the momentum balance:

$$\langle\mathbf{B}\cdot nm_i\frac{d\mathbf{u}_i}{dt}\rangle = -\langle\mathbf{B}\cdot\nabla\cdot\overleftrightarrow{\pi}_i\rangle^{(\mathrm{NEO})} - \langle\mathbf{B}\cdot\nabla\cdot\overleftrightarrow{\pi}_i\rangle^{(\mathrm{AN})}. \tag{1.24}$$

The viscous term is considered to originate from both the neoclassical viscous stress tensor and the shear anomalous viscosity. Since the pressure is only a function of the poloidal angle θ,

$$\langle\mathbf{B}\cdot\nabla p\rangle = \langle B_\theta\frac{\partial p}{\partial\theta}\rangle = \Theta\frac{B_0}{2\pi}\int\frac{\partial p}{\partial\theta}d\theta = 0.$$

On the other hand, although the parallel and the toroidal projections almost coincide, an important difference remains owing to the radial current. The radial current vanishes in Eq. (1.24), but the toroidal ϕ component of the flux average momentum balance yields the flux surface average radial current density

$$\langle j\rangle = \frac{c}{\Theta}\left(\langle n_i m_i\frac{\mathbf{B}_\phi}{B^2}\cdot\frac{d\mathbf{u}_i}{dt}\rangle + \langle\frac{\mathbf{B}_\phi}{B^2}\cdot\nabla\cdot\overleftrightarrow{\pi}_i\rangle^{(\mathrm{NEO})} + \langle\frac{\mathbf{B}_\phi}{B^2}\cdot\nabla\cdot\overleftrightarrow{\pi}_i\rangle^{(\mathrm{AN})}\right). \tag{1.25}$$

Equations (1.24)–(1.25) provide the velocities of the poloidal and toroidal rotations as a function of the radial current. In the steady state, the parallel momentum balance Eq. (1.24) yields, ignoring anomalous terms,

$$\langle\mathbf{B}\cdot\nabla\cdot\overleftrightarrow{\pi}_i\rangle^{(\mathrm{NEO})} = 0. \tag{1.26}$$

Equation (1.26) determines the velocity of the poloidal rotation [3, 10]. We assume that the neoclassical viscosity is determined

to the first order in $\rho_{c_i}/\Theta L$ by parallel viscosity, which has the Chew–Goldberger–Low form [59]

$$\overleftrightarrow{\pi}_i^{(\mathrm{NEO})} = \left(p_{i\|} - p_{i\perp}\right)\left(\mathbf{b}\cdot\mathbf{b} - \overleftrightarrow{I}/3\right), \tag{1.27}$$

where $p_{i\|}$ and $p_{i\perp}$ are the parallel and the perpendicular pressure, $\mathbf{b} = \mathbf{B}/B$, and $\overleftrightarrow{I}$ is the unit tensor. We employ the divergence of a symmetric tensor [60]

$$(\nabla\cdot\overleftrightarrow{\pi}_i)l = \frac{1}{\sqrt{|g|}}\frac{\partial(\sqrt{|g|}\pi_{il}^k)}{\partial x^k} - \frac{1}{2}\frac{\partial g_{km}}{\partial x^l}\pi_i^{km}, \tag{1.28}$$

where g_{km} is the metric tensor defined by $g_{11} = 1$, $g_{22} = r^2$, $g_{33} = (1+\varepsilon\cos\theta)^2$. Accounting for $(p_{\|} - p_{\perp})$ being a function only of θ and $\mathbf{B}_\phi = \mathbf{B}_\phi\cdot\mathbf{e}_\phi/\sqrt{|g|}$, where $\mathbf{e}_\phi$ is the contravariant basic vector, we obtain

$$\langle\mathbf{B}\cdot\nabla\cdot\overleftrightarrow{\pi}_i\rangle^{(\mathrm{NEO})} = -\langle\sin\theta(p_{i\|} - p_{i\perp})\rangle\Theta B_0/R, \tag{1.29}$$

where

$$\langle\mathbf{B}_\phi\cdot\nabla\cdot\overleftrightarrow{\pi}_i\rangle^{(\mathrm{NEO})} = -2\langle\mathbf{B}_\theta\cdot\nabla\cdot\overleftrightarrow{\pi}_i\rangle^{(\mathrm{NEO})}$$

and

$$\langle\mathbf{B}\cdot\nabla\cdot\overleftrightarrow{\pi}_i\rangle^{(\mathrm{NEO})} = -\langle\mathbf{B}_\theta\cdot\nabla\cdot\overleftrightarrow{\pi}_i\rangle^{(\mathrm{NEO})}.$$

The kinetic equation yields the parallel and perpendicular pressure. This is shown in the next section for the plateau regime. The resulting $\langle\mathbf{B}\cdot\nabla\cdot\overleftrightarrow{\pi}_i\rangle^{(\mathrm{NEO})}$ appears to be a function of the velocity of the poloidal rotation. Therefore the balance (1.26) yields the velocity of the poloidal rotation. The velocities of the poloidal rotation for regimes with different collisionalities are given by

$$V_\theta = \frac{c}{eB_0}k\frac{dT_i}{dr}, \tag{1.30}$$

where $k = 1.17$ for the banana, -0.5 for the plateau, and -2.1 for the Pfirsch–Schlüter regimes, respectively. The following approximate formula may be employed for k [2]:

$$k = \frac{1.17 - 0.35\nu_{i*}^{1/2} - 2.1\nu_{i*}^2\varepsilon^2}{1 + 0.7\nu_{i*}^{1/2} + \nu_{i*}^2\varepsilon^3}, \tag{1.31}$$

where $\nu_{i*} = \nu_i q R \varepsilon^{-3/2}/(2T_i/m_i)^{1/2}$. The term in Eq. (1.15) due to neoclassical viscosity may be recast to yield, using Eqs. (1.27)–(1.28),

$$\langle \mathbf{B}_\phi / B^2 \nabla \cdot \overleftrightarrow{\pi}_i \rangle^{(\mathrm{NEO})} = 0. \tag{1.32}$$

Note that here the neoclassical viscosity is averaged with a different weight than in Eq. (1.26). Therefore the flux-surface average viscosity cancels for an arbitrary poloidal rotation. Equation (1.32) implies that the parallel viscosity cannot affect the momentum transport toroidally. Indeed, Eq. (1.23) yields

$$n m_i du_{i\phi}/dt = \langle j \rangle \Theta B_0/c - B_0 \langle \mathbf{B}_\phi / B^2 \nabla \cdot \overleftrightarrow{\pi}_i \rangle^{(\mathrm{NEO})}.$$

Hence, Eq. (1.32) implies that the toroidal rotation may result only from the Lorenz force due to a radial current. Therefore, in a steady state the radial current has to cancel:

$$\langle j \rangle^{(\mathrm{NEO})} = 0. \tag{1.33}$$

Thence it is impossible to drive a radial current in a steady-state according to standard neoclassical theory. This fundamental prediction of standard neoclassical theory contradicts the experimental measurements, which clearly show a substantial radial current being excited by biasing an external electrode [48–51]. Therefore, in order to reconcile experimental results with neoclassical theory, the incorporation of novel terms stemming from plasma turbulence appears to be necessary. Furthermore, it can be asserted that these terms should maintain their importance in determining the L–H transition in general also when $\langle j \rangle = 0$. The anomalous viscosity and inertia are taken as a function of the parallel fluid velocity $u_{i\|}$:

$$F_i^{(\mathrm{AN})} = m_i n u_r^{(\mathrm{A})} du_{i\|}/dr,$$

$$\nabla \cdot \overleftrightarrow{\pi}_i^{(\mathrm{AN})} = -\frac{1}{r}\frac{d}{dr}\left(r\eta \frac{du_{i\|}}{dr} \right), \tag{1.34}$$

where η is the anomalous viscosity coefficient which may be evaluated as $\eta \sim D m_i n$. The existing models for the anomalous

viscosity [63, 64] also contain the parameter $m_e/(m_i\beta)$, where $\beta = 8\pi n(T_e + T_i)/B^2$, usually of the order unity. The flow velocity $u_{i\|}$ includes, besides the average toroidal motion $\bar{u}_\phi$, the harmonic toroidal flow, which is necessarily associated with the poloidal rotation. Anomalous viscosity and inertia affect differently the parallel and the toroidal balances. Employing Eq. (1.22) and $u_{i\|} = u_{i\phi} + \Theta u_\theta$ in Eq. (1.24), one obtains for slow rotations, when perturbations of density are small, $n_1/n \ll \varepsilon$,

$$(1+2q^2)q^{-1}nm_i\Theta B_0 u r^{(\mathrm{A})}\frac{dqV_\theta}{dr} + nm_i B_0 u r^{(\mathrm{A})}\frac{d\bar{u}_\phi}{dr}$$
$$-(1+2q^2)q^{-1}\Theta B_0\frac{d}{rdr}\left(r\eta\frac{dqV_\theta}{dr}\right) - B_0\frac{d}{rdr}\left(r\eta\frac{d\bar{u}_\phi}{dr}\right)$$
$$= -\langle \mathbf{B}\cdot\nabla\cdot\overleftrightarrow{\pi}_i\rangle^{(\mathrm{NEO})}. \qquad (1.35)$$

Hence, the parallel balance combines forces due to the radial transport of the average toroidal momentum with $\bar{u}_\phi$ and forces proportional to the derivatives of the poloidal rotation velocity resulting from the parallel Pfirsch–Schlüter component for ions. Equations (1.25) and (1.22) yield

$$\langle j\rangle = \frac{cnm_i}{\Theta B_0} u r^{(\mathrm{A})}\frac{d\bar{u}_\phi}{dr} - \frac{c}{\Theta B_0 r}\frac{d}{dr}\left(rh\frac{d\bar{u}_\phi}{dr}\right). \qquad (1.36)$$

Equations similar to Eqs. (1.35)–(1.36) were discussed in [40] if $\langle j\rangle = 0$. In addition to this analysis, the authors invoked poloidally asymmetric radial fluxes, which may exist within the plasma edge. Obviously, effects emerging due to the asymmetry can be incorporated into Eqs. (1.35)–(1.36). However, in order to maintain self-consistency the resulting perturbations of density and flows have to be retained in the particle balance as well. Therefore, the analysis of the effect of the asymmetry has to be carried out more carefully. In Eq. (1.36), terms owing to the neoclassical perpendicular viscosity have been neglected, because they emerge in the higher order in $\rho_{ci}/(\Theta L)$. These terms may result in additional torque in the toroidal direction. The estimate of the effect of the neoclassical perpendicular viscosity is obtained as follows. Since the main contribution to the

radial transport results from particles with poloidal velocities $V_0 + \Theta V_{||} \to 0$, their radial momentum transfer causes primarily a toroidal torque. For simplicity, in the banana regime the rate of the radial transport of toroidal momentum is approximately given by

$$\sqrt{em_i n \frac{V_0}{\Theta}} \sqrt{\frac{\varepsilon \chi^{(\mathrm{NEO})}}{r^2}} \sim \varepsilon m_i n c T_i \frac{\chi_i^{(\mathrm{NEO})}}{(\Theta e B r^3)}, \tag{1.37}$$

where $\chi_i^{(\mathrm{NEO})}$ is the ion neoclassical heat conductivity. Here the fraction of banana particles $\sim \sqrt{\varepsilon}$ and the value of V_0 has been taken into account. The exact expression has been obtained in [65, 66] in the banana regime and in [62] in the Pfirsch–Schlüter regime. Accounting for the neoclassical perpendicular viscosity, Eq. (1.36) takes the form

$$\langle j \rangle = \frac{cnm_i}{\Theta B_0} u_r^{(\mathrm{A})} \frac{d\bar{u}_\phi}{dr} - \frac{c}{\Theta B_0 r} \frac{d}{dr} \left[r \left(h + 0.1 q^2 \rho_{ci}^2 \nu_i n m_i \right) \frac{d\bar{u}_\phi}{dr} \right]$$
$$-0.35 \frac{cm_i}{\Theta B_0 r} \frac{d}{dr} \left[\frac{cnq^2 \rho_{ci}^2 \nu_i}{e \Theta B_0} \frac{d \left(\frac{r dT_i}{\sqrt{\varepsilon} dr} \right)}{dr} \right]. \tag{1.38}$$

Since $\eta/(nm_i) \sim D \gg q^2 \rho_{ci}^2 \nu_i$, the neoclassical perpendicular viscosity in the second term on the right-hand side of Eq. (1.38) can be neglected. The third term on the right-hand side of Eq. (1.38) provides the steady state of toroidal rotation when $\langle j \rangle = 0$. It yields the following estimate for the velocity of toroidal rotation $\bar{u}_\phi$:

$$\bar{u}_\phi \frac{cT_i}{(eBr\Theta)} \left[\frac{\varepsilon \chi_i^{(\mathrm{NEO})}}{D} \right] \sim \frac{V_\theta}{\Theta} \frac{\varepsilon \chi_i^{(\mathrm{NEO})}}{D}. \tag{1.39}$$

Hence, since in reality $\chi_i^{(\mathrm{NEO})} \ll D$, we have

$$\bar{u}_\phi \ll |V_\theta|/\Theta. \tag{1.40}$$

Thus, the velocity of toroidal rotation is bound to remain fairly small with accuracy of the order (1.40) unless an unbalanced

neutral beam or a radial current are injected in the tokamak. Therefore, the contribution of the toroidal rotation in Eq. (1.12) is small, and the poloidal rotation results from the electric and diamagnetic drifts. Hence, Eq. (1.36) is warranted with accuracy to the order of the validity of Eq. (1.39), and Eq. (1.39) yields $\bar{u}_\phi = 0$ when $\langle j \rangle = 0$. Terms owing to the neoclassical perpendicular viscosity can be added to Eq. (1.35), but they contribute only slightly to the order of small $\chi_i^{(\mathrm{NEO})}/(\varepsilon D)$. This conclusion is also maintained in Pfirsch–Schlüter and plateau regimes. We conclude that toroidal rotation may be neglected in Eq. (1.35) when $\langle j \rangle = 0$. Employing the neoclassical parallel viscosity, the terms in Eq. (1.35) are evaluated as follows. Terms owing to anomalous inertia and viscosity may be neglected compared to the neoclassical viscosity, provided the typical length scale of the poloidal rotation is of the order of minor radius r. If this is the case, $V_\theta \approx V_\theta^{(\mathrm{NEO})}$ results from Eq. (1.35) and is given by (1.30). However, steep profiles of V_θ emerge as well and are presented in Section 4. The system (1.35)–(1.36) has to be supplemented by the condition

$$\frac{d\,(r\langle j \rangle)}{rdr} = 0\,; \quad \frac{\langle j \rangle}{r} = \mathrm{const}\,, \tag{1.41}$$

which closes the system and thereby determines the profiles of the rotations. It should be emphasized that the parallel anomalous viscosity is ignored in Eq. (1.35). However, its origin remains elusive and there are no indications, either experimental or theoretical, providing for an incorporation of the effect into the kinetic equation. Nevertheless, it may happen in the future that novel terms owing to anomalous parallel viscosity will alter the parallel balance resulting, at present, in $V_\theta \neq V_\theta^{(\mathrm{NEO})}$ for gradual profiles. Finally, the equation for the radial electric field reads, taking into account the neoclassical parallel viscosity,

$$Er^{(\mathrm{NEO})} = \frac{T_i}{e}\left[\frac{d\ln n}{dr} + (1-k)\frac{d\ln T_i}{dr}\right] < 0. \tag{1.42}$$

2. Drift kinetic equation

2.1. Distribution function in the plateau regime

The drift kinetic equation can be written in drift coordinates as [55]

$$\frac{\partial f_j}{\partial t} + \mathbf{V}_{cj} \cdot \nabla f_j + \dot{V}_{j\|} \frac{\partial f_i}{\partial V_{j\|}} + \dot{V}_{j\perp} \frac{\partial f_i}{\partial V_{j\perp}} = \mathrm{St}\, f_j, \qquad (2.1)$$

where $\mathbf{V}_{cj}$ is the guiding center velocity and $\dot{V}_{j\|}$, $\dot{V}_{j\perp}$ are the rates of change of the parallel and perpendicular velocities for ions and electrons $j = i$ and ε, respectively. They are given by

$$\begin{aligned}
\mathbf{V}_{cj} &= -\frac{cm_i \left(V_{i\perp}^2/2 + V_{i\|}^2\right) (\mathbf{e}_\theta \cos\theta + \mathbf{e}_r \sin\theta)}{eBR} \\
&\quad + \frac{c\,(\mathbf{B} \times \nabla\varphi)}{B^2} + V_{j\|}\mathbf{e}_\phi + u r^{(\mathrm{A})} \mathbf{e}_r, \\
\dot{V}_{j\|} &= -\frac{e_j \Theta}{m_j r} \frac{\partial \varphi}{\partial \theta} - \frac{V_{j\perp}^2 \Theta \varepsilon \sin\theta}{2r} + \frac{V_0 V_{j\|} \varepsilon \sin\theta}{r}, \\
\dot{V}_{j\perp} &= \frac{V_{j\|} V_{j\perp} \Theta \varepsilon \sin\theta}{2r} + \frac{V_0 V_{j\perp} \varepsilon \sin\theta}{2r},
\end{aligned}$$

where u_r is the velocity of anomalous transport and $V_0 = (c/B) \cdot d\varphi_0/dr$ is the rotation speed in the radial electric field. The plateau collisional regime is defined by $\varepsilon^{3/2} \ll qR/\lambda_{\mathrm{mfp}} \ll 1$, where $\lambda_{\mathrm{mfp}} = V_{Tj}/\nu_j$ is the mean free path. In this regime, transport is independent of the collision frequency. The equilibrium equation, Eq. (2.1), can now be solved to the first order in the inverse aspect ratio $\varepsilon = r/R$. The solution is sought in the form

$$f_j = f_{0j}(r) + f_{1j}(r,\theta), \quad \varphi = \varphi_0(r) + \varphi_1(r,\theta),$$

where f_{0j} is the angle-average distribution function, close to Maxwellian, and f_{1j}, $\varphi_1 \sim \exp(i\theta)$ are the first-order perturbations. The conventional approach in solving the kinetic equation in the plateau regime yields

$$f_{1j} = \left[\mathrm{P.V.}\left\{\frac{1}{V_0 + \Theta V_{j\|}}\right\} + \pi\delta\left(V_0 + \Theta V_{j\|}\right)\frac{\partial}{\partial\theta}\right] \hat{A}_j f_{0j},$$

$$\hat{A}_j = \left[\frac{e_j\varphi_1}{m_j}\left(\Theta\frac{\partial}{\partial V_{j\|}} + \frac{cm_j}{e_jB}\frac{\partial}{\partial r}\right) - \frac{cm_j}{e_jB}\left(\frac{V_{j\perp}^2}{2} + V_{j\|}^2\right)\right. \quad (2.2)$$
$$\left.\varepsilon\cos\theta\frac{\partial}{\partial r} - \frac{m_j}{T_j}\left(V_{j\|}\left(V_{j\|} - \bar{u}_\phi\right) + \frac{V^2 j\perp}{2}\right)\varepsilon\cos\theta V_0\right],$$

where P.V.$\{1/(V_0 + \Theta V_{j\|})\}$ is the principal value integral. We choose f_{0j} as the Maxwellian in the frame of reference of the center of mass shifted to $\bar{u}_\phi$:

$$f_{0j} = n_0\left(\frac{2\pi T_j}{m_j}\right)^{-3/2}\exp\left[-m\frac{j\left(V_{j\|} - \bar{u}_\phi\right)^2}{2T_j} - m\frac{V_{j\perp}^2}{2T_j}\right]. \quad (2.3)$$

The distribution function given by Eq. (2.2) provides all the macroscopic quantities listed in the previous section. The poloidal electric field and the density perturbation are obtained from the quasi-neutrality condition on the magnetic surface. To apply this constraint the electron and ion densities must be evaluated by integrating Eq. (2.2) over the velocity:

$$n_1 = \int f_{1e}d\mathbf{V}_e = \int f_{1i}d\mathbf{V}_i. \quad (2.4)$$

The following conditions are universally valid for electrons:

$$|V_0| \sim |V_\theta| \ll \Theta\left(\frac{2Te}{m_e}\right)^{1/2} \quad \text{and} \quad |\bar{u}_\phi| \ll \left(\frac{2T_e}{m_e}\right)^{1/2};$$

therefore, the first term in A_e contributes mostly to Eq. (2.2), and the density perturbation for electrons results in the Boltzmann distribution for electrons

$$n_1/n_0 = e\varphi_1/T_e. \quad (2.5)$$

However, the relations between V_0, ΘC_S, $\bar{u}_\phi$, and C_S vary significantly. Starting from slow poloidal and toroidal rotations

$$|V_0| \sim |V_\theta| \ll \Theta C_S \quad \text{and} \quad \bar{u}_\phi \ll C_S, \quad (2.6)$$

and employing Eq. (2.5) and integrating f_{1i} over velocity space, we obtain

$$\frac{n_1}{n_0} = \frac{e\varphi_1}{Te} = \frac{\sqrt{\pi} e m_i^{1/2} \sin\theta}{\sqrt{2} T_i^{1/2} \Theta (1 + T_e/T_i)} \left(V_\theta + V_\theta^{(\mathrm{NEO})} \right), \tag{2.7}$$

where

$$V_\theta^{(\mathrm{NEO})} = -\frac{c}{2eB_0} \frac{dT_i}{dr}. \tag{2.8}$$

Hence, the density and potential perturbations are small to the order given by Eq. (1.20). Moreover, integrating f_{1j} with the weight $V_{j\|}$, we obtain the parallel flow velocity:

$$u_{j\|}^{(1)} = \frac{2\pi}{n_0} \int f_{1j} V_{j\|} V_{j\perp} dV_{j\|} dV_{j\perp}. \tag{2.9}$$

The principal-value term contributes mostly to Eq. (2.9) when the rotations are slow, and therefore the Pfirsch–Schlüter expression is given by Eq. (1.21). Defining the pressures within the magnetic surface as

$$\begin{aligned} p_{i\|} &= 2\pi \int m_i V_{i\|}^2 V_{i\perp} f_i \, dV_{i\|} \, dV_{i\perp} \\ p_{i\perp} &= \pi \int m_i V_{i\perp}^3 f_i \, dV_{i\|} \, dV_{i\perp}, \end{aligned}$$

and employing Eqs. (1.29) and (2.6), we obtain the expression for parallel viscosity as

$$\langle \mathbf{B} \cdot \nabla \cdot \overleftrightarrow{\pi}_i \rangle^{(\mathrm{NEO})} = \sqrt{\frac{\pi}{2r}} n \varepsilon^2 m_i^{1/2} T_i^{1/2} B_0 \left(V_\theta - V_\theta^{(\mathrm{NEO})} \right). \tag{2.10}$$

Thus, the parallel viscosity cancels when $V_\theta = V_\theta^{(\mathrm{NEO})}$. Moreover, Eq. (2.10) may be obtained directly from the kinetic equation without employing fluid relations such as (1.29). As outlined in [1], the kinetic equation averaged over angles yields

$$\frac{\partial f_{0i}}{\partial t} = \mathrm{St}_{QL} (f_{0i}),$$

where

$$\mathrm{St}_{QL}(f_{0i}) = \left(\Theta\frac{\partial}{\partial V_{i\|}} + \frac{m_i c\partial}{eB\partial r}\right) \times \left[\frac{\pi\varepsilon^2 V_{i\perp}^4}{8r}\delta\left(V_0 + \Theta V_{i\|}\right)\left(\Theta\frac{\partial}{\partial V_{i\|}} + \frac{m_i c\partial}{eB\partial r}\right) f_{0i}\right].$$

Hence, the flux-surface average parallel viscosity is due to the quasi-linear collisional term:

$$\langle \mathbf{B}\cdot\nabla\cdot\overleftrightarrow{\pi}_i\rangle^{(\mathrm{NEO})} = -\int m_i V_{i\|}\mathrm{St}_{QL}d\mathbf{V}_i. \tag{2.11}$$

Equation (2.10) is again obtained by integrating Eq. (2.11). Furthermore, the parallel neoclassical viscosity also yields the neoclassical radial ion flux (current). In a steady state, ignoring anomalous terms, the ionic current $\langle j\rangle_l$ reads

$$\langle j\rangle_l^{\mathrm{NEO}} = e\langle 2\pi\int dV_{i\|}dV_{i\perp}V_{i\perp}\left(V_{ci}\right)_r\left(f_{0i}+f_{1i}\right)\rangle, \tag{2.12}$$

where

$$\left(V_{ci}\right)_r = -\frac{c\varepsilon m_i\left(V_{i\perp}^2/2 + V_{i\|}^2\right)\sin\theta}{eB_0R} - \frac{c}{eB_0}\frac{\partial\varphi_1}{r\partial\theta}$$

is the radial component of the guiding center velocity. Indeed, employing Eq. (2.2) in Eq. (2.12), we obtain

$$\langle j\rangle_l^{\mathrm{NEO}} = -\frac{c}{\Theta B_0^2}\langle \mathbf{B}\cdot\nabla\cdot\overleftrightarrow{\pi}_i\rangle^{(\mathrm{NEO})}. \tag{2.13}$$

Note that the contribution from the perturbation of the electric potential φ_1, appearing both in f_{1i} and $(V_{ci})_r$, cancels in expressions (2.13). Thus, the neoclassical parallel viscosity and the radial current vanish concomitantly, provided the small (smaller than the flux given by Eq. (2.13) by a factor $(m_e/m_i)^{1/2}$) ambipolar neoclassical flux caused by the friction force is neglected..

2.2 Regimes with fast poloidal rotation ($|V_\theta| \geq \Theta C_S$)

Regimes with fast poloidal rotation are defined by the following estimate:

$$|V_0| \geq \Theta C_S. \tag{2.14}$$

Unless external forces are absent, toroidal rotation remains small, $|\bar{u}_\phi| \ll C_S$.

Regimes characterized by fast poloidal rotation or, alternatively, a strong radial electric field, emerge in the H-regime [15] or may be artificially excited by applying a large voltage ($U \gg T_i/e$) by means of a biased electrode [48–51]. Under these circumstances, the poloidal perturbation of the plasma density increases to a value of the order of the inverse aspect ratio ε. This results in significant modifications of the standard neoclassical viscosity and the parallel flow velocity. The expressions for the anomalous inertia and viscosity, crucial for both the poloidal and toroidal rotation, will be shown to be more complicated than those obtained before. In order to compute perturbations of the density and the potential, the Boltzmann distribution for electrons is employed as given by Eq. (2.5). Integrating f_{1i} given by Eq. (2.2) over the velocity space and employing $\Theta C_S \gg |u_{pi}|$ in agreement with (1.8), we obtain [28]

$$n_1/n = n_c^* \cos\theta + n_s^{**} \sin\theta,$$

where

$$\begin{aligned}
n_c^* &= \left\{-2\varepsilon\left[\frac{2\alpha^2+1}{2\alpha}K(\alpha) - \alpha\right]\left[1 + \frac{T_e\,(1-K(\alpha))}{T_i}\right]\right. \\
&\quad \left. +\pi\varepsilon\alpha^2\left(2\alpha^2+1\right)\exp\left(-2\alpha^2\right)T_e/T_i\right\}\Delta^{-1}, \\
n_s^{**} &= \left\{\left[1 + \frac{T_e}{T_i}\,(1-K(\alpha))\right]\left(2\alpha^2+1\right)\right. \\
&\quad \left. +\frac{2T_e}{T_i}\left[\frac{(2\alpha^2+1)\,K(\alpha)}{2\alpha} - \alpha\right]\right\}\sqrt{\pi}\varepsilon\alpha\exp\left(-a^2\right)\Delta^{-1}, \\
\Delta &= \left[1 + \frac{T_e(1-K(\alpha))}{T_i}\right]^2 + \pi\alpha^2\exp\left(-2\alpha^2\right)\frac{T_e^2}{T_i^2},
\end{aligned} \tag{2.15}$$

where $\alpha = V_0/\Theta C_S$, $C_S = (2T_i/m_i)^{1/2}$, and

$$K(\alpha) = 2\alpha \exp\left(-\alpha^2\right) D(\alpha) = 2\alpha \exp(-\alpha^2) \int \exp(t^2) dt, \quad (2.16)$$

where the $K(\alpha)$ is related to the Dawson function $D(\alpha)$ and is easily expressed through the well-known plasma dispersion function

$$\begin{aligned} K(\alpha) &= \mathbf{e}\left[\alpha \mathrm{I}_0(-\alpha)\right], \\ I_n(\alpha) &= (\pi)^{-1/2} \int \frac{x^n \exp\left(-x^2\right)}{x - \alpha} dx. \end{aligned} \quad (2.17)$$

The asymptotic values of density given by Eqs. (2.15) tend to zero when $\alpha \to 0$. In other words, the only remaining contribution is of the higher order in $\varepsilon \sin\theta \rho_{ci}/(\Theta Q L)$ and is not taken into account owing to $\Theta C_S \gg |u_{pi}|$. If $\alpha \sim 1$ the poloidal variation of density grows so that we obtain $n_1/n \sim \varepsilon$. Focusing on large values of α and employing the asymptotics of the function $K(\alpha)$, which reads

$$K(\alpha \to \infty) = \left(1 + \frac{1}{2\alpha^2} + \frac{3}{4\alpha^4}\right), \quad (2.18)$$

we obtain

$$\frac{n_1(\theta)}{n_0} = -2\varepsilon \cos\theta \left[1 + \frac{1 + T_e/2T_i}{\alpha^2}\right] \quad \text{for} \quad |\alpha| \gg 1. \quad (2.19)$$

Thence if $|\alpha| \gg 1$ the poloidal variation of the plasma density is located mostly at the inner half of the tokamak. The harmonic component of the parallel hydrodynamic flow equation (2.2) to the first order in ε and to zero order in $\rho_{ci}/\Theta L$ is given by

$$u_{i\|}(1)(\theta) = -\frac{V_0}{\Theta}\left(2\varepsilon \cos\theta + \frac{n_1}{n}\right), \quad (2.20)$$

where $u_{i\|}^{(1)}$ is the poloidally varying flow velocity. Equation (2.20) may be easily obtained from the continuity equation (1.18). Neglecting in (1.18) small terms containing dn_0/dr and u_{pi} and

assuming the flux-surface average $\langle(1+\varepsilon\cos\theta)u_{i\|}\rangle$ to be smaller than V_0/Θ in agreement with experimental results, Eq. (2.20) unfolds. In summary, Eqs. (2.19)–(2.20) are highly nonlinear functions of α, and consequently V_0. When $|\alpha| \gg 1$, employing Eq. (2.19) in Eq. (2.20), we obtain

$$u_{i\|}(1)(\theta) = +\frac{2\varepsilon\cos\theta C_S^2\Theta}{V_0}(1+0.5T_e/T_i). \tag{2.21}$$

Hence, the parallel flow velocity decreases as V_0^{-1} when V_0 grows. On the other hand, the parallel flow velocity is given by the well-known Pfirsch–Schlüter formula for $a \to 0$ or $|V_0| \ll \Theta C_S$:

$$u_{i\|}(\theta) = -2\varepsilon V_\theta\cos\theta/\Theta \quad \text{if} \quad |\alpha| \ll 1,$$

where $V_\theta = V_0 + u_{pi}$ is the speed of poloidal rotation and $u_{pi} = c(eBn_0)^{-1}dp_i/dr$ is the diamagnetic drift velocity. Note that the expression for $u_{i\|}^{(1)}(\theta)$ has opposite signs in Eqs. (2.20)–(2.21) and is smaller in the case given by Eq. (1.40) than by Eq. (1.41). Moreover, the variation of density is of a higher order in $\rho_{ci}/\Theta r$ when $|V_0| \ll \Theta C_S$. The substantial density variation $n_1/n \sim \varepsilon$ arises due to the balance between the inertial force acting on ions, $F^{(\mathrm{IN})} = nr^{-1}m_iV_\theta\partial u_{i\|}/\partial\theta$, and the pressure. This results in the peaking of the density at the inner half of the tokamak. In addition, this effect gives rise to the substantial poloidal electric field in order to provide for quasi-neutrality in accordance with the Boltzmann distribution for ions Eq. (2.5). Thus the variation of density contributes much more significantly to the flux-surface average flows in the case of $|V_0| \gg \Theta C_S$ than for $|V_0| \ll \Theta C_S$.

The same issue of the fast poloidal rotation has been addressed in [22] by Hazeltine, Lee, and Rosenbluth, employing the fluid approach. Their model, however, resulted in insufficient accuracy due to neglected parallel viscosity. Therefore although an expression similar to Eq. (2.15) has been obtained, the poloidal variation of the density has been found to diverge because the denominator disappears when $\alpha = 1$. This singularity, resulting in fact from the incompleteness of the model (neglecting the parallel viscosity), has been interpreted as the emergence of the shocks in plasma density at the inner half of

a torus. It is important to emphasize that the kinetic approach described above yields an accurate account of the parallel viscosity. Therefore, the denominator in Eq. (2.15) remains always positive and shocks do not emerge. However, the substantial peaking of the density at the inner half is maintained. This is reminiscent of the MARFE phenomenon. Note that the kinetic model presented in this section is fully justified only in the plateau regime. Therefore, the conclusion about the lack of shocks may change, provided the impact of the parallel viscosity is reduced compared to the nonlinear inertia. This might be the case in the banana regime. Since the effect of parallel viscosity is reduced in the banana regime and thereby the justification for neglecting viscosity recovers its validity, shock solutions may get back in the banana regime [68]. However the plasma edge, where the analysis has its main bearing, is in the plateau regime for most if not all modern tokamaks. In the banana regime the parallel viscosity drops with increasing collision frequency, but the inertial force $F^{(\mathrm{IN})}$ is almost independent. Therefore, the emergence of shocks appears plausible in the banana regime in agreement with [22]. The relevant computations are given in [68]. Furthermore, both the toroidal and the parallel (which governs the poloidal rotation) components of the momentum balance are dramatically modified when compared with Eqs. (1.35)–(1.36), provided the poloidal rotation is sufficiently fast. The average toroidal momentum is defined as

$$\bar{n}\bar{u}_\phi = \langle n u_{i\phi} B_0 / B_\phi \rangle. \tag{2.22}$$

In order to maintain Eq. (2.22) consistent with the expression for parallel velocity, terms of the second order in ε have to be included:

$$n u_{i\phi} = (n_0 + n_1) u_{i\phi}^{(1)}(\theta) + n_0 u_{i\phi}^{(2)}(\theta) + \overline{n u}_\phi, \tag{2.23}$$

where $u_{i\phi}^{(2)} = -\langle (B_0/B_\phi)(n_0 + n_1) u_{i\phi}^{(1)} \rangle$. Therefore, employing Eqs. (2.22)–(2.23), we obtain the generalized Eq. (1.36) as

$$\langle j \rangle = \frac{c m_i}{\Theta B_0} u_r^{(\mathrm{A})} \langle n \frac{\partial \left(u_{i\|} B_0 / B_\phi \right)}{\partial r} \rangle$$

$$-\frac{c}{\Theta B_0 r}\frac{\partial}{\partial r}\left(r\langle\eta\frac{\partial\left(u_{i\|}B_0/B_\phi\right)}{\partial r}\rangle\right)+\frac{cm_iV_0}{\Theta B_0 r}\langle\left(\frac{B_0^2}{B_\phi^2}n\frac{\partial u_{i\|}}{\partial\theta}\right)\rangle. \quad (2.24)$$

The momentum balance equation parallel to $\mathbf{B}$ is given by

$$\langle nm_iu_r^{(A)}\frac{\partial u_{i\|}B_\phi}{\partial r}\rangle-\langle\frac{\partial}{r\partial r}\left(r\eta\frac{\partial u_{i\|}B_\phi}{\partial r}\right)\rangle$$
$$=-\langle\mathbf{B}\cdot\nabla\cdot\overleftrightarrow{\pi}_i\rangle^{(\mathrm{NEO})}-\frac{m_iB_0V_0}{r}\langle\frac{n\partial u_{i\|}}{\partial\theta}\rangle. \quad (2.25)$$

The nonlinear neoclassical inertia emerges on the r.h.s. of Eq. (2.25), accompanying the parallel viscosity. They are of the same order when $|\alpha|\geq 1$. In order to evaluate the right-hand side of Eq. (2.25), the integration of the distribution function f_{1i} in Eq. (2.2) has to be performed including terms proportional to $\sin\theta$ of a higher order in $\rho_{ci}/\Theta L\ll 1$ than in Eq. (2.4) because the main term given by Eq. (2.20), which is proportional to $\cos\theta$, cancels upon averaging. Thus the flux surface averages of the parallel viscous and inertial force yield

$$F(V_0)=\langle\mathbf{B}\cdot\nabla\cdot\overleftrightarrow{\pi}_i\rangle^{(\mathrm{NEO})}-\frac{B_0m_iV_0}{r}\langle n\frac{\partial u_{\|i}}{\partial\theta}\rangle$$
$$+\frac{B_0m_iV_0}{r}\langle\frac{B_0^2}{B_\phi^2}n\frac{\partial u_{i\|}}{\partial\theta}\rangle, \quad (2.26)$$

which is to be used later. Taking into account

$$u_{i\|}(1)=u_{i\|}^{*}\cos\theta+u_{i\|}^{**}\sin\theta,$$

we obtain

$$\langle\left(B_0^2/B_\phi^2\right)n\partial u_{i\|}^{(1)}/\partial\theta\rangle-\langle n\partial u_{i\|}^{(1)}/\partial\theta\rangle=\varepsilon n_0u_{i\|}^{**}. \quad (2.27)$$

From Eqs. (2.26)–(2.27) and the expression for the parallel viscosity (1.29) we get the following relation between the function $F(\alpha)\cong F(V_0)$ and the ionic current with small poloidal velocities:

$$\langle j\rangle_l=\frac{cF(V_0)}{\Theta B_0^2}. \quad (2.28)$$

Equation (2.28) results from performing the integration given by (2.12) over the resonant part of f_{1i}, which is proportional to $\delta(V_0 + \Theta V_{i\|})$, hence from taking $V_0 = -\Theta V_{i\|}$. Performing the integration in Eq. (2.26) or in (1.29) we obtain

$$F(\alpha) = -\sqrt{\pi} n_0 T_i \varepsilon^2 \Theta B_0 \alpha (2\alpha^4 + 2\alpha^2 + 1) \exp\left(-\alpha^2\right)/r. \quad (2.29)$$

Equation (2.29) constitutes the generalized nonlinear parallel viscosity if $|V_0|$ is not much smaller than $O(\Theta C_S)$. The linear parallel viscosity, valid when $|V_0| \ll \Theta C_S$, was given in Section 1.1 by Eq. (2.10). The reason for the nonlinearity of the viscosity may be understood as follows. Trapped particles, characterized by small poloidal velocities $(V_0 + \Theta V_{i\|})$, contribute mostly to the parallel viscosity and inertia. When the poloidal rotation velocity V_0 increases, the parallel ion velocity for trapped particles is forced to grow in the opposite direction for trapped particles in order to balance the rotation. When $|\alpha| \geq 1$ the parallel velocity of trapped ions has to exceed their thermal speed V_{Ti}. Therefore the number of trapped particles decreases exponentially according to the Maxwellian distribution. This results in the "Maxwellian tail decrease" of the $F_i(\alpha)$ for $|\alpha| \to +\infty$. However, the nonlinear viscosity is damped significantly when $\alpha \gg 1$. Therefore, the contribution of nonresonant particles may become important and the Landau representation of the resonant denominator by $d(V_0 + \Theta V_{i\|})$ may have insufficient accuracy. As a result, the exponential decay changes to an algebraic decay. This calculation has been carried out in [69] for $\alpha \geq 1$, ignoring poloidal inertia and compressibility. A result similar to Eq. (2.29) has been obtained. The difference appears only in the algebraic decay instead of the exponential decay for $|\alpha| \gg 1$. However, this difference has only academic value because, in reality, the terms in (2.24)–(2.25), owing to turbulence, are important already when $\alpha \approx 1$. The particle flux given by Eq. (2.29) is $(m_i/m_e)^{1/2}$ times larger for ions than for electrons, regardless of the value of $\alpha = V_0/\Theta C_S$. Therefore, the ambipolarity requires $F(\alpha) \approx 0$ and Eq. (2.29) yields $V_0 \approx 0$. However, it is important to keep in mind that Eq. (2.29) has been derived under the assumption that $u_{pi} \ll \Theta C_s$. Thus,

more accurately the relation $V_0 = O(\Theta C_S)$ has been obtained. Accounting for the higher-order terms in $u_{pi}/\Theta C_S$ (this procedure corresponds to the next order expansion in the parameter $\rho_i/\Theta r$), the well-known expression from the neoclassical theory (see Eq. (1.30)) for the poloidal rotation velocity is obtained.

2.3. Regimes with fast toroidal rotation

The regimes with fast toroidal rotation velocities up to $\bar{u}_\phi \approx C_S$ emerge during an unbalanced neutral beam injection [7–9]. This rotation results in large perturbations of density and electric potential within a magnetic surface of order ε similar to the case of fast poloidal rotation. The inertia force along a major radius causes a redistribution of density due to a toroidal rotation $\mathbf{F}^{(\mathrm{IN})} = nm_i\bar{u}_\phi^2\mathbf{R}/R^2$.

It is counteracted by a poloidal pressure gradient, resulting in an excess of ions at the outer half, which brings about an electric field to provide for the quasineutrality within the magnetic surface. It has been shown in [23–26] that the velocity of the poloidal rotation maintains its neoclassical value for the case of fast toroidal rotation. Only the coefficient k in Eq. (1.30) is modified. Thus, the radial momentum balance (1.11) yields the growth of V_0 due to the increase in the radial electric field. The focus is on the fast toroidal rotation determined by

$$\Theta|\bar{u}_\phi| \gg \left|\frac{c}{eB_0 n}\frac{dp_i}{dr}\right| \approx |V_\theta|\,. \tag{2.30}$$

This results in Eq. (1.12) taking the form

$$V_0/\Theta \approx -\bar{u}_\phi. \tag{2.31}$$

Thence, the parallel momentum yields the perturbation of the density from the balance between the inertia and the pressure gradient, reading

$$-\frac{nm_i\bar{u}_\phi^2\Theta}{R}\sin\theta + \frac{nm_iV_p}{r}\frac{\partial u_{i\phi}}{\partial\theta} = -\Theta\,(T_e + T_i)\,\frac{\partial n_1}{r\partial\theta}, \tag{2.32}$$

where the perturbation of temperature has been ignored. The parallel viscosity has been neglected in (2.34), because it is small compared to inertia by the factor $V_\theta/(\Theta\bar{u}_\phi)$. Neglecting for the same reason the second term in Eq. (2.32), one obtains

$$\frac{n_1}{n_0} = \varepsilon\beta\cos\theta \quad \text{and} \quad \beta = \frac{mi\bar{u}_\phi^2}{T_e + T_i}. \tag{2.33}$$

The Boltzmann distribution of electrons with the potential φ_1 implies

$$\frac{e\varphi_1}{T_e} = \frac{n_1}{n_0} = \varepsilon\beta\cos\theta. \tag{2.34}$$

Thus, perturbations of density and potential are of the order ε for $\beta \approx 1$ and peak at the outer half, in contrast to fast poloidal rotation which peaks at the inner half. Employing the particle balance Eq. (1.18) and neglecting terms of order $|V_\theta|/|V_0|$, the fluid ion parallel velocity reads

$$u_{i\|}^{(1)}(\theta) = -\frac{2e}{\Theta}V_0\cos\theta - \frac{V_0}{\Theta}\frac{n_1}{n_0} - \varepsilon\bar{u}_\phi\cos\theta. \tag{2.35}$$

This relation is a generalization of Eq. (2.20). Employing the rotation velocity in the radial electric field determined by (2.31), we obtain

$$u_{i\|}^{(1)}(\theta) = (1+\beta)\varepsilon\bar{u}_\phi\cos\theta. \tag{2.36}$$

Note that the parallel velocity is the same for both electrons and ions with the accuracy employed here. The small difference between them provides for the Pfirsch–Schlüter current. The poloidal dependence in (2.36) shows that the toroidal rotation is directed parallel to $\bar{u}_\phi$ at the outer half. This is in contrast to the slow toroidal rotation given by Eq. (1.21). The perturbations of density and parallel velocity were obtained from the momentum balance and therefore are warranted for all collisionalities. Furthermore, Eqs. (2.33)–(2.36) can be obtained by the integration of the distribution function given by (2.2), as shown in [25]. Therefore, the assumptions employed above in order to neglect the temperature perturbation and the parallel viscosity are justified. The parallel and the toroidal momenta are modified

when an external toroidal force F is applied. The momentum balance equation parallel to $\mathbf{B}$ is given by

$$\langle nm_i u_r^{(A)} \frac{\partial \left(u_{i\|} B_\phi\right)}{\partial r} \rangle - \langle \frac{\partial}{r\partial r} \left[r\eta \frac{\partial \left(u_{i\|} B_\phi\right)}{\partial r} \right] \rangle$$

$$= B_0 F_\phi + \langle \frac{m_i n \bar{u}_\phi^2 \Theta B_\phi \sin\theta}{R} \rangle - \langle \mathbf{B} \cdot \nabla \cdot \overleftrightarrow{\pi}_i \rangle^{(NEO)}$$

$$- \frac{m_i B_\phi V_\phi}{r} \langle \frac{n \partial u_{i\|}}{\partial \theta} \rangle, \tag{2.37}$$

$$\langle j \rangle = \frac{cm_i}{\Theta B_0} u_r^{(A)} \langle n \frac{\partial \left(u_{i\|} \frac{B_0}{B_\phi}\right)}{\partial r} \rangle - \frac{c}{\Theta B_0 r} \frac{\partial}{\partial r} \left(r \langle \eta \frac{\partial \left(u_{i\|} \frac{B_0}{B_\phi}\right)}{\partial r} \rangle \right)$$

$$+ \frac{cm_i V_0}{\Theta B_0 r} \langle \left(\frac{B_0^2}{B_\phi} n \frac{\partial u_{i\|}}{\partial \theta} \right) \rangle - \frac{cF_\phi}{B_0 \Theta}. \tag{2.38}$$

Taking the sum and assuming $\langle j \rangle = 0$, we obtain

$$\langle nm_i u_r^{(A)} \frac{\partial \left(u_{i\|} B_\phi - u_{i\|} \frac{B_0^2}{B_\phi}\right)}{\partial r} \rangle - \langle \frac{\partial}{r\partial r} \left[r\eta \frac{\partial \left(u_{i\|} B_\phi - u_{i\|} \frac{B_0^2}{B_\phi}\right)}{\partial r} \right] \rangle$$

$$= -\langle \mathbf{B} \cdot \nabla \cdot \overleftrightarrow{\pi}_i \rangle^{(NEO)} + \langle \frac{m_i n \bar{u}_\phi^2 \Theta B_\phi \sin\theta}{R} \rangle$$

$$+ \langle \frac{m_i B_\phi V_\phi}{r} \left(\frac{B_0^2}{B_\phi^2} - 1 \right) \frac{n \partial u_{i\|}}{\partial \theta} \rangle. \tag{2.39}$$

The flux-surface average toroidal velocity cancels on the right-hand side of Eq. (2.39). Therefore, accounting for (2.23) and (2.33)–(2.34), we obtain

$$\langle n u_{i\|} B_\phi \rangle - \langle n u_{i\|} B_0^2 / B_\phi \rangle = \varepsilon (1 + \beta) \bar{u}_\phi.$$

Thus, the poloidal rotation velocity is determined by the constraint that the right-hand side of Eq. (2.39) be equal to zero, provided the anomalous terms on the left-hand side are small. This is true for the L regime of confinement. Then the constraint reads

$$F^*(V_\theta) = -\langle \mathbf{B} \cdot \nabla \cdot \overleftrightarrow{\pi}_i \rangle^{(NEO)} + \langle \frac{m_i n \bar{u}_\phi^2 \Theta B_\phi \sin\theta}{R} \rangle$$

$$+\langle\frac{m_i B_\phi V_\phi}{r}\left(\frac{B_0^2}{B_\phi^2}-1\right)\frac{n\partial u_{i\|}}{\partial\theta}\rangle=0. \tag{2.40}$$

Note that the first and second terms dominate on the right-hand side of Eq. (2.40). On the other hand, integrating the distribution function (2.2), we get

$$F^*(V_\theta)=\langle\int 2\pi V_{i\perp}\,dV_{i\|}\,dV_{i\perp}\left\{\frac{\varepsilon^2\sin^2\theta}{\omega_{ci}}\left(\frac{V_{i\perp}^2}{2}+\frac{V_0^2}{\Theta^2}\right)\right.$$
$$\times\pi\delta\left(V_0+\Theta V_{i\|}\right)\left[\frac{\partial}{\omega_{ci}\partial r}+\frac{m_i}{T_i}(V_0+\theta\bar{u}_\phi)\right]f_{0i}$$
$$\left.+\frac{(V_{i\perp}^2/2+V_0^2/\Theta^2)\sin\theta f_{1i}(\varphi_1)}{\omega_{ci}}-2\frac{c\partial\varphi_1}{rB_0\partial\theta}f_{1i}(\varphi_1)\right\}B_0\rangle=0,$$

where

$$f_{1i}(\varphi_1)=\left[\text{p.v.}\left(\frac{1}{V_0+\Theta V_{j\|}}\right)+\pi\delta\left(V_0+\Theta V_{i\|}\right)\right]$$
$$\times\frac{\partial}{\partial\theta}\left\{\frac{e\varphi_1}{m_i}\left(\Theta\frac{\partial}{\partial V_{i\|}}+\frac{m_i c\partial}{eB\partial r}\right)\right\}f_{0i}.$$

Hence, Eq. (2.41) yields the poloidal rotation velocity [22]

$$V_\theta^{(\text{NEO})}=k\frac{c}{eB}\frac{dT_i}{dr}, \tag{2.41}$$

$$k=\frac{-1+\beta+3\beta^2/2}{2+2\beta+\beta^2}. \tag{2.42}$$

The same result has been obtained in [23–26] for the isothermic plasma. In [24], the last term in Eq. (2.41) caused by the vertical drift due to the poloidal electric field has been ignored. This resulted in a slightly different coefficient k for $T_e\approx T_i$. The value of k for different regimes of collisionality has been computed in [26]. The function $F^*(V_\theta)$ yields the same expression for the current carried by ions with small poloidal velocities as for the case of fast poloidal rotation:

$$\langle j\rangle_1=\frac{cF^*(V_\theta)}{\Theta B_0^2}. \tag{2.43}$$

This relation can be verified by a direct comparison of Eq. (2.41) with Eq. (2.12). In summary, the increase in the velocity of toroidal rotation results from the external toroidal force until the growing anomalous viscosity and inertia balance this force. The emerging quasi-steady state leads to the large radial electric field and the resulting fast $\mathbf{E} \times \mathbf{B}$ drift. On the other hand, the poloidal rotation velocity remains unchanged in order of magnitude and is given by Eq. (2.42). In [70], the fast damping of the toroidal rotation has been suggested to result from the enhanced neoclassical perpendicular viscosity occurring due to the increase in the density perturbation up to the value of ε. The additional perpendicular inertia has been demonstrated in [70] to yield

$$\frac{c^2\varepsilon^2 m_i}{\Theta e B_0^2 r}\frac{\partial(\bar{u}_\phi n T_i)}{\partial r}.$$

In order for this term to have an impact, it must have the same order of magnitude as the perpendicular inertia in Eq. (2.45):

$$\frac{cm_i}{\Theta r}\langle\frac{V_\theta}{B_\phi}n\frac{\partial u_{i\|}}{\partial r}\rangle$$

because $\partial u_{i\|}/\partial\theta = -e(1+\beta)\bar{u}_\phi \sin\theta$.

However, the inertial term is much smaller in reality, reading

$$\frac{cm_i}{\Theta r}\frac{V_\theta}{B}\varepsilon^2\bar{u}_\phi(1+\beta)\beta\rho_{ci}/(\theta r).$$

The factor $\rho_{ci}/(\Theta r)$ results because the highest-order term of the product of n_1 and $u_{i\|}^{(1)}$ vanishes when averaged over a magnetic surface due to the dependence on the same function $\cos\theta$. Therefore, the higher-order terms in $\rho_{ci}/(\Theta r)$ turn out to be the largest ones. In [70], this fact was overlooked, and this resulted in a largely inaccurate value for the neoclassical perpendicular viscosity. The correct ratio of the neoclassical inertia or viscosity to the anomalous ones is

$$\varepsilon^2 V_\theta^{(\mathrm{NEO})}(1+\beta)\beta\rho_{ci}/(\Theta D),$$

where D is the anomalous diffusion coefficient. The ratio is always smaller than 1, even when $\bar{u}_\phi \approx C_S$. Therefore, in reality,

the toroidal momentum input is damped by anomalous inertia and viscosity. In contrast, the anomalous terms are small in the parallel momentum balance, in particular in comparison with $\langle nm_i u_\phi^2 \Theta B_\phi \sin\theta/R \rangle$.

Fast toroidal rotation is also found to modify the neoclassical transport coefficients. For example, employing Eq. (2.12), the neoclassical heat conductivity yields [23, 25]

$$\chi_{i\perp} = \chi_{i\perp}^{(\mathrm{NEO})} [1 + f(\beta)], \tag{2.44}$$

where

$$f(\beta) = \frac{\beta(4\beta^2 + 9\beta + 6)}{3(\beta^2 + 4\beta + 6)}$$

and $\chi_{i\perp}^{(\mathrm{NEO})}$ is the standard neoclassical heat conductivity in the plateau regime

$$\chi_{i\perp}^{(\mathrm{NEO})} = \frac{3(\pi/2)^{1/2}\varepsilon^2 c^2 m_i^{1/2} T_i^{1/2}}{\Theta r \varepsilon^2 B^2}. \tag{2.45}$$

3. The ontogeny of the poloidal and the toroidal rotations

3.1. Linear relaxation

Considering first the linear regime of relaxation of V_θ to $V_\theta^{(\mathrm{NEO})}$, it is assumed that $\Delta V_\theta \sim V_\theta \sim V_\theta^{(\mathrm{NEO})}$. Anomalous terms in the parallel momentum balance are not considered in this section. Substituting the parallel ion flow velocity, which is approximately equal to the toroidal velocity, and neglecting the rate of relaxation of $\bar{u}_\phi$, we obtain the results described below. The neoclassical flux surface averaged parallel momentum balance governs the evolution when $V_\theta \sim V_\theta^{(\mathrm{NEO})}$, showing that the parallel viscous force damps the poloidal flow to its neoclassical value according to the following equation [10]:

$$nm_i B_0 \Theta (1 + 2q^2) \frac{\partial V_\theta}{\partial t} = -\langle \mathbf{B} \cdot \nabla \overleftrightarrow{\pi}_{i\parallel} \rangle^{(\mathrm{NEO})}. \tag{3.1}$$

Since the parallel neoclassical viscosity is proportional to $V_\theta - V_\theta^{(\mathrm{NEO})}$ when $\Delta V_\theta \sim V_\theta^{(\mathrm{NEO})}$, Eq. (3.1) results in the exponential relaxation of V_θ to $V_\theta^{(\mathrm{NEO})}$ given by

$$V_\theta(t) = \left[V_\theta(0) - V_\theta^{(\mathrm{NEO})}\right] \exp\left(-t/\tau\right) + V_\theta^{(\mathrm{NEO})}. \tag{3.2}$$

Using in Eq. (3.1) the parallel viscosity for the plateau regime given by Eq. (2.10), we obtain

$$\tau = \frac{2q^2+1}{q^2}\left(\frac{2}{\pi}\right)^{1/2} qR\frac{m_i^{1/2}}{T_i^{1/2}}, \tag{3.3}$$

where τ is the typical relaxation time and $q = \varepsilon/\Theta$ is the safety factor. On the other hand, the relaxation of toroidal rotation is governed by anomalous processes, inertia and viscosity (see Eq. (1.36)). For $\langle j \rangle = 0$

$$nm_i\frac{\partial \bar{u}_\phi}{\partial t} = -n_i m_i u_r^{(\mathrm{A})}\frac{\partial \bar{u}_\phi}{\partial r} + \frac{1}{r}\frac{\partial}{\partial r}\left(r\eta\frac{\partial \bar{u}_\phi}{\partial r}\right). \tag{3.4}$$

Thus, the time scale for relaxation of $\bar{u}_\phi$ is determined by the anomalous diffusion across a tokamak and it is much longer than τ given by Eq. (3.3). On the other hand, the relaxation of the poloidal rotation velocity occurs primarily due to the radial electric field varying in time and the $\mathbf{E}\times\mathbf{B}$ drift resulting from it. The physical interpretation is as follows. The flux of ions with small poloidal velocities emerges when $V_\phi \partial V_\phi^{(\mathrm{NEO})}$. It is determined by Eq. (2.12) and is related to parallel viscosity by Eq. (2.13). Since the total flux has to cancel, the counter ion flux with thermal velocities is induced by the varying-in-time radial electric field. It reads

$$\begin{aligned}\langle j_h \rangle &= -\langle j_l \rangle = \frac{c}{\Theta B_0^2}\langle \mathbf{B}\cdot\nabla\cdot\overleftrightarrow{\pi}_i\rangle^{(\mathrm{NEO})} \\ &= -\frac{nm_i c}{B_0}\left(1+2q^2\right)\frac{\partial V_\theta}{\partial t} = \frac{nm_i c^2}{B_0^2}\left(1+2q^2\right)\frac{\partial Er}{\partial t}.\end{aligned} \tag{3.5}$$

The first term on the right-hand side of Eq. (3.5) arises due to the polarization drift in a varying-in-time electric field inside a

straight cylinder. The second term stems from the inertial force in a torus. Note that the stationary distribution function has been employed in deriving both the left- and right-hand side of Eq. (3.1). However, the nonstationary kinetic equation including $\partial f_i/\partial t$ is warranted in addressing nonstationary phenomena. An example of the solution of the general kinetic equation and the derivation of the macroscopic inertia and viscosity from it is described in Appendix 2. There expressions for inertia and viscosity are derived. They can be reduced to the simple ones derived from the quasi-stationary distribution function, provided $\tau \gg qR/C_S$. However, this constraint is not fulfilled during the linear relaxation presented above because $\tau \sim qR/C_S$ according to Eqs. (3.2)–(3.3). Therefore, in reality, Eqs. (3.2)–(3.3) are valid only in order of magnitude. Moreover, it is crucial to account for the nonstationary distribution function in the banana regime as shown in the next section. For completeness, the time scale of the linear relaxation in the Pfirsch–Schlüter regime accounting for the quasi-stationarity reads

$$\tau = 0.75\left(1+2q^2\right)\frac{m_i R^2 \nu_i}{T_i}, \quad \text{where} \quad \nu_i \gg \frac{T_i^{1/2}}{m_i^{1/2} qR}, \tag{3.6}$$

which is close to the one derived in [10, 71] (the slight difference in the numerical coefficient stems from the approximation employed in the parallel viscosity).

3.2. Distinctive features of the theory in the banana regime

Kinetic equation (3.1), employing the quasi-stationary parallel neoclassical viscosity, yields a solution for the damping time scale [10]

$$\tau = \frac{1.3\varepsilon^{3/2}\left(1+2q^2\right)}{q^2}\nu_i^{-1}.$$

However, this time scale is shorter than the collisional time scale for banana ions $\tau \sim \varepsilon\nu_i^{-1}$. Thus, the approach employing the quasi-stationary assumption does not provide an accurate value.

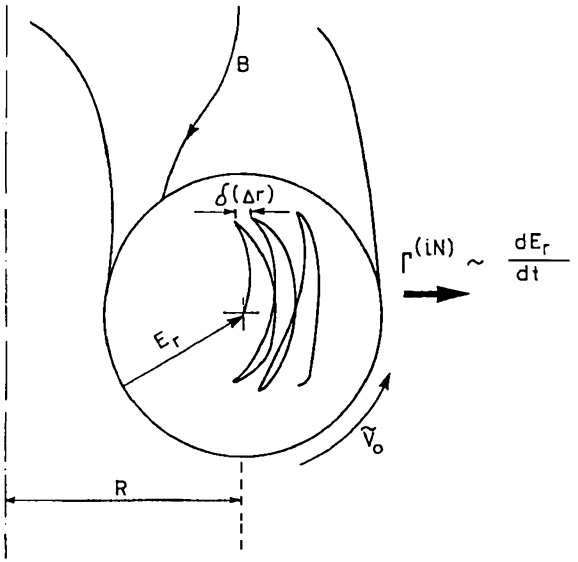

Fig. 3.1. Trajectories of banana particles in the temporal and spatial varying electric field.

The correct value of the relaxation time differs by an order of magnitude from this value and results in a significantly longer time scale [72, 73]. The physical reason for the discrepancy stems from a novel flux of trapped ions [74] and the parallel inertia resulting from it. In [73] this effect has been termed "the time-dependent viscosity." Here, for simplicity, "random walk" arguments are employed. The poloidal velocity $V_0 + \Theta V_{i\|}$ depends on time because the mean velocity of a trapped particle is different on the inner and outer halves of the banana trajectory. Therefore, the resulting trajectory becomes untrapped (see Fig. 3.1).

The resulting outward ion flux directed along a major radius is estimated as

$$\Gamma^{(IN)} = \sqrt{\epsilon} n \delta(\Delta r) \nu^b. \tag{3.7}$$

Here, $\sqrt{\epsilon}$ accounts for the fraction of trapped particles, $\nu^b = \Theta\langle V_{i\|}\rangle/r$ is the untrapped particle bounce frequency, Δr is the

banana width, and $\delta(\Delta r)$ is the variation of Δr during one bounce period. Employing

$$\Delta r = V^T r / \left(V_0 + \Theta\langle|V_{i\|}|\rangle\right), \tag{3.8}$$

where $V^T = cm_i V_\perp^2/2eBR$ is the toroidal drift velocity and

$$\delta(\Delta r) = (\delta\Delta r/dV_0)\,(\partial V_0/\partial t)\,(\nu\beta)^{-1}, \tag{3.9}$$

we obtain

$$\delta(\Delta r) = -V^T r \left(V_0 + \Theta\langle|V_{i\|}|\rangle\right)^{-2} \partial V_0/\partial t(\nu^b)^{(-1)}. \tag{3.10}$$

Using the mean values $\langle|V_{i\|}|\rangle \sim \sqrt{\varepsilon}C_S$, $V_{i\perp} \sim C_S$, Eqs. (3.7)–(3.10) yield for $|V_0| \ll \Theta C_S$

$$\langle j^{(\mathrm{IN})}\rangle = e\Gamma^{(\mathrm{IN})} \approx -\sqrt{\varepsilon} n c m_i \left(B\Theta^2\right)^{-1} \partial V_0/\partial t. \tag{3.11}$$

This effect is similar in nature to the well-known "Ware pinch" effect [1], occurring, however, due to a parallel electric field. Equation (3.11) yields an ion flux m_i/m_e times larger than the electron one. This flux corresponds to the term proportional to inertia in the flux surface average momentum balance in the same way as the flux of trapped particles given by Eq. (2.13) corresponds to neoclassical viscosity:

$$F^{(\mathrm{IN})} = B_0\Theta\langle j^{(\mathrm{IN})}\rangle/c. \tag{3.12}$$

This effect enhances significantly the inertia in the banana regime in comparison with the plateau and therefore must be included in Eq. (3.1) together with the first term there:

$$nm_i B_0\theta\left(1+2q^2\right)\frac{\partial V_\theta}{\partial t} + \frac{cnm_i\sqrt{\varepsilon}B_0}{\Theta}\frac{\partial V_\theta}{\partial t} = -\langle \mathbf{B}\cdot\nabla\cdot\overleftrightarrow{\pi}_i\rangle^{(\mathrm{NEO})}. \tag{3.13}$$

The numerical coefficient in front of the second term in Eq. (3.13) has been calculated in [73] and found to be of order 1. It is easy

to show that the additional inertia given by the second term in Eq. (3.13) is enhanced by a factor $\varepsilon^{-3/2}$ in comparison with the first term and therefore has the most significant effect in the banana regime. Employing the linearized neoclassical viscosity in the banana regime obtained along the lines of [1]

$$\langle \mathbf{B} \cdot \nabla \cdot \overleftrightarrow{\pi}_i \rangle^{(\mathrm{NEO})} = \frac{1.1\sqrt{\varepsilon} n_0 m_i \nu_i B_0}{\Theta} \left(V_\theta - V_\theta^{(\mathrm{NEO})} \right), \qquad (3.14)$$

the relaxation of $V_\theta(t)$ to $V_\theta^{(\mathrm{NEO})}$ follows Eq. (3.2) [72, 73] during the time τ,

$$\tau = \nu_i^{-1}. \qquad (3.15)$$

Expressing Eq. (3.13) in terms of currents driven by inertia caused by thermal ions $\langle j_h \rangle$, by banana particles $\langle j^{(\mathrm{IN})} \rangle$, and by viscosity $\langle j_l \rangle$ due to trapped particles, which depends on $V_\theta - V_\theta^{(\mathrm{NEO})}$, we obtain

$$\langle j_l \rangle = -\langle j_h \rangle - \langle j^{(\mathrm{IN})} \rangle.$$

3.3 Nonlinear effects resulting from fast rotations

Here, we consider the temporal evolution of the V_θ deviating significantly from $V_\theta^{(\mathrm{NEO})}$ when $\Delta V_\theta \geq \Theta C_S$. We presently ignore anomalous effects. The analysis is focused on the plateau regime. Hence, the evolution is determined by a system analogous to (2.24)-(2.25):

$$\langle n m_i \frac{\partial u_{i\phi} B_0}{\partial t B_\phi} \rangle = -\frac{\Theta B_0 \langle j \rangle}{c} - \frac{m_i V_\theta}{r} \langle \frac{B_0^2}{B_\phi 2} \frac{n \partial u_i \phi}{\partial \theta} \rangle, \qquad (3.16)$$

$$\langle B_\phi n m_i \frac{\partial u_{i\|}}{\partial r} \rangle = -\langle \mathbf{B} \cdot \nabla \cdot \overleftrightarrow{\pi}_i \rangle^{(\mathrm{NEO})} - \frac{m_i B_0 V_\theta}{r} \langle \frac{n \partial u_{i\|}}{\partial \theta} \rangle. \qquad (3.17)$$

In the absence of a radial current, subtracting Eq. (3.16) from (3.17), one obtains

$$F(V_0) = \langle B_\phi n m_i \partial u_{i\|} / \partial t \rangle - \langle (B_0 / B_\phi) n m_i \partial u_{i\phi} / \partial t \rangle, \qquad (3.18)$$

where $F(V_0)$ is determined by (2.26) and is given by (2.29). Substituting into Eq. (3.18) the toroidal rotation (2.23), one gets

$$F(\alpha) \cong F(V_0) = B_0 \Theta n m_i \partial V_\theta / \partial t - \frac{B_0}{2\pi} \int (1 + \varepsilon \cos\theta)^2 n_0 m_i \frac{\partial u_{\phi i}^{(1)}}{\partial t}. \quad (3.19)$$

The toroidal harmonic $u_{i\phi}^{(1)}$ in Eq. (3.19) is given by Eqs. (2.15), (2.20). Employing the Pfirsch–Schlüter velocity $u_{i\phi}^{(1)}$, one obtains, defining $\alpha = V_0/\Theta C_S$,

$$\frac{dA(\alpha)}{d\alpha} \frac{\partial \alpha}{\partial t} = F(\alpha), \quad (3.20)$$

where

$$A(\alpha) = 2 n_0 \varepsilon^2 C_S m_i B_0 \alpha \left[1 + \frac{1}{2q^2} + \frac{n_c^*}{2\varepsilon}\right] \quad (3.21)$$

and n_c^* has been defined by Eq. (2.15). Equations (3.20)–(3.21) govern the ontogeny of an arbitrary poloidal rotation. It is easily seen that if $\alpha \ll 1$, the third term in Eq. (3.21) is negligibly small, and

$$F(\alpha) \approx -\langle \mathbf{B} \cdot \nabla \cdot \overleftrightarrow{\pi}_{i\|} \rangle^{(\mathrm{NEO})},$$

then Eq. (3.20) is reduced to Eq. (3.1). On the contrary, for large deviations from the neoclassical steady state, $V_\theta \partial V_\theta^{(\mathrm{NEO})}$, when $|\alpha| \gg 1$, Eq. (3.20) is grossly nonlinear, and, thereby, an arbitrary poloidal rotation velocity might both decrease and increase ("rotational runaway") in time [28]. Hence, the poloidally varying density and parallel velocity undergo qualitative changes. The function $A(\alpha)$ is shown in Fig. 3.2.

If $\alpha \gg \alpha_2$, to be defined below, Eq. (3.20) takes the following form:

$$(2/\pi)^{1/2} (1 + T_e/2T_i) (qR/C_S) (d\alpha/dt) = -a^7 \exp\left(-\alpha^2\right), \quad (3.22)$$

which yields the slowly decaying poloidal rotation on the time scale estimated as

$$\tau = (2/\pi)^{1/2} \frac{qR}{C_S} \frac{\exp(\alpha^2)}{a^7}. \quad (3.23)$$

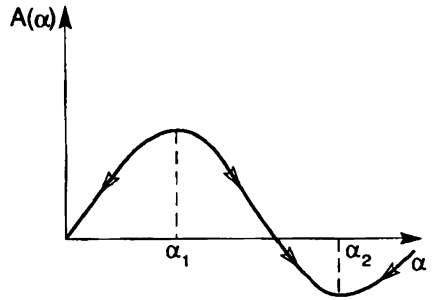

Fig. 3.2. The profile of the function $A(\alpha)$, governing the temporal evolution. The temporal evolution of an arbitrary poloidal rotational steady state is shown by arrows.

An arbitrary $\alpha < \alpha_2$ acquires the value α_2, determined by $dA/d\alpha = 0$. The relaxation occurs on a finite time scale. When $\alpha_1 < |\alpha| < \alpha_2$, the velocity of poloidal rotation increases to reach α_2 after a finite time scale. Only if $|\alpha| < \alpha_1$ does the velocity of poloidal rotation obtain its neoclassical value.

One interesting consequence emerges, focusing on the concomitant evolution of the toroidal rotation for arbitrary values of α, which is in contrast to the case of linear relaxation $\alpha \ll 1$ addressed in the previous section.

In the absence of radial current and unbalanced neutral beam injection, for $V_\theta \sim V_\theta^{(\mathrm{NEO})}$ the neoclassical parallel viscosity averaged over a magnetic surface with weight B_0/B_ϕ cancels and thereby does not affect toroidal rotation. In this nonlinear regime the parallel inertia averaged with weight B_0/B_ϕ contributes to the toroidal momentum balance equation (3.16). The left-hand side of Eq. (3.16) yields

$$\langle n m_i \frac{B_0}{B_\phi} \frac{u_{i\phi}}{\partial t} \rangle = m_i \frac{n \bar{u}_\phi}{\partial t} - m_i \langle u_{i\phi}^{(1)} \frac{dn^{(1)}}{dV_0} \frac{\partial V_0}{\partial t} \rangle .$$

Thus, the inertial force results in two terms. For example, if $|\alpha| \approx 1$, then $n^{(1)}/n_0 \sim \varepsilon$ and $u_{i\phi}^{(1)} \sim eV_0/\Theta$ and the toroidal momentum resulting on the time scale of relaxation given by

Eq. (3.23) yields

$$\bar{n}\bar{u}_\phi \sim n\varepsilon^2 V_0/\Theta.$$

However, when V_0 approaches the value V_{02}, corresponding to the minimum of $A(V_0)$, the derivative $\partial V_0/\partial t \to \infty$ and thereby forces $\partial n\bar{u}_\phi/\partial t \to \infty$. In other words, toroidal rotation increases to $\sim V_0/\Theta$ and contributes significantly to the velocity of the poloidal rotation. In summary, our approach yields an increase in poloidal rotation, i.e., "rotational runaway" when $\alpha_1 < \alpha < \alpha_2$. This effect may appear to result from the reduced parallel viscosity. Finally, it should be emphasized that only the neoclassical analysis has been offered in this section. The crucial effects of anomalous transport driven by turbulence, which actually determine the real rotational steady states, are addressed in the next section.

4. Fast poloidal rotation and L–H transitions

4.1. Suppression of turbulence by a shear of the poloidal rotation

It is well documented on many tokamaks that sometimes a transition may occur from a steady state characterized by a low level of confinement — termed the L-mode — to another steady state with significantly improved confinement (by approximately a factor of 2), defined as the H-mode. The reduction of transport occurs primarily at the edge of tokamak plasmas. The profiles of density and temperature are much steeper at the edge in the H-mode than in the L-mode. The amplitude of turbulent fluctuations is dramatically reduced during the transition. The velocity of poloidal rotation and the radial electric field grow very significantly during the transition [15–18]. The typical length scale of the electric field profile is of the order of 1 cm, as shown for a D–IIID tokamak in Fig. 4.1.

The transition from the L to the H regime can be triggered artificially either by injecting an electron beam into the periphery, by a minor radius compression of a tokamak, or by driving a current from a biased electrode immersed into a plasma inside a

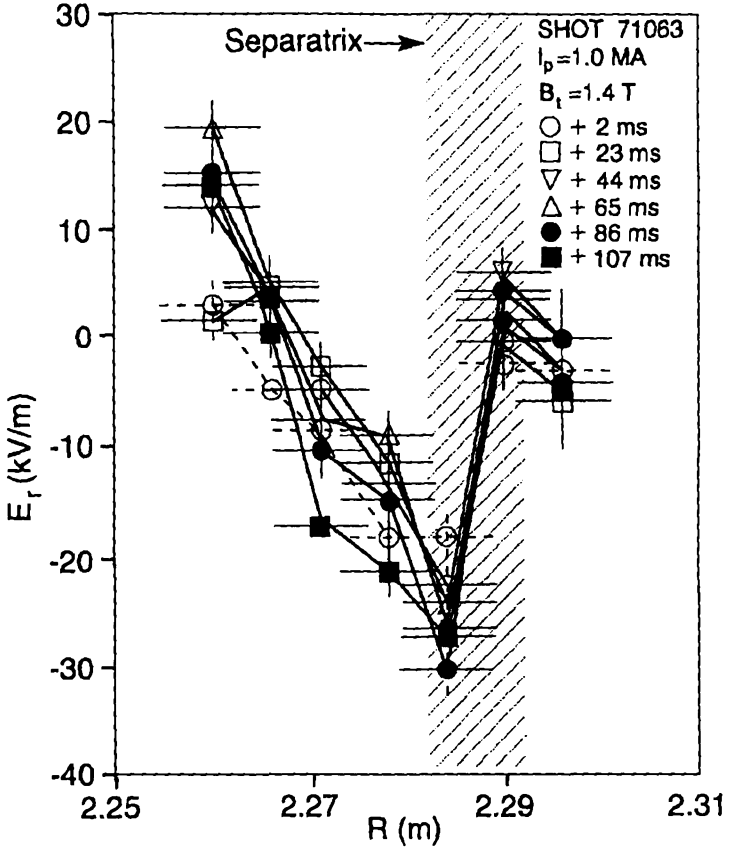

Fig. 4.1. The profile of the radial electric field as measured on D–IIID for the H-regime [66]; I_p = 1.0 MA and B_0 = 1.4 T.

separatrix [48–51]. Recently, the L–H transition has been shown to occur when triggered by short and powerful gas puff impulses [53, 76] or pellet injection of small pellets into the vicinity of the separatrix [77].

Data obtained on many tokamaks suggest that a growth in poloidal rotation is a fundamental feature of the L–H transition. The mechanism providing for improvement in confinement has been suggested to result from the suppression of turbulence by decorrelation of fluctuations due to a shear in the poloidal

rotation in [19]. It seems that this idea was first put forward implicitly in [78]. The physical explanation is as follows. In the absence of a significant rotation, the level of turbulence is determined by the balance between the increment of an instability and the damping rate causing anomalous diffusion. The damping time is then given by

$$\tau_t^{-1} = \omega_t = 4D/\delta_0^2, \tag{4.1}$$

where D is the coefficient of anomalous diffusion and δ_0 is the typical radial correlation length. It will be shown that the value of δ_0 is significantly reduced provided a significant shear in poloidal rotation is applied. A perturbation of any fluctuating parameter (this may be density, temperature, or potential) in a rotating plasma moves not only a distance δ_0 during ω_t^{-1}, but also k_θ^{-1} in the poloidal direction with respect to background fluctuations. Therefore, the radial correlation length δ is determined by

$$\left| -\frac{V_0}{r} + \frac{dV_0}{dr} \right| \delta k_\theta = 4\frac{D}{\delta^2}. \tag{4.2}$$

Note that the resulting fluctuations are smeared poloidally in a cylindrical geometry even in the absence of shear. However, effects owing to poloidal rotation are significant provided the shear length is smaller than approximately 1 cm. Hence, the first term on the left-hand of Eq. (4.2) can be neglected. Equation (4.2) yields for the radial correlation length

$$\delta = \left[4\frac{D}{k_\theta \left| dV_0/dr \right|} \right]^{1/3}. \tag{4.3}$$

The typical time scale resulting from the combined effect of rotation and diffusion is

$$\tau_c^{-1} = \omega_c = \left(4Dk_\theta^2 \right)^{1/2} \left(dV_0/dr \right)^{2/3}. \tag{4.4}$$

Introducing the frequency ω_s as

$$\omega_s = k_\theta \delta \left| \frac{dV_0}{dr} - \frac{V_0}{r} \right|,$$

Eq. (4.4) reads

$$\omega_c = \left(\omega_s^2 \omega_t\right)^{1/3}. \tag{4.5}$$

Note that the shear has a more significant effect in Eqs. (4.4)–(4.5) than the diffusion, and the typical time scale does not depend on the sign of dV_θ/dr. The constraint on the validity of Eqs. (4.4)–(4.5) follows from the condition $\delta < \delta_0$ and reads

$$\omega_s = k_\theta \delta \left| \frac{dV_0}{dr} - \frac{V_0}{r} \right|. \tag{4.6}$$

This condition implies the stringent constraint that the value of shear must be sufficiently large in order to affect the level of turbulence. If this is not fulfilled, the shear does not affect turbulence strongly and the damping time scale may be determined by Eq. (4.1). Yet, the nonlinear theory of Biglari et al. indicates that the given level of microturbulence is reduced even below the flow shear given by Eq. (4.6). The reduction depends crucially on the characteristics of the turbulence itself. The analysis is carried out in [19] along the lines of [79]. The equation governing the fluctuating parameter ξ reads

$$\left(\frac{\partial}{\partial t} + \left(V_0 + \tilde{V}\right) \times \nabla + \tilde{L}\right) \xi = S, \tag{4.7}$$

where $\tilde{V}$ is the fluctuating flow velocity, S is a free energy source, and $\hat{L}$ is an operator providing the free energy dissipation. Focusing on fluctuations extended along a magnetic field, the analysis is reduced to a two-point correlation function $\langle \xi(1)\xi(2) \rangle$, as shown in [63]:

$$\left[\frac{\partial}{\partial t} + \left(\frac{dV_0}{dr} - \frac{V_0}{r_+}\right) r_- \frac{\partial}{\partial y_-} - \frac{\partial}{\partial r_-} D \frac{\partial}{\partial r_-} + \hat{L}\right] \times \langle \xi(1)\xi(2) \rangle = \tilde{S}, \tag{4.8}$$

where 1 and 2 correspond to arbitrary coordinates at two different locations, $+$ is a coordinate of the center of mass, $y_- = r_+\theta_-$, $r_- = r_1 - r_2$, and $\theta_- = \theta_1 - \theta_2$.

Obtaining the moments of Eq. (4.8) and neglecting dissipation, which results only in "smearing" of the correlation function, one obtains

$$\begin{aligned}
\frac{\partial}{\partial t}\langle r_-^2\rangle &= \Delta\omega_t\left[3\langle r_-^2\rangle + k_\theta^2\delta^2\langle y_-\rangle^2\right],\\
\frac{\partial}{\partial t}\langle y_-^2\rangle &= 2k_\theta^{-1}\delta^{-1}\omega_s\langle r_-y_-\rangle,\\
\frac{\partial}{\partial t}\langle r_-y_-\rangle &= k_\theta^{-1}\delta^{-1}\omega_s\langle r_-^2\rangle + \Delta\omega_t\langle r_-y_-\rangle,
\end{aligned} \tag{4.9}$$

where

$$\langle f\rangle = \int dr_-\, dy_-\, G(r_-, y_-)$$

and $G(r_-, y_-)$ is a double-point Green function. Equation (4.9), taking into account Eq. (4.6), $\omega_s > \omega_t$, yields the following equation for $\langle r_-^2\rangle$:

$$\frac{\partial^3}{\partial t^3}\langle r_-^2\rangle - 2\omega_s^2\omega_t\langle\Delta r_-\rangle = 0 \tag{4.10}$$

provided the initial conditions are

$$\begin{aligned}
\langle r_-^2\rangle\Big|_{t=0} &= r_-^2, \quad \frac{\partial}{\partial t}\langle r_-^2\rangle\Big|_{t=0} = \omega_t\left[3r_-^2 + k_\theta^2\delta^2 y_-^2\right],\\
\frac{\partial^2}{\partial^2 t}\langle r_-^2\rangle\Big|_{t=0} &= 3\omega_t^2\left[3r_-^2 + k_\theta^2\delta^2 y_-^2 - 6\omega_s\omega_t k_\theta^{-1}\delta^{-1}r_-y_-\right].
\end{aligned}$$

Analogously, the equation governing $\langle y_-\rangle$ is obtained. Equation (4.10) easily yields Eq. (4.5). Hence, the length of the radial correlation is reduced significantly provided that Eq. (4.6) is fulfilled. The reduction results in suppression of the level of turbulence, and thereby in reduced transport coefficients. It is asserted that the effect provides the H-regime of confinement. An analysis specified for the drift-dissipative instability [80] and the kinetic ion temperature gradient modes [92] has been carried out. In [92] it is demonstrated that the existence of a maximum

in the turbulent viscosity due to the ion temperature modes can play a role in the bifurcation theory of the H-mode.

A linear analysis of the combined effect of the shear of poloidal rotation and the magnetic field shear, resulting also in the reduction of the radial correlation length, is offered below. Indeed, drift-like instabilities occur in the vicinity of magnetic surfaces with $k_{||} \approx 0$, where $k_{||} = (k_\theta B_\theta + k_\phi B_\phi)/B$ in a sheared magnetic field. The spatial width d of an instability is determined by the impact of Landau damping within the variation range of parallel phase velocity $\omega/k_{||}$. The width is specified for different instabilities in [80]. Stabilization occurs provided the frequency range due to shear in the poloidal rotation obtains the order of the frequency or the increment of an instability. The resulting width δ contracts and, thereby, an unstable wave is damped. The condition that causes a significant damping is

$$\left|\frac{dV_0}{dr}\right| \delta_0 k_\theta \geq \omega. \tag{4.11}$$

Equation (4.11) provides the constraint given by Eq. (4.6). Assuming that $\omega \approx D/\delta_0'$, these two constraints coincide.

As it stands, Eq. (4.11) seems to suggest that the critical $|dV_0/dr|$ is proportional to $\omega/\delta_0 k_\theta$ and thereby is crucially dependent on the mode in question and the wave number. However, a lot of tokamak microinstabilities, which may affect transport, are "soundlike" [80, 81], meaning that linear mode widths are determined by $k_{||} C_S \approx \omega$. Since $k_{||} = k_{||}' \delta \approx k_\theta' \delta / L_S$ (where L_S is the scale of the magnetic shear), the ratio (4.11) becomes

$$\left|\frac{dV_0}{dr}\right| \geq C_S/L_S,$$

being independent of k_θ and details of the mode. This has been borne out for drift waves [87], the η_i modes [83, 84], the $V_{||}'$ mode [87], and the resistive g and ballooning modes. An interesting result that emerges is that not only does flow shear stabilize tokamak microinstabilities, but, also, the same critical shear is sufficient to stabilize all wave numbers and all these instabilities.

This "universal" feature enables us to address the issue of the generation of strong electric fields at the periphery without specifying the cause or nature of turbulence. In the next chapter it will be shown that profiles of poloidal rotation with the shear required by Eqs. (4.6)-(4.11) emerge in reality at the edge during the H-mode.

In the presence of strong toroidal rotation the characteristic decorrelation time ω_s^{-1} has an additional term which can be obtained from the following simple arguments. The Doppler shift to the wave frequency is given by

$$\Delta\omega = (V_0 + \Theta\bar{u}_\phi)k_\theta + k_\phi\bar{u}_\phi = V_0k_\theta + k_{||}\bar{u}_\phi.$$

The effect of the rotation shear is proportional to $d\Delta\omega/dr$. Thus, for the most significant resonance modes with $k_{||} \to 0$ one obtains

$$\frac{d\delta\omega}{dr} = rk_\theta\frac{d(V_0/r)}{dr} + rk_\theta\bar{u}_\phi\frac{d}{dr}(\Theta/r).$$

As a result the shear of the rotation associated with the electric field in Eqs. (4.2)-(4.6) should be replaced by

$$\frac{d(V_0/r)}{dr} \to \frac{d(V_0/r)}{dr} + \bar{u}_\phi\frac{d}{dr}(\Theta/r).$$

4.2. Anomalous transport and steep radial profiles of the poloidal rotation velocity in edge plasmas

Here, we address the effects governing radial profiles of the poloidal rotation velocity in the steady state and without biasing. Hence, Eqs. (2.24)-(2.25) or Eqs. (1.35)-(1.36) when $|V_0| \ll \Theta C_S$ are employed. Two qualitatively different kinds of profiles emerge — steep and gradual ones. The gradual profiles occur provided all other terms in Eq. (1.35) are small compared to $\langle \mathbf{B}\cdot\nabla\cdot\overleftrightarrow{\pi}_i\rangle^{(\mathrm{NEO})}$. If this is the case, the discharge is in the L-regime because the value of the poloidal rotation velocity is close to the neoclassical $V_\theta^{(\mathrm{NEO})}$, thereby implying the gradual profile of V_θ. In contrast, the steep profiles occur when all terms in Eq. (1.35) are of the same order, thereby causing dramatically varying V_θ in the vicinity of the separatrix or the last closed

flux surface (LCFS). The resulting profiles appear during the H-mode and provide the large shear in V_θ, which brings about the decreased anomalous transport.

Neglecting here the radial current and the toroidal rotation, one obtains from Eqs. (1.35)–(1.36) for $|\alpha| < \alpha_1$ [13, 14]

$$q^{-1}\frac{\delta(qV_\theta)}{dr} + \beta(r)\left(V_\theta - V_\theta^{(\mathrm{NEO})}\right) = \left(\left(1+2q^2\right) m_i n r u_r^{(\mathrm{A})}\right)^{-1} \frac{d\left[rn\eta\left(1+2q^2\right)(dV_\theta/dr)\right]}{dr}, \quad (4.12)$$

where

$$\beta(r) = \left(\sqrt{\pi/2}\right)\varepsilon^2 (T_i/m_i)^{1/2}\left(r u_r^{(\mathrm{A})}\Theta\left(1+2q^2\right)\right)^{-1},$$

and $V_\theta^{(\mathrm{NEO})}$ is the neoclassical profile of the rotation velocity. Equation (4.12) governs the spatial relaxation of the V_θ profile. Using the definition of the particle confinement time τ_p employed at the periphery

$$4\pi^2 a R n(a) u_r^{(\mathrm{A})} = 2\pi 2a^2 R\bar{n}/\tau_p,$$

where $\bar{n}$ is the average density and a is the minor radius, one obtains

$$\beta(r) = \frac{\sqrt{\pi} q^2 \Theta n(a) C_S \tau_p}{n a^2 \left(1+2q^2\right)}. \quad (4.13)$$

Since in the L-regime the particle confinement time τ_p is much longer than the bounce period $a/(\Theta C_S)$ and despite the fact that $n(a) \ll \bar{n}$, the following estimate results: $\beta(a) \gg a^{-1}$. Thus, the first and third terms in Eq. (4.12) are negligibly small compared with the second term. This implies that the neoclassical viscosity is dominant. Then the standard neoclassics yields the poloidal rotation profile as $V_\theta \approx V_\theta^{(\mathrm{NEO})}$. However, when a steep gradient of the poloidal rotation velocity occurs, which may result due to $\beta(a) \approx L_{V_\theta}^{-1}$ because steep density and temperature profiles emerge during the H-mode, all terms in Eq. (4.12) are equally important.

Now we will show that the anomalous inertia and viscosity are significantly amplified in the banana regime compared to the plateau. Considering the contributions of banana orbits on either side of the flux surface, a trapped ion flow in the toroidal direction emerges, as was discussed in Section 3.2. A steady state requires that momentum gained by the trapped ions in the process of the collisional trapping is removed by collisional detrapping. Thus, by identifying the mean ion flow with the untrapped ion flow and employing a reference frame moving in the toroidal direction with the velocity cE_r/B_θ, one obtains an additional significant parallel flux $\sqrt{\varepsilon}n\left(V_0/\Theta + u_{pi}/\Theta\right)$ owing to the banana ions. This largest parallel flow results in an enhanced anomalous inertia and viscosity yielding the following equation instead of Eq. (4.12):

$$\frac{nm_i\sqrt{\varepsilon}B_0}{\Theta}\frac{dV_\theta}{dt} + \frac{\sqrt{\varepsilon}}{\Theta}\frac{B_0}{r}\frac{d}{dr}\left(r\eta\frac{dV_\theta}{dr}\right) = -\frac{1.1\sqrt{\varepsilon}nm_i\nu_iB_0}{\Theta}\left(V_\theta - V_\theta^{(\mathrm{NEO})}\right). \tag{4.14}$$

Equation (4.14) in combination with the well-known flux surface averaged radial momentum balance

$$V_\theta = V_0 + u_{pi} + \Theta\bar{u}_\phi$$

yields the following conclusions. Two typical length scales emerge in the banana regime, depending on the collisionality ν_i. The first one is

$$L_{V_\theta} = u_r^{(\mathrm{A})}/\nu_i \sim D/L_n\nu_i,$$

where $L_n = \left(d\ln n/dr\right)^{-1}$ provided $\nu_i^* \sim 1$. In contrast, L_{V_0} is of order L_n when $\nu^* \ll 1$ and $L_n^2 \ll D/\nu_i$. If $\nu^* \ll 1$, and this is the case for the largest tokamaks such as JET and JT-60, then the neoclassical viscosity in Eq. (4.14) is negligible with respect to the other anomalous terms. So for small collisionality the poloidal rotation is reduced to zero within the scale L_n. Neglecting the neoclassical viscosity and employing $u_r^{(\mathrm{A})} = -Dd\ln n/dr$, one obtains the equation for the poloidal rotation profile

$$\frac{dV_\theta}{dr} = \frac{\mathrm{const}\,(r)}{n^{1+\gamma}},$$

where $\gamma = \eta/(nm_iD)$. In summary, Eq. (4.14) yields the poloidal rotation profile decreasing to zero inwards from the separatrix within a length scale of order L_n. It may be either positive or negative. For a given u_{pi} and $\bar{u}_\phi$ the last equation also yields the radial electric field profile proportional to V_0. The constant in this equation is determined by the density profile on the separatrix. Indeed, if the u_{pi} dominates, it governs the electric field there. In conclusion, variations of the poloidal rotation and electric field profiles occur within L_n and not within the "squeezed" banana width due to radial electric field shear. The significance of the first two terms on the l.h.s. of Eq. (4.14) as opposed to the neoclassical viscosity appears to yield steep profiles of the poloidal rotation velocity typical at the very edge for the H regime. Yet, the impact of terms due to the profile in toroidal rotation may be more dramatic deeper in a tokamak, thereby bringing about the high-shear electric field in the plasma outer region. Therefore, we present here the complete set of equations including toroidal rotation and external toroidal force F resulting from unbalanced neutral beam injection:

$$\begin{aligned}
&\frac{nm_i\sqrt{\varepsilon}B_0}{\Theta}\frac{d}{dt}(V_0 + u_{pi} + \Theta\bar{u}_\phi) \\
&\quad + nm_iB_0\frac{d}{dt}\left[\bar{u}_\phi + \Theta(1+2q^2)(V_0+u_{pi}) + \varepsilon^2\bar{u}_\phi\right] \\
&\quad - \frac{B_0}{r}\frac{d}{dt}\left\{r\eta\frac{d}{dt}\left[\bar{u}_\phi + \Theta(1+2q^2)(V_0+u_{pi}) + \varepsilon^2\bar{u}_\phi\right]\right\} \\
&\quad - \frac{B_0}{r}\frac{d}{dr}\left\{r\eta\frac{d}{dr}\left[(\bar{u}_\phi + V_0 + u_{pi})\sqrt{\varepsilon}\Theta^{-1}\bar{u}_\phi\right]\right\} \\
&\quad = -\langle \mathbf{B}\cdot\nabla\cdot\overleftrightarrow{\pi}_i\rangle^{(\mathrm{NEO})} + F, \\
&nm_i\frac{d\bar{u}_\phi}{dt} - \frac{1}{r}\frac{d}{dr}\left(r\eta\frac{d\bar{u}_\phi}{dr}\right) = F
\end{aligned} \tag{4.15}$$

Furthermore, the poloidal rotation at the separatrix may be of the order ΘC_S and the nonlinear effects addressed in Eqs. (2.24)–(2.25) also have to be included along the lines described in the previous section. In [42] the option of generating a poloidal rotation by the inertia, emerging due to anisotropy of

turbulence given by $\langle \partial(\tilde{u}_r \partial \tilde{u}_\theta/\partial r)/\partial r \rangle$, where $\tilde{u}_r$ and $\tilde{u}_\theta$ are turbulent fluctuations, has been pointed out. The turbulent fluctuations result also in a current $\langle j \rangle = e\langle \tilde{u}_r(n_i - n_e) \rangle$ driven by turbulence. However, the analysis has been restricted by the choice of the cylindrical geometry. In the real toroidal geometry their approach appears to be equivalent to the one described above, in which the anisotropy stems from the nonlinear interaction between the neoclassical parallel (or its poloidal component) flow and the radial anomalous flow. In other words, the radial current driven by the anomalous inertia and viscosity emerges, thereby counteracting the neoclassical current driven by the parallel viscosity.

Boundary conditions on the separatrix or alternatively on the LCFS will be addressed in the next section.

4.3. The electric field at the separatrix

The issue of boundary conditions for V_0 on a separatrix or last closed flux surface is addressed in this section. Initially, the problem was formulated in [38] from a strictly neoclassical point of view. Yet, the transport is largely anomalous. However, the underlying physical mechanism determining the electric field at a separatrix is maintained. Since the banana width for ions is much larger than for electrons and the trapped ions move along $\mathbf{B}$ as well, a fraction of the trapped ions hits the divertor plates or the limiter. This effect implies a nonambipolar flux of banana ions through a separatrix. Then the ambipolar electric field is mainly determined by the requirement for the large ion banana flux to annul at a separatrix (provided there is no biasing electrode). This results in a detrapping potential of the order of the mean energy of trapped particles, $\Delta\varphi \approx \varepsilon T_i/e$. Thereby the longitudinal energy of a banana ion changes about $e\Delta\varphi$ because the energy in the perpendicular motion remains unchanged due to the conservation of the invariant $m_i V_{i\perp}^2/(2B)$. Therefore a banana ion detraps and does not cross a separatrix. This is termed in the literature as the "squeezing" effect. This potential is applied within one banana width $\approx \sqrt{\varepsilon}\rho_{ci}/\Theta$. The resulting change in the $\mathbf{E} \times \mathbf{B}$ rotation velocity is $\Delta V_0 \approx \sqrt{\varepsilon}\Theta C_S$. This

value is the most significant because even when $\Delta\varphi < \varepsilon T_i/e$, the variation $\Delta V_0 \approx \sqrt{\varepsilon}\Theta C_S$ always results in detrapping. Hence, the boundary condition at the separatrix $V_0(a)$ acquires the form

$$V_0(a) \approx \sqrt{\varepsilon}\Theta C_S + V_0^{(\mathrm{SOL})},$$

where $V_0^{(\mathrm{SOL})}$ is the poloidal rotation within the scrape-off layer (SOL) addressed in the following sections. It appears that this estimate remains valid in the plateau regime as well (probably with accuracy of the order $\sqrt{\varepsilon}$).

An attempt was made to compute the radial electric field on a separatrix in [34]. However, the ion current resulting from ions on loss orbits has been balanced by the current owing to the neoclassical parallel viscosity. It is asserted that the notion of the parallel viscosity within microscopic scales of the order $\sqrt{\varepsilon}\rho_{ci}/\Theta$ is not truly warranted.

In [39] the case with hot plasmas in the vicinity of a separatrix was addressed numerically. It was assumed that the typical time scale $\tau \approx qR/C_S$ for losses onto divertor plates is much shorter than the collision time and the confinement time inside the separatrix. New kinds of ion trajectories emerge which either intersect or do not intersect plates or a limiter. For simplicity, the symmetric double-null configuration shown in Fig. 4.2 was considered.

It is shown in Fig. 4.2 that both trapped and passing ions might either intersect or not intersect, depending on the direction and magnitude of the initial velocity and on both radial and poloidal coordinates. Ions on loss trajectories hit a plate and become neutrals, thereby emptying these trajectories. In contrast, electrons almost do not deviate from magnetic surfaces and therefore fill in almost all trajectories. In [39] the ion density profile was computed assuming that the ion distribution function on nonintersecting trajectories is given by the Maxwell–Boltzmann distribution function

$$f_i = n_0 \left(\frac{m_i}{2\pi T_i}\right)^{3/2} \exp\left(-\frac{m_i V_i^2}{2T_i} - \frac{e\varphi}{T_i}\right).$$

On the other hand, the distribution on loss trajectories has been assumed to be zero. The profiles of the electric field $\varphi_0(r)$

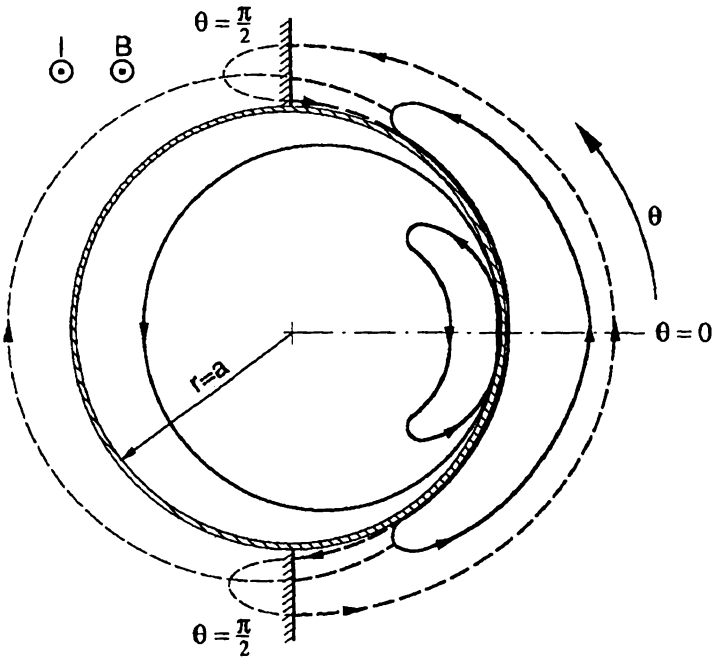

Fig. 4.2. Schematic trajectories of trapped and untrapped particles in the vicinity of the separatrix at $r = a$, $\theta = 0$. Two kinds of trajectories are shown. (a) Solid lines — filled nonintersecting orbits; (b) dashed lines — empty intersecting orbits.

were iterated until the ion density profile did not coincide with a given electron density profile taken from the measurements. Furthermore, the resulting ion density profile has been found to be poloidally asymmetric. Hence, the poloidally dependent perturbation $\varphi_1(r, \theta)$ has been added in order to provide for the quasi-neutrality. The latter resulted in the redistribution of electrons within a magnetic surface:

$$\frac{e\varphi_1}{T_e} = \frac{n_{e1}(r, \theta)}{n} = \frac{n_{i1}(r, \theta)}{n}, \quad \varphi = \varphi_0(r) + \varphi_1(r, \theta).$$

It was shown that there is an important causal relationship between the density gradient and the value of the electric field at

the separatrix. Steeper density profiles imply stronger negative radial electric fields and vice versa. A significant poloidal electric field results as well. Focusing on the alternative collisional case, we consider the loss trajectories to be filled due to a significant anomalous transport and the ionization of neutrals. Thus, the outflow and the inflow occur on the separatrix. The net flux through the separatrix has to cancel, provided the potential distribution in the vicinity is given by the Boltzmann law. We have neglected the ion–ion collision frequency compared to C_S/qR. Hence, the radial electric field on the separatrix yields

$$E_r(r=a) = \frac{T_i}{e}\frac{d\ln n}{dr}. \tag{4.16}$$

Quantitatively, the estimate (4.16) turns out to be the same as the one obtained for the collisionless case employing the notion of a significant deformation of trajectories (dubbed "squeezing"), assuming that the scale of the density profile occurs within the poloidal Larmor radius $\approx \rho_{ci}/\Theta$.

In summary, we conclude that the electric field at the separatrix is very sensitive to the density profile there.

4.4. Radial current in experiments with a biased electrode

A radial electric field can be brought about within the core of a tokamak by immersing an electrode some centimeters inside the separatrix and applying a voltage with either negative or positive polarity to the electrode. Then a significant radial current results. These experiments offer a crucial test in verifying different theories for the poloidal and the toroidal rotation and models for the L–H transitions. For example, standard neoclassical theory predicts that in the steady state the radial current has to be zero if anomalous transport and the perpendicular neoclassical viscosity are neglected. However, accounting for anomalous processes, the relation between applied voltage and the radial current has been obtained in [14, 53]. Focusing at first on small currents driven by small radial electric fields in the plateau regime, one obtains the following results for $|V_0| \ll \Theta C_S$. The

profiles of the poloidal and toroidal rotation are determined by Eqs. (1.35)–(1.36). Subtracting Eq. (1.36) from Eq. (1.35) and excluding the toroidal rotation, one obtains

$$\langle j\rangle = -\frac{\langle \mathbf{B}\cdot\nabla\cdot\overleftrightarrow{\pi}_i\rangle^{(\mathrm{NEO})}}{\Theta B_0^2} - \frac{c\left(1+2q^2\right)cnm_i}{qB_0}u_r^{(\mathrm{A})}\frac{d\left(qV_\theta\right)}{dr} + \frac{c}{B_0}\frac{d}{rdr}\left[r\left(1+2q^2\right)\eta\frac{d\left(qV_\theta\right)}{qdr}\right]. \tag{4.17}$$

In the L-regime, when the shear in poloidal rotation and the current due to biasing are small and

$$\left|V_\theta - V_\theta^{(\mathrm{NEO})}\right| \ll \left|V_\theta^{(\mathrm{NEO})}\right|,$$

the second and third terms on the right-hand side of Eq. (4.17) are small compared to the first one. Indeed, their ratio yields

$$\left[\frac{(1+2q^2)cnm_i}{qB_0}u_r^{(\mathrm{A})}\frac{d(qV_\theta)}{dr}\right] \Big/ \frac{\langle \mathbf{B}\cdot\nabla\cdot\overleftrightarrow{\pi}_i\rangle^{(\mathrm{NEO})}}{\Theta B_0^2}$$

$$\approx \frac{u_r^{(\mathrm{A})}qR}{rC_S} = \frac{\bar{n}qR}{2n(a)\tau_p C_S} \ll 1.$$

Thus, for small currents one obtains

$$\langle j\rangle \approx -\frac{c\langle \mathbf{B}\cdot\nabla\cdot\overleftrightarrow{\pi}_i\rangle^{(\mathrm{NEO})}}{\Theta B_0^2}. \tag{4.18}$$

Therefore, for small values of the radial current, it is determined by the neoclassical parallel viscosity, and the anomalous terms vanish. The physical reason for this result is that the radial current causes a toroidal rotation in a steady state determined by the Lorenz force being balanced by the force acting due to the radial transport of toroidal momentum (1.36). This force also emerges in the parallel component of the momentum balance where it is compensated by the neoclassical parallel viscosity. The net result yields Eq. (4.18). Since for small currents the parallel viscosity is a linear function of $(V_\theta - V_\theta^{(\mathrm{NEO})})$ and the

velocity of toroidal rotation remains small, thereby affecting V_θ only slightly, the perpendicular conductivity emerges as

$$\langle j \rangle \approx \sigma_\perp \left(E_r - E_r^{(\mathrm{NEO})} \right), \tag{4.19}$$

where

$$E_r^{(\mathrm{NEO})} = \frac{T_i}{e} \left[\frac{d \ln n}{dr} + (1-k) \frac{d \ln T_i}{dr} \right], \tag{4.20}$$

where $k = -0.5$. Employing the expression for $\langle \mathbf{B} \cdot \nabla \cdot \overleftrightarrow{\pi}_i \rangle^{(\mathrm{NEO})}$ in the plateau regime (2.10) one obtains

$$\sigma_\perp = \frac{\sqrt{\pi/2} n \varepsilon^2 c^2 m i^{1/2} T_i^{1/2}}{\Theta B_0^2 r}. \tag{4.21}$$

In the banana regime, employing (3.14) one obtains

$$\sigma_\perp = \frac{1.1 n \varepsilon^{1/2} c^2 m_i n_i}{\Theta 2 B_0^2} \tag{4.22}$$

and $k = 1.17$. More importantly, for $|V_0| \geq \Theta C_S$, the nonlinear effects described in Section 2 become crucial. For large values of V_0 the parallel viscosity decreases with growing V_0. Furthermore, additional inertia emerges, poloidal perturbation of the density grows to reach the order ε, and flows are modified. Thus, the more general equations (2.24)–(2.25) have to be employed instead of Eqs. (1.35)–(1.36). They yield

$$\begin{aligned} \langle j \rangle \; = \; & \frac{cF(\alpha)}{\Theta B_0^2} + \left\langle \frac{cnm_i u_r^{(\mathrm{A})}}{\Theta B_0} \frac{d \left[u_{\|i} \left(\frac{B_0}{B_\phi} - \frac{B_\phi}{B_0} \right) \right]}{dr} \right\rangle \\ & - \left\langle \frac{c}{B_0} \frac{d}{\Theta r dr} \left\{ \eta \frac{d \left[u_{\|i} \left(\frac{B_0}{B_\phi} - \frac{B_\phi}{B_0} \right) \right]}{dr} \right\} \right\rangle. \end{aligned} \tag{4.23}$$

Note that the flux surface average velocity of the toroidal rotation has canceled in Eq. (4.23). Unless anomalous terms in Eq. (4.23) may be neglected, one obtains from Eq. (4.23), employing the nonlinear viscosity given by Eq. (2.29),

$$\langle j \rangle = -\frac{\sqrt{\pi} n c T_i \varepsilon^2}{B_0 r} \alpha \left(2\alpha^4 + 2\alpha^2 + 1 \right) \exp\left(-\alpha^2 \right), \tag{4.24}$$

where $\alpha = V_0/\Theta C_S$. The current given by Eq. (4.24) (or for the linear case by (4.18)) is driven by trapped ions (2.12) (see also (2.28)) occurring due to $V_\theta \neq V_\theta^{(\mathrm{NEO})}$. Furthermore, the maximum value of the radial current is determined by the maximum of $F(\alpha)$, which occurs at $|V_0| = \sqrt{2}\Theta C_S$, and is estimated as

$$I^{(\max)} \approx \langle j \rangle^{(\max)} 4\pi^2 r R \approx c 4\pi^2 r R/(\Theta B_0^2)\max(F).$$

Employing Eq. (2.29), we have

$$I^{(\max)} \sim c 4\pi^2 r R/(\Theta B_0^2) F(\sqrt{2}) = 7\sqrt{2}\pi 5/2 R n c T_i \varepsilon^2/B_0. \quad (4.25)$$

In summary, the effective conductivity becomes nonlinear when $|V_0| \approx \Theta C_S$ and drops when $|V_0| > \Theta C_S$ with a growth of V_0. The current flows in the direction of the electric field. This results in positive conductivity. It is important to keep in mind that the anomalous terms become significant when $|V_0| > \Theta C_S$ ($F(a)$ measuring the impact of the neoclassical parallel viscosity decreases), and the transition to the H-mode results. Therefore, these terms have to be included. The effect of these terms is further amplified when $|V_0| \gg \Theta C_S$. Indeed, when an even larger voltage is applied to the electrode ($|V_0| \gg \Theta C_S$) the neoclassical parallel viscosity and inertia become exponentially small compared to the effects occurring due to turbulence. Excluding the toroidal rotation, one obtains for the nonlinear regime $|V_0| \gg \Theta C_S$

$$\langle j \rangle = n\lambda \left\{ \frac{\delta(1/V_0)}{dr} - \frac{1}{m_i u_r^{(\mathrm{A})} r} \frac{d[r\eta d(1/V_0)/n dr]}{dr} \right\}, \quad (4.26)$$

where $\lambda = 2m_i q^2 B_0 \Theta^3 C_S^2 u_r^{(\mathrm{A})}(1 + T_e/2T_i)$. Considering the case $L_{V_\theta} \ll L_n < r$, the solution of Eq. (4.26) is

$$\frac{1}{V_0} = \frac{\langle j \rangle}{\lambda} \int \frac{dr'}{n(r')} \left\{ 1 - \exp\left[-\frac{\eta(r - r')}{m_i n u_r^{(\mathrm{A})}} \right] \right\} \frac{\eta}{m_i n u_r^{(\mathrm{A})}}. \quad (4.27)$$

The constant C is a function of the boundary condition on the electric field imposed in order to provide for a given value of $\langle j \rangle$ at the separatrix. The profile of $\langle j \rangle$ is determined by the

equation $\nabla \cdot \langle j \rangle = 0$ and results in a slowly varying function ($\langle j \rangle \sim r^{-1}$). Thus, the profile $\langle j \rangle$ has been approximated to be a constant in deriving Eq. (4.27). The value of the current is determined by the potential applied to the plasma:

$$\Delta\varphi_p = \int \frac{V_0 B_0}{c} dr.$$

This equation and Eq. (4.27) yield $\langle j \rangle$ inversely proportional to $\Delta\varphi_p$ if $|V_0| \gg \Theta C_S$ and the coefficient as a function of temperature and density profiles within r_0 and a. Upon application of a electrode bias, the voltage on the electrode versus the limiter U differs from the potential difference in the plasma, $\Delta\varphi_p$, by the sheath potential on both the electrode and the limiter. The focus is on a tokamak with a poloidal limiter, in agreement with experiments carried out on CCT and TUMAN 3 [48–51, 53]. We start from the case of a negative polarity on the electrode. Then

$$U = \Delta\varphi_p + \Delta\varphi_{s\eta}^{(-)} + \Delta\varphi_{s\eta}^{(+)}, \tag{4.28}$$

$\Delta\varphi_p$ is the potential difference within the plasma, $\Delta\varphi_{s\eta}^{(-)}$ is the sheath drop on the electrode, and $\Delta\varphi_{s\eta}^{(+)}$ is the sheath drop on the limiter. Since the electron flux on an electrode significantly exceeds the current in the biasing circuit, the sheath is impermeable to electrons. Thence, the current through the electrode biased negatively is

$$I = en^{(-)}S^{(-)}\left[0.6\frac{\sqrt{T_e^{(-)}}}{m_i} - \frac{1}{2\pi}\frac{\sqrt{T_e^{(-)}}}{m_e}\exp\left(-e\frac{\Delta\varphi_{s\eta}^{(-)}}{T_e^{(-)}}\right)\right], \tag{4.29}$$

where $n^{(-)}$, $T_e^{(-)}$, and $S^{(-)}$ are density, temperature, and cross-section at the negative electrode and I is the current. However, the ion flux at the positive electrode (at present the limiter) estimated from the global particle confinement time is much larger than the current in the biasing circuit. This yields that the limiter is at the floating potential

$$\Delta\varphi_{s\eta}^{(+)} = \frac{T_e^{(+)}}{e}\ln\left[\frac{(m_i/m_e)^{1/2}}{0.6\sqrt{2\pi}}\right] \approx \frac{T_e^{(+)}}{e}. \tag{4.30}$$

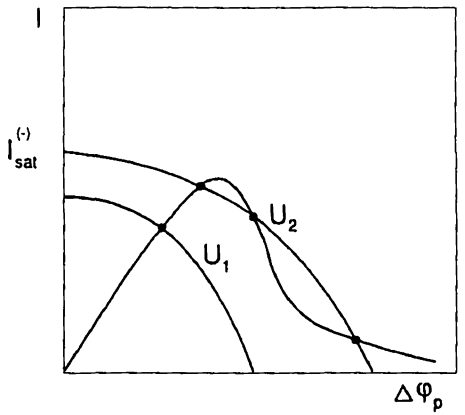

Fig. 4.3. Different scenarios for intersection of solutions to (4.24) and the loading curves. Here, U is the potential drop between the electrode and the limiter, $\Delta\varphi_p$ is the potential applied within the plasma, and I is the current to the electrode, $U_2 > U_1$.

Excluding sheath potentials, one obtains the current as a function of the applied voltage and the potential drop within the plasma

$$I = 0.6en^{(-)}S^{(-)}\sqrt{T_e^{(-)}/m_i} \times \left\{1 - \left(\sqrt{T_e^{(-)}/T_e^{(+)}}\right)^{1/2} \exp\left[-\frac{e\,(U - \Delta\varphi_p)}{T_e^{(-)}}\right]\right\}. \quad (4.31)$$

For a given voltage U, the electric field at the plasma periphery is determined by Eqs. (4.23) or (4.24)–(4.31). Assuming that the radial current is determined by Eq. (4.24), one obtains that the value of $\Delta\varphi_p$ occurs at a cross point of the curves given by (4.24) and (4.31) (see Fig. 4.3).

Thus, for sufficiently large values of U, there may be three values of $\Delta\varphi_p$ and currents [14, 53]. A similar approach is developed in [89]. It may happen that a large fraction of the applied voltage is located within the sheath and only a very small potential is applied to the plasma. In the two other cross points

the voltage is applied largely to the plasma. Then the H-mode results. When a positive voltage is applied to the electrode, the situation is drastically modified. In this case $\Delta\varphi_{s\eta}^{(+)}$ remains of the order $T_e^{(+)}$ because the sheath is impermeable to electrons. The electron flux to the electrode is compensated by the enhanced ion flux to the limiter. The limiter sheath is still at the floating potential $\approx 3T_e^{(-)}/e$. Thus, when the voltage is high, a significant fraction of it has to be applied to the plasma. For a voltage with negative polarity applied to an external electrode, the current in the biasing circuit is limited by the ion saturation current, whereas for positive biasing the current is limited only by the finite resistivity or equivalently by Eq. (4.25) (or a very large saturation current of the limiter). The theory is borne out in experiments on CCT and TUMAN 3.

4.5. Comparison with experiments

A radial electric field directed inward at the periphery has been observed on most tokamaks [5, 6, 15–17, 91]. The measured profiles of the electric field inside the separatrix seem to be consistent with Eq. (1.42), provided the unbalanced neutral beam injection is absent with the exception of low densities. A comparison of the measured profile with the computed profile from Eq. (1.42) is shown in Fig. 4.4 for the ohmic heating case. On the other hand, a much stronger electric field has been demonstrated during the H-mode discharges, also directed inwards in the vicinity of the separatrix.

This is shown in Fig. 4.1, measured on D–DIII [90]. The $\mathbf{E} \times \mathbf{B}$ drift velocity during the H-mode is $V_0 \approx \Theta C_S$. On the other hand, the temperature and density profiles are very steep within the thermal layer in the H-regime of confinement, and therefore the velocities of diamagnetic drift u_{pi} turn out to be of the same order, about ΘC_S. Thus the poloidal rotation velocity in the vicinity of a separatrix might approach its neoclassical value. This coincidence has been exploited to suggest that the poloidal rotation is well described by neoclassics. This assumption is fundamental in the model for L–H transitions advocated by Hinton [46]. On the other hand, the significant

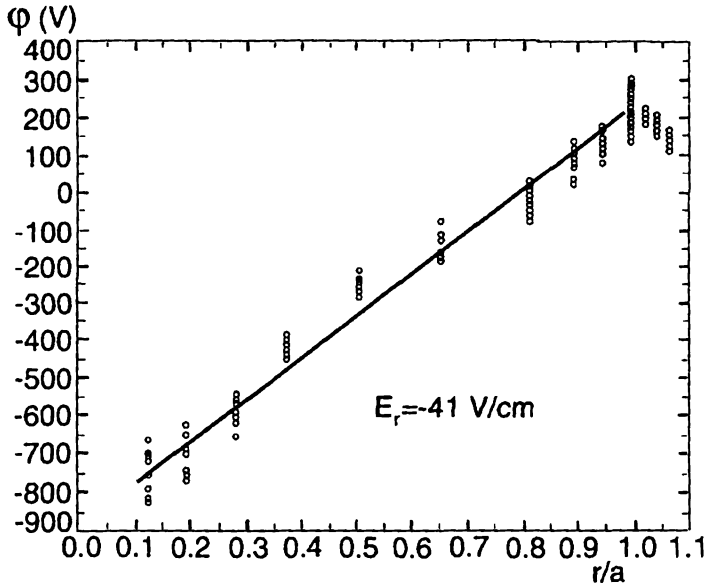

Fig. 4.4. The potential profile obtained on TEXT [91]. The solid line is the result obtained using Eq. (1.42).

shear in V_0, reported by D–DIII, JFT–2M and other teams, is probably inconsistent with the neoclassical formula for $V_p^{(\mathrm{NEO})}$ (1.30) because the radial dependence of T_i turns out to be close to a linear one. The scale of the profile of the V_0 is not obtained by the estimate $\alpha^{-1}(a)$, where $\alpha(a)$ is given by (4.13). A more detailed comparison is aggravated by the fact that in most cases studied so far, an unbalanced neutral beam injection resulting in a fast toroidal rotation has been employed. The complexity of the issue is further aggravated by the difficulties of diagnostics employing impurity lines for measurements of poloidal rotation. It is based upon the relations

$$V_{pI} = V_0 + u_{pI} + \Theta \bar{u}_\phi\,, \qquad u_{pI} = -\frac{c}{ZeBn_I}\frac{dp_I}{dr}. \tag{4.32}$$

Thus, in order to obtain V_0 from the measurements it is necessary to subtract u_{pI}, which is usually not very well known.

Hence, it is asserted that the crucial test to theories is offered by experiments with a biased electrode [48–51]. These experiments allow an electric field to be excited at the plasma edge in a tokamak in a controlled manner and thereby to increase V_p to obtain values much larger than ΘC_S. The first experiment has been carried out on the tokamak CCT [48], where V_0 reached an even higher value of C_S, whereas the velocity of the toroidal rotation remained insignificant. These results undoubtedly point out flaws in the neoclassical approach. Indeed, the result that $\langle j \rangle \neq 0$ cannot be reconciled with standard neoclassics without invoking anomalous terms. A comparison of the extended neoclassics presented here with experiments carried out on TUMAN 3 has been reported in [53]. A fundamental consistency has been found. Examples of the voltage–current characteristics for the circuit electrode–plasma–limiter are shown in Fig. 4.5. For small currents the formula (4.19) was employed, assuming that $E_r = U/d$, where d is the location of the electrode head measured from the LCFS and the density $\bar{n} = [n(a)+n(a-d)]/2$ is the average. $\tilde{R} = dU/dI \approx 2\,\Omega$ resulted for the L-mode and $\tilde{R} \approx 1\,\Omega$ for the H-mode. Thus, currents of the order 50–100 A for an applied voltage of 100 V (Fig. 4.5) appear to be in reasonable agreement with the theory.

The radial electric field has been measured within $a-d$ and a on CCT, thereby providing the average value for the radial conductivity. The agreement between the conductivity obtained from Eq. (4.19) and the measured one appears to be within a factor of 2 (of the same order as the inaccuracy in determining the sheath potentials). The maximum values of currents measured on TUMAN 3 and CCT are consistent with the value given by Eq. (4.25), and this maximum results approximately for $V_0 = \sqrt{2}\Theta C_S$ in agreement with (4.24). However, in CCT the maximum current with positive polarity is three times larger than with negative polarity, whereas in TUMAN 3 both maxima are approximately the same. This difference results from the fact that the ion saturation current to the electrode coincided with the maximum current in TUMAN 3, whereas the $I^{(\max)}$ is much larger than the ion saturation current to the electrode. Finally, the current decreases with growing potential in both TUMAN 3

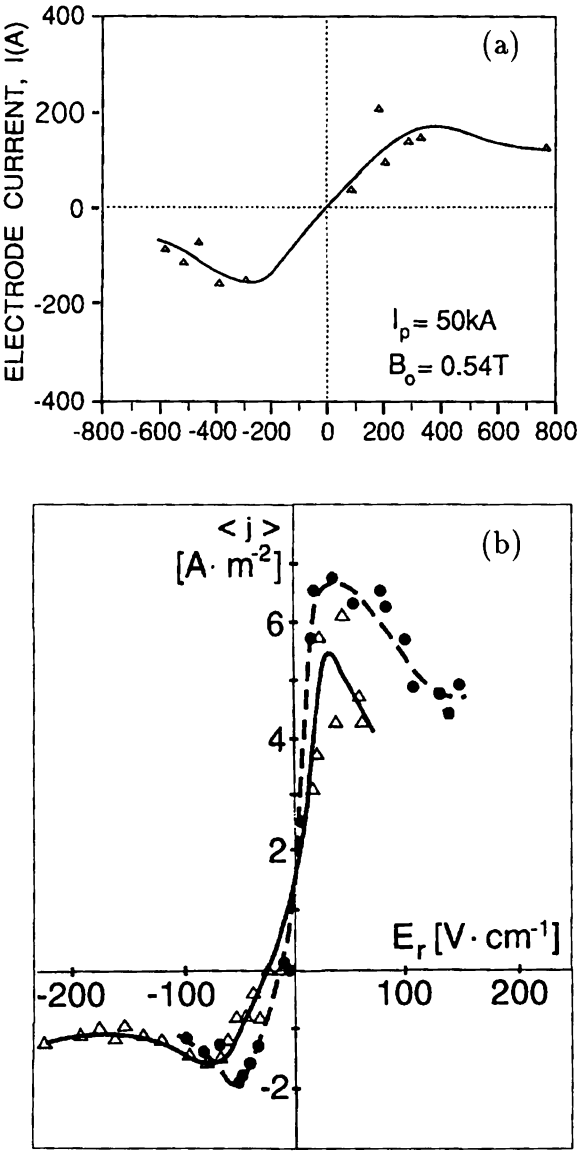

Fig. 4.5. The voltage–current characteristics for experiments with a biased electrode carried out on (a) TUMAN 3 [41] with $I_p = 50\,\mathrm{kA}$, $B_0 = 0.54\,\mathrm{T}$, $n(r=0) = 1.0 - 1.4 \times 10^{19}\,\mathrm{m}^{-3}$; (b) CCT [37], $I_p = 25\,\mathrm{kA}$, $B_0 = 0.25\,\mathrm{T}$, Δ — $\bar{n} = 1.6 \times 10^{18}\,\mathrm{m}^{-3}$, $\bullet$ — $\bar{n} = 3.6 \times 10^{18}\,\mathrm{m}^{-3}$.

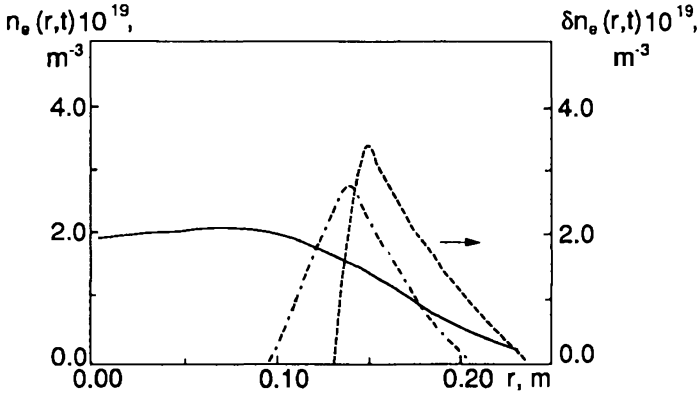

Fig. 4.6. Changes in the density profiles caused by pellet injection into TUMAN 3. Profile 1 has resulted in the L–H transition. Profile 2 has not triggered the L–H transition.

and CCT. In summary, experiments with a biased electrode appear to agree well with this model. However, many details of the natural L–H transition await a further analysis. Most importantly, it has been shown here that the radial electric field in the vicinity of the separatrix or LCFS is a sensitive function of plasma profiles, especially of the density profile. Indeed, the radial electric field given by Eq. (1.42) depends crucially on $d(\ln n)/dr$ during the L-mode. This is also true on the separatrix. Furthermore, the profile of the electric field determined by Eq. (4.12) during the H-mode also yields a strong dependence on the density gradient. Therefore, it appears most likely that the L–H transition benefits from creating steep density gradients close to the separatrix, resulting in profiles of the electric field with a large shear. An experiment along these lines has been carried out on TUMAN 3. Slow LiH pellets were injected with a velocity of the order 100 m/sec. The pellets, which caused a significant steepening of the density profile in the vicinity of the separatrix, triggered the L–H transition (see Fig. 4.6).

However, larger and faster pellets, which did not affect the density profile at the edge, did not trigger the transition.

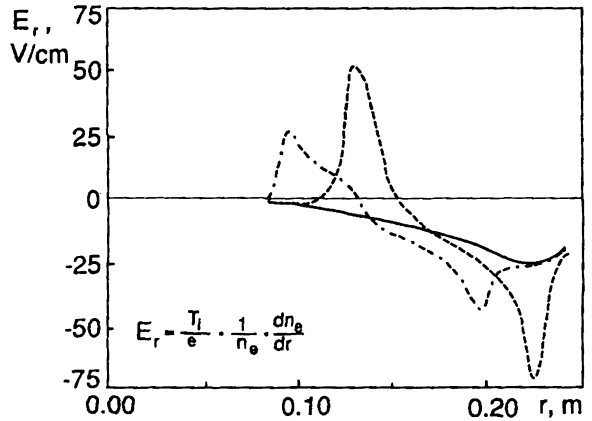

Fig. 4.7. Profiles of the radial electric field corresponding to the density profiles shown in Fig. 4.6.

The profiles of the electric field, computed from Eq. (1.42) for the two cases, are shown in Fig. 4.7.

It appears that the L–H transition results only when the profile of the radial electric field or the poloidal rotation obtain a large shear. In conclusion, our model yields both steep and gradual profiles of the poloidal rotation velocity corresponding to the H and L regimes respectively. It is also consistent with the basic features of the voltage–current characteristics obtained in experiments with biased electrodes.

5. The effect of rotation on impurity transport

5.1. Poloidal perturbation of the impurity densities and their fluxes within a magnetic surface

Poloidal rotation affects impurities more dramatically than the main ions. Their flows and distribution over a magnetic surface are the parameters most affected by a poloidal rotation. Many important phenomena connected with impurities emerge due to poloidal rotation, such as the enhancement of the poloidal electric field, the modification of the neoclassical radial transport

and so on. Indeed, nonlinear effects caused by the rotation occur for impurities at smaller fields because $V_0 \approx \Theta C_{SI}$, where $C_{SI} = \sqrt{2T_I/m_I}$ is obtained for impurities before it is obtained for the main ions. The issue of the poloidal and toroidal rotation of impurities is not only of academic interest because their velocities are measured experimentally by the Doppler shift technique in order to unravel information on rotation for a main plasma.

The standard neoclassical theory of impurity transport developed by many scientists has been presented in [3]. The density within a magnetic surface has been assumed to be a constant. However, this assumption is subject to stringent constraints, in particular for a cold plasma at the edge, where impurities are in the Pfirsch–Schlüter regime [54]. The result has also been obtained in [55, 57]. The underlying physical arguments are as follows. The collision frequency of impurities with main ions is larger than with impurity ions because the impurity density is much smaller than the plasma density. Therefore, the friction force with main ions results in a redistribution of impurities on the magnetic surface, which is "smeared" by the poloidal rotation. The perturbation within a magnetic surface obtains the order of ε and the criterion for a significant impact is

$$\frac{\nu_i r}{\theta C_S} \gg \frac{Z^2 \rho_{ci}}{r\theta}, \tag{5.1}$$

where Z is the charge number. Here, we have assumed that the typical scale of plasma parameters is of the order of the minor radius.

Note that for impurities with not-too-small values of Z this constraint may be fulfilled even when the main ions are in the plateau regime and the impurities are in the Pfirsch–Schlüter regime. Below we focus on this case. The condition for employing the hydrodynamic regime is

$$\nu_i r/\theta c_s \gg (m_I/m_i)^{1/2} Z^{-2}, \tag{5.2}$$

where m_I is the mass of impurities. The collision frequencies

are defined as follows:

$$\nu_i = \frac{4\sqrt{\pi}}{3\sqrt{m_i}} \frac{e^4 \Lambda n_i}{T_i^{3/2}}, \qquad \nu_{iI} = \frac{4\sqrt{2\pi} e^4 \Lambda Z^2 n_I}{3\sqrt{m_i} T_i^{3/2}},$$

$$\nu_I = \frac{4\sqrt{\pi}}{3\sqrt{m_I}} \frac{e^4 \Lambda n_I}{T_I^{3/2}}, \quad \nu_{iI} \sim \nu_i \sim \nu_I \left(\frac{m_I}{m_i}\right)^{1/2} Z^{-2}. \tag{5.3}$$

We assume that $n_I Z^2 / n_i \approx 1$ ($Z_{\text{eff}} \approx 2$). We consider only one kind of impurities. Their distribution function is almost Maxwellian, provided Eq. (5.2) is satisfied. Employing the collisional operator from [93] one obtains

$$\begin{aligned} \mathrm{St}\,(f_I, f_i) \;=\; & \frac{m_i n_i}{m_I n_I} \nu_{iI} \frac{\partial}{\partial \nu_{I\alpha}} \left(\nu_{I\alpha} f_I + \frac{T_i}{m_I} \frac{\partial f_I}{\partial \nu_{I\alpha}} \right) \\ & + \frac{1}{m_I n_I} R_{iI} \frac{\partial f_I}{\partial \nu_I}, \end{aligned} \tag{5.4}$$

where V_α are Cartesian coordinates in the velocity space, and R_{iI} is the friction force between the main ions and the impurities. This friction force, estimated as

$$R_{iI} \sim m_i n_i \nu_{iI} \left(u_{i\|} - u_{I\|} \right) \sim m_i n_i \nu_{iI} \varepsilon V_p / \Theta,$$

exceeds the parallel gradient of the impurity pressure and the parallel electric field, provided Eq. (5.1) is satisfied. This easily follows from $n_{1I}/n_I \approx \varepsilon$. Some other ramifications of the additional electric field brought about by the perturbation of the impurity density within a magnetic surface are addressed in [56]. The parallel viscosity for impurities can be neglected compared to R_{iI}, because

$$\begin{aligned} \nabla \overleftrightarrow{\pi}_I \;\sim\; & \frac{n_I T_I \theta^2 u_{I\|}^{(1)}(\theta)}{\nu_I r^2} \\ & \approx R_{iI} \left(\frac{\nu_I r}{\theta c_s} \right)^2 \frac{n_i}{n_I Z^2} \left(\frac{m_I}{m_i} \right)^{1/2} Z^{-2} \ll R_{iI}. \end{aligned} \tag{5.5}$$

Thus, the hydrodynamic velocity of the impurity ions versus the main ions can be obtained from

$$R_{iI} = -R_{Ii} = \int m_i V_{i\|} \mathrm{St}\,(f_i, f_I)\, dV_i = 0.$$

The collisional operator is reduced to [93]

$$\mathrm{St}\,(f_i, f_I) = \frac{3\sqrt{\pi}}{8}\nu_{iI}\left(\frac{2T_I}{m_i}\right)^{3/2}\left[\frac{\partial}{\partial V_{i\alpha}}V_{\alpha\beta}\frac{\partial f_i}{\partial V_{i\beta}} + O\left(\frac{m_i}{m_I}\right)\right], \quad (5.6)$$

where in the frame of reference at rest with impurities

$$V_{\alpha\beta} = \frac{1}{V_i^3}\left(V_i^3\delta_{\alpha\beta} - V_{i\alpha}V_{i\beta}\right).$$

Employing integration by parts, the integral yielding the friction force is

$$I = \int V_{i\|}V_{\alpha\beta}\frac{\partial f_{1i}}{\partial V_{i\alpha}V_{i\beta}}d\nu_i = -\int\frac{2V_{i\|}}{V_i^3}f_{1i}dV_i. \quad (5.7)$$

Substituting into Eq. (5.7) the distribution function for main ions in the plateau regime [Eq. (2.2)] and employing (5.5)–(5.6), one obtains for the parallel friction force between main ions and impurities

$$\begin{aligned} R_{iI} &= n_i m_i \nu_{iI}\frac{2\varepsilon}{\Theta}\cos\theta\left(v_0 + \frac{1}{2}\Theta\bar{u}_\phi + \frac{cT_i}{eB}\frac{d\ln n}{dr} - \frac{1}{2}\frac{c}{eB}\frac{dT_i}{dr}\right) \\ &\quad + n_i m_i \nu_{iI}\left[u_{I\|}^{(1)}(\theta) - u_{i\|}^{(1)}(\theta)\right]. \end{aligned} \quad (5.8)$$

Here, it has been taken into account that f_{0i} is shifted to the hydrodynamic velocity of impurities in the chosen frame of reference. The first term in Eq. (5.8) is the thermoforce dependent on the poloidal angle θ and the second is the conventional friction force. This becomes obvious when the neoclassical value for V_θ is substituted into Eq. (5.8). Employing $R_{iI} \approx 0$, one obtains

$$\begin{aligned} u_{I\|}^{(1)}(\theta) - u_{i\|}^{(1)}(\theta) &= -\frac{2\varepsilon}{\Theta}\left(v_0 + \frac{1}{2}\Theta\bar{U}\right. \\ &\quad \left. + \frac{cT_i}{eB}\frac{d\ln n}{dr} - \frac{1}{2}\frac{c}{eB}\frac{dT_i}{dr}\right)\cos\theta. \end{aligned} \quad (5.9)$$

Equation (5.9) yields the parallel velocity of impurities along a field line, thereby showing a difference of the order $\sim qV_\theta$ (if

the toroidal velocities are the same). Note that the velocities of poloidal rotation differ for ions and impurities due to diamagnetic drifts. The flux surface average poloidal rotation for impurities is given by (4.32). This conclusion is borne out in [47].

In order to determine the perturbation of the impurity density on the magnetic surface we employ the density balance:

$$\frac{V_0}{r}\frac{\partial n_{1I}}{\partial\theta} + \frac{\Theta}{r}\frac{\partial}{\partial\theta}\left[n_I u_{I\|}(1+\varepsilon\cos\theta)\right] - \frac{c}{Br}\frac{\partial\varphi_1}{\partial\theta}\frac{dn_I}{dr}$$

$$- \frac{2c}{ZeBr}\varepsilon\sin\theta\frac{dp_I}{dr} - 2\varepsilon v_0\sin\theta = 0. \tag{5.10}$$

For simplicity, we neglect the gradient of the impurity density:

$$\frac{d\ln n_i}{dr} \gg \frac{d\ln n_I}{dr}\frac{1}{Z}. \tag{5.11}$$

Therefore, neglecting in the particle balance the small term containing φ_1, one obtains for the perturbation of the impurity density within the magnetic surface

$$\frac{n_{1I}}{n_I} = -\frac{2\varepsilon V_0\cos\theta}{v_0+\Theta\bar{U}_\phi} - \frac{\Theta\bar{u}_\phi}{v_0+\Theta\bar{u}_\phi}\varepsilon\cos\theta$$

$$-\frac{\Theta}{v_0+\Theta\bar{u}_\phi}\left[u^{(1)}_{I\|}(\theta)u^{(1)}_{i\|}(\theta)\right]. \tag{5.12}$$

This equation may be recast as

$$\frac{n_{1I}}{n_I} = -2\varepsilon\cos\theta - \frac{\Theta\tilde{u}^{(1)}_{I\|}(\theta)}{v_0+\Theta\bar{u}_\phi}, \tag{5.13}$$

where the parameter $\bar{U}^{(1)}_{I\|}(\theta)$ is defined as

$$\tilde{u}^{(1)}_{I\|}(\theta) = -\frac{2\varepsilon}{\Theta}\cos\theta\left(V_0+\Theta\bar{u}_\phi + \frac{c}{eB}\frac{d\ln n}{dr} - \frac{1}{2}\frac{c}{eB}\frac{dT_i}{dr}\right). \tag{5.14}$$

Employing in (5.13)–(5.14) the neoclassical value $V_\theta = V_\theta^{(\mathrm{NEO})}$ from Eq. (2.8), one obtains

$$\begin{aligned} \tilde{u}_{I\|}^{(1)}(\theta) &= \frac{4\varepsilon}{\Theta}\frac{c}{eB}\frac{dT_i}{dr}\cos\theta \\ \frac{n_{1I}}{n_I} &= -2\varepsilon\cos\theta\left(1-\frac{2\eta_i}{1+3/2\eta_i}\right), \end{aligned} \tag{5.15}$$

where $\eta_i = d\ln T_i/d\ln n$. In conclusion, the perturbation of the impurity density turns out to be of the order ε even within the framework of the standard neoclassical theory, which implies that the poloidal rotation is governed by the parallel viscosity of the main ions. Moreover, the resonance may emerge for an arbitrary V_0 provided the denominator in (5.13) tends to zero. This would result in a further enhanced perturbation of the impurity density, determined by terms which were neglected in the particle balance.

5.2. Radial transport of impurities

The flux of impurities is governed by the toroidal component of the friction force

$$\Gamma_I = cR_{iI}/(eB\Theta). \tag{5.16}$$

As usual, the toroidal component almost coincides with the parallel one, which is balanced by the projections of the poloidal electric field and the gradient of the pressure of impurities on a magnetic field surface. Upon averaging over magnetic surfaces the pressure gradient vanishes and only the drift in the poloidal electric field remains:

$$\Gamma_I = -\int_0^{2\pi}\frac{d\theta}{2\pi}(1+\varepsilon\cos\theta)^2\frac{c}{B}(n_{0I}+n_{1I})\frac{1}{r}\frac{\partial\varphi_1}{\partial\theta}, \tag{5.17}$$

where the poloidal electric field is assumed to be determined by Eq. (2.7), which has been derived without accounting for the

effect of impurities. Integrating, one obtains

$$\Gamma_I = -\sqrt{\frac{\pi}{2}}\varepsilon^2 \frac{T_e}{T_e+T_i}\frac{cm_i^{1/2}T_i^{1/2}n_I}{\Theta eBr}(V_0+\Theta\bar{u}_\phi)^{-1} \times\left(V_0+\Theta\bar{u}_\phi+\frac{1}{2}\frac{c}{eB}\frac{dT_i}{dr}+\frac{cT_i}{eB}\frac{d\ln n}{dr}\right) \times\left(V_0+\Theta\bar{u}_\phi+\frac{1}{2}\frac{c}{eB}\frac{dT_i}{dr}-\frac{cT_i}{eB}\frac{d\ln n}{dr}\right). \quad (5.18)$$

Hence, the impurity flux is largely convective and is directed inwards, provided there is a strong inward radial electric field (assuming the absence of a fast toroidal rotation). On the contrary, if a strong electric field is directed outward, then the impurity flux reverses to become positive. The neoclassical value of the poloidal rotation yields

$$\Gamma_I^{(\mathrm{NEO})} = -\sqrt{\frac{\pi}{2}}\frac{T_e}{T_e+T_i}\frac{cm_i^{1/2}T_i^{1/2}n_I}{\theta e^2B^2r}\frac{\eta_i}{1+\eta_i}\frac{dT_i}{dr}, \quad (5.19)$$

resulting in the inward flux. The magnitude of the total outflux of impurities given by Eq. (5.19) is of the order of the ion heat conductivity in the plateau regime. Since the impurity flux is governed by the toroidal friction force, it becomes intrinsically ambipolar, thereby implying the counter influx of main ions, $Z\Gamma_I = -\Gamma_i$. The impurity flux in the Pfirsch–Schlüter regime reads as follows [44]:

$$\Gamma_I^{(\mathrm{NEO})} = \frac{25c_2}{2c_1c_3}\frac{T_e}{T_e+T_i}\left(\frac{\nu_i}{\nu_{iI}}\right)^2\left(1+\frac{c_2^2\nu_i}{c_1c_3\nu_{iI}}\right)^{-2} \times\frac{\eta_i}{1+3\eta_i}n_Iq^2\frac{cm_i\nu_{iI}}{e^2B^2}\frac{dT_i}{dr}, \quad (5.20)$$

where c_1, c_2, c_3 are the kinetic coefficients given in [93], yielding $c_1 = 12.5$, $c_2 = 1.5$, and $c_3 = 0.29$.

For heavy impurities, the centrifugal force, caused, for example, by a fast toroidal rotation, forces an additional perturbation of the impurity density at larger major radii and may alter the radial transport described above.

6. Plasma rotation and flows within the scrape-off layer

6.1. Convection within the SOL in a tokamak with a poloidal limiter

At present, plasma edge physics is emerging as a major domain of tokamak physics research. On the one side the edge plasma interfaces with the core plasma and on the other side it interfaces with material boundaries. The plasma dynamics within the SOL is determined by a variety of concurrent physical effects. However, a unified theory addressing all phenomena occurring in the SOL plasma does not yet exist. Here, we focus on fundamental 3-D flows and the physical effects caused by them. Indeed, the 3-D electric field distributions and the resulting plasma convection are of fundamental physical importance because on the one side they affect confinement on closed field lines and on the other side determine the particle and energy fluxes onto the surrounding material elements. For example, the poloidal plasma rotation within the SOL is governed by a radial electric field. Indeed, in contrast to the plasma bulk, located inside the separatrix, the plasma potential outside the separatrix is primarily affected by a "line-tying" to a limiter or a divertor plate and can be easily found. Since the chaotic thermal flux of electrons to the limiter significantly exceeds the ion thermal flux, the electrons are trapped, thereby forcing a Boltzmann distribution on the plasma potential

$$\varphi = \frac{T_e}{e}\frac{(T_e/m_e)^{1/2}}{2\sqrt{\pi}\Gamma_{e\|lS}}, \tag{6.1}$$

where $\Gamma_{e\|lS}$ is the electron flux parallel to a magnetic field onto the limiter. Assuming that the limiter is insulated and there is no current flowing through it, one obtains $\Gamma_{e\|lS} = \Gamma_{i\|lS}$. On the other hand, employing the Bohm criterion for the ion flux onto the limiter [94],

$$\Gamma_{i\|lS} = 0.6\,(T_e/m_i)^{1/2}\,n, \tag{6.2}$$

one obtains the plasma potential given by the floating value

$$\varphi = \varphi_f = \frac{T_e}{e} \ln \left[0.47 \left(m_i/m_e\right)^{1/2}\right] . = k_T T_e/e \tag{6.3}$$

Since the electron temperature decreases outward, the resulting electric field is positive (directed outward) and is mostly governed by the profile of the electron temperature. The velocity of poloidal rotation resulting from the electric field given by Eq. (6.3) is

$$V_0^{(\mathrm{SOL})} = k_T \frac{c}{eB} \frac{dT_e}{dr}. \tag{6.4}$$

However, the plasma potential differs from the floating value if the effect of toroidicity is taken into account. This is due to the grounding of grad B drift by parallel currents in the SOL [95, 58]. Therefore, Eq. (6.3) is modified to read

$$\varphi = \frac{T_e}{e} \ln \frac{\left(T_e/m_e\right)^{1/2}}{\sqrt{2}\pi \left[0.6 \left(T_e/m_i\right)^{1/2} - j_{\|\mathrm{IS}}/en\right]}, \tag{6.5}$$

where the parallel current $j_{\|\mathrm{IS}}$ is to be defined later from the condition of global ambipolarity

$$2j_{\|\mathrm{IS}} + \int dl \nabla \cdot j_\perp = 0.$$

Considering only high q discharges and thereby obtaining almost straight field lines, we use

$$\nabla \cdot \mathbf{j}_\perp = \nabla \perp \cdot \left[\frac{c(\mathbf{B} \times \nabla p)}{B^2}\right] = c \frac{dp}{dr} \frac{\sin\theta}{BR}, \tag{6.6}$$

where θ is the poloidal angle coordinate. Substituting Eq. (6.6) into Eq. (6.5), one obtains for $j_\|$ smaller than the ion saturation current

$$j = \frac{T_e}{e} \left(k_T - \pi c \frac{dp}{dr} \left(\frac{m_e}{T_e}\right)^{1/2} \frac{\sin\theta}{eBn}\right). \tag{6.7}$$

The constraint that the parallel current be smaller than the ion saturation current reads

$$\pi \rho_{ci} \ll \delta, \tag{6.8}$$

where δ is the typical scale of a pressure profile within the SOL.

Note that the correction to the floating potential is positive in the lower half of the torus and negative in the upper half. Hence, the emerging poloidal electric field causes the $\mathbf{E} \times \mathbf{B}$ drift to be directed outward in the outer half of the torus and inward at the inner half, thereby causing poloidal asymmetries in the density profile. This effect enhances the well-known poloidal asymmetry of an anomalous transport, also favoring plasma losses at the larger major radius side of a tokamak. Indeed, it is now well documented that most, if not all, tokamaks exhibit strong poloidal asymmetries in the cross-field, turbulence-driven transport coefficients both for particles and energy [58]. The outflux through the outer part of the separatrix or the last close flux surface exceeds significantly the outflux through the inner half. The combined effect of the poloidal rotation and turbulence is addressed below. It is shown to result in displacement of the maximum of the density e-folding length in the direction of the ion grad B drift. This effect has been observed experimentally on the tokamak Alcator C [96].

Assuming anomalous transport to be of a diffusive nature and employing for a typical loss time scale $\tau = \pi R/C_S$, the model equation reads

$$-D\frac{\partial^2 n}{\partial x^2} + \frac{V_0}{r}\frac{\partial n}{\partial \theta}. = -\frac{n}{\tau}. \tag{6.9}$$

Here $x = r - a$, and V_0 is given by Eq. (6.4). $D(r, \theta)$ is approximated by $D = D_0 + D_1 \cos\theta$, where $D_1 \ll D_0$, thereby providing for the enhancement of a turbulent diffusion at the outer half of a tokamak. Thence, the perturbative method for solving Eq. (6.9) is employed:

$$n(x, \theta) = n_0(x) + n_1(x, \theta) = n_0(x) + n_1^*(x)\cos\theta + n_1^{**}(x)\cos\theta,$$

where the zero-order solution reads

$$n_0 = n_0(0)\exp(-x/\delta_0), \quad \delta_0 = \sqrt{D_0\tau}. \tag{6.10}$$

The first-order solution for the density perturbation in the com-

plex form $n_1(x,\theta) = p\exp(i\theta)$ reads

$$\frac{d^2p}{dx^2} + \omega_0^2 p = F,$$

where

$$\omega_0^2 = -\frac{1}{D_0}\left(\frac{1}{\tau} + \frac{iV_0}{r}\right), \qquad F = -\frac{D_1}{D_0}\frac{n_0}{\delta_0^2}.$$

For a constant V_0, the solution of Eq. (6.11) yields

$$\begin{aligned} n_1^* &= \frac{D_1}{D_0}\frac{1}{1+V_0^2\tau^2/r^2} n_0(0)\exp\left(-\frac{x}{\delta_0}\right), \\ n_1^{**} &= -\frac{D_1}{D_0}\frac{|V_0|\tau/r}{1+V_0^2\tau^2/r^2} n_0(0)\exp\left(-\frac{x}{\delta_0}\right). \end{aligned} \tag{6.11}$$

Here, it is taken into account that the radial electric field is positive within the SOL and the poloidal rotation is clockwise. From Eqs. (6.11) it follows that the poloidal location of the maximum of the density is at the poloidal angle θ given by

$$\theta = -\arctan\left(|V_0|\,\tau/r\right). \tag{6.12}$$

The maximum is shifted in the direction of the ion toroidal drift. Thus, the poloidal rotation has a significant effect provided $|V_0|\tau/r \geq 1$. This yields

$$\frac{k_T \pi \rho_{ci} R}{\delta_T r} \geq 1, \tag{6.13}$$

where δ_T is the typical scale of the temperature profile within the SOL and $k_T \approx 3$. This constraint may be easily fulfilled in real tokamaks, thereby providing the shift in density in the direction of the grad B drift. In addition, since the asymmetry of anomalous flux is maintained for the energy flow as well, the same analysis may be applied to the heat transport, with the resulting temperature being a function of the poloidal angle. Therefore, the plasma potential depends on the poloidal angle too, because the potential is a linear function of the temperature according to Eq. (6.3). Thus, the poloidal electric field emerges

in addition to the radial electric field discussed before. This poloidal electric field causes the radial drift. For a regime with high recycling $\delta_T \ll \delta_0$ the impact of this drift is small in comparison with the term $V_0 \partial n / r \partial \theta$. In reality, both effects have to be accounted for and the profiles $n(x,\theta)$ and $T(x,\theta)$ have to be obtained by numerical methods. The asymmetry with respect to the magnetic field has been demonstrated on tokamaks with a poloidal limiter. The ion side of the limiter has been more eroded than the electron side, thereby indicating a higher density and a directed motion along the main current (positive in our frame of reference). This effect can be derived from the particle and momentum balances as follows. Here, we neglect the effects of poloidal asymmetry in transport coefficients and toroidicity. Employing the toroidal component of the momentum balance, we have

$$m_i \frac{d(nu_{iz}^2)}{dz} + m_i \frac{\partial (nu_r^{(A)} u_{iz})}{r\partial r} = -\frac{\partial p}{\partial z} + \frac{1}{r}\frac{\partial \left(r\eta \frac{\partial u_{iz}}{\partial r}\right)}{r\partial r} + \frac{1}{c} j_r B_\theta. \quad (6.14)$$

For simplicity, we assume that $T_e = T_i = T$ and neglect the parallel viscosity as compared with the pressure gradient; the z axis denotes the toroidal coordinate $R\phi$. The parallel component of the momentum balance is

$$m_i \frac{d\left(nu_{iz}u_{i\|}\right)}{dz} + m_i \frac{\partial \left(nu_r^{(A)} u_{i\|}\right)}{r\partial r} = -\frac{\partial p}{\partial z} + \frac{1}{r}\frac{\partial \left(r\eta \frac{\partial u_{i\|}}{\partial r}\right)}{r\partial r}. \quad (6.15)$$

Taking into account the relation between the poloidal and the toroidal rotations, which easily follows from the radial component of the momentum balance, we get

$$u_{i\theta} = V_0 + u_{pi} + \Theta u_{iz}, \quad (6.16)$$

where

$$V_0 = -\frac{cE_r}{B}, \quad u_{pi} = \frac{c}{eBn}\frac{dp_i}{dr},$$

The parallel and the toroidal component are related as

$$u_{i\|} = u_{iz} + \Theta u_{i\theta}. \quad (6.17)$$

We integrate Eq. (6.15) along z and take into account that $u_{iz}^{\pm} = \pm C_S^{\pm}$, according to the Bohm criterion, where $C_S = \sqrt{2T_i/m_i}$ and $+$ and $-$ correspond to different sides of the limiter. Employing (6.16), we obtain

$$p^- - p^+ = -\frac{m_i C_S}{2}\left(n^+ + n^-\right)\left(\Theta V_0 + \Theta u_{pi} + \bar{u}_\phi\right) + \pi R m_i n u_r^{(A)} \frac{\partial \bar{u}_\phi}{\partial r} - \frac{\pi R}{r}\frac{\partial\left(r\eta \frac{\partial \bar{u}_\phi}{\partial r}\right)}{r\partial r}. \quad (6.18)$$

The integration of the toroidal component Eq. (6.14) yields

$$\begin{aligned} I = 2\pi r \int j_r dz = \frac{m_i c}{B_\theta} 2\pi r \Big\{ & -(n^+ + n^-)(V_0 + u_{pi})\Theta C_S \\ & + (n^- - n^+)\Theta 2 C_S^2 - 2\pi r n \Theta u_r^{(A)} \frac{\partial\left(V_0 + u_{pi} + \Theta \bar{u}_\phi\right)}{\partial r} \\ & + \frac{2\pi R}{m_i r}\frac{\partial}{\partial r}\left[r\eta \frac{\partial (V_0 + u_{pi} + \Theta \bar{u}_\phi)}{\partial r}\right] \\ & + \left(V_0 + u_{pi} + \Theta \bar{u}_\phi\right)\Theta C_S \left(n^+ + n^-\right)\Big\}. \end{aligned}$$

We employ the particle balance

$$\frac{\partial n u_{iz}}{\partial z} = -\frac{1}{r}\frac{\partial\left(r n u_r^{(A)}\right)}{\partial r} = Q.$$

Integrating the continuity equation along z and assuming the source Q to be constant, we obtain

$$n u_{iz} = Qz + \frac{n^+ - n^-}{2} C_S, \quad (6.19)$$

where the integration constant has been determined by boundary conditions. Assuming now the temperature to be a constant along field lines, we employ Eq. (6.18) to yield the difference in densities in the expression for the current and Eq. (6.19).

Then, assuming that $n^{\pm} \approx \bar{n} \approx n$ and combining the average of Eq. (6.19) with the current, we obtain

$$I = -\frac{m_i c}{B} 4\pi^2 r R \left[n u_r^{(A)} \frac{\partial (V_0 + u_{pi} + \Theta \bar{u}_\phi)}{\partial r} + \frac{1}{m_i r} \frac{\partial}{\partial r} \left[r\eta \frac{\partial (V_0 + u_{pi} + \theta \bar{u}_\phi)}{\partial r} \right] \right],$$

$$p^- - p^+ = -2 m_i n C_S \bar{u}_\phi. \tag{6.20}$$

Note that on the LCFS the total radial current has to cancel. Therefore one obtains

$$\bar{u}_\phi = -\frac{V_0 + u_{pi}}{\Theta}. \tag{6.21}$$

Hence, the average motion along the main plasma current emerges on the LCFS. Moreover, this motion also exists in the bulk of the SOL penetrating due to viscosity and inertia.

We employ the poloidal rotation velocity given by Eq. (6.4):

$$\frac{\bar{u}_\phi}{C_S} = \frac{cT}{\Theta e B C_S} \left[\frac{d \ln T}{dr} (k_T + 1) + \frac{d \ln n}{dr} \right].$$

In order of magnitude the ratio yields $\approx 3\rho_{ci}/(\Theta \delta_T)$, where δ_T is the typical scale of the temperature profile within the SOL. It may attain the order 1 in a tokamak, thereby resulting in an average plasma flow with approximately the speed of sound. Therefore, the parallel density profile is strongly nonuniform along z. The flow is directed along the main plasma current. Equation (6.21) is warranted on the LCFS. However, this effect is maintained in the SOL because of perpendicular anomalous viscosity and inertia. Furthermore, the effect is synergetic with the effects of the poloidal asymmetry of turbulent transport and the toroidicity. Yet, qualitatively, the plasma flows in the direction of the ohmic current.

6.2. Flows within the SOL in a tokamak with a divertor

Convection of plasma, resulting from the electric field, is also fundamental for tokamaks with a divertor. This has been

asserted recently by a number of authors [97–101]. Therefore, in our opinion models addressing the plasma dynamics in the SOL have to be three dimensional. Two different approaches to describing the plasma potential have been suggested so far. The first employs the fluid approach [98–101]. Indeed dotting with B the momentum balance for electrons, we obtain

$$en\frac{\partial\varphi}{\partial z} - \frac{\partial p_e}{\partial z} - 0.51 m_e n \nu_{ei}\,(u_{ez} - u_{iz}) - 0.71 n \frac{\partial T_e}{\partial z} = 0.$$

For a high recycling, the plasma motion is assumed to be significantly subsonic, thereby implying $p_e = \mathrm{const}\,(z)$. In the absence of a parallel current, we have

$$\varphi = 0.71 T_e(0)/e - 0.71 T_e(B)/e + \Delta\varphi_{sh}. \qquad (6.22)$$

Here, $\Delta\varphi_{sh}$ is the sheath potential of a divertor plate, $T_e(B)$ is the temperature in the plate's vicinity, and $T_e(0)$ is the temperature in the SOL's bulk. The underlying geometry is shown in Fig. 6.1.

Similarly, the potential may be counted from the plate A. The sheath potential, in the absence of current, is given by $\Delta\varphi_{sh} = k_T T_e(B)/e$. If $T_e(0) \gg T_e(B)$, Eq. (6.22) yields $j = 0.71 T_e(0)/e$. This potential results in the following radial electric field and poloidal drift, because the temperature is a function of the radius:

$$V_0^{(\mathrm{SOL})} = \frac{c}{B}\frac{d\varphi}{dr} = 0.71\,\frac{c}{eB}\frac{dT_e(0)}{dr}.$$

Assuming very large parallel heat conductivity, the poloidal electric field cancels within the framework of this model. This is shown by numerical methods in [101]. A different, more realistic approach has been developed in [97]. Indeed, in reality, the electron mean free path is not significantly less than the typical scales of variation of plasma parameters along a field line. This is borne out in JET, especially in the H regime [102]. Moreover, even when the mean free path of thermal electrons turns out to be much less than the connection length, this is not true for electrons with energies of the order $3T_e$, which are well known to

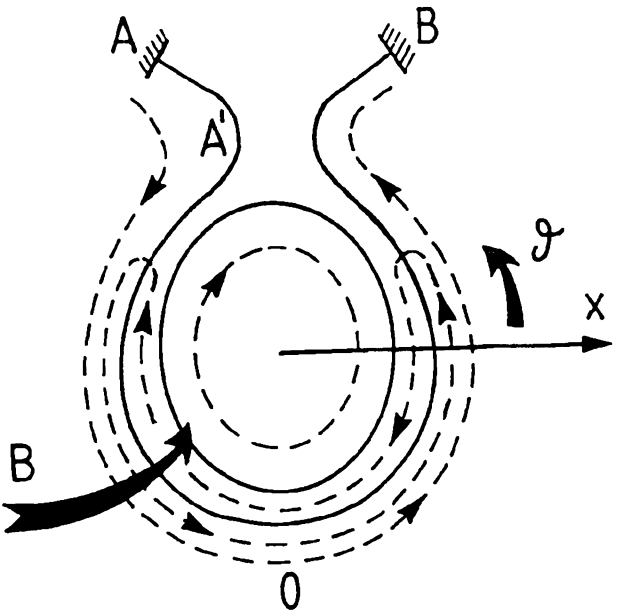

Fig. 6.1. Schematic plot of a single-null configuration. A and B are the inner and outer divertor plates. Below the straightened field line, the coordinate x denotes the radial direction. Directions of drifts in electric and magnetic fields are shown by arrows both inside and outside the separatrix.

contribute mostly to the heat conduction along field lines [103]. Therefore, a much better approximation results when the nonlocal approximation is employed in the heat balance for electrons [101, 103]. Furthermore, the plasma potential is not determined locally as well, because hot electrons may reach a plate directly from the hot plasma. The constraint on the hydrodynamic description is very stringent, $\lambda/L \ll 10^{-2}$ [103], where λ is the mean free path and L is the typical scale. Therefore, the focus is on the opposite case when all hot electrons from the SOL hit a divertor plate. Hence, the potential at an arbitrary point with

density n within the SOL reads

$$\varphi = \frac{T_e}{e} \ln \left[\frac{n(T_e/me)^{1/2}}{(2\pi)^{1/2}\Gamma_{e\|\|S}} \right], \tag{6.23}$$

where $\Gamma_{e\|\|S}$ is the electron flux onto a divertor plate. In the absence of current, it is

$$\Gamma_{e\|\|S} = 0.6 n_c (T_{ec}/m_i)^{1/2}, \tag{6.24}$$

equal to the ion flux at a plate, where n_c, T_c are the density and temperature on a plate.

Employing the assumption that the flow is significantly subsonic, the pressure is almost constant along a field line and $nT_e = ncT_{ec}$. Then Eq. (6.24) yields

$$\varphi = \frac{T_e}{e} \left[k_T - 0.5 \ln \left(\frac{T_e}{T_{ec}} \right) \right]. \tag{6.25}$$

The potential given by Eqs. (6.23) or (6.25) and (6.22) yields the radial electric field, thereby causing poloidal drift even within the framework of the fluid approach. The main difference between the fluid and kinetic approaches bears on the value of the numerical factor k_T. Moreover, the potential given by Eq. (6.23) and $nT_e \neq n_c T_{ec}$ causes a poloidal electric field due to inhomogeneity of the density. Therefore, the electric drifts are borne out as shown in Fig. 6.2.

Note that the direction of poloidal rotation inside the separatrix is determined by different effects, as discussed above, and is in the opposite direction compared to the SOL. The magnitude of poloidal drift within the SOL may be of the order of the parallel flow resulting from the pressure gradient. For the case of strong recycling, even hot electrons may not reach the divertor plates. Then the flux of hot electrons flowing from the SOL onto the plates becomes compensated by cold electrons extracted from the plates by a parallel electric field. This case is considered in [104, 105]. The sheath emerging between cold and hot plasmas is obtained from

$$\varphi = k_T \frac{T_e}{e}, \quad \text{where} \quad k_T = 1.7 - 1.8 \tag{6.26}$$

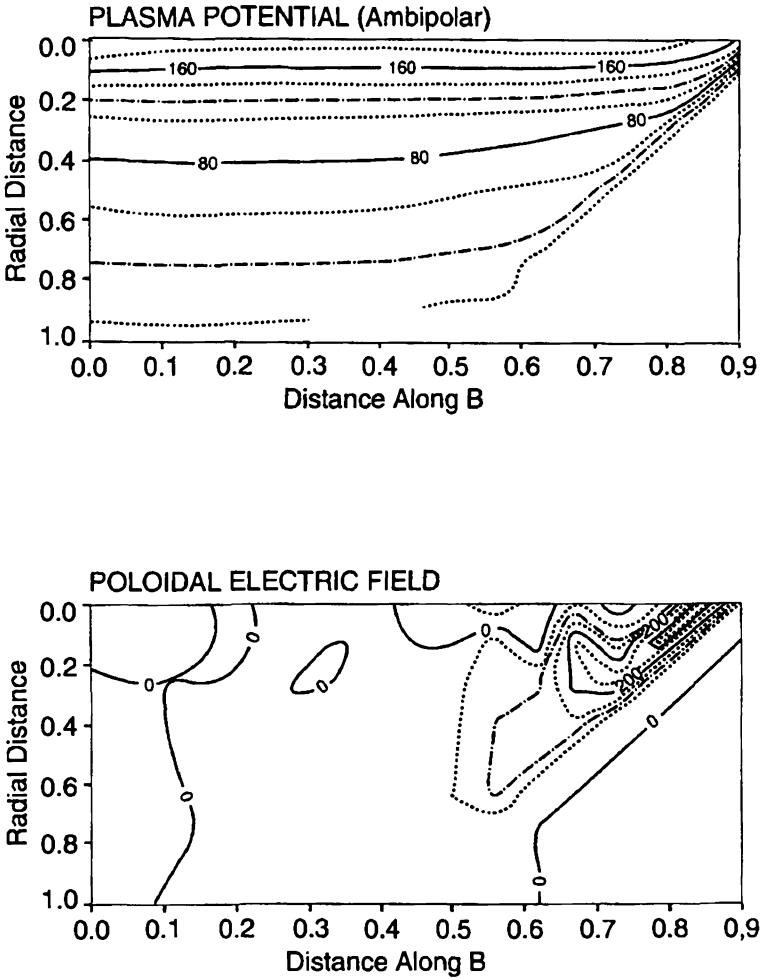

Fig. 6.2. Plasma potential and the poloidal electric field within the SOL. The abscissa is the distance along the poloidal B field, the ordinate is the flux surface coordinate. The separatrix is at the top, the first wall is at the bottom, the divertor plate is to the right, the median plane between plates is to the left. The divertor region is to the right of $x = 0.5$. The potential is measured in eV/e, the poloidal field is in V/m.

for hydrogen and deuterium, respectively. Therefore, the model demonstrates that the electric potential of hot plasmas with respect to cold plasmas is also determined by the temperature of hot electrons (with accuracy T_{ec}/e with respect to the divertor plates). Note that the model is also applicable to cold electrons because they are accelerated by the electric field reaching sufficiently high temperatures, thereby providing for a collisionless constraint. In summary, all of the above models predict the same order of magnitude for the electric field, as follows from Eqs. (6.22), (6.25)–(6.26). Thus, the plasma flow in a divertor is primarily governed by the poloidal rotation, thereby becoming poloidally asymmetric [97]. This is shown in Fig. 6.3, where the flux of particles and energy (the heat flux is mainly carried by particles) onto the outer plate significantly exceeds the one onto the inner plate.

Therefore, the outer divertor plate is more loaded than the inner one, even when the heat flux through the separatrix is assumed to be poloidally symmetric. This effect was demonstrated on JET [102] and some other tokamaks. In contrast to the case shown in Fig. 6.1, a reversal of the toroidal magnetic field results in equilibration of the heat loads on the plates, as demonstrated on JFT-2M [106] and JET. The results of [97] were borne out in numerical studies described in [101]. There it was shown that the particle flow far from plates is governed mainly by the poloidal drift in the radial electric field (see Figs. 6.2–6.3 computed for the double null configuration in Alcator-C MOD). Indeed, the poloidal flux is due to poloidal rotation within X-points (less than 0.5 in Figs. 6.2–6.3), but outside X-points, within the private region the poloidal flux results from the pressure gradient. However, the effect of poloidal rotation on the density profile resulting from the particle balance has been overlooked in [101]. Indeed, the value V_0+u_{pi} appears in the continuity equation and thereby affects the density profile. Because of this, the profiles of toroidal velocity were incorrectly found to be symmetric with respect to the equatorial plane. In contrast, the effect of rotation causes an asymmetric toroidal flux and density profile. This fact is elaborated below. We take the potential with respect to the plate B as

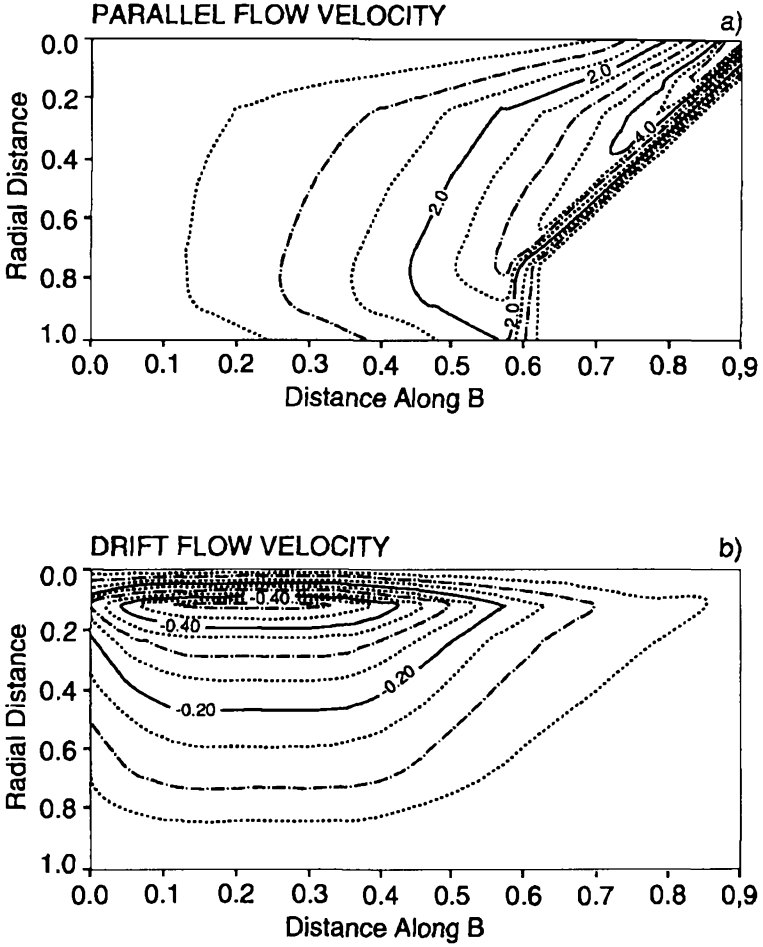

Fig. 6.3. Parallel and drift velocity $(V_0 + u_{pi})$ contours in 10^4 m/sec units. It is demonstrated that the parallel velocity is small and the poloidal velocity is large within the bulk of the SOL.

$$\varphi = \frac{T_e}{e} \ln n/n_{b'} + \delta\varphi(B', B), \tag{6.1}$$

where $\delta\varphi(B', B)$ is yielded by Eqs. (6.23)–(6.24), (6.26) or may be modified in order to account for collisions. It is asserted that

Eq. (6.27) is warranted within the bulk of the SOL because the electron temperature is almost constant along the field line due to the high parallel heat conductivity. Thus, the density profile is determined by the particle balance

$$\nabla\perp\cdot\Gamma_{i\perp}+\frac{\Theta\partial}{r\partial\theta}\left(nu_{i\|}\right)=P-\frac{\partial}{r\partial r}\left(rnu_r^{(\mathrm{A})}\right)=Q, \qquad (6.28)$$

where P is a source due to ionization and $u_r^{(\mathrm{A})}$ is the velocity of anomalous transport. $\Gamma_\perp$ is the convective flux which contains both radial and poloidal components

$$\Gamma_{i\perp}=\frac{c}{eB^2}\left[\mathbf{B}\times\nabla p_i\right]+\frac{c}{nB^2}\left[\mathbf{B}\times\nabla\varphi\right].$$

Substituting $\Gamma_{i\perp}$ into Eq. (6.28) we obtain

$$\frac{V_0^{(\mathrm{eff})}}{r}\frac{\partial n}{\partial\theta}+\frac{\Theta}{r}\frac{\partial u_{i\|}}{\partial\theta}=Q, \qquad (6.29)$$

where

$$V_0^{(\mathrm{eff})}=-\frac{c}{eB}\left(1+\ln\frac{n}{nb'}+\frac{e\delta\varphi}{T_e}\right)\frac{\partial T_e}{\partial r}.$$

Thus, the convective terms result in the effective poloidal particle flux, thereby shifting the maximum density out of the midplane and causing the asymmetries in the particle and heat fluxes to the divertor plates.

6.3. The impact of the biasing radial electric field on parameters of the SOL

A strong radial electric field can be induced within the SOL in a divertor tokamak by applying a voltage to the divertor plates with respect to the first wall. This biasing scheme results in a strong radial electric field much larger than the natural electric field discussed above. Experiments employing the biasing scheme were carried out on the tokamak TdeV [108]. Many

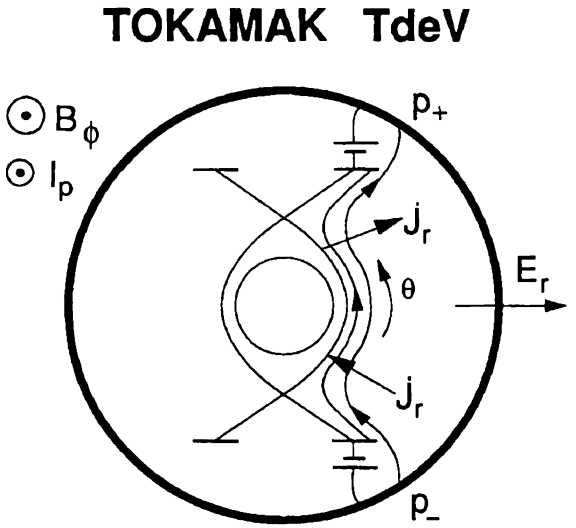

Fig. 6.1. The radial electric field is brought about by biasing of the divertor plates with respect to the first wall. The direction of the current carried by ions is shown by arrows for a positive E_r.

interesting effects, such as modifications of the density profile and radial transport of impurities as a function of the polarity and the magnitude of the biasing voltage, the emergence of the average toroidal rotation proportional to the applied voltage, redistribution of the plasma outflow onto divertor plates, and so on, were reported to result from the biasing. Furthermore, in contrast to studies carried out employing another biasing scheme and resulting in a poloidal electric field, a strong radial electric field has been shown to affect the SOL much more significantly than the poloidal electric field [109]. Here, we aim to show that the main effects observed experimentally follow from the analysis in which continuity and momentum balances are adopted, invoking anomalous viscosity and inertia [110]. For simplicity, we consider the double-null configuration with circular magnetic surfaces shown in Fig. 6.4.

The continuity equation (6.29) is adopted. The radial current is obtained from the current continuity equation

$$\frac{1}{r}\frac{\partial j_\theta}{\partial \theta} + \frac{1}{r}\frac{\partial (r j_r)}{\partial r} = 0.$$

We employ toroidal and parallel components given by

$$\frac{m_i}{r}\frac{\partial \left(r n u_r^{(A)} u_{i\phi}\right)}{\partial r} + \frac{m_i}{r}\frac{\partial \left(n u_{i\theta} u_{i\phi}\right)}{\partial \theta} = -\left(\nabla \cdot \overleftrightarrow{\pi}_i\right)_\phi + \frac{1}{c} j_r B_\theta, \quad (6.30)$$

$$\frac{m_i}{r}\frac{\partial \left(r n u_r^{(A)} u_{i\|}\right)}{\partial r} + \frac{m_i}{r}\frac{\partial \left(n u_{i\theta} u_{i\|}\right)}{\partial \theta} = -\left(\nabla \cdot \overleftrightarrow{\pi}_i\right)_\| - \nabla_\| p. \quad (6.31)$$

The parallel and toroidal velocities are related by

$$u_{i\|} = u_{i\phi} + \Theta u_{i\theta}.$$

Moreover, the following relation is maintained within the SOL:

$$u_{i\theta} = V_0 + u_{pi} + \Theta u_{i\phi}, \quad (6.32)$$

which follows from the radial component of the momentum balance. Note that Eq. (6.32) is valid locally. Assuming that the potential brought about by biasing significantly exceeds T_e/e, one obtains that the radial distribution of the plasma potential is governed by the potential drop on plates and thereby determines the velocity of poloidal rotation V_0. For given values of V_0, the radial electric field results in a much larger value than the poloidal electric field.

Combining Eqs. (6.31) and (6.32) and neglecting a weak parallel viscosity compared with the pressure gradient, one obtains

$$\frac{1}{r} j_r B_\theta = -\frac{\Theta}{r}\frac{\partial p}{\partial q}. \quad (6.33)$$

Note that the effects owing to toroidicity were neglected. Integrating (6.33) over a magnetic surface, the total current is obtained as

$$I = \frac{2\pi R c}{B}\left(p_- - p_+\right), \quad (6.34)$$

where p_- and p_+ are plasma pressures at the ends of a magnetic line, tying either to a divertor plate or the first wall (see Fig. 6.4). Equation (6.34) describes the case where a strong radial electric field and current are induced only at the outer half of the torus. If the same voltage is applied at the inner half, the current given by Eq. (6.34) has to be amplified by a factor of 2. Qualitatively, Eq. (6.33) yields opposite currents at the upper and lower halves of a magnetic surface, resulting in the total current being governed by the pressure asymmetry in the vicinity of the material surface. Flux-surface averaging Eq. (6.31) and neglecting the classical viscosity, one gets

$$\frac{\pi m_i}{r}\frac{\partial\left(rnu_r^{(A)}\bar{u}_{i\|}\right)}{\partial r}+\frac{m_i}{r}\left(n^+u_{i\theta}^+u_{i\|}^+-n^-u_{i\theta}^-u_{i\|}^-\right)$$
$$=\frac{\Theta}{r}(p_+-p_-)-\pi\langle\left(\nabla\overleftrightarrow{\pi}\right)_{\|}^{(AN)}\rangle. \tag{6.35}$$

Here, $\bar{f}=\int f d\theta/\pi$ stands for the averaging over the outer half of a magnetic surface, $u_{i\|}=\bar{u}_\phi$ is the average toroidal velocity, and the anomalous viscosity is determined by Eq. (1.34). Focusing on the intersection with the material boundary, one may employ the Bohm criterion for the poloidal velocity component, provided the biasing electric field is not too strong, $|V_0|<\Theta C_S$. The derivation of the criterion can be carried out based on a similarity with the case without a magnetic field. Hence, at the interface with the material boundary plasma flows with the speed of sound along a field line according to the Bohm criterion. Thus

$$u_{i\theta}^{\pm}=\pm\Theta C_S^{\pm};\quad C_S=\sqrt{(T_e+T_i)/m_i}. \tag{6.36}$$

Accounting for Eq. (6.32), one obtains

$$V_0+u_{pi}+\Theta u_{i\|}^+=\Theta C_S^+, \tag{6.37}$$
$$V_0+u_{pi}+\Theta u_{i\|}^-=-\Theta C_S^-.$$

Note that Eqs. (6.36)–(6.37) are valid only when the velocity V_0 happens to be much smaller than ΘC_S. Then the parallel electric field affects slightly the parallel velocity of ions as

compared to the case $V_0 = 0$. Yet, a more general condition $|V_0| \geq \Theta C_S$ unfolds if the electric field is increased even further. It is worthwhile to emphasize again that V_0 is a constant along a field line because a strong electric field is applied externally. Substituting boundary conditions into Eq. (6.35), one obtains

$$p^+ - p^- = \frac{m_i (V_0 + u_{pi})}{2\Theta} \left(n^+ C_S^+ + n^- C_S^-\right) - \frac{\pi m_i}{2\theta} \frac{\partial \left(r n u_r^{(A)} \bar{u}_{i\phi}^-\right)}{\partial r} + \frac{\pi}{2\Theta} \frac{d\left(r\eta \frac{d\bar{u}_\phi}{dr}\right)}{dr}. \quad (6.38)$$

Substituting the current given by Eq. (6.34) into Eq. (6.38), one obtains

$$I = -\frac{\pi R c m_i (V_0 + u_{pi})}{B\Theta} \left(n^+ C_S^+ + n^- C_S^-\right) + \frac{\pi 2 R c m_i}{2\Theta} \frac{\partial \left(r n u_r^{(A)} \bar{u}_{i\phi}^-\right)}{\partial r} - \frac{\pi}{2\Theta} \frac{d\left(r\eta \frac{d\bar{u}_\phi}{dr}\right)}{dr}. \quad (6.39)$$

In order to close the system we employ the continuity equation

$$\frac{1}{r} \frac{\partial u_{i\theta}}{\partial \theta} = Q. \quad (6.40)$$

Here, we have neglected the neoclassical radial transport. Integrating over the field line, one obtains

$$n (V_0 + u_{pi} + \Theta u_\phi) = \int Q(\theta) r d\theta + C. \quad (6.41)$$

The constant C is determined by boundary conditions at the ends of a field line interfacing with the material surface

$$n^+ \left(V_0 + u_{pi} + \Theta u_\phi^+\right) = \int Q d\theta + C = n^+ \Theta C_S^+, \quad (6.42)$$

$$n^- \left(V_0 + u_{pi} + \Theta u_\phi^-\right) = -\int Q d\theta + C = -n^- \Theta C_S^+.$$

The sum of Eqs. (6.42) yields the constant C, provided the symmetry with respect to the midplane is maintained:

$$C = \frac{n^+ C_S^+ - n^- C_S^-}{2} \Theta. \quad (6.43)$$

Assuming the temperatures to be equal at the ends of a magnetic field line $T_e^{\pm} = T_i^{\pm} = T_c$, one obtains C as a function of the radial current I from Eq. (6.34):

$$C = -\frac{IB_\phi\Theta}{4\sqrt{2}\pi RcT_c^{1/2}m_i^{1/2}}. \tag{6.44}$$

Now Eqs. (6.41)–(6.44) yield the relation between the toroidal velocity in the equatorial plane $u_\phi(\theta = 0)$, measured experimentally, the radial electric field, and the total current I. Substituting Eq. (6.44) into Eq. (6.41) and taking $\theta = 0$, one obtains

$$V_0 + u_{pi} + \Theta u_\phi(0) = -\frac{IB_\phi\Theta}{4\sqrt{2}\pi Rn(0)cT_c^{1/2}m_i^{1/2}}. \tag{6.45}$$

In low recycling divertors, the toroidal velocity at the midplane $u - \phi(0)$ is of the same order as the toroidal rotation velocity $\bar{u}_\phi$ in Eq. (6.39). Hence, the system of Eqs. (6.39) and (6.45) yields the magnitude and profile of the toroidal rotation velocity and the current for a given radial profile of the electric field. A more accurate solution may be obtained numerically by solving the system of equations (6.31)–(6.41) for a given distribution of Q.

If the radial scale of the toroidal rotation profile δ_u is larger than the SOL width δ (this is the case in experiments on TdeV [108]), then one obtains from Eqs. (6.39)–(6.45), assuming $\bar{u}_\phi \approx u_\phi(0)$,

$$V_0 + u_{pi} + \theta u_\phi(0) \approx 0. \tag{6.46}$$

However, all the terms in Eqs. (6.39)–(6.45) are of the same order, provided $\delta_u \approx \delta$, and the system has to be solved numerically. Equation (6.46) yields the dependence of toroidal velocity on the applied voltage, which is in good agreement with that measured on TdeV (see Fig. 6.5). Note that in the absence of the external bias, Eq. (6.46) is satisfied exactly. This implies that the toroidal rotation velocity emerges within the SOL coparallel to the ohmic heating current even when the radial current through separatrix is equal to zero. The same effect has been shown to emerge for a poloidal limiter. The main reason is the positive

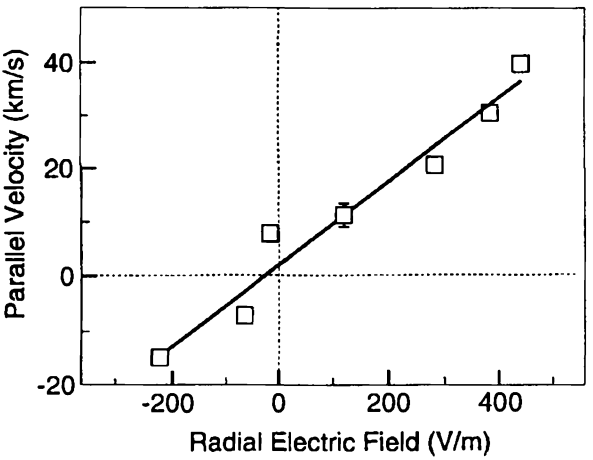

Fig. 6.5. The parallel rotation velocity as a function of the radial electric field observed on the tokamak TdeV.

natural electric field existing within the SOL. The value of the current is obtained from (6.39)–(6.45), for $|n^+ - n^-| \ll n^\pm = n_c$, as

$$I = \frac{[1 - 0.5e^{0.5}]^{-1}\,\pi 2Rcr}{\Theta B}\left[nu_r^{(A)}m_i\frac{\partial \bar{u_{i\phi}}}{\partial r} - \frac{d\left(r\eta\frac{d\bar{u}_\phi}{dr}\right)}{rdr}\right]. \quad (6.2)$$

Here, the relation $n_c/n(0) = \exp(-0.5)$, which follows from the parallel momentum balance, has been employed. Note that Eq. (6.47) is qualitatively the same as Eq. (1.36), yielding the profile of the toroidal rotation velocity caused by a biased electrode inside the separatrix. However, quantitatively, the cross-field radial conductivity turns out to be much larger outside the separatrix within the SOL. Indeed, employing in (6.39) $\bar{u}_\phi = -(V_0 + u_{pi})/\Theta$, one obtains

$$I = \frac{k\pi^2 Rnm_i^{1/2}T_i^{1/2}c^2}{\Theta B^2}\left(E_r - \frac{dp_i}{endr}\right), \quad (6.3)$$

where k is a coefficient of the order 1. A comparison with the voltage–current characteristics measured on TdeV yields $k \approx 2$..

The linear dependence of current on the electric field is maintained unless the pressure asymmetry on the ends of the magnetic field line becomes significant, $n^+ - n^- \approx \max(n^+, n^-)$. Equation (6.34) yields the maximum value of the total radial current

$$I^{(\max)} = \frac{4\pi RcnT_i}{B}, \tag{6.49}$$

which is obtained for the electric field

$$|V_0| \approx \Theta C_S. \tag{6.50}$$

The Bohm criterion under this circumstance takes the form of the inequality

$$|u_\theta^\pm| \geq \Theta C_S. \tag{6.51}$$

If $|V_0| > \Theta C_S$, the bulk of the plasma on a given magnetic surface gets carried away onto a divertor plate with velocity V_0, thereby yielding

$$\pi \frac{d\left(rnu_r^{(A)}\right)}{dr} \approx n^- V_0, \qquad E_r > 0,$$
$$\pi \frac{d\left(rnu_r^{(A)}\right)}{dr} \approx n^+ V_0, \qquad E_r < 0.$$

On the other hand, the density is small on the opposite plate. For example, the continuity equation shows that the plasma density is a linear function of θ. The parallel component of the momentum balance when $|V_0| > \Theta C_S$ is

$$m_i V_0 u_{i\|} + (T_e + T_i) \ln n = \text{const}. \tag{6.52}$$

Since the maximum attainable velocity $u_{i\|} + = -C_S$ for $E_r < 0$, the parallel ion velocity does not change significantly, as follows from Eq. (6.52). Therefore $n^+/n(0) = 2$ because of the linear density dependence. Furthermore, the parallel ion velocity is almost uniform and of the order C_S:

$$u_{i\|}(0) \approx u_\phi(0) = -C_S. \tag{6.53}$$

When $n \to n^-$ the velocity $u_{i\|}$ becomes supersonic, thereby providing

$$V_0 + \Theta u_{i\|}^- = \Theta C_S. \tag{6.54}$$

Equations (6.52)–(6.54) yield the small density n^-. If $E_r > 0$, one obtains by direct analogy $u_\phi(0) = C_S$. In summary, the velocity of the toroidal rotation saturates at the sound speed in the equatorial plane and does not depend on the biasing electric field anymore when $|V_0| > \Theta C_S$.

Moreover, when these large values of the electric field are reached, a substantial redistribution of the plasma outflow between divertor plates occurs. When $E_r > 0$, the preferential outflow takes place into the low divertor chamber for the direction of the magnetic field shown in Fig. 6.4. The effect has been demonstrated on TdeV. In the high recycling regime, the situation remains essentially the same. The maximum velocity averaged over the magnetic surface is obtained from $u_r = j_r/en$ as

$$u_r^{(\max)} = \frac{2cT_i}{erB}, \tag{6.55}$$

which yields a ratio of $u_r^{(\max)}$ to the anomalous transport $u_r^{(A)}$ of the order 1:

$$\frac{u_r^{(\max)}}{ur^{(A)}} \approx \frac{\pi \rho_{ci}}{\Theta \delta} \leq 1. \tag{6.56}$$

Therefore, the following important effect results from this estimate. The option to control the density profile within the SOL by imposing a strong electric field of the order $V_0 \approx \Theta C_S$ arises. A negative polarity of the bias results in a more uniform profile and a positive polarity results in a steeper one. This effect has also been observed on TdeV.

Finally, to address the impurity transport, the toroidal and the parallel components of the momentum balance are employed:

$$\frac{m_I}{r}\frac{\partial\left(rn_I u_{rI}^{(A)} u_{I\phi}\right)}{\partial r} + \frac{m_I}{r}\frac{\partial\left(n_I u_{I\theta} u_{I\phi}\right)}{\partial\theta} = -\left(\nabla \overleftrightarrow{\pi}\right)_{I\phi} + \frac{1}{c} j_{Ir} B_\theta - m_I n_I \nu_{Ii}\left(u_{I\phi} - u_{i\phi}\right), \tag{6.57}$$

$$\frac{m_I}{r}\frac{\partial\left(rn_I u_{rI}^{(A)} u_{I\|}\right)}{\partial r} + \frac{m_I}{r}\frac{\partial\left(n_I u_{I\theta} u_{I\|}\right)}{\partial\theta}$$
$$= -\left(\nabla\overleftrightarrow{\pi}\right)_{I\|} - \nabla_\| p_I - Zen_I\nabla_\|\varphi$$
$$- m_I n_I \nu_{Ii}\left(u_{I\phi} - u_{i\phi}\right). \tag{6.58}$$

Neglecting viscosity terms compared to pressure and the small difference between $u_{i\|}$ and $u_{i\phi}$, one obtains for the current due to impurities

$$j_{Ir} = -\frac{c}{Br}\left(\frac{\partial pI}{\partial\theta} + Zn_I T_e\frac{\partial\ln n}{\partial\theta}\right). \tag{6.59}$$

Assuming that $T_e = T_I = T = \text{const}\,(\theta)$ and the Boltzmann distribution of impurities within a magnetic surface is $n_I/n = \text{const}\,(\theta)$, one obtains after averaging

$$I_{rI} = \frac{1+Z}{Z} I\frac{n_I}{n}, \tag{6.60}$$

where I is the current carried by ions. Thus, the average outflow velocity of impurities is equal, up to accuracy of the coefficient $(1+Z)/Z$, to the radial transport of the main ions driven by the electric field.

Conclusions

In summary, the fundamental concepts on plasma rotation in tokamaks are as follows. The velocity of poloidal rotation is given by the neoclassical equation (1.30) during the L-mode in the ohmic heating or balanced neutral beam injection regimes. However, the toroidal rotation remains negligible in Eq. (1.12) in contradiction to the predictions of neoclassical theory. Indeed, the velocity of toroidal rotation is limited by the anomalous inertia and viscosity and therefore does not agree with the neoclassical theory. In other words, the radial electric field is determined by the neoclassical expression (4.20) with

zero toroidal velocity and corresponds to a negative potential in the core with respect to the separatrix. In contrast, the radial electric field changes sign within the SOL because the electric field potential is proportional to the electron temperature, which decreases outward. However, the velocity of toroidal rotation increases when unbalanced neutral beam injection is employed, whereas the velocity of poloidal rotation remains almost the same with a slightly varying numerical coefficient given by Eq. (2.44). The toroidal relaxation is determined by anomalous cross-field transport, whereas the poloidal relaxation is well described by the neoclassical theory provided the departure from equilibrium remains weak. In contrast, departing strongly from the neoclassical equilibrium the poloidal relaxation is changed drastically. The theory presented yields both steep and gradual (neoclassical) profiles for the poloidal rotation velocity at the edge but inside the separatrix. They correspond to the H and L regimes of confinement, respectively. Steep profiles result because the anomalous inertia and viscosity terms are of the order of the neoclassical parallel viscosity. Thence, the shear of poloidal rotation suppresses the anomalous transport and causes a steepening of density and temperature profiles, thereby improving the global confinement. Yet, temporal details of the L–H and H–L transitions remain elusive. The bifurcation is sensitive to the initial conditions and the value of the velocity of poloidal rotation on the separatrix. The latter is determined by the electric field, which depends on the density gradient, adopted in order to provide for a zero current through the separatrix. The electric field may be found by solving (numerically) the kinetic equation in the vicinity of the separatrix, taking into account anomalous fluxes, probably poloidally asymmetric, and processes occurring in the SOL. To this end, the option to control the radial electric field in a tokamak appears to be particularly attractive. Besides the well-known method to alter the radial electric field in a tokamak by means of unbalanced neutral beam injection, the novel option to impose an arbitrary electric field inside a separatrix has been demonstrated recently. It is based upon employing an electrode biased with respect to a limiter or a divertor plate. A strong radial electric field results and triggers the L–H and

H–L transitions. Moreover, a large cross-field current emerges. Its value is determined by the nonlinear cross-field conductivity. The unfolding voltage–current characteristics point out flaws in the standard neoclassical theory because the latter predicts the cross-field current to be exactly zero. In contrast, the synergy of anomalous effects with the neoclassical theory leads to satisfactory agreement with experimental findings. Another option to control the radial electric field emerges by employing external coils, which provides for stochastization of the magnetic field. It is currently investigated on the tokamaks TEXT and TORE-SUPRA. The stochastization decreases the negative electric field in the bulk because of the nonambipolar electron flux resulting from it. Yet, the issue of radial electric fields in stochastic magnetic fields remains unresolved. In our opinion, novel methods to bring about radial electric fields and rotations in a tokamak may arise in the near future. This conjecture is also true within the SOL, where the biasing of a divertor plate or a limiter has been demonstrated to affect both the flows, primarily convective, and the boundary value of the electric field on a separatrix. Lastly, the impact of rotation remains unknown for new regimes with improved confinement such as the VH regime, recently discovered on D–DIII [107]. This problem is very topical at present.

This review was prepared for publication in 1993. Since then a lot of papers concerning plasma rotation in tokamaks have appeared, and here we shall briefly mention some of them. Spectroscopic measurements of poloidal rotation in D–DIII have shown [111] that in the H-regime the main ions rotate in the ion diamagnetic direction at a speed somewhat less than the ion diamagnetic speed. The poloidal rotation predicted by neoclassical theory has the same direction but is much smaller than the experimentally observed one. Several attempts were made to extend neoclassical theory to the case of steep gradients when the gradient length is comparable to the ion poloidal gyroradius. In [112, 113], the effect of orbit squeezing was taken into account and the poloidal rotation velocity was calculated:

$$V_\theta = \frac{c}{eB_0 n}\left(1 - S^{-1}\right)\frac{d\left(nT_i\right)}{dr} + k\frac{c}{eB_0}\frac{dT_i}{dr},$$

where

$$S = 1 - \frac{m_i c^2}{eB_\theta^2} \frac{dE_r}{dr}.$$

But even this reconsidered neoclassical theory still predicts the poloidal rotation to be much smaller than the observed one. This model was criticized by the authors of [114], who stated that poloidal rotation is unaffected by the squeezing. In [115], neoclassical inertia and gyroviscosity have been calculated for the steep density profile near the separatrix in the collisional plasma. These effects, in principle, could contribute to the anomalous inertia and viscosity discussed in the present review.

On the other hand, experiments on large tokamaks such as JET, D-DIII, and JT-60 demonstrated that regimes with improved confinement were observed for the parameters when neoclassical viscosity is negligible in comparison with anomalous terms, as was discussed in Section 4.2; see also [116]. According to this approach the poloidal rotation profile in the H-regime is determined by the density profile near the edge, which is consistent with D–DIII experiments. Moreover, recent experiments revealed the necessity of introducing the anomalous transport of toroidal momentum into any model. We can mention here the investigation of the parametric dependence of the electric field profile in JET-2M [117] and the analysis of the toroidal rotation profile in JET [118].

Recent papers analyzing the current–voltage characteristic of a biased electrode [119, 120] showed that pure neoclassics is not sufficient to explain the observed results. In [119] the hydrodynamic ion-neutral friction has been introduced. The friction force results in the additional conductivity

$$\sigma_\perp = n m_i c^2 \left(1 + 2q^2\right) \frac{\nu_{\text{in}}}{B^2},$$

where ν_{in} is the ion-neutral collision frequency. This conductivity is to be added to the one determined by the viscous force given by Eq. (4.21). In [120] the ion conductivity produced by

the banana particles due to ion-neutral collisions was estimated. Following their arguments one obtains

$$\sigma_\perp \approx nm_i c^2 \sqrt{\varepsilon}\, \frac{\nu_{\text{in}}}{B^2\Theta^2 \left[1 + \left(\frac{cE_r}{B\Theta\sqrt{T_i/m_i}}\right)^2\right]},$$

which is $\varepsilon^{-3/2}$ times larger than the hydrodynamic one. Of course, the question remains for both of these models whether the neutral density at the edge is sufficient to produce a significant effect. In [121] discontinuities in the potential profile during biasing were predicted, which is a direct indication of the role of anomalous momentum transport. In [122, 123], an explanation of the VH regime has been put forward based on the dependence of the turbulence level on the shear of the toroidal rotation (this effect is discussed in Section 4.1). Unfortunately, these arguments cannot be applied to regimes with the improved confinement without neutral beam injection, such as the hot mode in JET. An interesting effect of a "dithering"-periodic L–H and H–L transition observed in the ASDEX-Upgrade was described in [124]. The main idea was that oscillations are caused by the difference in response of the system to a rise of either density or temperature. This effect deserves further consideration on the basis of the more justified models.

In some recent papers [125, 126], the electric field just at a separatrix has been considered. The calculations supported the main idea discussed in Section 4.3 that both the radial and poloidal component of an electric field exist at a separatrix due to the particle loss to the divertor plates.

Significant progress was achieved in TdeV [127, 128]. Detailed measurements in the SOL during the biasing experiments were performed. Many features predicted theoretically in Section 6.3 (see also [129]) were observed. The scaling of the I–V characteristic on the parameters showed that fitting with the suggested ion mobility is reasonable with the exception of the high-density regimes where ion-neutral collisions could be important.

Appendices

A.1.

Here, we list some formulas in tokamak magnetic flux coordinates. The magnetic field in flux coordinates reads

$$\mathbf{B} = \mathbf{B}_\phi + \mathbf{B}_\theta = I(\Psi)\nabla\Phi + \nabla\Phi \times \nabla\Psi, \tag{A.1.1}$$

where Ψ is the poloidal magnetic flux and $I(\Psi) = RB_t$ is the value proportional to the current in toroidal coils plus the poloidal current in a plasma.

The averaging over magnetic surfaces (1.7) reads in these coordinates

$$\langle f \rangle = \oint \frac{dl_\theta}{B_\theta} f \Big/ \oint \frac{dl_\theta}{B_\theta} = \oint \frac{d\Theta}{\mathbf{B}\cdot\nabla\Theta} f \Big/ \oint \frac{d\Theta}{\mathbf{B}\cdot\nabla\Theta}. \tag{A.1.2}$$

For a weak toroidicity one obtains

$$\oint f \frac{dl_p}{B_p} = \frac{qR_0}{2\pi B_0}\sqrt{1+\varepsilon^2} \oint d\theta (1 - \varepsilon\cos\theta) f(\theta).$$

Therefore, Eq. (A.1.2) is equivalent to Eq. (1.7). Assuming the plasma density to be a constant within a flux surface, which implies $\nabla \cdot u_i = 0$, the flow velocity within a magnetic surface yields [11]

$$\begin{aligned} \mathbf{u}_i(\Psi) &= K_i(\Psi)\mathbf{B} + \omega(\Psi)R\mathbf{e}_\psi, \\ \omega(\Psi) &= -\frac{c}{RB_p}\left(\frac{dp_i}{ned\Psi} + \frac{d\varphi}{d\Psi}\right). \end{aligned} \tag{A.1.3}$$

For circular magnetic surfaces, dotting (A.1.3) with B, taking the toroidal component, and excluding $K_i(\Psi)$, we obtain relations (1.12) and (1.22). The parallel neoclassical viscosity takes the form [3]

$$\begin{aligned} \langle \mathbf{B}\cdot\nabla \overleftrightarrow{\pi} \rangle^{(\mathrm{NEO})} &= 3\langle \left(\frac{\mathbf{B}}{B}\cdot\nabla B\right)^2 \rangle \\ &\times \left[m_{i1} u_{i\theta}(\Psi) + \frac{2}{5} m_i^2 \frac{q_{i\theta}(\Psi)}{p_i} \right], \end{aligned} \tag{A.1.4}$$

where $u_{i\theta}$ and $q_{i\theta}$ are the poloidal velocity and heat flux, determined by

$$u_{i\theta}(\Psi) = \frac{\mathbf{u}_i \cdot \nabla\Theta}{B \cdot \Theta}, \qquad q_{i\theta}(\Psi) = \frac{\mathbf{q}_i \cdot \nabla\Theta}{B \cdot \Theta}.$$

The neoclassical coefficients m_{i1} and m_{i2} depend on the regime of collisionality. The equation for linear relaxation of the poloidal rotation takes the form [10]

$$m_i n \frac{\partial}{\partial t}\left[(1+2\hat{q}2)\langle \mathbf{u}_i \mathbf{B}_\theta\rangle + \langle RB_\phi\rangle\langle R^2\nabla\Phi\mathbf{u}_i\rangle/\langle R^2\rangle\right]$$
$$= -\langle \mathbf{B}\cdot\nabla\overleftrightarrow{\pi}\rangle^{(\mathrm{NEO})}, \quad \text{where} \quad \hat{q}^2 = \frac{\langle B_\phi^2\rangle - \langle B_\phi^{-2}\rangle^{-1}}{2\langle B_\theta^2\rangle}. \quad \text{(A.1.5)}$$

Neglecting the second term in Eq. (A.1.5), which describes the temporal evolution of the toroidal rotation, Eq. (A.1.5) is reduced to Eq. (3.1). Employing (A.1.4), the time scale of relaxation of poloidal rotation reads

$$t = \frac{1}{3}(1+2\hat{q}2)\frac{\langle B_\theta^2\rangle}{\langle(\mathbf{B}/B\cdot\nabla B)^2\rangle}\frac{m_i n}{m_{i1}}$$
$$\times\left[1 + k_p^{-1}\left(\frac{\langle B^2\rangle}{\langle B_\theta^2\rangle}(1+2\hat{q}^2)^{-1}\right)\right]\left(1+k_p^{-1}\right)^{-1}, \quad \text{(A.1.6)}$$

where $k_p = 4\pi n m_i c^2\langle R^2\rangle/\langle R^2 B_p^2\rangle$.

A.2.

Here, the expression for the radial flux of particles is derived for both spatially and temporally varying radial electric fields. We start from the drift kinetic equation

$$\frac{\partial f_j}{\partial t} + \mathbf{V}_{cj}\frac{\partial f_j}{\partial r} + \dot{V}_{j\|}\frac{\partial f_j}{\partial V_{j\|}} + \dot{V}_{j\perp}\frac{\partial f_j}{\partial V_{j\perp}} = \mathrm{St}_j, \quad \text{(A.2.1)}$$

where the anomalous transport velocity $u_r^{(\mathrm{A})}$ is included in the guiding center drift velocity $\mathbf{V}_{cj}$ as follows:

$$\mathbf{V}_{cj} = \mathbf{V}_{gj} - \frac{c}{B^2}[\nabla\varphi\times\mathbf{B}] + V_{j\|}\mathbf{e}_z + \mathbf{u}_r^{(\mathrm{A})}\mathbf{e}_r,$$

$$\begin{aligned}
\mathbf{V}_{gi} &= -\frac{c\left(V_{j\perp}^2/2 + V_{j\|}^2\right) m_j}{e_j B_0 R}\left(\sin\theta \mathbf{e}_r + \cos\theta \mathbf{e}_\theta\right), \\
\dot{\mathbf{V}}_{j\|} &= -\frac{e_j \Theta}{m_j}\frac{\partial \varphi}{r\partial\theta} - \frac{V_{j\|}^2}{2}\frac{\Theta\varepsilon\sin\theta}{r} + \frac{V_0 V_{j\|}\varepsilon\sin\theta}{r}, \\
\dot{V}_{j\perp} &= \frac{V_{j\|}V_{j\perp}}{2r}\Theta\varepsilon\sin\theta + \frac{V_0 V_{j\perp}}{2r}\varepsilon\sin\theta.
\end{aligned}$$

The distribution function and the potential are sought in the same form as in the stationary case

$$f_j = f_j(r) + f_{1j}(r,\theta), \qquad \varphi(r,\theta) = \varphi_0(r) + \varphi_1(r,\theta), \quad \text{(A.2.2)}$$

where f_{1j} and $\varphi_1 \sim \exp(i\theta)$ are first-order perturbations. Employing the Fourier expansion technique, we have

$$\begin{aligned}
f_{1j} &= \frac{1}{(2\pi)^2}\iint \tilde{f}_{1j}\exp(-i\omega t + ik_r r)d\omega dk_r, \\
V_0 &= \frac{1}{(2\pi)^2}\iint \tilde{V}_0\exp(-i\omega t + ik_r r)d\omega dk_r, \\
\varphi_1 &= \frac{1}{(2\pi)^2}\iint \tilde{\varphi}_1\exp(-i\omega t + ik_r r)d\omega dk_r. \quad \text{(A.2.3)}
\end{aligned}$$

We assume that the typical time scale of V_0 is much shorter than the typical time scales of the temperature and density profiles ($\partial \ln f_j/\partial r \ll \partial \ln V_0/\partial r$). The linearized kinetic equation for ions takes the form

$$\begin{aligned}
&i\left(\frac{\Theta V_{i\|}}{r} + k_r u_r^{(A)} - \omega\right)\tilde{f}_{1i} - \frac{ic\tilde{\varphi}_1}{Br}\frac{\partial f_{0i}}{\partial r} \\
&+\frac{ic}{eBr}\left(\frac{V_{i\perp}^2}{2} + V_{i\|}^2\right)\varepsilon\delta(\omega)\delta\left(k_r u_r^{(A)}\right)\exp(i\theta)\frac{\partial f_{0i}}{\partial r} \\
&+\frac{ie\Theta\varphi_1}{rm_i}\frac{\partial f_{0i}}{\partial V_{i\|}} + \frac{i\varepsilon m_i}{rT_i}f_{0i}\left(V_{i\|}^2 + \frac{V_{i\perp}^2}{2}\right)\tilde{V}_0\exp(i\theta) \\
&= \hat{\nu}\left(V_{i\|}, V_{i\perp}\right)\tilde{f}_{1i}. \quad \text{(A.2.4)}
\end{aligned}$$

Here, V_0 has been assumed to be much smaller than ΘC_S. In the plateau regime one obtains

$$\tilde{f}_{1i} = \left[\mathrm{PV}\left(\frac{1}{\Theta V_{i\|}/r + k_r u_r^{(\mathrm{A})} - \omega}\right) + i\pi\delta\left(\frac{\Theta V_{i\|}}{r} + k_r u_r^{(\mathrm{A})} - \omega\right)\right]$$
$$\frac{c\tilde{\varphi}_1}{Br}\frac{\partial f_{0i}}{\partial r} + \frac{c}{eBr}\left(\frac{V_{i\perp}^2}{2} + V_{i\|}^2\right)\varepsilon\delta(\omega)\delta\left(k_r u_r^{(\mathrm{A})}\right)\exp(i\theta)\frac{\partial f_{0i}}{\partial r}$$
$$+\frac{e\Theta\varphi_1}{rm_i}\frac{\partial f_{0i}}{\partial V_{i\|}} - \frac{\varepsilon m_i}{rT_i}f_{0i}\left(V_{i\|}^2 + \frac{V_{i\perp}^2}{2}\right)\tilde{V}_0\exp(i\theta), \qquad \text{(A.2.5)}$$

where PV is the principal value of an integral. Flux-surface averaging the distribution function, one obtains the total current carried by ions:

$$\langle j\rangle = e\int(\mathbf{V}_{ci})_r\,(f_{0i} + f_{1i})\,d\mathbf{V}_i. \qquad \text{(A.2.6)}$$

We substitute the distribution functions from (A.2.3), (A.2.5) into (A.2.6),

$$\langle j\rangle = \frac{1}{(2\pi)^2}\int d\omega\int dk_r\int d\mathbf{V}_i\int\frac{d\theta}{2\pi}\frac{cm_i\varepsilon^2}{eBR}\left(V_{i\|}^2 + \frac{V_{i\perp}^2}{2}\right)\sin\theta\exp(i\theta)$$
$$\times\left[\mathrm{PV}\left(\frac{1}{\Theta V_{i\|}/r + k_r u_r^{(\mathrm{A})} - \omega}\right) + i\pi\delta\left(\frac{\Theta V_{i\|}}{r} + k_r u_r^{(\mathrm{A})} - \omega\right)\right]$$
$$\times\left[\frac{cm_i}{eB}\delta(\omega)\delta\left(k_r u_r^{(\mathrm{A})}\right)\frac{\partial f_0}{\partial r} + \frac{m_i\tilde{V}_0}{T_i}f_{0i}\right] = \langle j_l\rangle + \langle j_h\rangle,$$

where

$$\langle j_l\rangle = -\frac{c}{\Theta B_0^2}\langle\mathbf{B}\cdot\nabla\overleftrightarrow{\pi}_i\rangle^{(\mathrm{NEO})} \qquad \text{(A.2.7)}$$

is the neoclassical current carried by ions with small poloidal velocities under the stationary conditions (2.12), (2.13) and $\langle j_h\rangle$ is the counter current carried by thermal particles owing to temporal and spatial variations of the radial electric field (see Eq. (3.5)). The integration in (A.2.7) can be carried out provided $\omega \ll \Theta C_S/r$ and $k_r u_r^{(\mathrm{A})} \ll \Theta C_S/r$. If this is the case, the

integral resulting from $i\pi\delta\left(\Theta V_{i\|}/r + k_r u_r^{(A)} - \omega\right)$ provides $\langle j_l \rangle$, which reads after the integration

$$\langle j_l \rangle = -\sqrt{\frac{\pi}{2}} \frac{n\varepsilon^2 c m_i^{1/2} T_i^{1/2}}{r\Theta B} \left(V_\theta - V_\theta^{(NEO)}\right), \qquad (A.2.8)$$

where

$$V_\theta^{(NEO)} = -\frac{c}{2eB_0}\frac{dT_i}{dr}$$

in accordance with (2.8), (2.10), and (2.13). The principal value integral in (A.2.7) may be reduced to

$$\langle j_h \rangle = \frac{1}{(2\pi)^2} \int d\omega \int dk_r \int \frac{d\theta}{2\pi} 2ecm_i\varepsilon^2 \left(\omega - k_r u_r^{(A)}\right) \times \tilde{V}_0 \sin\theta(\sin\theta + i\cos\theta). \qquad (A.2.9)$$

Accounting for

$$\frac{1}{(2\pi)^2} \int d\omega \int dk_r \left(\omega - k_r u_r^{(A)}\right) \tilde{V}_0 = i\left(\frac{\partial V_0}{\partial t} + u_r^{(A)}\frac{\partial V_0}{\partial r}\right)$$

one obtains

$$\langle j_h \rangle = -2q^2 \frac{cm_i n}{B}\frac{dV_0}{dt} \approx -2q^2 \frac{cm_i n}{B}\frac{dV_\theta}{dt}, \qquad (A.2.10)$$

where

$$\frac{d}{dt} = \frac{\partial}{\partial t} + u_r^{(A)}\frac{\partial}{\partial r}.$$

In Eq. (A.2.10) the conventional polarization (inertial) drift occurring in cylindrical geometry is ignored. Adding this drift to Eq. (A.2.10), we have

$$\langle j_h \rangle = -\left(1 + 2q^2\right)\frac{cm_i n}{B}\frac{dV_\theta}{dt}. \qquad (A.2.11)$$

Hence the current continuity

$$\langle j \rangle = \langle j_l \rangle + \langle j_h \rangle = 0 \qquad (A.2.12)$$

results in Eq. (3.1), describing the temporal relaxation of the poloidal rotation velocity.

REFERENCES

1. A. A. Galeev and R. Z. Sagdeev, in: *Reviews of Plasma Physics* (edited by M. A. Leontovich), Vol. 7, Consultants Bureau, New York (1979), p. 257.
2. F. L. Hinton and R. D. Hazeltine, *Rev. Mod. Phys.*, **48**, 239–308 (1976).
3. S. P. Hirshman and D. J. Sigmar, *Nucl. Fusion*, **21**, 1079–1201 (1981).
4. L. M. Kovrizhnykh, *Itogi Nauki i Tehniki: Fizika Plazmy*, Vol. 3 (1982), pp. 239–281.
5. D. G. Bulyginsky, S. G. Goncharov, S. A. Grashin, et al., *Proc. 10th Int. Conf. on Controlled Fusion and Plasma Physics*, Vol. 1, London (1984), pp. 491–501.
6. V. I. Bugaraya, A. V. Gorshkov, S. A. Grashin, I. V. Ivanov, V. A. Krupin, A. V. Mel'nikov, K. A. Razumova, Yu. A. Sokolov, V. M. Trukhin, A. V. Chankin, P. N. Yushmanov, L. I. Krupnik, and I. S. Nedzel'skij, *Nucl. Fusion*, **25**, 1707 (1985).
7. S. Suckewer, H. P. Eubank, R. J. Goldston, et al., *Nucl. Fusion*, **21**, 1301–1309 (1981).
8. K. Brau, M. Bitter, R. J. Goldston, et al., *Nucl. Fusion*, **23**, 1301–1309 (1983).
9. G. A. Hallock, J. Mathew, W. C. Jennings, R. L. Hickok, A. J. Wotton, and R. C. Isler, *Phys. Rev. Lett.*, **56**, 1248 (1986).
10. S. P. Hirshman, *Nucl. Fusion*, **18**, 917–927 (1978).
11. S. P. Hirshman, *Phys. Fluids*, **21**, 224–229 (1978).
12. M. Tendler and V. Rozhansky, in: *Proceedings of the 17th European Conference on Controlled Fusion-Plasma Physics* (edited by G. Briffod, A. Nijsen-Vis, and F. C. Schüller) Vol. 14B, Part 2, European Physical Society, Amsterdam (1990), pp. 744–747.
13. V. A. Rozhansky and M. B. Tendler, *Sov. Phys., JETP Lett.*, **53**, 82–84 (1991).
14. V. Rozhansky and M. Tendler, *Phys. Fluids*, **B4**, 1877–1888 (1992).
15. R. J. Groebner, K. H. Burrell, and R. P. Saraydarian, *Phys. Rev. Lett.*, **64**, 3015 (1990), and references therein.

16. K. Ida, S. Hidekuma, Y. Miura, et al., *Phys. Rev. Lett.*, **65**, 1364–1367 (1990).
17. K. Ida, S. Hidekuma, M. Kojima, et al., *Phys. Fluids*, **B4**, 2552–2559 (1992).
18. A. R. Field, G. Fussman, J. V. Hofmann, and the ASDEX Team, *Nucl. Fusion*, **32**, 1191–1208 (1992).
19. H. Biglari, P. Diamond, and P. Terry, *Phys. Fluids*, **B2**, 1 (1990).
20. T. E. Stringer, *Phys. Rev. Lett.*, **22**, 770–773 (1969).
21. T. E. Stringer, *Phys. Fluids*, **13**, 1586–1595 (1970).
22. R. D. Hazeltine, E. P. Lee, and M. N. Rosenbluth, *Phys. Rev. Lett.*, **25**, 427 (1970); *Phys. Fluids*, **14**, 361–370 (1971).
23. S. K. Wong and K. Burrel, *Phys. Fluids*, **25**, 1863–1870 (1982).
24. A. B. Mikhailovsky, *Fiz. Plazmy*, **9**, 926–937 (1983).
25. V. A. Rozhansky, *Fiz. Plazmy*, **11**, 250–253 (1985).
26. V. S. Tsypin, *Fiz. Plazmy*, **11**, 344–351 (1985).
27. V. A. Rozhansky and L. D. Tsendin, *Fiz. Plazmy*, **5**, 1257–1263 (1979).
28. V. Rozhansky, A. Samain, and M. Tendler, *Proc. 18th Conf. on Controlled Fusion and Plasma Physics*, Vol. 15, Part IV, Berlin (1991), pp. 133–136.
29. M. Tendler and D. Heifetz, *Fusion Technol.*, **11**, 289–310 (1987).
30. S. I. Itoh and K. Itoh, *Phys. Rev. Lett.*, **60**, 2276–2279 (1988).
31. S. I. Itoh and K. Itoh, *Nucl. Fusion*, **29**, 1031–1045 (1989).
32. K. C. Shaing and E. C. Crume, *Phys. Rev. Lett.*, **63**, 2369–2372 (1989).
33. K. C. Shaing, *Phys. Fluids*, **B2**, 2847–2849 (1990).
34. K. C. Shaing, E. C. Crume, and W. A. Houlberg, *Phys. Fluids*, **B2**, 1492–1498 (1990).
35. K. C. Shaing, *Phys. Fluids*, **B4**, 171–175 (1992).
36. K. C. Shaing, *Phys. Fluids*, **B4**, 290–291 (1992).
37. K. C. Shaing, *Phys. Fluids*, **B4**, 3310–3315 (1992).
38. R. D. Hazeltine, *Phys. Fluids*, **B1**, 2031 (1989).

39. M. Tendler, U. Daybelge, and V. Rozhansky, in: *Proceedings of the 14th International Conference on Plasma Physics and Controlled Fusion Research*, Vol. 2, paper IAEA-CN-56/D-4-8, Wurzburg (1992).

40. A. B. Hassam, T. M. Antonsen, J. F. Drake, and C. S. Liu, *Phys. Rev. Lett.*, **66**, 309–312 (1991).

41. J. F. Drake, A. B. Hassam, P. N. Guzdar, C. S. Liu, and D. Mc Carthy, *Nucl. Fusion*, **32**, 1657–1661 (1992).

42. P. H. Diamond and Y. B. Kim, *Phys. Fluids*, **B3**, 2050–2061 (1991).

43. J. F. Drake, J. M. Finn, P. N. Guzdar, et al., *Phys. Fluids*, **B4**, 488–491 (1992).

44. J. M. Finn, J. F. Drake, P. N. Guzdar, et al., *Phys. Fluids*, **B4**, 2758–2768 (1992).

45. N. Mattor, *Phys. Fluids*, **B4**, 3448–3450 (1992).

46. F. L. Hinton, *Phys. Fluids*, **B3**, 696–704 (1991).

47. Y. B. Kim, P. H. Diamond, and R. Groebner, *Phys. Fluids*, **B3**, 2050–2061 (1991).

48. R. J. Taylor, M. L. Braun, B. D. Fried, H. Grote, J. R. Liberati, G. J. Morales, and P. Prybil, *Phys. Rev. Lett.*, **63**, 2365 (1989).

49. R. Van Nienwenhove, G. Van Oost, R. Weynants, et al., in: *Proc. 18th European Conference on Controlled Fusion and Plasma Physics*, Vol. 15C, Part 1, Berlin (1991), pp. 405–408.

50. L. G. Askinazi, V. E. Golant, E. R. Its, et al., in: *Proc. 18th European Conference on Controlled Fusion and Plasma Physics*, Vol. 15C, Part 1, Berlin (1991), pp. 401–404.

51. R. Weynants, G. Van Oost, G. Bertschinger, et al., *Nucl. Fusion*, **92**, 837–8853 (1992).

52. Y. B. Kim and F. L. Hinton, *Phys. Fluids*, **B4**, 278–279 (1992).

53. L. G. Askinazi, V. E. Golant, S. V. Lebedev, V. A. Rozhansky, and M. Tendler, *Nucl. Fusion*, **32**, 271–277 (1992).

54. V. A. Rozhansky and L. D. Tsendin, *Fiz. Plazmy*, **5**, 771–776 (1979).

55. M. Tendler, *Proc. 8th Conf. on Plasma Phys. and Controlled Fusion Research*, Vol. 1, IAEA, Brussels (1980), pp. 765–773.

56. V. A. Rozhansky, *Fiz. Plazmy*, **6**, 850–859, (1980) and **10**, 254–259, (1984).
57. V. A. Krupin and P. V. Yushmanov, *Proc. 14th European Conf. on Controlled Fusion and Plasma Phys.*, Vol. IID, Part 2, Madrid (1987), p. 761.
58. A. V. Nedospasov and M. Z. Tokar, in: *Reviews of Plasma Physics* (edited by B. B. Kadomtsev), Vol. 18, Consultants Bureau, New York (1993), pp. 77–238.
59. G. F. Chew, M. L. Goldberger, and F. E. Low, *Proc. R. Soc., London*, **236A**, 112–122 (1956).
60. L. D. Landau and E. M. Lifshits, *The Classical Theory of Fields*, Addison-Wesley, New York (1951).
61. F. L. Hinton and M. N. Rosenbluth, *Phys. Fluids*, **16**, 836–864 (1973).
62. R. D. Hazeltine, *Phys. Fluids*, **17**, 961–968 (1974).
63. B. B. Kadomtsev, D. H. Morozov, and O. P. Pogutse, *Pis'ma Zh. Eksp. Teor. Fiz.*, **40**, 80–82 (1984).
64. D. H. Morozov and O. P. Pogutse, *Fiz. Plazmy*, **12**, 666–676 (1986).
65. M. N. Rosenbluth, P. H. Rutherford, J. B. Taylor, E. A. Frieman, and L. M. Kovrizhnikh, in: *Plasma Physics and Controlled Nuclear Fusion Research*, Vol. 2, International Atomic Energy Agency, Vienna (1972), pp. 495–507.
66. K. T. Tsang and E. A. Frieman, *Phys. Fluids*, **19**, 747–756 (1976).
67. D. V. Sivukhin, in: *Reviews of Plasma Physics* (edited by M. Leontovich), Vol. 1, Gosatomizdat (1963), pp. 7–97. English translation: Consultants Bureau, New York (1965).
68. K. C. Shaing, R. D. Hazeltine, and H. Sanuki, *Phys. Fluids*, **B4**, 404–410 (1992).
69. K. C. Shaing, *Phys. Fluids*, **B2**, 2847–2849 (1992).
70. W. M. Stacey Jr. and D. J. Sigmar, *Phys. Fluids*, **28**, 2800–2807 (1985).
71. A. B. Mikhailovsky and V. S. Tsypin, *Fiz. Plazmy*, **10**, 245–253 (1984).
72. S. M. Egorov, B.V. Kuteev, and V. A. Rozhansky, *Pis'ma Zh. Eksp. Teor. Fiz.*, **13**, 569–573 (1987).

73. K. C. Shaing and S. P. Hirhman, *Phys. Fluids*, **B1**, 705–707 (1989).

74. F. L. Hinton and J. A. Robertson, *Phys. Fluids*, **27**, 1243–1247 (1984).

75. R. J. Taylor and L. Oren, *Phys. Rev. Lett.*, **42**, 446–449 (1979).

76. Z. A. Pietrzyk, A. Pochelon, R. Behn, et al., *Nucl. Fusion*, **32**, 1735–1753 (1992).

77. L. G. Askinazi, V. E. Golant, S. V. Lebedev et al., *Phys. Fluids*, **B5**, 2420–2427 (1993).

78. B. Lehnert, *Phys. Fluids*, **9**, 1367–1372 (1966).

79. T. H. Dupree, *Phys. Fluids*, **15**, 334–347 (1972).

80. Y. B. Kim, P. H. Diamond, H. Biglari, and P. W. Terry, *Phys. Fluids*, **B2**, 2143–2150 (1990).

81. B. B. Kadomtsev and O. P. Pogutse, in: *Reviews of Plasma Physics* (edited by M. Leontovich), Vol. 5 (1967), pp. 209–350. English translation: Consultants Bureau, New York (1970).

82. A. B. Hassam, *Phys. Fluids*, **B4**, 485–487 (1992).

83. G. M. Staebler and R. R. Dominguez, *Nucl. Fusion*, **31**, 1891–1898 (1991).

84. X. H. Wang, P. H. Diamond, and M. N. Rosenbluth, *Phys. Fluids*, **B4**, 2402–2410 (1992).

85. B. Basu and B. Coppi, *Phys. Fluids*, **B4**, 2817–2822 (1992).

86. M. Wakatani, K. Watanabe, H. Sugama, and A. Hasegawa, *Phys. Fluids*, **B4**, 1754–1765 (1992).

87. F. L. Waelbroeck, T. M. Antonsen, P. N. Guzdar, and A. B. Hassam, *Phys. Fluids*, **B4**, 2441–2447 (1992).

88. B. A. Carreras, K. Sidikman, P. H. Diamond, P. W. Terry, and L. Carcia, *Phys. Fluids*, **B4**, 3115–3131 (1992).

89. R. R. Weynants and R. J. Taylor, *Nucl. Fusion*, **30**, 945–949 (1990).

90. P. H. Gohil et al., *Proc. 18th Eur. Conf. on Controlled Fusion and Plasma Physics*, Vol. 15C, Part 1 (1991), pp. 289–293.

91. X. Z. Yang, B. Z. Zhang, A. J. Wootton, P. M. Schoh, B. Richards, D. Baldwin, D. L. Brower, G. G. Castle, R. D. Hazeltine, J. W. Heard, R. L. Hickok, W. L. Li, H. Lin,

S. C. McCool, V. J. Simcic, Ch. P. Ritz, and C. X. Yu, *Phys. Fluids*, **B3**, 3448 (1991).

92. G. M. Staebler and R. R. Dominguez, *Nucl. Fusion*, **33**, 77–82 (1993).
93. S. I. Braginski, in: *Reviews of Plasma Physics* (edited by M. Leontovich), Vol. 1 (1963), pp. 183–271. English translation: Consultants Bureau, New York (1965).
94. D. Bohm, in: *The Characteristics of Electrical Discharges in Magnetic Fields* (edited by A. Gurthrie and R. Wakerling), Chapters 1, 2, 9, McGraw-Hill, New York (1949).
95. A. V. Nedospasov and V. G. Petrov, *Nucl. Fusion*, **26**, 1529–1536 (1986).
96. B. La Bombard and B. Lipchultz, *Nucl. Fusion*, **27**, 81–89 (1987).
97. M. Tendler and V. Rozhansky, *Comments Plasma Phys. Controlled Fusion*, **13**, 191–206 (1990).
98. G. M. Staebler, *Nucl. Fusion*, **31**, 729–737 (1993).
99. G. M. Staebler and F. L. Hinton, *Nucl. Fusion*, **29**, 1820–1824 (1989).
100. P. B. Parks, *Nucl. Fusion*, **29**, 373–378 (1989).
101. E. L. Void, F. Najmabadi, and R. Conn, *Phys. Fluids*, **B3**, 3132–3152 (1991).
102. JET Team, *Proc. 12th Int. Conf. Plasma Phys. and Controlled Fusion*, Vol. 3, paper IAEA-CN-50/A-III-2, Nice (1988).
103. J. F. Luciani and P. Mora, *Phys. Rev. Lett.*, **67**, 3098–3101 (1991).
104. V. Rozhansky, *Sov. J. Plasma Physics*, **15**, 638 (1989).
105. V. Rozanski, *Contrib. Plasma Phys.*, **34**, 144–150 (1994).
106. I. Nakazawa et al., *Proc. 16th Eur. Conf. on Controlled Fusion and Plasma Physics*, Vol. 13B, (1989), pp. 887–890.
107. G. L. Jackson, J. Winter, T. S. Taylor, et al., *Phys. Rev. Lett.*, **67**, 3098–3101 (1991).
108. B. Terreault, P. Couture, B. L. Stansfield, et al., *Nucl. Fusion*, **32**, 1181–1190 (1992).
109. M. J. Schaffer, M. A. Mahdavi, C. C. Klepper, D. N. Hill, and M. E. Rensink, *Nucl. Fusion*, **32**, 855–861 (1992).

110. H. Berk and K. Molvig, *Phys. Fluids*, **26**, 1385–1389 (1983).

111. J. Kim, K. H. Burrel, P. Gohil, et al., *Phys. Rev. Lett.*, **72**, 2199–2204 (1994).

112. F. L. Hinton, Y. B. Kim, A. Brizard, and K. H. Burrel, *Phys. Rev. Lett.*, **72**, 1216–1219 (1994).

113. F. L. Hinton and Y. B. Kim, *Plasmas*, **2**, 159–166 (1995).

114. K. S. Shaing, C. T. Hsu, and R. D. Hazeltine, *Phys. Plasmas*, **1**, 3365–3368 (1994).

115. A. L. Rogister, *Phys. Plasmas*, **1**, 619–635 (1994).

116. V. Rozansky and M. Tendler, *Proc. 21th Eur. Conf. on Controlled Fusion and Plasma Phys.*, **18B**, Part 1, pp. 516–519 (1994).

117. K. Ida, K. Itoh, S. I. Itoh, et al., *Phys. Plasmas*, **1**, 116–119 (1994).

118. R. Sabot and V. Parail, *Proc. 21th Eur. Conf. on Controlled Fusion and Plasma Phys.*, **18B**, Part 1, 350–354 (1994).

119. J. Cornelius, R. Sporken, G. Van Oost, and R. R. Weynants, *Nucl. Fusion*, **34**, 171–183 (1994).

120. H. Xiao, R. D. Hazeltine, Y. Z. Zhang, and P. M. Valanju, *Phys. Fluids*, **B5**, 4499–4501 (1993).

121. T. E. Stringer, *Nucl. Fusion*, **33**, 1249–1265 (1993).

122. K. S. Shaing, *Phys. Fluids*, **B5**, 2122–2124 (1993).

123. K. S. Shaing, *Phys. Plasmas*, **1**, 219–221 (1994).

124. H. Zohm et al., *Phys. Rev. Lett.*, **72** 222–225 (1994).

125. P. V. Yushmanov, J. Q. Dong, W. Horton, X. N. Su, and S. I. Krasheninnikov, *Phys. Plasmas*, **1**, 1583–1591 (1994).

126. H. Xiao, R. D. Hazeltine, and P. M. Valanju, *Phys. Plasmas*, **1**, 3641–3645 (1994).

127. R. Decoste et al., *Phys. Plasmas*, **1**, 1497–1502 (1994).

128. J.-L. Lachambre et al., *Nucl. Fusion*, **34**, 1431–1445 (1994).

129. V. Rozanski and M. Tendler, *Phys. Plasmas*, **1**, 2711–2717 (1994).